EWEM

Master of Science Thesis

3D Aerodynamic Effects and Circulation Control of Vertical Axis Wind Turbines

Wessel Jan Tonnis Keijer

24 July 2020

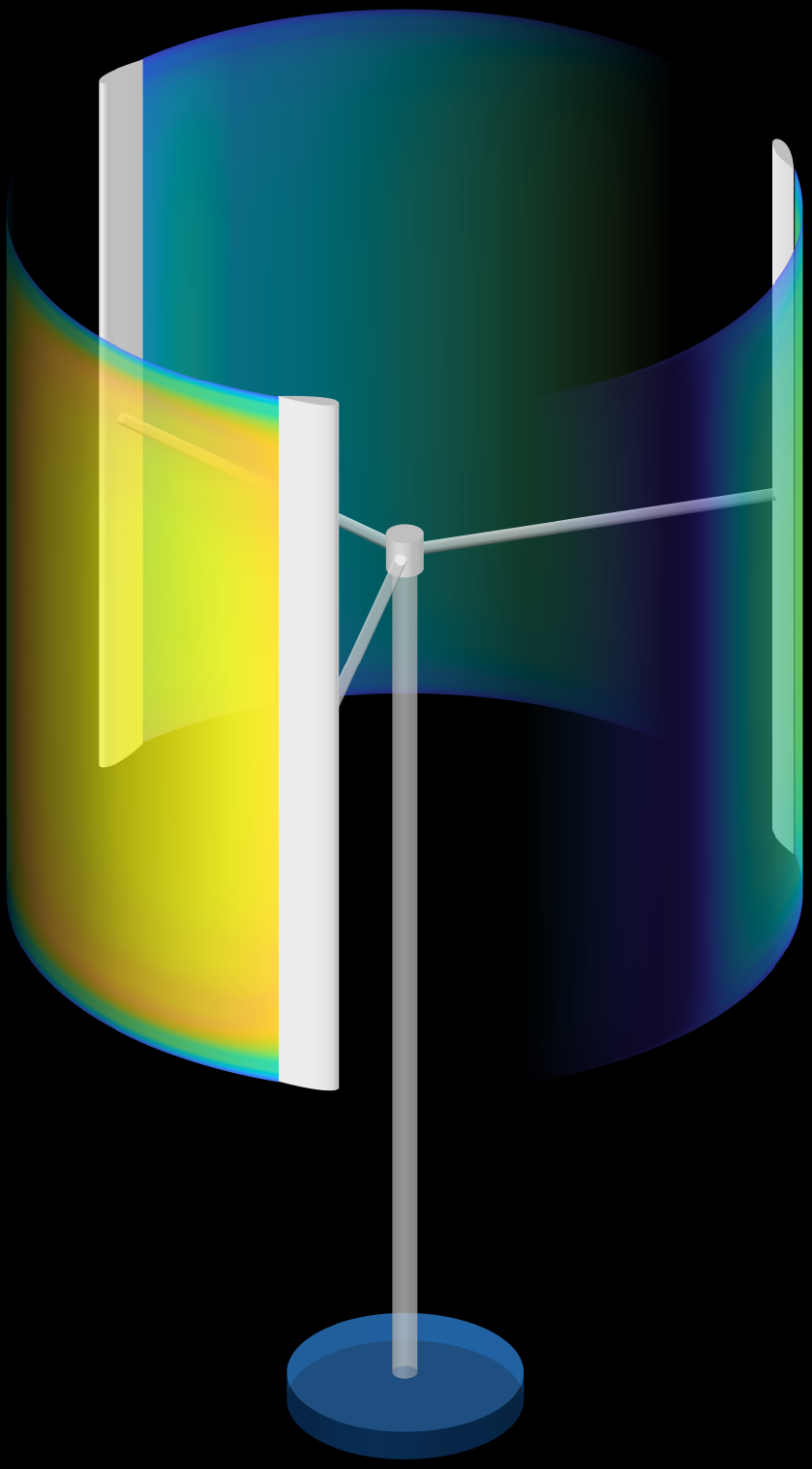

DTU

TU Delft

EWEM

Master of Science Thesis

To obtain the degree of:
Master of Science in **Aerospace Engineering** at Delft University of Technology
Master of Science in **Engineering (European Wind Energy)** at Technical University of Denmark

Author:
Wessel Jan Tonnis Keijer

Student, European Wind Energy Master, Rotor Design track, Aerodynamics profile
Wind Energy Group, Faculty of Aerospace Engineering, Delft University of Technology
Department of Wind Energy, Technical University of Denmark

Supervisors

Carlos Simão Ferreira	Professor	Delft University of Technology
Delphine De Tavernier	PhD Candidate	Delft University of Technology
Uwe Schmidt Paulsen	Senior Scientist	Technical University of Denmark
Martin O.L. Hansen	Associate Professor	Technical University of Denmark
Georg Pirrung	Researcher	Technical University of Denmark

An electronic version of this thesis is available at repository.tudelft.nl and findit.dtu.dk.

DTU TUDelft

Abstract

The vertical axis wind turbine (VAWT) concept in its current, fixed-pitch iteration is hindered by lower aerodynamic efficiency compared to existing horizontal axis wind turbines. Implementing a form of circulation control on the VAWT by actively pitching the blades throughout the turbine's rotation could potentially enhance power capture efficiency and reduce loads variability. In this thesis, circulation control is investigated in 3D, since the 3D flow field differs significantly from the 2D equivalent.[89]

After a review of available 2D and 3D aerodynamic models for the VAWT, a suitable candidate emerges in the form of HAWC2 NW,[78] which is a lifting-line based extension to popular aeroelastic modelling suite HAWC2[54] designed to model trailed vorticity in the near wake of the blade. HAWC2 NW is used to conduct fast 3D aerodynamic simulations of a highly simplified vertical axis wind turbine geometry to demonstrate the influence of 3D effects on the flow field surrounding the VAWT. The slenderness of the turbine geometry, expressed using the turbine aspect ratio H/D, turns out to be a major factor in determining the performance losses due to 3D effects.

Subsequently, HAWC2 NW is used to analyze optimized pitch sequences with various objectives, such as maximum power or a certain normal loading distribution. A relationship is found between the ratio of upwind and downwind normal loading, the turbine aspect ratio H/D and the 3D power coefficient $C_{P,3D}$. The most important conclusion is that when considering the design of a vertical axis wind turbine with a turbine aspect ratio $H/D < 5$, losses due to 3D effects can be minimized by implementing a circulation control strategy in such a way that the normal loading is uniformly distributed between the upwind and downwind half-cycles.

Acknowledgements

I would like to express my sincere gratitude to the following people, without whom this project would not have been possible:

- Uwe Schmidt Paulsen, my DTU main supervisor, who inspired me to pursue the topic of vertical axis wind turbine circulation control in particular, assembled a formidable team of supervisors to support me and was always there to give me feedback on drafts or chapters I wrote.
- Carlos Simão Ferreira, my TU Delft main supervisor, who inspired me to combine an investigation into 3D effects and circulation control and was able to see at the very beginning of the project what I only saw much later: a beautifully symmetric relationship between power coefficient and load distribution in 3D!
- Delphine De Tavernier, who had the unfortunate luck of sharing an office with me at DTU Risø while I asked her non-stop questions about VAWT aerodynamics, a topic I had little previous knowledge of before starting this project. Additionally, she introduced me to the actuator cylinder model and provided the CACTUS and actuator line CFD simulation results essential to the first part of this thesis. She was also kind enough to give me my first co-authorship of a paper on 3D aerodynamic models for VAWT[24], for which I am very grateful.
- Georg Pirrung, who not only provided the HAWC2 NW near-wake model for VAWTs with variable pitch implementation but also supported me with informative replies to my many e-mails about this largely undocumented aerodynamic model.
- Martin Hansen, whose lecture on vertical axis wind turbine aerodynamics during the Wind Turbine Technology and Aerodynamics course at DTU sparked my interest in VAWTs, as well as providing the Unsteady BEM model and interesting discussions regarding specific research avenues to pursue throughout the thesis projects.
- Jennifer Rinker, who introduced me to Uwe and taught me how to use HAWC2 both during the Loads, Aerodynamics & Control course at DTU and after, at the beginning of the thesis project, when I kept messing up basic stuff in my models!
- Everyone else at the Loads & Control and Aerodynamic Design sections of DTU Wind Energy in Risø who provided me with interesting discussions and brainstorm sessions during the weeks I was there in the beginning of 2020.

Preface

This thesis is the culmination of my studies in the European Wind Energy Master's Rotor Design track, specifically the MSc in Aerospace Engineering at TU Delft and the MSc in Engineering - Wind Energy at the Technical University of Denmark. Part of the project has been carried out at DTU Wind Energy in Risø, Denmark and part of it at home, in close collaboration with experts from both universities, over the course of the last 9 months. I have been lucky enough to benefit from the supervision of 5 experts in the field of vertical axis wind turbine aerodynamics, who, even during a global pandemic, managed to guide me to the goals I had set out to achieve in the beginning of the project through countless hours of online meetings and reviewing my many drafts and presentation slides filled with crazy ideas.

Contents

List of Figures

List of Tables

List of symbols

Symbol	Explanation	Unit
α_{geom}	Geometric angle of attack	deg
α	Angle of attack	deg
Δp	Pressure jump across actuator cylinder	Pa
Γ	Circulation	$\frac{m^2}{s}$
λ	Tip speed ratio $\frac{\omega R}{V_\infty}$	-
ω	Rotational speed	rad/s
ρ	Air density	$\frac{kg}{m^3}$
σ	Rotor solidity $\frac{Bc}{2R}$	-
θ_p	Blade pitch angle	deg
θ	Azimuth angle	deg
a_n	Induction factor in the normal direction (rotor coord. system)	-
a	Streamwise induction factor	-
A	Turbine frontal area	m^2
B	Number of blades	-
b	Loadform shape parameter	-
$C_{P,2D}$	2D power coefficient $\frac{P}{\frac{1}{2}\rho c V_\infty^3}$	-
$C_{P,3D}$	3D power coefficient $\frac{P}{\frac{1}{2}\rho A V_\infty^3}$	-
$C_{P,i}$	Ideal power coefficient	-
$C_{T,2D}$	2D thrust coefficient	-
$C_{T,3D}$	3D thrust coefficient	-
$C_{Tdownwind}$	Thrust coefficient of the downwind half-cycle	-
$C_{Tupwind}$	Thrust coefficient of the upwind half-cycle	-
C_D	Drag coefficient	-
C_L	Lift coefficient	-
C_n	Normal force coefficient	-
C_P	Power coefficient	-
C_T	Thrust coefficient	-
C_t	Tangential force coefficient	-
c	Blade chord	m
D	Turbine diameter	m
D	Aerodynamic drag	N
F_n	Force in normal (radial) direction	N/m
F_t	Force in tangential direction	N/m
H/D	Turbine aspect ratio	-
H	Turbine height (blade length)	m
k_a	Mod-lin correction factor	-
K_T	Upwind/downwind load distribution ratio	-
L	Aerodynamic lift	N
M	Aerodynamic moment	N

Symbol	Explanation	Unit
$Q_{n,max}$	Maximum normal loading	-
Q_n	Normal loading	-
Q_t	Tangential loading	-
R	Turbine radius	m
V_{rel}	Relative velocity	m/s
V_∞	Freestream velocity	m/s
V_n	Velocity in normal (radial) direction (rotor coord. system)	m/s
V_t	Velocity in tangential direction (rotor coord. system)	m/s
V_x	Velocity in x-direction (global coord. system)	m/s
V_y	Velocity in y-direction (global coord. system)	m/s
W_x	Induced velocity in the x-direction (global coord. system)	m/s
W_y	Induced velocity in the y-direction (global coord. system)	m/s

List of abbreviations

Abbreviation	Definition
AC	Actuator Cylinder
AD	Actuator Disk
AL	Actuator-Line
BEM	Blade Element Momentum
CACTUS	Code for Axial and Cross-flow Turbine Simulations
CFD	Computational Fluid Dynamics
DMST	Double Multiple Stream-tube
DNS	Direct Numerical Simulations
HAWC2	Horizontal Axis Wind turbine simulation Code 2nd generation
HAWC2 NW	HAWC2 with lifting-line based near-wake correction model
HAWT	Horizontal Axis Wind Turbine
LES	Large Eddy Simulations
Mod-Lin ACM	Modified Linear Actuator Cylinder Model
MST	Multiple Stream-tube
RANS	Reynolds-averaged Navier-Stokes
UBEM	Unsteady BEM
VAWT	Vertical Axis Wind Turbine

Chapter 1

Introduction

In a world where the importance of renewable energy solutions is paramount, no stone should be left unturned. In the wind energy field, horizontal axis wind turbines (HAWT's) have traditionally reigned supreme, but radically different solutions exist and could potentially disrupt future markets. One such solution is the vertical axis wind turbine (VAWT), of which several types exist as shown in Figure 1.1.

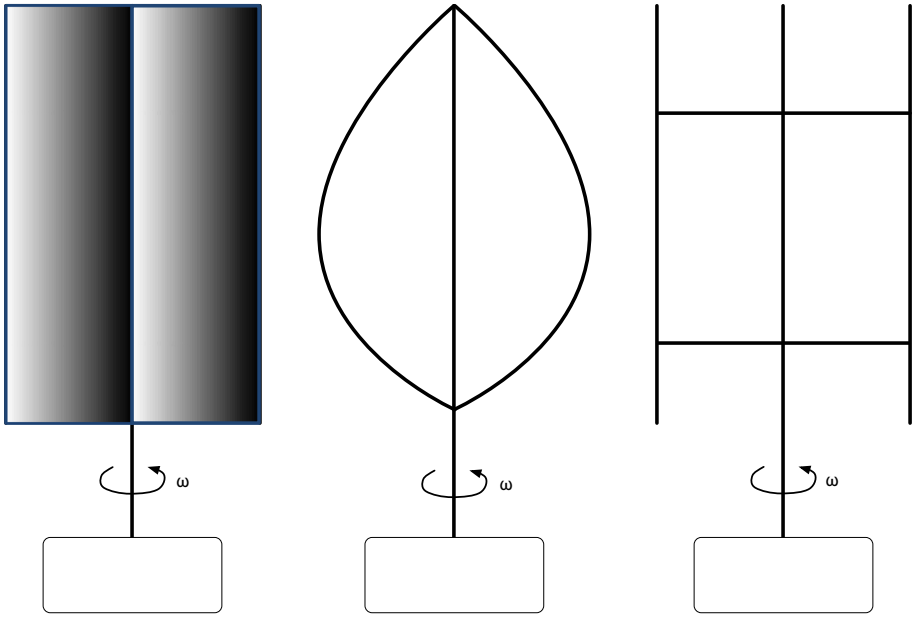

(a) Savonius (b) Darrieus (c) H-rotor (gyromill)

Figure 1.1: Principal types of vertical axis wind turbines. Adapted from [38, p.151].

The Savonius-rotor shown in Figure 1.1a is a drag-driven design. Although its design is simple and straightforward, it has inherently poor aerodynamic performance and is not often used. Figures 1.1b and 1.1c show the Darrieus and H-rotor type lift-driven vertical axis wind turbines. The Darrieus turbine is known for its phi-shape, with the blades shaped in a so-called troposkein curve [1]. This particular shape is ideal to reduce the internal bending stresses of the blades that arise due to high centrifugal forces whilst in operation. The H-rotor VAWT, shown in Figure 1.1c, is the simplest of

[1] The troposkein curve can be described as the shape assumed by a rope when spun around a certain axis.

the three at first glance, though one of the most complex in terms of its aerodynamics. This VAWT type will be investigated in this thesis, as its long straight blades are suitable for circulation control by means of full-blade pitching.

The fixed pitch H-rotor VAWT traditionally has several advantages and disadvantages, as outlined by Liu et al.[57].

Advantages

- Insensitivity to wind direction
- Relatively low noise emissions
- Simplified blade geometry
- Easy maintenance access due to wear-sensitive components, such as the drivetrain, being located at ground or sea level

Disadvantages

- Large angle of attack variation with every revolution
- Cyclic loading of blades and other components (detrimental to fatigue performance)
- Relatively low power coefficient C_p in fixed-pitch configurations
- Large required starting torque resulting in poor low-speed performance

Disadvantages mainly arise from the cyclic variation in the angle of attack within a single revolution; a phenomenon inherent to the VAWT that the HAWT does not suffer from. This thesis aims to explore some of the phenomena that make up the VAWT's complex aerodynamic nature, describe & compare models to capture these phenomena and introduce and validate new techniques to improve the efficiency and operating parameters of the VAWT. Specifically, aerodynamic effects that occur in 3D will be investigated, both in terms of how accurately they can be modelled using existing tools and how they might affect methods to increase the performance of the VAWT, such as circulation control.

Circulation control in this thesis refers to a means of achieving a certain prescribed loading on the turbine depending on the set objective. This could potentially have various benefits:

- Reducing dynamic stall effects arising from rapid changes in angle of attack of the blades
- Reducing cyclical loading of components and thereby improve fatigue performance
- Improving overall power capture efficiency (raised C_p, better power curve)
- Improving starting torque compared to fixed-pitch VAWTs
- To reduce loads during extreme wind-speed events by minimizing cross-sectional area
- To optimize the wake resulting in better downstream turbine performance
- Functioning as an aerodynamic brake in high-wind conditions and/or as a means of eliminating vibrations in standstill conditions.

11744

Circulation control is commonly achieved using some type of active blade pitching mechanism, although several other methods exist, which will be treated in Chapter 2. This thesis will focus primarily on full-blade pitch control, whilst briefly highlighting some more complex methods that exist, such as flap control or partial blade pitching.

1.1 Objective and research questions

The objective of the research is to take three-dimensional studies of circulation control for vertical axis wind turbines forward, through understanding and modelling the effects that lead to the 3D flow

field being significantly different from the 2D equivalent and revealing how this affects circulation control strategies in 3D. To further specify this objective, the following research questions have been formulated.

- To what extent can 3D effects be resolved by available VAWT aerodynamic models?
  - What are the specific types of 3D effects encountered in VAWT aerodynamics?
  - What are the fundamental differences in 3D effects between HAWTs and VAWTs?
  - What modelling techniques exist to model VAWTs?
  - To what extent do these modelling approaches capture the 3D effects?
  - How do the VAWT aerodynamic models compare internally and optionally with experimental data, in terms of their ability to resolve 3D and tip effects?
  - What is the percentage improvement in tip loss prediction using HAWC2 NW versus the current version of HAWC2?
- How can circulation control for VAWTs be used to achieve power, load or wake control in 3D?
  - What objectives can be of interest in terms of circulation control? (e.g. maximising power, minimising loads)
  - How can circulation control be achieved practically, using pitch control, flaps, etc.?
  - What are the differences between 2D and 3D circulation control?
  - To what extent does 2D circulation optimisation (for a certain objective) apply to the 3D case?

1.2 Methodology

The aforementioned research questions are answered in the body of this thesis. The overall structure in which this is done is as follows:

- Chapter 2 establishes the theoretical basis of the research through a thorough review of available literature in the field. A research gap is identified, justifying the relevance of the aforementioned proposed research objective.
- Chapter 3 presents a closer look at the differences between one-, two- and three-dimensional VAWT aerodynamics, as well as how it compares to traditional HAWT aerodynamic modelling.
- Chapter 4 attempts to answer the first set of research questions related to the current state of aerodynamic modelling for VAWT in 2D and 3D. Several relevant aerodynamic models are introduced, explained and tested, allowing for a comparison with a focus on how (if at all) these models resolve 3D effects.
- Chapter 5 introduces the concept of circulation control through active pitching and establishes a means of modelling and optimizing pitch sequences using the 2D actuator cylinder model. This chapter forms the 2D theoretical basis for Chapter 6 to compare against.
- Chapter 6 treats the analysis of circulation control in 3D using HAWC2 NW using various circulation control objectives. The concept of load uniformity and its effect on 3D VAWT aerodynamics is investigated. The 2D optimization strategy outlined in Chapter 5 is tested in 3D and results are compared.
- Chapter 7 summarizes the findings that have been obtained throughout this thesis, as well as offering a series of recommendations for future research regarding model validation and 3D VAWT aerodynamic design. A brief description of the contribution of the thesis to the field of vertical axis wind turbine aerodynamics research is also provided.

Chapter 2

State of the art

In this chapter, the theoretical basis as well as relevant prior research output will be established for four aspects of VAWT aerodynamics that are pertinent to the aim of this thesis:

- Aerodynamic phenomena
- Circulation control
- Farm performance
- 3D effects

In doing so, a research gap will be identified, providing a subspace of VAWT aerodynamics research in which this thesis will operate.

2.1 Aerodynamic phenomena in the VAWT

During operation, the aerodynamics of the VAWT are affected by a range of aerodynamic phenomena. In this section, the most prominent of these phenomena will be described, as well as their relevance to the VAWT.

2.1.1 Stall

Stall is an important aerodynamic concept for wind turbines in general, but specifically the VAWT since it experiences stall on its blades multiple times in a single revolution. McCullough and Gault[67] describe three primary types of stall:

- **Trailing edge stall**, where the flow separation point moves from the trailing edge to the leading edge as the angle of attack increases. Possible flow reattachment if angle of attack is sufficiently small.
- **Leading edge stall**, flow separation that originates at the leading edge, typically at high angles of attack. Flow doesn't reattach.
- **Thin airfoil stall**, which, as its name implies, occurs on thin airfoils where the flow separates abruptly at the leading edge but reattaches further towards the trailing edge with increasing angle of attack.

Trailing edge stall is typical for wind turbines due to the relatively thick airfoils that are usually used. For vertical axis wind turbines, power production increases with increasing airfoil thickness[71]. For horizontal axis wind turbines, thick airfoils are often chosen for structural considerations, allowing resistance against the large flapwise bending moment. For vertical axis wind turbines, leading edge stall is more pertinent than trailing edge stall due to the large range of angle of attacks its blades experience while in operation.

2.1.2 Dynamic stall

The three different types of stall described in the previous section are steady aerodynamic phenomena. On real wind turbine blades however, dynamic stall becomes an issue.

Gaunaa[33] defines dynamic stall as an unsteady aerodynamic phenomenon that occurs when the angle of attack that an airfoil is exposed to exceeds the static stall angle while moving in a transient manner compared to the freestream velocity. It is characterized by large flow separation events and vortex shedding. It is relevant because if large pitch changes occur, the resulting dynamic loads due to dynamic stall can far exceed their static counterparts.

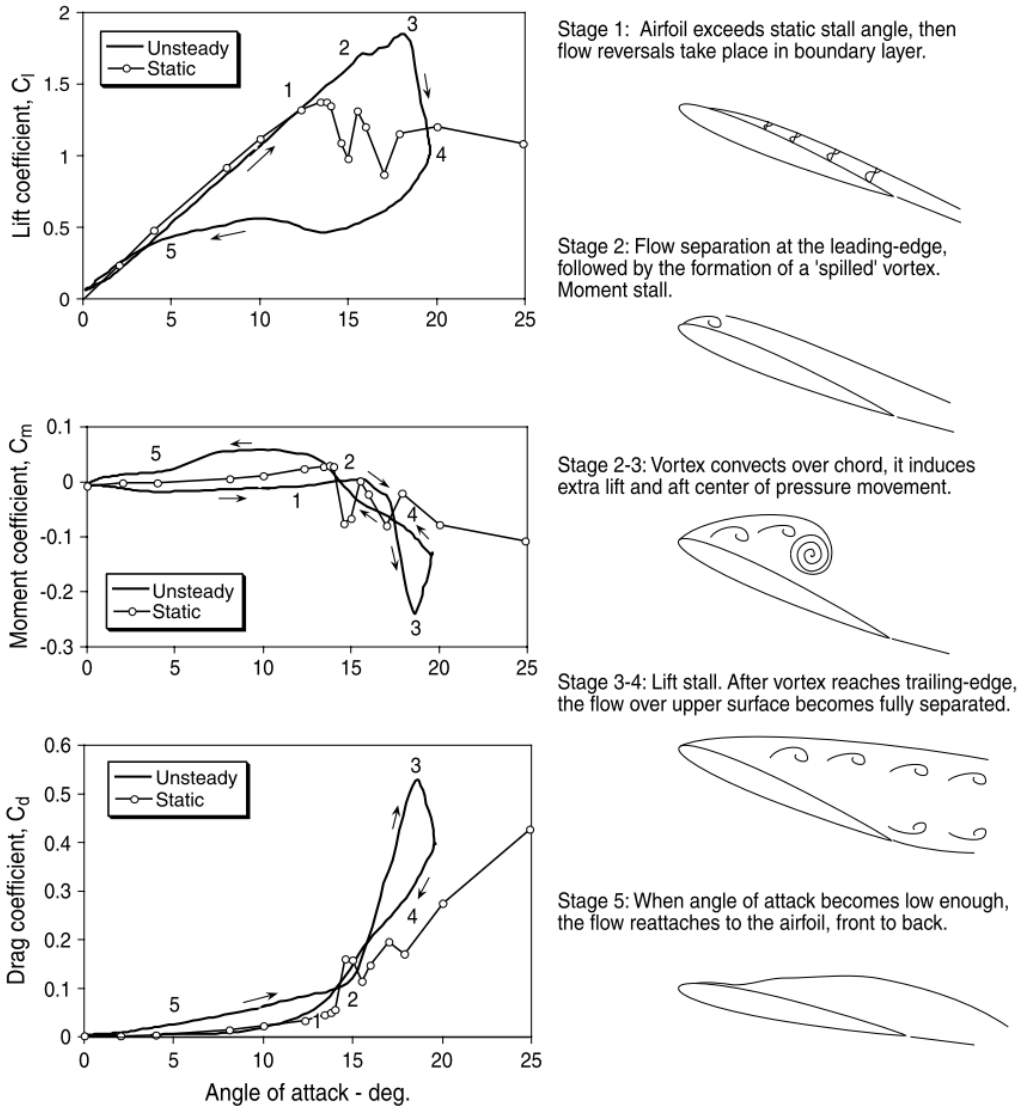

Figure 2.1: The process of dynamic leading edge stall (reproduced from Leishman[55]).

Figure 2.1 describes the physical process of dynamic stall, starting with the angle of attack exceeding the static stall angle. The figure shows both the lift and drag coefficient of the airfoil increasing significantly beyond their maximum static counterparts, causing large additional loading.

Stig Øye[100] proposed a dynamic stall model that is specifically intended for the field of wind turbine aerodynamics. It takes into account both trailing edge and leading edge separation, unlike the Theodorsen theory, which solely deals with attached flow. The Stig Øye model uses a so-called

separation function f_s and an expression that gives the lift coefficient for fully separated flow (Equation (2.1),[100]). The separation function indicates at what point along the airfoil separation occurs.

$$C_L^{fs} = \frac{C_L^{st} - C_L^{\alpha}(\alpha - \alpha_0)f_{st}}{1 - f_{st}} \tag{2.1}$$

Leishman and Beddoes[56] improved upon the aforementioned models by also treating several corrections for the drag and moment coefficients of the airfoil, rather than just correcting the lift. It also eliminates the incompressible flow assumption of the Theodorsen theory and Stig Øye model[38, p.85].

Aside from the Stig Øye and Beddoes-Leishman models, several other dynamic stall models exist. Holierhoek et al.[43] compares the aforementioned with the following additional models:

- Risø model[37]
- Snel model[94]
- Onera model[66]

Holierhoek et al.[43] conducted experiments using stereo-PIV measurements in the blade root region of a HAWT. They concluded that the dynamic stall models under investigation create ample room for improvement, as they sometimes produce errors that would significantly affect the accuracy of an aeroelastic simulation that makes use of the model. While there is no clear winner in terms of accuracy, Holierhoek does note that the ONERA and Beddoes-Leishman methods do take into account airfoil parameters whereas the Snel method does not, meaning they cannot be compared to each other in a fair manner.

HAWT blades typically experience dynamic stall due to turbulence, gusts, shear or yaw effects[16], which, while important, are neglected in simpler aerodynamic models such as the steady Blade Element Momentum method (see Chapter 4). For VAWTs however, dynamic stall is an inherent phenomenon, caused by the rapid variation of its blades through a wide range of angles of attack. Ignoring it in a simple aerodynamic model will result in significant errors in estimating the induced velocity, particularly at low tip speed ratios.

The importance of accurate dynamic stall modelling for vertical axis wind turbines was outlined by Buchner et al.[14]. They also proved experimentally that while the tip speed ratio is a large determining factor of dynamic stall, the blade chord length, pitch rate and freestream velocity also play an important role.

Pirrung and Gaunaa[81] describe several modifications that can be made to the Beddoes-Leishman model used in the aero-servo-elastic time simulation tool HAWC2 .[54] The modifications would allow for better modelling of dynamic stall on the VAWT, because the original model was designed more specifically for HAWTs. The primary differences arise from the greater angle of attack variation that VAWT blades experience, as well as the normal acceleration the airfoil sections of the VAWT blades experience while under rotation.

2.1.3 Unsteady airfoil aerodynamics in attached flow

Theodorsen[104] devised a theory to calculate the transient lift effects brought about by rapidly pitching airfoils, provided the flow remains attached during the pitching event. This theory is formulated in terms of the Theodorsen and Wagner functions, respectively in frequency and time domain. The Theodorsen function is a function of the reduced frequency k, which represents the degree of unsteadiness of the flow. k=0 is considered to be steady, values of k under 0.05 indicate quasi-steadiness and anything above this is fully unsteady. The Wagner indicial lift response function is derived by applying an inverse Fourier transformation to the Theodorsen equation, resulting in a time-domain expression of the Wagner function $\Phi(t^*)$, which represents the ratio between steady state lift and

circulatory lift (which contains transient effects). This is shown in Figure 2.2b, where it can be seen that the instantaneous lift available after a sudden change in angle of attack is only 50% of the steady state lift. Over time, the lift on the airfoil tends towards the steady state lift.

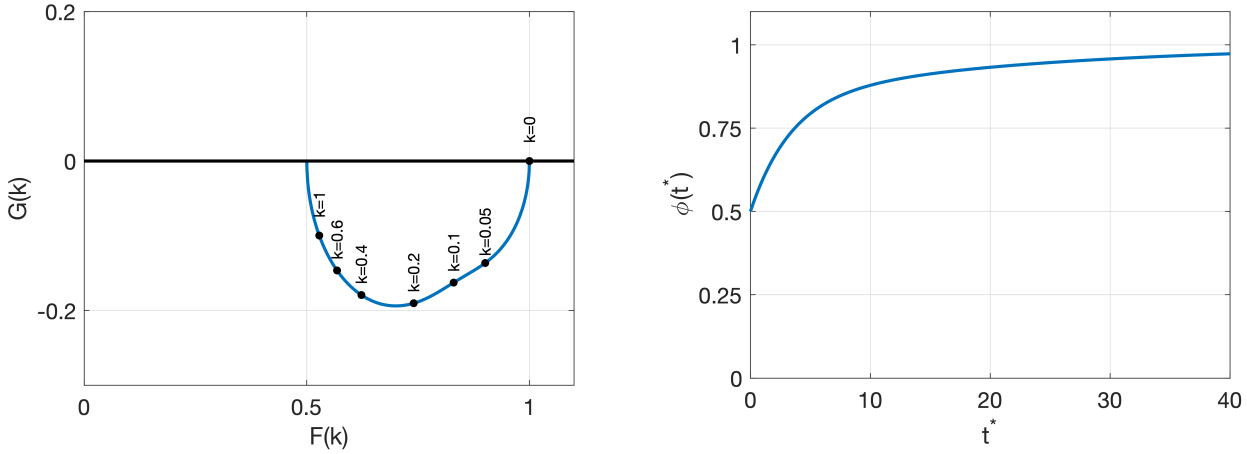

(a) Frequency domain: Theodorsen function

(b) Time domain: Wagner function

Figure 2.2: Functions describing transient lift on an airfoil experiencing rapid pitching motion in attached flow, according to Theodorsen [104]. Values are plotted using the approximation by Jones [46].

The Jones [46] approximation of the Theodorsen function shown in Figure 2.2a is only valid for a flat plate. Bergami et al. [9] set about deriving an empirical relation to extend this indicial lift response to that of a finite-thickness airfoil, which exhibits different behaviour from the flat-plate assumption. The paper also goes on to describe the relevance of several different indicial function approximations to wind turbine aeroelastic modelling, although it concludes that the difference between the flat-plate and finite-thickness situations is only slight and would result in a minor increase in fatigue and ultimate loads.

2.1.4 Blade-vortex interaction

During operation, the blade tips of the VAWT generate trailing vortices with a circulation that is on the same order of that of the bound vortex on the blade. [91] Any subsequent blade passing through this wake will therefore experience a significant flow disturbance as compared to the steady inflow that arises only from the freestream velocity and rotation of the turbine.

This phenomenon is called blade-vortex interaction and was studied extensively by Scheurich et al. [87]. They showed that the aforementioned flow disturbance due to blade-vortex interaction indeed has a sizeable effect on blade loading. Additionally, the omission of blade-vortex interaction in lower-fidelity codes may lead to significant disagreements between models and experimental data.

Ferrer and Willden [31] developed a method that could be used to predict the operating conditions (particularly tip speed ratio λ) under which blade wake interaction is a significant factor. Additionally, they predict several different types of blade-wake interactions and the tip speed ratios at which they are expected to occur, depending on the axial induction factor the turbine is operating at.

Simão Ferreira et al. [91] studied the 3D wake dynamics of the VAWT using particle image velocimetry. They identified one of the regions of the near-wake of the VAWT as being dominated by blade-wake interaction. This is the downwind region, where the blade is interacting with trailed vorticity that has been shed by blades passing through the upwind region. The blade-vortex interaction in this region results in an increased induction and therefore a decrease in efficiency as compared to the 2D case, without shed vorticity from the blade tips.

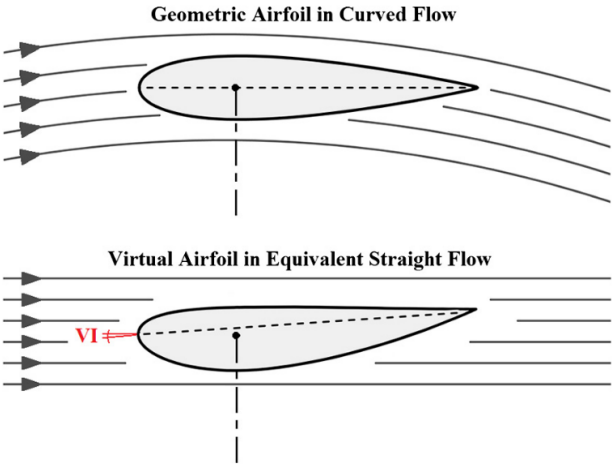

Figure 2.3: Effects of flow curvature on streamlines and airfoil shape in straight flow. Reproduced from Bianchini et al.[10].

2.1.5 Flow curvature

Airfoil sections as seen in aircraft wings and, to some extent, HAWT blades are subject to flow that can be described using linear streamlines. For a VAWT however, the continuous rotation of the blades with respect to the freestream results in the streamlines being curvilinear as seen from the frame of reference of the airfoil section.

The flow curvature phenomenon was investigated by Migliore et al.[70], who demonstrated that there is a significant difference in lift, drag and moment coefficients between airfoils in straight and in curvilinear flow. They also devised a technique with which the actual airfoil shape can be mapped to a virtual equivalent, different only in camber and angle of incidence, that exhibits similar behaviour in straight flow as the original airfoil would in curvilinear flow. Figure 2.3 shows this technique, where the virtual airfoil in equivalent straight flow has a different airfoil shape as well as a new 'virtual' incidence angle with the straight flow.

The virtual airfoil mapping technique was further investigated by Akimoto et al.[2]. They, along with Migliore et al.[70], proposed that the mapping should preserve local surface angles. Van Der Horst et al.[107] present an overview of the aforementioned methods, in addition to other methods that do not preserve local surface angles and instead merely transform the camber line and reconstruct the original airfoil around this. This paper supplements the original study by Migliore et al.[70] by simulating the effects of having a finite-thickness airfoil using XFOIL, rather than the flat-plate assumption made in the original paper.

Taking into account flow curvature effects is crucial, for instance when designing new airfoils for the VAWT. Conducting wind tunnel tests on these airfoils and using the resulting data to predict their performance when implemented in a VAWT will result in significant errors. The primary determinants of these errors are the chord to radius ratio c/R, the blade pitch angle, azimuthal angle and the tip speed ratio.[70]

Flow curvature effects are also commonly included in the attached flow part of the unsteady aerodynamics model (see Section 2.1.3) using acceleration and pitch rate terms[81]. Therefore, before implementing any kind of flow curvature correction, one should ensure that the attached flow part of the dynamic stall model explicitly excludes flow curvature effects to avoid correcting twice, which may lead to erroneous results.

2.1.6 Dynamic inflow

Unsteady aerodynamic effects such as dynamic stall and blade-vortex interaction occur at the rotor plane scale, with a characteristic time scale on the same order of the time needed for a full revolution of the rotor. Dynamic inflow however is an unsteady phenomenon that can cause fluctuations of the inflow velocity on a time scale much larger than this, on the order of D/U (rotor diameter and wind speed) according to Snel and Schepers [95].

In their report, Snel and Schepers evaluate several engineering models of the dynamic inflow phenomenon, because computations using fully unsteady flow models that resolve the entire wake required an prohibitive amount of computational effort at the time of writing (1991). While processing power has increased immensely since then, fast engineering models are still desirable as they can be used in time-series simulation software to account for the influence of such dynamic phenomena at every timestep.

Knudsen and Bak [51] discussed the range of different dynamic inflow models and their application to wind turbine control. The simplest ones merely simulate the transient behaviour using a lead-lag filter on their static counterparts. This results in a similar response, but is an approximation and not very physically correct. The most complex dynamic inflow models make use of the blade element momentum method with an additional equation that dynamically calculates the induction factor, which is quite computationally expensive because it has to reach convergence for all blade elements and all timesteps. In the paper, Knudsen and Bak propose a model that is positioned in between these two extremes, being relatively computationally efficient whilst being more accurate than a simple lead-lag filter.

Henriksen et al. [40] conducted a comparative study comprising several aerodynamic models to study the effect of dynamic inflow and compare the results to the aero-servo-elastic time series simulation tool HAWC2. [54] The models they discussed were:

- HAWC2, which uses an unsteady BEM aerodynamic model as described by Madsen et al. [65].
- Full BEM-based dynamic inflow model (BEM^{full}) which takes into account the converged dynamic induction at all blade elements. It is based on a model originally developed by Stig Øye [99].
- Simplified BEM-based dynamic inflow model (BEM^{simple}, the main objective of the paper) where the simplification is achieved by having an average axial induction instead of calculating it for each blade element and assuming the tangential induction is quasi-steady.
- Quasi-steady BEM-based model (BEM^{qs}) that does not take into account dynamic inflow, meaning the wake changes instantly when the turbine is subjected to a change in wind speed or pitch angle.

Figure 2.4 shows a result of their efforts, demonstrating the importance of having some kind of dynamic inflow model as there are large initial differences in both the torque and thrust of the simulated turbine when subjecting it to a wind speed step input. The full BEM approach can be seen to be in good agreement with HAWC2 results, but most importantly, the simple BEM dynamic inflow model is not far behind in terms of accuracy whilst requiring much less computational effort.

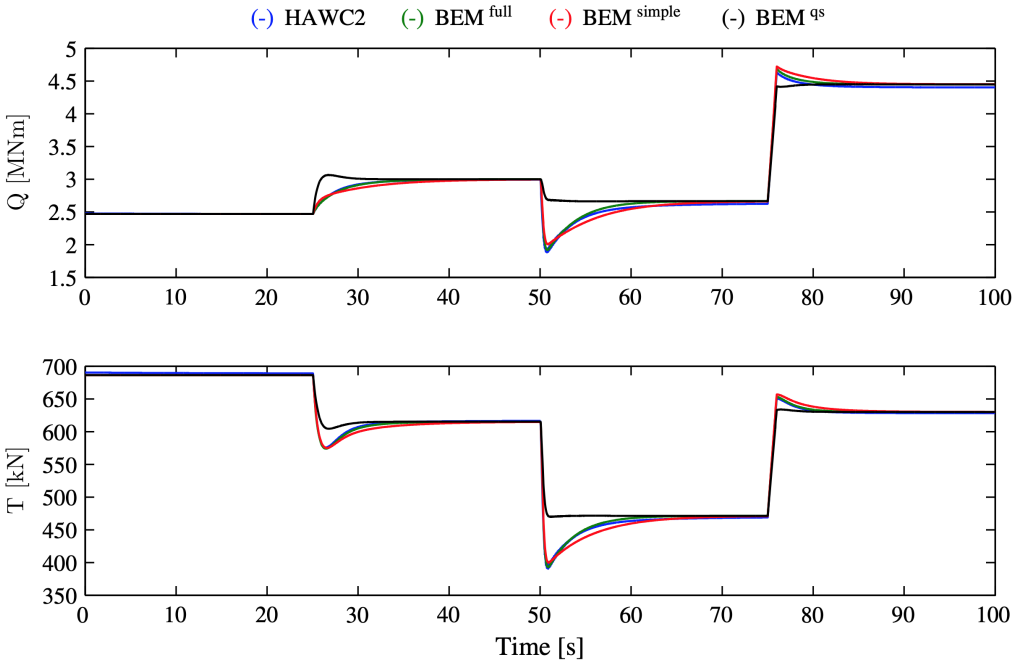

Figure 2.4: Comparison of aerodynamic models and their response to step inputs in wind speed on the NREL 5MW reference turbine (reproduced from Henriksen et al. [40]).

De Tavernier and Simão Ferreira [22] described the need for accurate dynamic inflow modelling for the VAWT, as an important use case of this turbine is on floating offshore platforms. In such conditions, hydrodynamic forces may induce significant motions to the turbine, which causes variation in the flow conditions at the rotor. Waves in a certain direction may, for example, induce a rolling motion that results in higher torque on the rotor, which in turn again has an effect on the overall dynamics of the turbine-platform combination. More so than with HAWTs, the dynamic inflow phenomenon for VAWTs poses a complex, highly coupled problem. Several models, one of which being HAWC2 ,[61] already allow for the modelling of this coupled behaviour, but include dynamic inflow models that were originally designed for horizontal axis wind turbines.

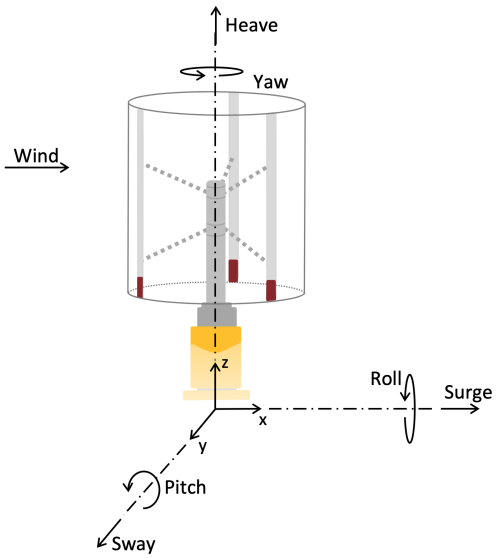

Figure 2.5: Types of motions on a VAWT located on a floating platform (reproduced from De Tavernier and Simão Ferreira [22]).

De Tavernier and Simão Ferreira [22] stated that while current dynamic inflow engineering models are primarily focused on HAWTs, they mostly work for VAWTs as well, except at certain time steps, when the aerodynamic model without dynamic inflow actually works better. They conclude that it is probably worth looking into modelling approaches specific to VAWTs to better capture its behaviour when subjected to dynamic inflow conditions such as on a floating platform.

2.2 Circulation control

Circulation control is a multi-faceted concept that usually indicates some implementation of active flow control over a wing or blade with the intention of improving its aerodynamic performance at one or multiple operating points. In aeronautics, circulation control has been used to improve the maximum lift coefficients of aircraft wings, delay stall and/or flow separation or even modify the effective camber and chord of the airfoil section. Early research dates back as far as 1938 and was concerned mostly with the concept of blown flaps, which experienced an increase in lift with the addition of high-velocity air jets on their surface.[1] Some research also focused on the use of circulation control for control surfaces, requiring little to no mechanical actuation compared to conventional methods. There are large theoretical benefits associated with using circulation control methods to augment lift on aircraft and thus improve performance at slow speeds or other difficult operating conditions. Traditional methods of achieving this, such as trailing edge or leading edge high-lift devices, generate large amounts of drag, both in use and when stowed, whereas active circulation control methods do not, or do so in a negligible manner. Practically however, the addition of (redundant) systems to drive the circulation controlled wing resulted in large increases in complexity and weight which often negated the aforementioned theoretical benefits. [52]

In the 1970s, helicopter rotors also started to become a potentially interesting application for circulation control methods, with researchers trying to increase the lift to drag ratio in order to improve performance. One study also examined potential acoustic benefits that come with circulation controlled rotors [113]. As with many other rotary wing engineering research areas (such as aeroelasticity), these techniques eventually trickled down into the wind turbine rotor field. Tongchitpakdee et al. [106] studied the effect of active (using a Coanda jet) and passive (using a Gurney flap) circulation control methods on an NREL baseline rotor configuration and found that some power increases can be obtained, although both methods become ineffective with the advent of flow separation at higher wind speeds.

Additionally, Baleriola et al. [5] demonstrated experimentally the potential benefits of a horizontal axis wind turbine blade with blowing jets on its trailing edge, which significantly altered the pressure distribution around the blade. An increase in C_L of up to 0.3 was observed for the non-rotating case (blade in straight flow) and reductions in bending moment fluctuation were visible when tested in a rotating configuration.

For the VAWT, circulation control has also been an active research area. Wilhelm et al. [112] investigated the potential performance improvements of circulation controlled blades on an H-rotor vertical axis wind turbine. The blades were fitted with blowing slots on their trailing edge towards both tips and an increase in power production of 24% was observed compared to the turbine's performance when the blowing slots were inactive. Wilhelm used the results from these experiments to validate a momentum-based modelling approach based on the multiple streamtube model of Strickland [101], as well as a vortex-based approach.

[1] The method of using blowing slots on wing or blade leading or trailing edges makes use of the Coanda effect . [58]

Where the aforementioned circulation control methods were mostly blowing-slot based, Rezaeiha et al.[85] used leading edge slot suction rather than trailing edge slot blowing to achieve separation control on a VAWT blade. Their results are based on a CFD model of the VAWT and give an indication of the dependence of the aforementioned power increases on several operational conditions, such as the tip speed ratio, Reynolds number and turbulence intensity. It is shown that operation at low tip speed ratios, where VAWTs are known to perform poorly, is particularly improved using this method of circulation control.

Another method of circulation control is by plasma actuators. The work of Greenblatt et al.[35] studies the power enhancement of a vertical axis wind turbine fitted with plasma actuators on the leading edges of the rotor blades. By controlling flow separation on the upwind half of the turbine revolution, they achieved power coefficient increases of their scale model in the wind tunnel of up to 38%. Perhaps most importantly, the authors showed that this could be achieved using only 1.7%-3.3% of the turbine's generated power to power the plasma actuators, yielding a significant net power increase.

Further research by Greenblatt et al.[36] investigated dynamic stall control with these same plasma actuators, visualizing its effects using phase-locked particle image velocimetry. The plasma actuation has the effect of reducing the size of dynamic stall vortices and moving them closer to the surface of the blade, although the power required to drive the actuators in this case was much larger than the potential power gains, resulting in a net power loss.

Lastly, probably the most well-known method of circulation control for aircraft, HAWTs and VAWTs is through some kind of blade pitch or flap control. Pitch control is an integral part of modern HAWTs in operation today and enables cost-effective operation in a wide range of site conditions. For VAWTs however, limited operational pitch-controlled examples exist.

Early work on VAWT pitch control, its advantages and the need for accurate aerodynamic modelling tools for this application was carried out by Walters and Migliore[111]. They stated that future applications of vertical axis wind turbines as cost-effective energy conversion systems are heavily dependent upon accurate aerodynamic modelling of both the fixed-pitch and circulation controlled VAWT.

The most rudimentary form of VAWT pitch control is exemplified by the cycloturbine or gyromill, invented in the 1970s by Herman Drees as outlined in the report of Noll et al.[75]. It uses a form of passive pitch control, or first-order pitch control, to reduce or even eliminate the effects of dynamic stall on the blades throughout the revolution and obtain significantly higher power coefficients than were deemed possible at the time.

Firstly, Vandenberghe and Dick[109] were among the first to implement and test in a wind tunnel a second order pitch control scheme for a model VAWT. They also devised a mathematical model based on the free vortex wake method to predict the performance of this second order pitch controlled turbine.

More recently, Chougule et al.[18] used a DMST model to estimate the performance of a newly designed VAWT with actively pitching blades as a means of circulation control. The new VAWT design uses three double-section blades, consisting of a normal blade with a slat section in front of its leading edge. They showed improvements in power coefficient as well as in starting performance when varying the pitch of the double-section blade as a whole throughout the rotation of the turbine.

A similar DMST model to predict the performance of an actively pitching VAWT was devised by Soraghan et al.[96]. Their model included aerodynamic phenomena that are important for the VAWT, such as flow curvature effects, tip and root losses and dynamic stall.

Flap control has also been an important part of the research efforts into VAWT circulation control.

Ertem et al.[30] investigated the aerodynamics of adding a trailing edge flap to the straight turbine blades, using the modified linear actuator cylinder model. The objectives they aimed to achieve with active flap control were as follows:

- Power efficiency (C_P)
- Rated power control
- Peak load alleviation

Some of the most interesting findings from this work do not originate from the part where the trailing edge flap is studied. The preparatory part of the study investigated, for a VAWT with an infinite number of blades, the optimum aerodynamic loadings using the Mod-Lin ACM (see Section 4.3). The 2D formulation of the actuator cylinder model is used to devise a Matlab model which is subsequently validated against aeroelastic design tool HAWC2[54] (which itself uses an implementation of mod-lin ACM as its aerodynamic model). The concept of the 'loadform' is then introduced, which indicates the the azimuthal distribution of the normal loading on the actuator cylinder that can be used to compute parameters such as the induction and relevant velocities, according to Madsen et al.[62]. One of the interesting conclusions from this analysis is that the power coefficient can be kept constant for different thrust loadings (a unique property of the VAWT). This is shown visually in Figure 2.6, where a region of high C_P for varying C_T can be observed. This phenomenon can be utilized by changing the ratio of upwind to downwind loading on the actuator cylinder.

It has also been studied extensively by Simão Ferreira and Scheurich[90], who employed a 2D panel method and a vorticity transport method to show that the instantaneous aerodynamic loading on the blade is indeed decoupled from the turbine generated power. This enables a range of different blade loadings and thus blade shapes to achieve the same optimum power objective (in 2D).

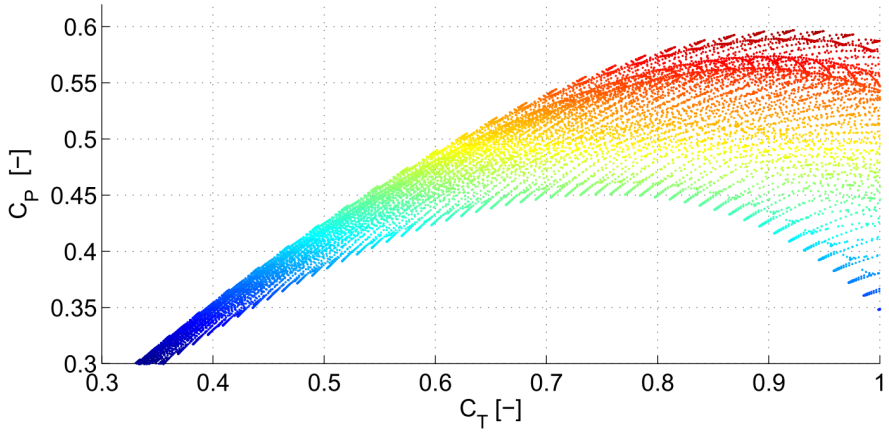

Figure 2.6: Design space of the VAWT zoomed in to where maximum C_P can be achieved (reproduced from Ertem et al.[30]).

The paper of Ertem et al.[30] goes on to present the plots shown in Figure 2.7, which show several different loadforms that all achieve the same C_T and thus similar induction, but do so using drastically different loading distributions throughout the rotation of the turbine.

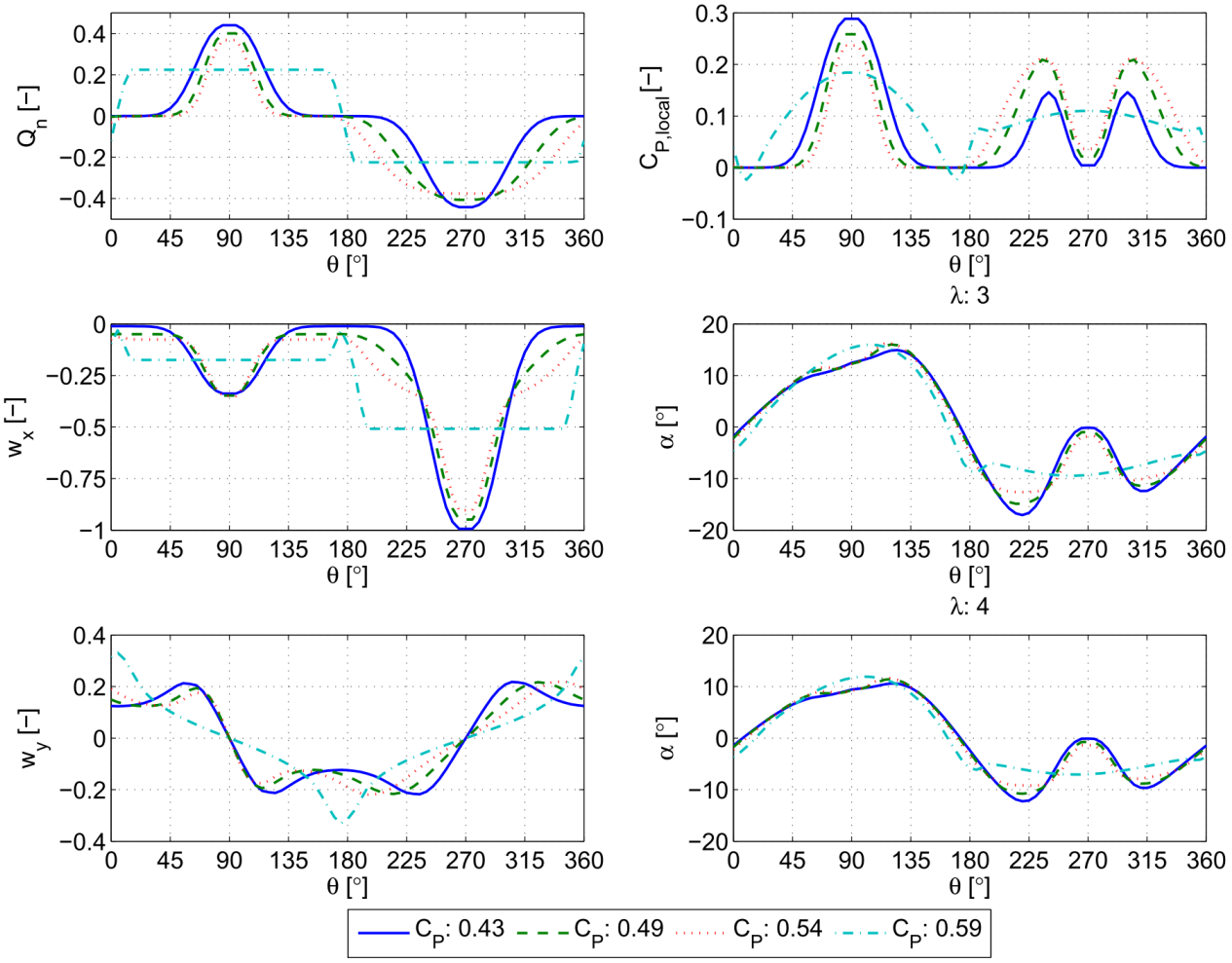

Figure 2.7: Load forms on the actuator cylinder that all lead to the same C_T, but different C_P (reproduced from Ertem et al. [30]).

Figure 2.7 is a pertinent example of the potential benefits of circulation control for vertical axis wind turbines. Theoretically, the azimuthal loading can be distributed in different ways between the upwind/downwind halves of the 2D actuator cylinder, resulting in the same power or thrust coefficient but drastically different loadings. This can be beneficial for load control and power control, amongst other things. A method to achieve this would be the active flap control strategies that the authors subsequently calculate using a hybrid numerical optimization model.

2.3 The VAWT in a wind farm

Due to a variety of characteristics that differentiate it from the HAWT, the VAWT has shown promise when used in an (offshore) wind farm configuration. Studies of the vertical axis wind turbine in farm configuration are vital to its future as a large-scale wind energy conversion system. The VAWT will have to offer significant technological and commercial advantages for it to be favored over HAWTs for farm applications (although some studies [114] show they could also coexist and complement each other). While this thesis will mostly focus on rotor-scale aerodynamics of the VAWT, this section is presented to put the potential benefits into perspective and show its technological relevance on a larger scale.

2.3.1 Studies

Dabiri[19] described the advantages of using VAWTs in a wind farm configuration, since they can be arranged in much more densely-packed layouts, increasing the power density per unit area of the wind farm. Dabiri also introduced the concept of using pairs of counter-rotating VAWTs in a farm configuration as a means of increasing power density. Full-scale experiments were performed and showed promising results that indicated an order of magnitude improvement is to be gained from this specific turbine arrangement.

The exact reasons for this phenomenon are described in a subsequent paper[50] that deals with the energy exchange in such a VAWT wind farm. The reason suggested by the authors for the increased farm efficiency is the fact that the VAWT farm achieves a significantly higher planform kinetic energy flux as compared to the horizontal energy flux that is usually the dominant factor for HAWT wind farms. In other words, the VAWT farm manages to extract more energy from above the wind farm, significantly decreasing the distance needed for the wind speed to recover to near its original value. According to Kinzel et al.[50], the turbine pairs are also able to extract energy from neighbouring turbine's wakes, suggesting a constructive wake effect rather than a destructive one that is characteristic for HAWTs.

The conclusions of Kinzel and Dabiri's papers are supported by Hezaveh and Bou-Zeid[42] to a certain extent, demonstrating that for a sufficiently large VAWT farm, the mean kinetic energy is replenished from above due to the planform kinetic energy flux, allowing for larger wind farms with higher power density. While they studied various different staggered arrangements, they conclude that more research needs to be done into irregular layouts that would allow for greater mean kinetic energy replenishment for larger farms.

In the experimental field, Lam and Peng[53] studied in detail the wake geometry of co-and counter-rotating VAWTs in wind tunnel tests. They showed that counter-rotating, particularly *counter-forward-rotating* VAWT pairs, exhibit fast wake recovery, decreased wake expansion and greater power output compared to co-rotating or counter-backward-rotating pairs and can potentially be used to increase the density of wind-farm layouts and thus power density. Recent wind tunnel tests by Vergaerde et al.[110] confirmed some of the results of Lam and Peng[53] and focused more on the potential for power coefficient improvement. They demonstrated that, for the counter-forward-rotating pair, an increase in collective power coefficient of up to 16% could be achieved, depending on factors such as the tip speed ratio and the distance between the turbines in the pair.

Whereas many studies discuss the potential of VAWT-only wind farms, a study by Xie et al.[114] investigated the potential of placing vertical axis and horizontal axis turbines in the same wind farm in a vertically staggered arrangement. Vertical staggering has been studied extensively before[15,116] but never using a VAWT/HAWT combination. Using a LES simulation, the authors demonstrated a 32% increase in overall power production of the wind farm. This included a 10% increase in power production of just the HAWTs in the wind farm, compared to those same HAWTs in a farm without VAWTs interspersed between them. While the study does not take into account the economical cost of adding VAWTs to an existing wind farm, the results are promising overall and hold up even when wind directions other than the prevailing wind are analyzed.

Lastly, Mendoza and Goude[68] investigated the effects of active pitching of blade struts to deflect the VAWT wake and thus improve power generation of downstream turbines. Using an actuator line model in OpenFOAM, they showed that significant reductions in wake losses of downstream turbines can be achieved whilst minimizing additional losses in the upstream turbine.

2.3.2 Modelling

In order to study the interaction between VAWTs and their performance in wind farm configurations, modelling advancements have been made. Ning[74] modified the actuator cylinder model by

Madsen [59] to be able to simultaneously predict the behaviour of multiple vertical axis wind turbines, taking into account the interaction between them. The method was briefly validated against 2D and 3D unsteady Reynolds-averaged Navier-Stokes (RANS) simulations, which showed promising results in the 2D case and a slight discrepancy in the 3D case. The author is careful to suggest further research may be necessary to eliminate this discrepancy, but is overall optimistic with regards to the viability of this approach for the modelling of multiple VAWTs in close proximity.

Bremseth and Duraisamy [13] conducted an unsteady RANS simulation of different arrangements of VAWTs in a wind farm. They showed that the interference between the turbines and the resulting turbulence is, in this case, a favorable effect, as the surrounding VAWTs are able to capture energy from this turbulence.

In order to optimize wind farm layouts, reduced order models are often used as their relatively low computational requirements make them ideally suited to iterative optimization algorithms. Tingey and Ning [105] proposed such a model for the VAWT wake, in the form of a Gaussian distribution fitted on data from CFD simulations. While some inaccuracies remained in the model compared to the CFD simulations, the reduction of computation time from nearly a day to mere hundredths of a second was deemed to be worth the reduction in accuracy. It can be seen as the VAWT equivalent to the model of Jensen [45].

2.4 3D effects

This thesis will compare some of the the aforementioned aerodynamic models on their performance with regards to predicting 3D effects and tip effects of the H-rotor VAWT. Most aerodynamic models of the VAWT *in 2D* take into account unsteady effects such as dynamic stall and blade-wake interaction. When modelling the VAWT *in 3D* however, spanwise effects as well as trailing vorticity (including tip vortices) come into play. The main focus of this thesis will be on 3D-blade effects and tip vortices, which are further explained in this section, in addition to a comprehensive review of how these effects have been taken into account in various aerodynamic models.

When moving from an unsteady 2D aerodynamic model of the H-rotor VAWT to a 3D one, an important difference arises from the fact that the blade span is no longer assumed to be infinite. A finite blade span results in a spanwise distribution of circulation, that, due to the VAWT's rotation, also varies azimuthally. The spanwise distribution of circulation leads to a spanwise variation in induction as well, which needs to be accounted for. Simão Ferreira [89] showed experimentally that the midspan induction of the 3D rotor is higher than the 2D case, leading to a decrease in efficiency of the rotor when moving from 2D to 3D aerodynamic modelling. This is primarily due to the generation of trailing vorticity along the blade which is not present in the 2D flow.

This trailing vorticity is largely manifested in the form of tip vortices, which have been shown to be the main contributors to potential losses in aerodynamic performance.[91] The magnitude of the tip vortex is closely related to the trailing vorticity, as it is generated by the trailing vorticity rolling up in the spanwise direction.

Traditionally, in horizontal axis wind turbines, the losses due to tip vortices have been taken into account using Prandtl's tip loss correction.[38] This correction results in a higher induction factor at the root and tip of the blade, with the effect being more pronounced at lower tip speed ratios. This higher induction factor subsequently reduces the local power coefficient and therefore the overall power coefficient of the rotor.

Simão Ferreira [89] showed that the 3D wake of the VAWT is radically different from that of the HAWT. The HAWT wake undergoes radial expansion of the wake, with the tip vortex being convected outboard, which is not necessarily the case for the VAWT. This illustrates the importance of accurate

3D wake modelling specifically tailored to the VAWT, as the inability of a model to capture such tip vorticity and thus wake expansion, can severely impact its accuracy.

2.5 Synthesis

All of the discussed topics in this literature study are critical for this thesis, which will aim to use accurate aerodynamic modelling to take into account these aerodynamic phenomena, whilst modifying the performance using circulation control to potentially achieve greater farm performance. In studying these aspects, it has become apparent that there is a need for detailed VAWT aerodynamic modelling, in particular with regards to 3D effects. This will be explained in further detail in Chapter 3. Another key takeaway from this literature study is that the VAWT can be a viable turbine concept in a farm configuration, provided the necessary aerodynamic improvements are made.

Chapter 3

From 1D to 3D

Analyses in wind turbine aerodynamics often rely on 2D simplifications of the complex 3D flow fields. This may be done with computational limitations in mind, or simply because the accuracy of the 2D approximation is sufficient for the analysis in question. In reducing the dimension of the problem however, one strays further away from the true physics of it and corrections may need to be implemented. This chapter discusses the differences between 2D and 3D flow for the HAWT and the VAWT and in doing so attempts to explain why 3D effects need to be taken into account for the VAWT.

3.1 1D

The simplest representation of an ideal horizontal axis wind turbine is the one-dimensional momentum theory by Froude[32]. The ideal rotor is represented by a smooth, frictionless, permeable disk that interacts with the incoming wind, hence the designation 'actuator disk theory'. Here, the only dimension is a line in the streamwise direction, which experiences a velocity decrease and a pressure fluctuation as it passes through the rotor disk, as can be seen in Figure 3.1.

It is this pressure fluctuation that causes a velocity decrease from V_0 far upstream to u at the rotor disk, all the way to u_1 in the far wake. This change in velocity represents the extraction of kinetic energy from the flow by the disk.

The streamwise slowdown of the flow is quantified using the axial induction factor a, as defined in Equation (3.1).

$$u = (1 - a)V_0 \tag{3.1}$$

The most important limitation of one-dimensional momentum theory is the fact that the concept of an ideal rotor (for example, an actuator disk) is used. This means the individual blades are not considered; the rotor is assumed to be a one-dimensional construct, with the flow through it being isotropic in the crossflow direction. Only the theoretical maximum aerodynamic power output can be calculated from the velocity deficit over the rotor control volume. Important parameters such as rotational speed, actual rotor aerodynamic power and thrust can only be computed once the blade aerodynamics are taken into account, as described in the next section (Section 3.2.1). Additional assumptions are that the flow is inviscid, incompressible and lacks any unsteady/time variant properties such as turbulence or dynamic inflow.

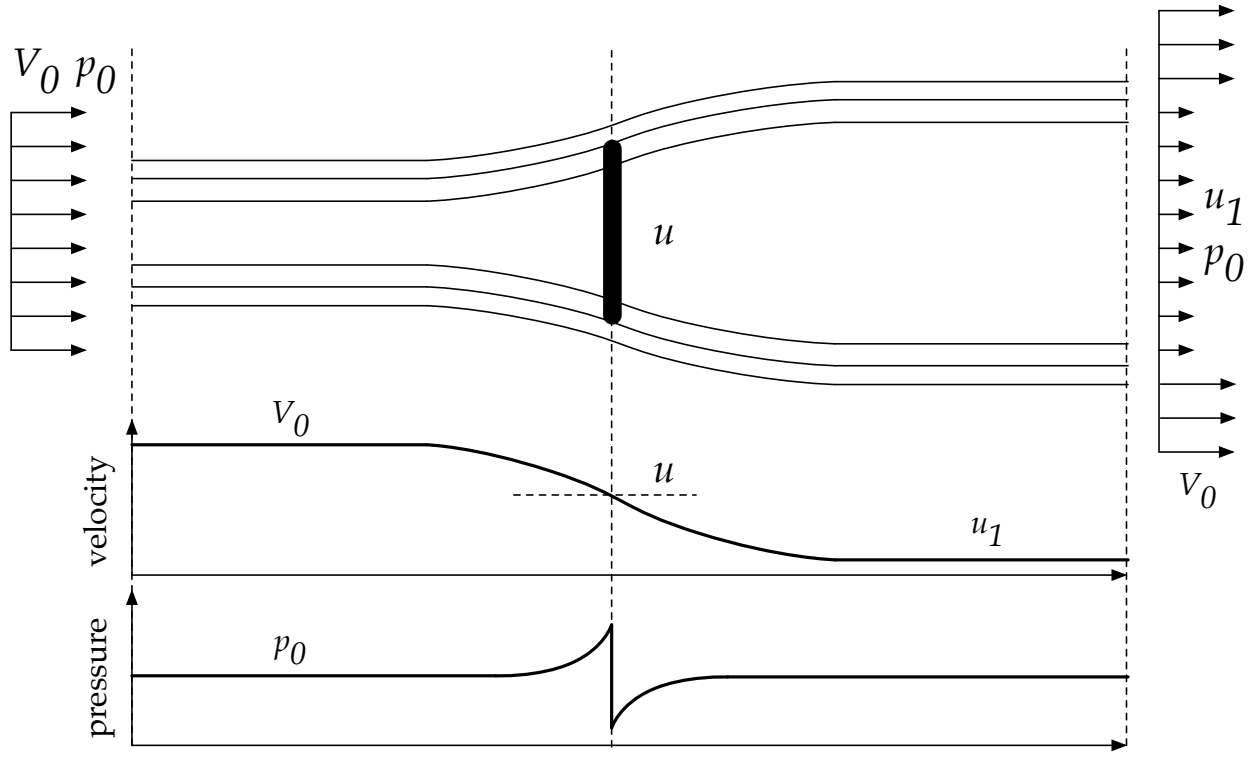

Figure 3.1: Graphical representation of 1D-momentum theory for wind turbines, including velocity and pressure profiles in streamwise direction (adapted from Hansen [38]).

Although one-dimensional momentum theory is a powerful tool, it is still very much a simplified analysis. Even in this simplified analysis however, some problems start to become apparent. van Kuik [108] discussed an important limitation of the actuator disc concept that leads to a 10-15% underestimation of the average velocity through the rotor compared to experimental data. The study shows that this could be due to a naturally occurring concentration of flow, the effects of which rather resemble those in a shrouded rotor, except no shroud is actually in place. A modification to the actuator-disk approach is proposed whereby forces on the edge of the disk are added. These forces are perpendicular to the direction of the flow, so therefore do not do any work, but they are part of the total rotor loading. Whereas Froude [32] assumed 100% of the load is converted into power, van Kuik's inclusion of edge-forces means only part of the load is converted into power, which aligns better with experimental results.

Lastly, it should be noted that although in this brief analysis the horizontal axis wind turbine was considered, one-dimensional momentum theory can also be applied to H-rotor vertical axis wind turbines. The difference is that the actuation surface of the ideal rotor is not disk-shaped but conforming to the 2D projection of the VAWT on the plane perpendicular to the freestream direction. The application of one-dimensional momentum theory to the VAWT was studied by Templin [103], Strickland [101] and Newman [73].

3.2 2D

3.2.1 HAWT

In order to account for the wind turbine blades and some wake rotation, one-dimensional momentum theory was extended by Glauert et al.[34]. The aerodynamic forces on the wind turbine blades result in an equal and opposite reaction on the air, causing the air to rotate contrary to the direction of rotation of the rotor, which is seen as wake rotation. The result is the blade element momentum theory, which is still commonly used as a fast and effective tool for horizontal axis wind turbine performance calculations.

Where Froude's one-dimensional momentum theory only dealt with axial induction, Glauert introduced an azimuthal induction factor a' as well. The azimuthal induction is necessary to compute the aerodynamic torque generated by the rotor blades, which in turn allows for the calculation of the aerodynamic power when multiplied with the rotational speed.

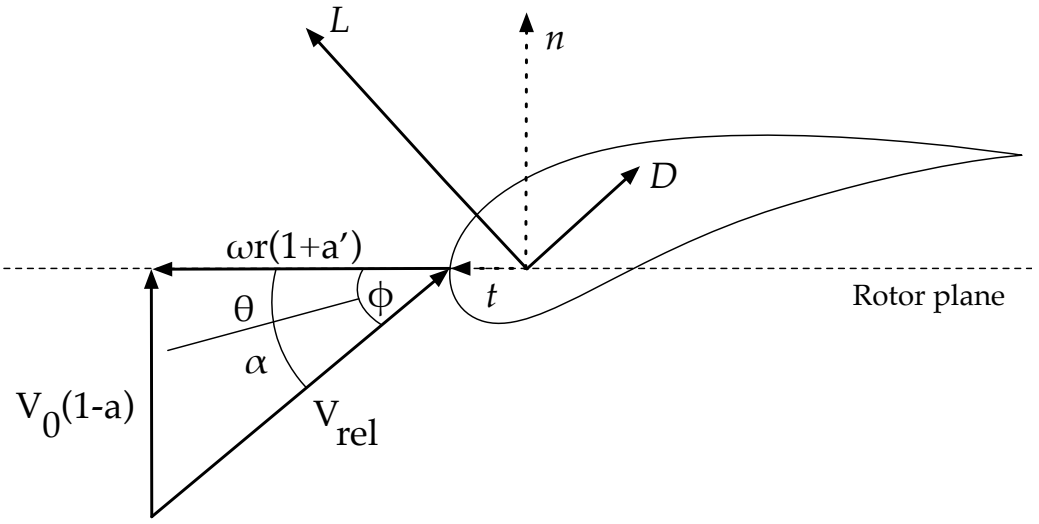

Figure 3.2: 2D blade section with relative velocity and aerodynamic forces shown.

Blade element momentum theory discretizes the rotor into a number of annuli, consisting of the part of the rotor area swept by the respective blade element. The aerodynamic forces on the individual blade elements are calculated using the relative velocity due to the incoming wind and the rotation of the rotor, as shown in Figure 3.2. The component of the flow in spanwise direction over the blade is assumed to be of negligible magnitude compared to the streamwise direction, hence the annuli are said to be independent. This assumption, while it allows for the use of 2D airfoil aerodynamics to be used to compute the blade forces, results in a couple of important limitations:

- Airfoil polars are obtained in a 2D configuration, either experimentally or using numerical methods, resulting in a 2D airfoil polar that may not be accurate when used in an actual blade.
- A blade of infinite length is assumed, meaning that root and tip effects are not taken into account. A correction for this was proposed by Prandtl and Betz[83] and is widely used.

Implementing a tip loss correction in such a 2D HAWT model is intended to account for not only for losses due to tip vorticity, but also the effects of having a finite number of blades. These two effects cannot be readily decoupled for HAWT as they can be for VAWT, which is explained in further detail in the remainder of this chapter.

3.2.2 VAWT

Compared to the VAWT, the 2D analysis of a horizontal axis wind turbine is less intuitive and difficult to understand, due to it being an axial turbine design whereas the VAWT is a cross-flow turbine. Representing the workings of a VAWT in 2D is more straightforward, as shown in Figure 3.3, since the rotating action is in the same plane as the incoming wind.

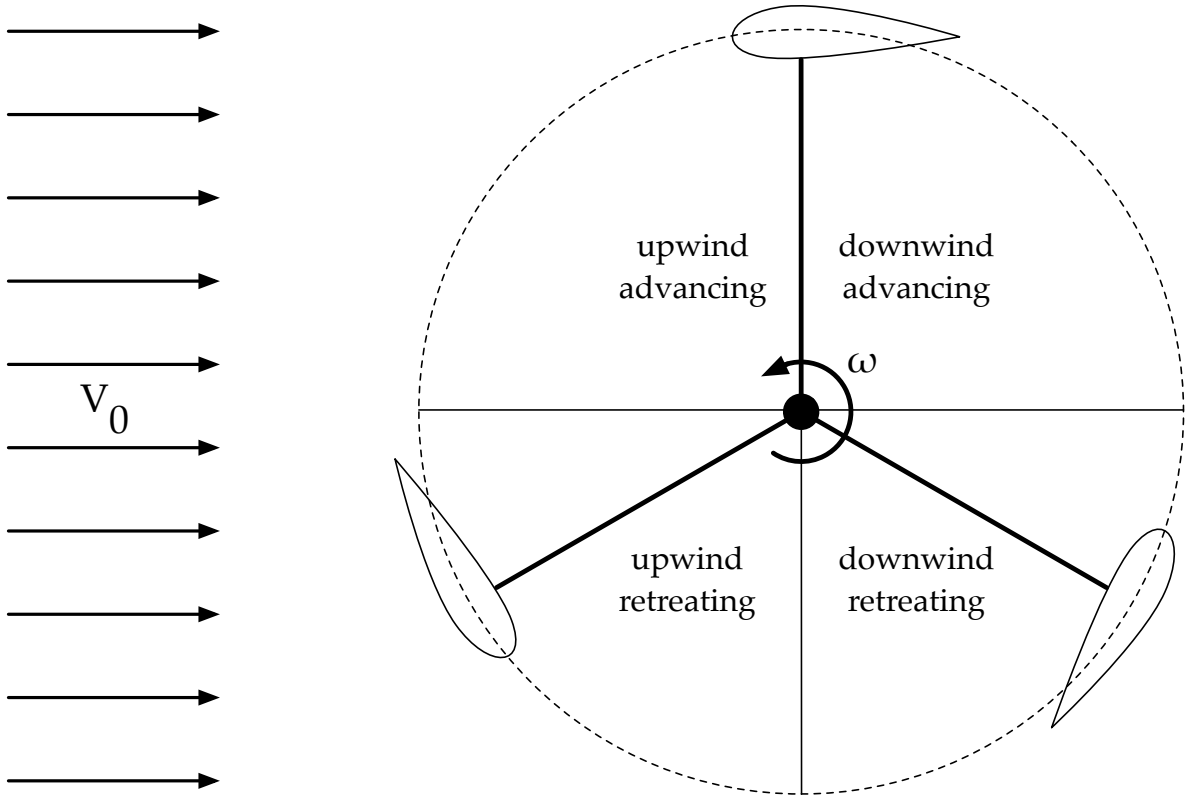

Figure 3.3: Simple 2D representation of a three-bladed VAWT, including terminology used to label the quadrants of the revolution.

Although 2D VAWT aerodynamics can be modelled using momentum-based methods such as multiple streamtube models, studies have shown that these are of insufficient accuracy.[92] Higher-fidelity models such as the actuator cylinder and 2D vortex models exhibited much better behaviour, likely due to the fact that they model upstream and downstream induction separately, with the upstream induction influencing the downstream induction.

The 2D aerodynamics of the VAWT are characterized by shed wake vorticity originating from the bound circulation on the blade. As the blades rotate, this bound circulation varies in time, resulting in vortex shedding. This is in line with Kelvin's circulation theorem, which states that a change in the bound circulation on a blade must result in an equal and opposite amount of circulation in the form of a vortex being shed. It is this phenomenon that makes the aerodynamics of the VAWT highly unsteady.

Figure 3.8a by Boudreau and Dumas[12] shows the near and far wake generated by a 1-bladed 2D cross-flow turbine in terms of the instantaneous spanwise vorticity. Vorticity with opposing sign is being shed from the upper (blade advancing) and lower (blade retreating) halves of the revolution, respectively. During the downstream half of the revolution, no large spanwise vortices are being shed, but instead a shear layer develops, which can also be seen in the near wake part of Figure 3.8a.

This is due to the bound circulation on the blade staying nearly constant during this part of the rotation, as demonstrated by Simão Ferreira et al.[91].

3.3 3D

3.3.1 HAWT

Before moving to a fully 3D HAWT rotor with blades, its rotor can also be represented in 3D with an infinite number of blades, in the form of the 3D actuator disk. This concept, as described by Sørensen et al.[98], adds aerodynamic features such as tip vortices and other kinds of trailing vorticity, but does not yet take into account the effect of having a finite number of blades. Effectively, the wake of this actuator disk will consist primarily of vortex rings composed of vorticity trailed from the blade tips.

The blades of the HAWT rotor in 3D can be represented by lines of bound vorticity which generate wake vorticity as they rotate. This vortex theory representation also dictates a resulting helicoidal wake composed of free vortices, starting at the trailing edges of the blades. This is shown for an ideal wind turbine with a finite number of blades in Figure 3.5, including the induced velocity distribution w due to the wake.

Having a finite number of blades results in a significant performance decrease compared to the ideal rotor. Okulov and Sørensen[76] showed this theoretically for an ideal wind turbine with a finite number of blades, resulting in a significant effect, particularly at low tip speed ratios.

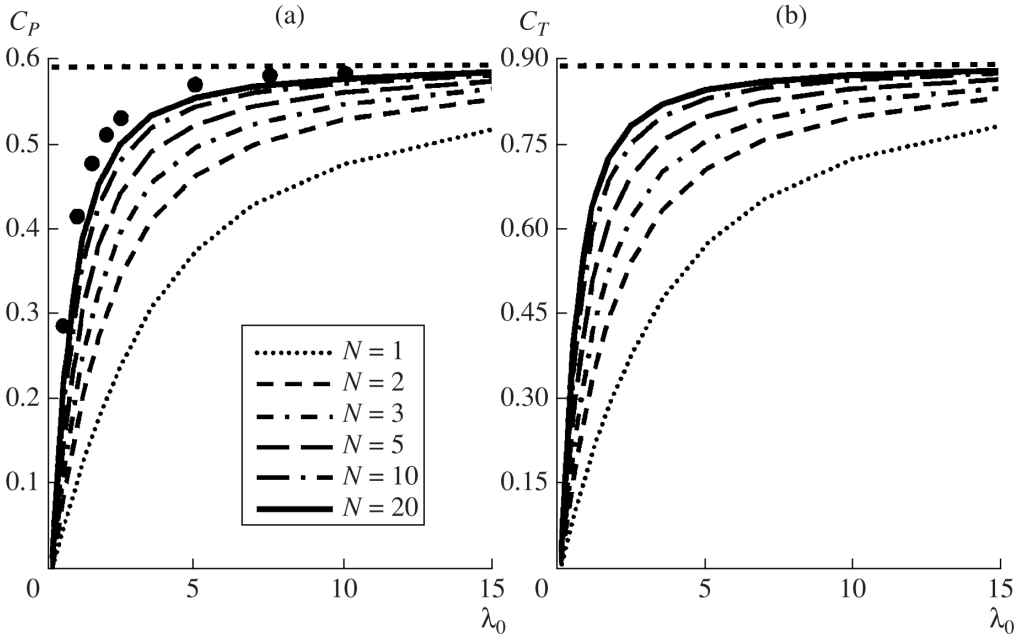

Figure 3.4: Performance coefficients C_P and C_T as a function of tip speed ratio, for different numbers of blades (reproduced from Okulov and Sørensen[76]).

The wake vortices shed by the HAWT blade, with a magnitude far smaller than the tip or root vortices, are convected downstream by the local wind flow, out of the way of the upcoming blade. This means that the blade-wake interaction phenomenon is of far less significance for the HAWT than for the VAWT, where blade-wake interaction happens because shed and trailing vortices are continuously 'intercepted' by incoming rotor blades, before they get a chance to be convected downstream by the local wind component.

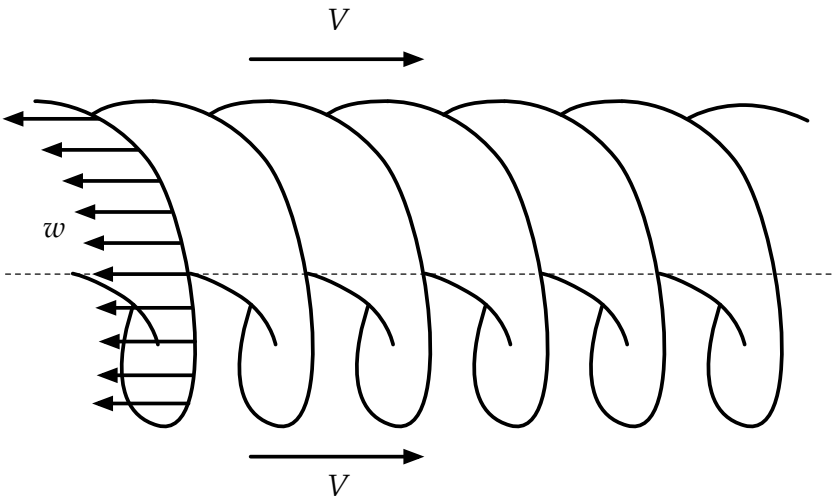

Figure 3.5: Helicoidal wake of a horizontal axis wind turbine. w indicates the velocity induced by the wake on the blades and V_0 is the local wind flow. (adapted from Okulov and Sørensen [76]).

The bound vorticity distributions on the lifting lines that represent the blades can be used to compute the lift and drag forces on the rotor using the Kutta-Joukowski theorem (Equation (3.2)).

$$d\vec{L} = \rho V \times \vec{\Gamma} d\vec{r} \tag{3.2}$$

Important differences between the 2D and 3D flow around a HAWT rotor must be distinguished first. The 3D flow contains root and tip effects that significantly increase induction at these locations, resulting in lower local power coefficients, for example. [1,41] Secondly, the flow around the blades is now no longer assumed to be locally two-dimensional, which may lead to radial flows occurring in the inboard region of the blade. [6]

Figure 3.7a by Boudreau and Dumas [11] shows a volume rendering of the vorticity generated by an axial flow (horizontal axis) wind turbine in 3D, with the convection of root and tip vortices clearly visible. Both types of vortices are convected downstream following a helical path, but the root vortices can be seen to become unstable sooner than the tip vortices. Note that the vorticity is mainly originating from the tip and root of the blade because that is where the bound circulation on the blade ends in space, therefore there exists a gradient. In between the root and the tip, the bound circulation on the blade remains constant throughout the rotation, because the angle of attack does not change significantly (contrary to the VAWT, which will be demonstrated later). Eventually, both helicoidal vortex systems break down, resulting in turbulent mixing.

In conclusion, the main 3D effect that can be identified for the HAWT is the existence of tip and root vorticity, due to the blades being of finite length and thus having distributions of bound vorticity that end in space, resulting in tip and root vortices being convected. These are often called trailing vortices, as they are trailed behind when the blade moves to its next position. Contrary to the VAWT, the 3D flow around the HAWT does not contain shed vorticity when operating in a steady flow, due to the constant angle of attack throughout the rotation.

3.3.2 VAWT

Similar to the HAWT, the VAWT can also be represented using a three-dimensional actuator surface, except in this case, the surface is cylindrical, not disk-shaped. Such a representation allows for the

simplified modelling of the complex wake of the VAWT. This is shown in Figure 3.6 by De Tavernier et al.[25], who showed the wake development for a finite aspect ratio 3D actuator cylinder for different load distributions upwind/downwind and a prescribed thrust coefficient. Here it is shown that even though the blades are not yet included, the shape of the actuator surface alone is an important determinant of its wake characteristics.

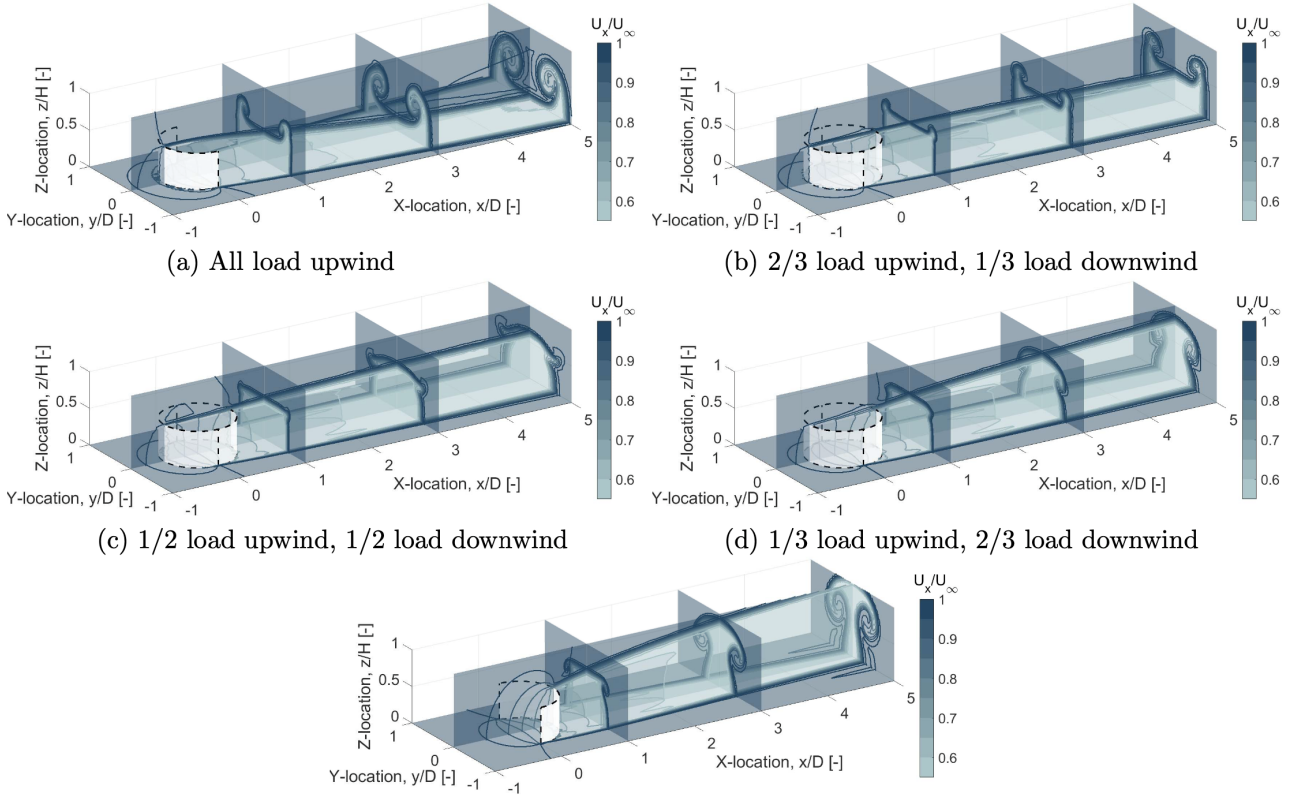

(a) All load upwind

(b) 2/3 load upwind, 1/3 load downwind

(c) 1/2 load upwind, 1/2 load downwind

(d) 1/3 load upwind, 2/3 load downwind

(e) All load downwind

Figure 3.6: Normalized streamwise velocity in the wake of cylindrical actuation surface, computed using an actuator line CFD model, for $C_T = 0.67$ and turbine aspect ratio $H/D = 1$. Reproduced from De Tavernier et al.[25].

The 2D aerodynamics of the VAWT rotor including a finite number of blades are (contrary to the HAWT) primarily dominated by shed vorticity due to the rapid pitching effect caused by the blades turning in a circular manner. The 3D flow field differs significantly, with trailing vorticity due to the variation of bound circulation on the blades and tip vortices generated by the lower and upper blade tips.

Simão Ferreira[89] showed that the 3D wake of the VAWT is radically different from that of the HAWT. The HAWT wake undergoes radial expansion of the wake, with the tip vortex being convected outboard, which is not necessarily the case for the VAWT. This illustrates the importance of accurate 3D wake modelling specifically tailored to the VAWT, as the inability of a model to capture such tip vorticity - and thus wake expansion - can severely impact its accuracy.

Simão Ferreira et al.[91] showed experimentally that the tip vortices of the VAWT rotor are convected inboard because of the wake's curvature, also demonstrating that the tip shape has a significant effect on tip vortex evolution. The inclusion of tip vorticity illustrates an important difference between the 2D and 3D vortex dynamics of the VAWT. The 2D wake shown in Figure 3.8a (from Boudreau and Dumas[12]) does not start to break down until $x/D = 8$, whereas the 3D wake including tip vorticity already shows severe turbulent interaction from $x/D = 2$ onwards. Figure 3.8c shows that this is due

to the inboard convection of tip vortices which collide approximately at the spanwise midplane at $x/D = 2.5$.

Aside from tip vortices, 3D effects due to there being a finite number of blades are also significant for the 3D aerodynamics of the VAWT, for a number of reasons. Simply having a finite number of blades results in the phenomenon of blade vortex interaction, where, even with only a single blade, the shed and trailed vortices from the blade can be affected by that same blade's second or third pass. Conversely, the aerodynamics around the blade are affected when cutting through these vortices. This is particularly an issue at high tip speed ratios, where the blade rotates many times faster relative to the speed at which the vortices are convected downstream. Ferrer and Willden [31] quantified the effect of the number of blades on blade wake interaction and subsequent effects on the aerodynamic forces at the blades and found that it is highly variable with the number of blades.

The performance of a real VAWT rotor versus an ideal rotor is also severely affected by having an finite number of blades, similar to what was shown for the HAWT (Figure 3.4). For the VAWT however, loads variability also plays an important role in turbine operation. Due to the large variation in angle of attack experienced by a blade in a single revolution and the resulting variation in bound circulation, the aerodynamic loads vary in a cyclical manner. With an increasing number of blades, the variations in aerodynamic loads induced by each blade are superimposed and the total load as seen from the tower becomes increasingly constant as the number of blades tends towards infinity. The individual load on the blade however does become more cyclic, with higher frequency oscillations, which may have adverse effects on the fatigue performance of the blade.

Spanwise flows also start to play a major role in the wake of the VAWT, where they are of much higher significance than for axial flow turbines, according to Boudreau and Dumas [11]. They observed spanwise velocity components of as much as $0.4 \cdot V_\infty$ on the midplane of the turbine and predicted that this depends heavily on the turbine's height-to-diameter ratio (henceforth referred to as turbine aspect ratio ,H/D).

A recent study by De Tavernier et al. [25] investigated the dependence of the VAWT rotor induction on this turbine aspect ratio and found that the wake is affected significantly by this parameter. For high turbine aspect ratios ($H/D > 5$), the flow conditions at the mid-plane resembled those that would be expected from the 2D case with little to no effect on the power production, whereas low turbine aspect ratios ($H/D = 0.5$) resulted in highly asymmetrical wake shapes and up to 15% lower power coefficients. It is worth noting that this analysis focused primarily on the effects of the tip vortices and was conducted for a finite cylinder, but still with an infinite number of blades.

De Tavernier et al. [25] also examined different rotor loading distributions and their effects on the wake, which relates favorably to the objective of this thesis. As can be seen in Figure 3.6, it was shown that distributing the loading to be predominantly upwind or downwind could result in drastically different wake shapes, for a constant thrust coefficient. Focusing the load on the upwind half of the actuator contributed favorably to the re-energising of the turbine wake, albeit with a drastic reduction in power, which means that for this effect to prove useful, a trade-off needs to be made. The method to achieve these varying rotor loading distributions is circulation control and these results suggest that the analysis should be performed with 3D effects taken into account to be able to make an accurate prediction.

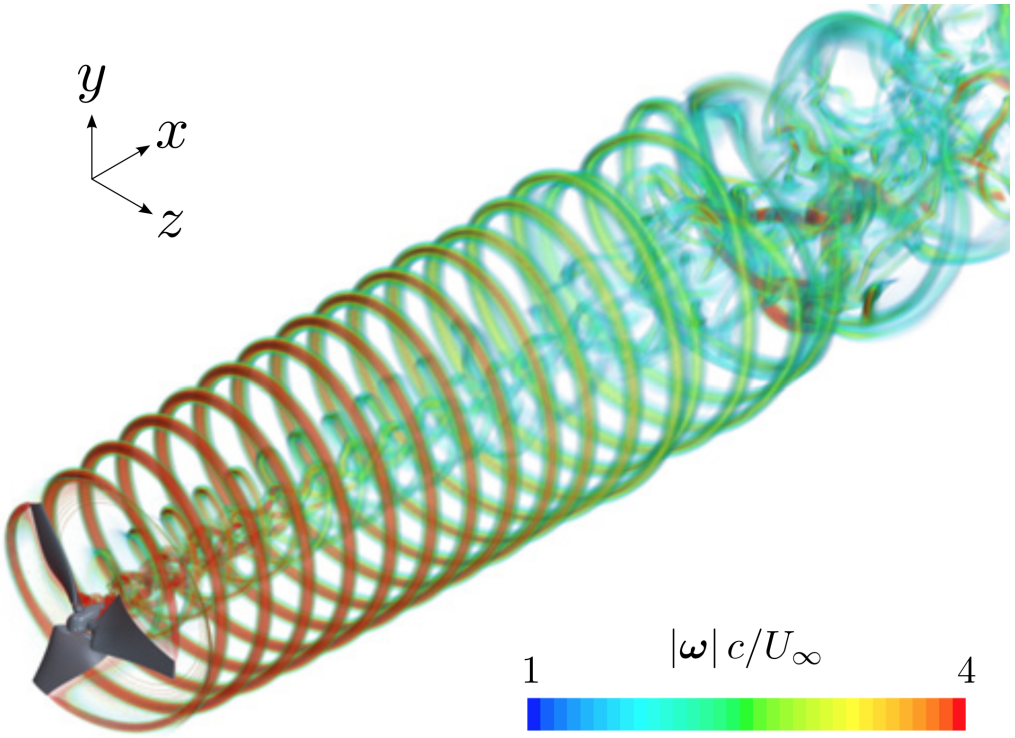

(a) Axial flow turbine

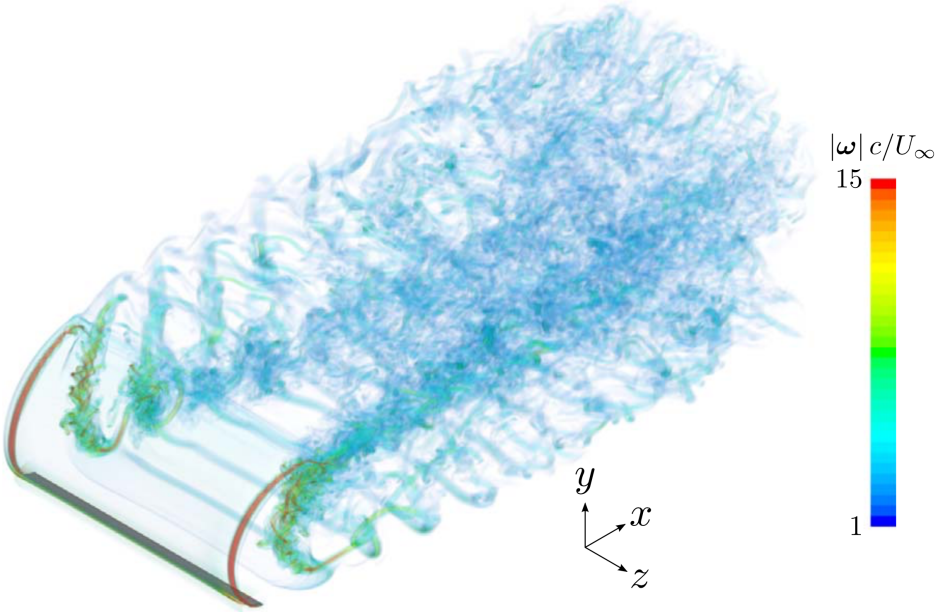

(b) Cross-flow turbine (3D)

Figure 3.7: Magnitude of vorticity in the wakes of an axial-flow and a cross-flow turbine (reproduced from Boudreau and Dumas [11]).

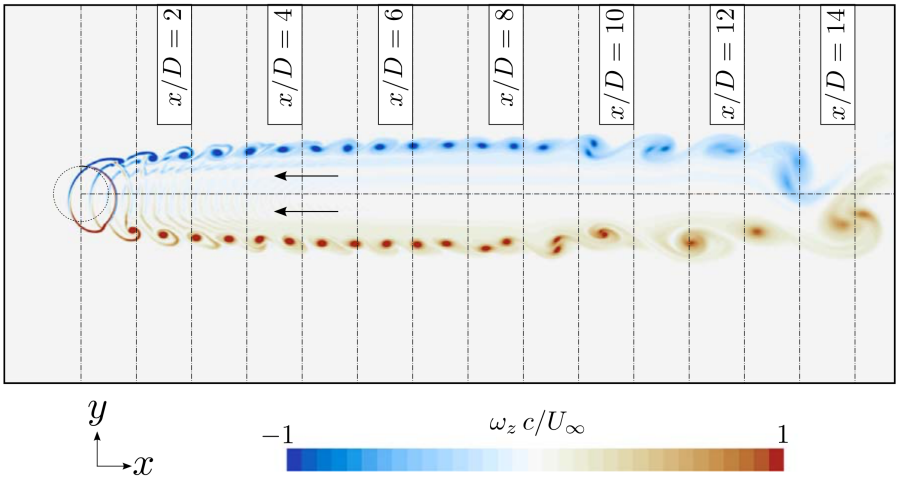

(a) 2D y − x plane

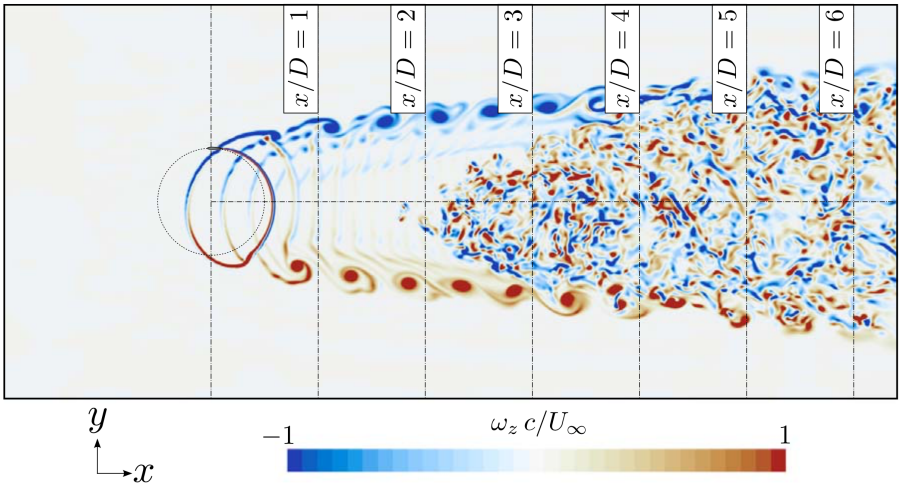

(b) 3D y − x plane

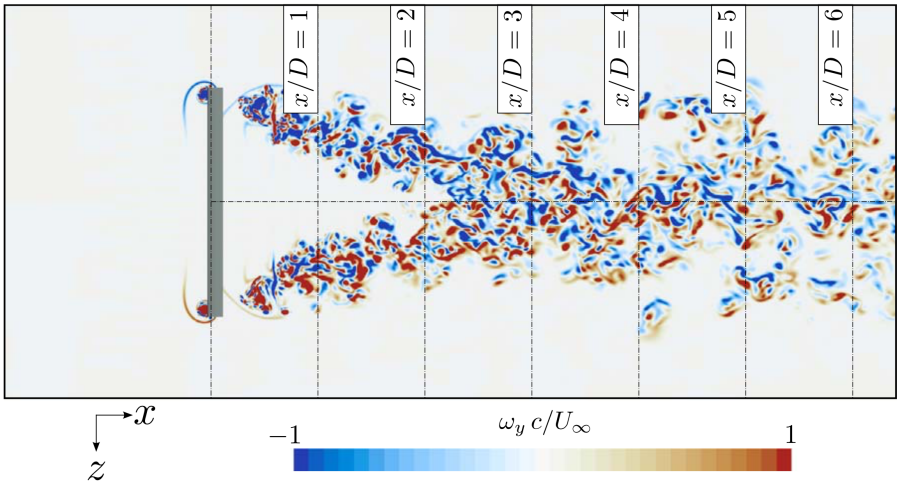

(c) 3D z − x plane

Figure 3.8: Instantaneous spanwise vorticity for a 2D and 3D cross-flow turbine (reproduced from Boudreau and Dumas [12]).

3.4 Synthesis

Having taken a closer look at the vortex dynamics of the VAWT as compared to the HAWT, it has become apparent that both turbine types require different aerodynamic modelling approaches in order to fully predict their performance. HAWTs experience radial wake expansion as tip vortices are convected outboard, whereas the VAWT wake actually contracts due to its tip vortices being convected inboard. It is this same phenomenon of tip vortex convection which results in the significant differences between the 2D and 3D flow field for the VAWT, causing an "early" (compared to 2D) breakdown of the vortex structures in the wake. The wake structure itself is affected significantly by this and can have a detrimental effect on the performance of the rotor. Additionally, having a finite number of blades is, in both turbine types, a significant complicating factor for the overall flow field. In VAWTs however, it is especially important, since the bound circulation on VAWT blades is changing throughout the rotation, whereas on HAWT blades it is not, in steady conditions. This change in bound circulation results in large vortices being shed into the wake, with a significant effect on performance. HAWTs do not experience this type of shed vorticity in steady flows, due to their constant angle of attack throughout a rotation. Altogether, a compelling case is made for the need for accurate 3D modelling of the flow field surrounding the VAWT rotor, paving the way for some of the objectives of this thesis:

- Quantifying performance improvements due to circulation control
- Examining the difference between the effects of circulation control in 2D and 3D
- Optimizing circulation control strategies such that they function optimally in 3D

Chapter 4

Aerodynamic modelling for VAWT

Research into accurately estimating the aerodynamic performance of the Darrieus-type VAWT has been ongoing since its invention by Darrieus [20]. This section will outline the most significant aerodynamic models that have been developed since, as well as describe their corresponding advantages, disadvantages and how they compare to their HAWT-equivalent.

Madsen [59] divided the available aerodynamic models for the VAWT up into two categories, as shown in Figure 4.1.

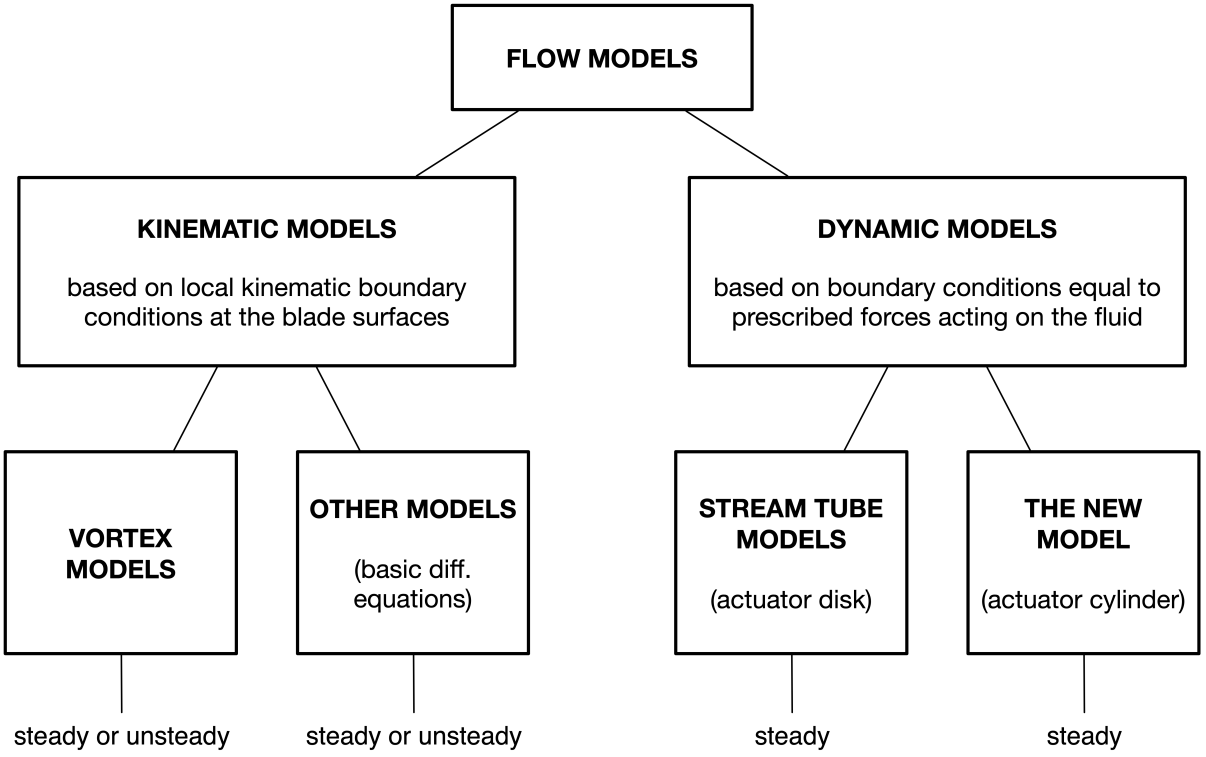

Figure 4.1: Flow model categorization adapted from Madsen [59].

The kinematic flow models are characterised by equations that describe the boundary conditions at the surface of the blades, whereas the dynamic models rely on the idea that blade forces acting on the

Parameter	Symbol	Value	Unit
Radius	R	2.5	m
n° of blades	B	3	-
Height	H	5	m
Turbine aspect ratio	H/D	1	-
Solidity	$\sigma = \frac{Bc}{2R}$	0.085	-
Blade chord	c	0.142	m
Tip speed ratio	λ	3	-
Freestream velocity	V_∞	1	m/s
Tower influence neglected			
Strut influence neglected			

Table 4.1: Reference VAWT parameters for benchmarking purposes.

fluid are responsible for generating the flow field. The aerodynamic models discussed in this chapter fall into one of these two categories. The BEM models, including multiple streamtube (MST) and double multiple streamtube (DMST), as well as the actuator cylinder model (ACM) are examples of dynamic models, whereas vortex methods, panel methods and CFD models belong to the kinematic category.

In this chapter, several specifically chosen aerodynamic models will be introduced and tested to investigate their ability to resolve the complex aerodynamics of the VAWT. The selected models are:

- **Unsteady BEM model**: a proprietary time-domain method of calculating the unsteady blade forces and performance of the VAWT, devised by Hansen.[8]
- **Double-Multiple Streamtube (DMST) model)**: an extension to the multiple streamtube models by Strickland[101].
- **2D Actuator Cylinder model**: a version of actuator surface momentum theory specifically for VAWTs, originally formulated by Madsen[59].
- **HAWC2**: aeroelastic design code in the time-domain with a VAWT aerodynamic model that is based on the actuator cylinder method. Unlike the actuator cylinder model, which is a purely aerodynamic model, HAWC2 is also able to take into account structural and aeroelastic response, as well as time-dependent inflow conditions such as turbulence and dynamic inflow.
- **HAWC2 NW**: same as HAWC2 but with a near-wake correction model implemented by Pirrung et al.[78].
- **CACTUS: Code for Axial and Cross-flow Turbines**: a free wake vortex method by Murray and Barone[72].
- **turbinesFoam**: a CFD model based on the actuator line method, implemented by Bachant et al.[4].

Each model family will be introduced, followed by the chosen model that is used in the quantitative analysis. This specific model is described, including underlying equations and assumptions. Limitations of the model will then be summarized, followed by a brief presentation of some results.

The chapter will conclude with a model comparison, both in 2D and 3D, followed by recommendations as to their ability to resolve 3D effects, in line with the purpose of this thesis.

The aerodynamic models have all been run using the parameters of the reference VAWT as described in Table 4.1. An inviscid, 18% thickness airfoil polar with zero drag ($C_l = 1.11 \cdot 2\pi \cdot \sin\alpha, C_d = 0$) is used for all the models. This simplification is applicable because the objective in this case is to compare the induction models behind all the models, not the blade element methods. The implications of using such an inviscid linear airfoil polar are that drag and other viscous effects are neglected, which

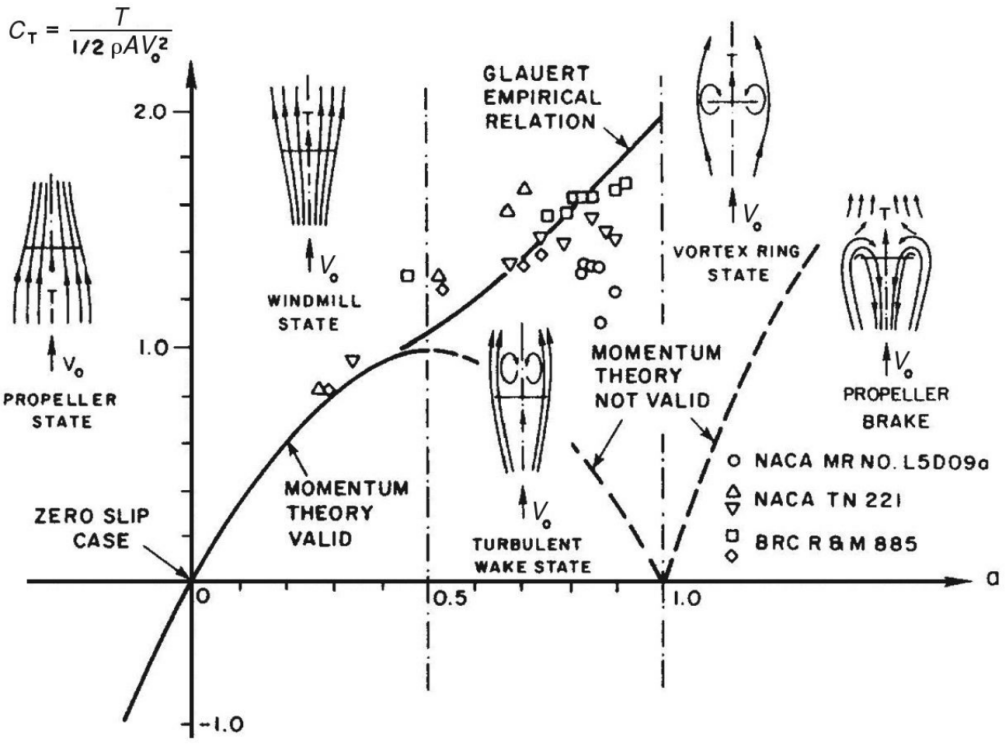

Figure 4.2: Rotor thrust coefficient C_T and corresponding states[29]

has a significant effect on the performance of the rotor. Results should therefore only be used to compare models to one another, as the performance without drag will likely be grossly overestimated. Lastly, for all models, unsteady effects such as dynamic stall, dynamic inflow or flow curvature are not included (although some models inherently account for this).

4.1 Blade element momentum models

4.1.1 Background

The Blade Element Momentum method consists of a combination of two concepts:

- Blade Element theory, which divides a rotor blade up into sections for which individual local aerodynamic forces can be calculated. It was originally derived by Froude and Drzewiecki.
- Momentum theory, which uses an actuator-disk representation of the propeller (or an impeller, in the case of a wind turbine) to calculate an acceleration/deceleration of the flow based on a pressure difference before and after the actuator disk. It is often attributed to Rankine and Froude.

38

The combination of the two theories mentioned above was conceptualized by Froude in 1878 but further developed by Glauert et al.[34] into the form in which it is used to this day. Glauert famously developed an empirical relation to correct the performance of rotors with high loading, where momentum theory is invalid, as shown in Figure 4.2.

The procedure of calculating aerodynamic forces using blade element momentum theory can be summarized as follows:[38]

- The blade is discretized into annular elements with the assumption that no cross-flow exists

between the elements.

- The axial induction factor a is determined on all blade elements, using local forces on airfoil section.
- Loads distribution over the entire blade is calculated using momentum theory and the computed induction factors.
- Power and thrust can be calculated from loads.
- Additional corrections are applied after or during computation, such as:
  - Prandtl's tip loss correction to mitigate the effects of the 'infinite-number-of-blades assumption'.
  - Glauert's empirical correction for highly loaded rotors.

4.1.2 Unsteady blade element momentum model

The unsteady blade element momentum model is a time-domain aerodynamic model for the VAWT by Hansen (first used by Bangga et al.[8]) that is able to include some unsteady effects, unlike streamtube models which are steady. The model being in the time-domain also allows for the inclusion of unsteady inputs such as atmospheric turbulence or dynamic inflow.

Fundamental equations

The unsteady BEM model consists of a blade element model and a method to estimate the induction due to each blade at each point in time. For each blade, the normal and tangential velocities V_n and V_t are computed using the azimuthal position θ and induced velocities W_x and W_y as in Equation (4.1). Using the normal and tangential velocities, the relative velocity V_{rel} and angle of attack α can subsequently be calculated. The azimuth angle θ is defined to be positive counterclockwise starting from the positive y-axis.

$$\begin{aligned} V_n &= (V_\infty + W_x)\sin\theta - W_y\cos\theta \\ V_t &= (V_\infty + W_x)\cos\theta + W_y\sin\theta + \omega R \\ V_{rel} &= V_n^2 + V_t^2 \\ \alpha &= \arctan\left(\frac{V_n}{V_t}\right) \end{aligned} \tag{4.1}$$

Using the angle of attack and relative velocity, the lift and drag forces acting on the blade at all points in time can be calculated, as well as the resultant blade loads. Averaging the azimuthal variation of these loads in the correct coordinate system and nondimensionalizing them results in the power and thrust coefficients.

The induction model of the unsteady BEM approach calculates the local induction W_x and W_y based on the global induction due to the overall thrust of the turbine. For every timestep, the thrust coefficient C_T is calculated as in Equation (4.2).

$$C_T = \frac{(dT/dr)\cdot dr}{\frac{1}{2}\rho V_0^2 2\cdot R\cdot dr} = \frac{(dT/dr)}{\rho V_0^2 R} = \frac{\sum_1^B p_x}{\rho V_0^2 R} \tag{4.2}$$

where dT/dR is the sum over all blades of the load in x-direction, p_x.

A global axial induction factor a is then found using the Glauert relation in Equation (4.3).

$$C_T = 4a^{new}(1 - \frac{1}{4}(5 - 3a^{old})a^{old}) \tag{4.3}$$

A time-delay is introduced in the axial induction factor to account for unsteadiness:

$$a(t) = a^{new} + a(t - \Delta t) - a^{new} e^{\frac{-\Delta t}{\tau}} \tag{4.4}$$

where $\tau = \frac{2R}{V_0}$ is a time constant proportional to the radius and freestream velocity.

The global induction velocity in freestream direction then becomes:

$$W_{x,glob} = a(t) V_0 \tag{4.5}$$

In order to calculate the loads on the blades in the next iteration, at certain azimuthal positions, this global induction velocity needs to be translated to the local induction velocity at every timestep i, $W_{x,i}$, as in Equation (4.6), using a streamwise slope.

$$W_{x,i} = Wx, glob + \frac{W_{x,glob}}{L}(-R \sin \theta_i) \tag{4.6}$$

The constant L is found by comparing results from the unsteady BEM model for different L to those of a vortex model.

Similarly, the induction in the crossflow direction can be calculated by applying the continuity equation as in Equation (4.7).

$$\begin{aligned} \frac{\partial V_y}{\partial y} &= -\frac{\partial V_x}{\partial x} \\ \frac{\Delta W_{y,i}}{\Delta y} \approx \frac{W_{y,i}}{R \cos \theta_i} &= -\frac{\Delta W_{x,i}}{\Delta x} \approx \frac{W_{x,i}}{L} \end{aligned} \tag{4.7}$$

$$W_{y,i} = \frac{R}{L} W_{x,i} \cos(\theta_i) \tag{4.8}$$

Extensions and corrections

A method of modelling dynamic stall is included, which uses an inviscid and a fully separated airfoil polar that provide a lift coefficient dependent on the separation point position. The separation point position is calculated using an exponential function with a predetermined time constant. Another exponential function simulates the lagging behaviour of the attached flow angle of attack that is typical for the dynamic stall phenomenon, which implies that the lift available due to a sudden change in angle of attack (which happens continuously as a VAWT blade rotates) is not available instantly, but instead builds up over time.

The unsteady BEM model is fully two-dimensional and utilizes no form of correcting the loads such that they approach zero at the blade tips.

Results

Figure 4.3 shows good agreement for the integral parameter C_P between the unsteady BEM model and a 2D classic vortex model (based on similar theory as described in Section 4.5.2). The agreement is especially good in the first, low λ section, but as λ increases, so does rotor loading and the results start to deviate.

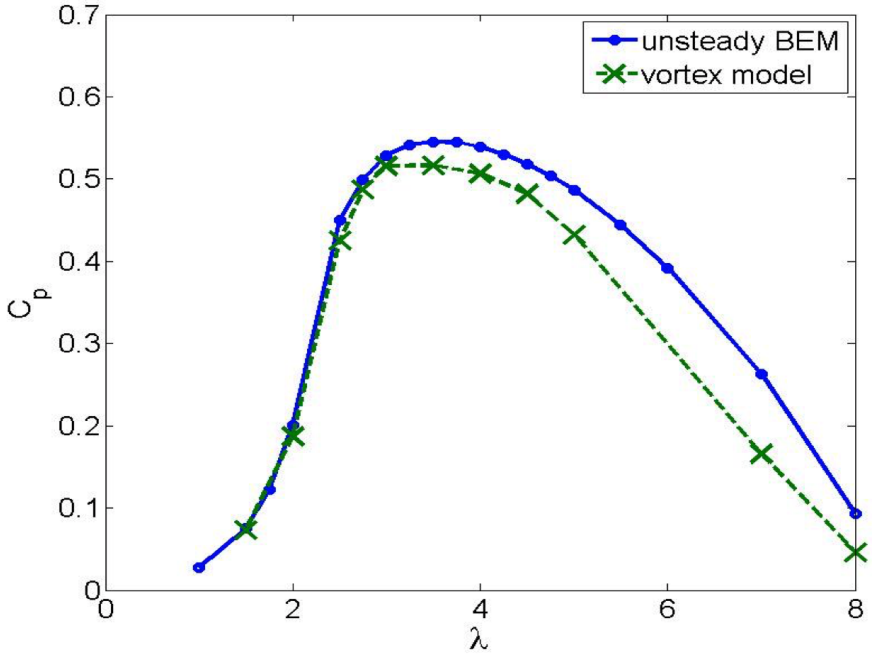

Figure 4.3: Power coefficient C_P versus tip speed ratio, for the Unsteady BEM model compared to a 2D classic vortex model.

A comparison of this model against other models is given in Section 4.7.

Limitations

- The local induction is assumed to have a streamwise slope and is distributed evenly using Equation (4.6). Its magnitude is based on the global induction velocity $W_{x,glob}$. Therefore, it acts much like a single streamtube model, since the induction is only updated globally. There is however some interaction at the azimuthal level, since the loads are computed using the local induction velocity.
- Due to the single-streamtube nature of the model, there is no separation of the upwind and downwind actuator halves, possibly leading to an overestimation of the downwind loading and an underestimation of the upwind loading.
- Fully two-dimensional.
- Reliant upon the determination of a constant L, from a vortex model or otherwise, which reduces validity for combinations of solidities and tip speed ratios for which an L has not been determined.
- The flow field is not predicted in any way, either around or inside the rotor. Disturbances to the flow field, such as those caused by blade vortex interaction, are not modelled.
- Reliant on 2D airfoil data for blade element component
- 2D model neglecting tip effects and spanwise flow

4.2 Multiple streamtube models

4.2.1 Background

BEM models are still widely used as a fast means of computing the performance of horizontal axis wind turbines. For vertical axis wind turbines, the Blade Element Momentum method can also be

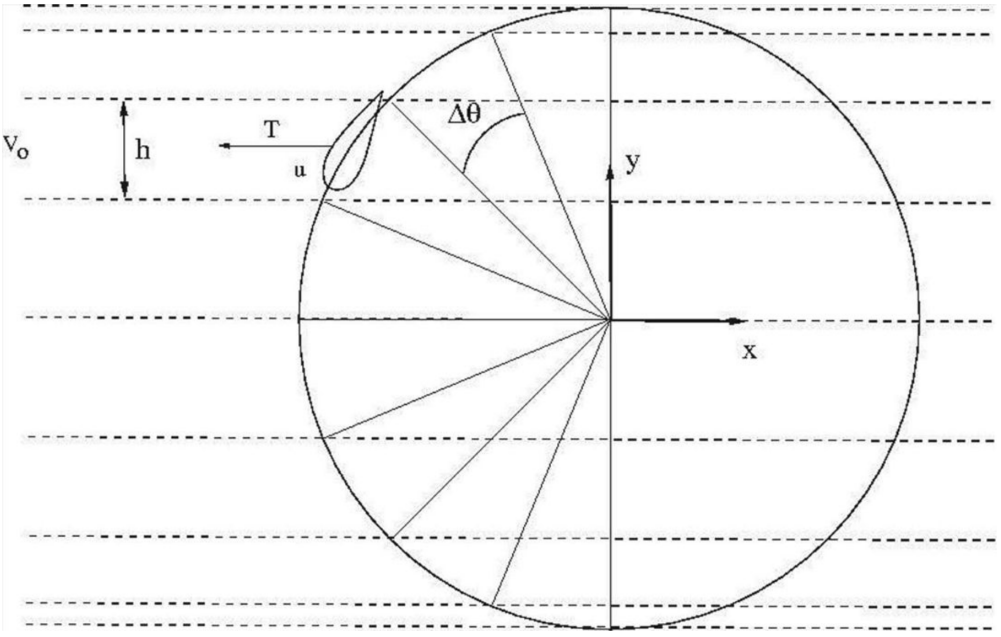

Figure 4.4: The multiple streamtube method, where the rotor is divided into non-equidistant streamtubes in the crosswind direction (reproduced from Hansen [38]).

used, albeit with some caveats. This was first demonstrated by Templin [103], who applied momentum theory to a single streamtube containing the VAWT rotor and thus derived expressions for its performance. This was extended into the so-called multiple streamtube model, first derived by Strickland [101]. In this paper, Strickland demonstrates that this multiple streamtube model is much more accurate than the single streamtube model due to the fact that it takes into account the variation in inflow velocity across the width of the turbine. The paper also validates this newly derived multiple streamtube model using wind tunnel measurements. An illustration of how the rotor is divided into streamtubes is shown in Figure 4.4.

4.2.2 Double multiple streamtube model (DMST)

The double multiple streamtube model is a refinement of the multiple streamtube model by Strickland [101], in itself an improvement over the single streamtube models developed by Templin [103]. The multiple streamtube model slices the rotor into several independent streamtubes and applies one-dimensional momentum theory and the blade element method to each. Figure 4.5 shows an arbitrary streamtube characterised by its position θ and angular width $d\theta$. The model calculates a value for the induction through every streamtube based on the relative velocity. Therefore, it forces on the blade section at that particular position in the revolution and is thus able to predict the performance of the rotor.

The *double*-multiple streamtube model splits the revolution of the VAWT into an upwind and a downwind section. Instead of computing a single induction value for every streamtube, first the upwind half of the revolution is computed, with the resulting induction values subsequently being used as input to compute the downwind half of the revolution. This results in a significant improvement in accuracy of the model, because it accounts for the effect of the wake of the upwind actuator on the downwind actuator (although the reverse is not true).[92] Paraschivoiu [77] developed the model and likened it to having two actuator disks in tandem, with the inflow of the downwind disk determined by the induction of the upwind disk. This enables the model to account for the decreased induction in the downwind half as opposed to the upwind half, thereby predicting the azimuthal variation of blade loads in a more accurate manner.

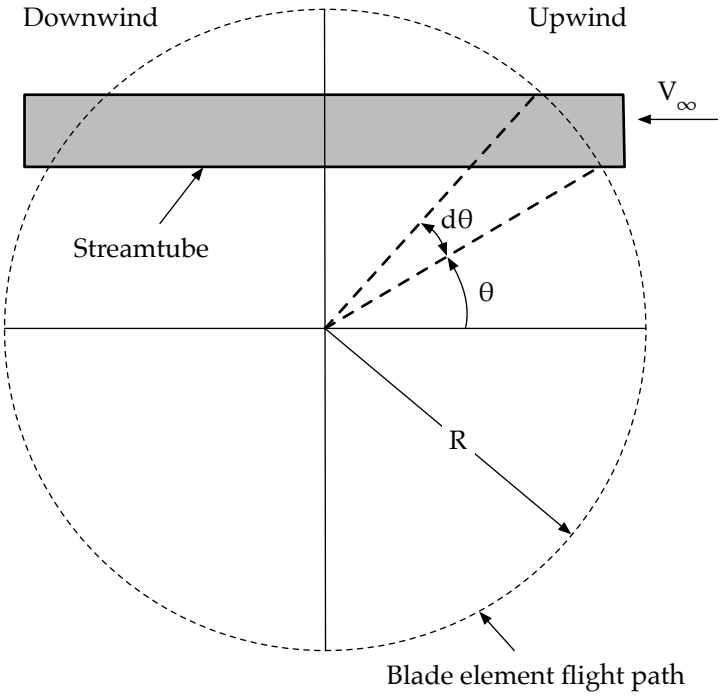

Figure 4.5: Illustration of the multiple streamtube concept.

In a comparison study of different VAWT aerodynamic models, Simão Ferreira et al.[92] conclude that the performance of multiple streamtube models, both double and single, is simply inaccurate when compared to models that allow for the explicit modelling of the VAWT wake (such as the subsequently treated actuator cylinder and vortex-based models). Ferreira concludes that double multiple streamtube methods need significant correction for them to be useful and sufficiently accurate. Studies by Bangga et al.[7], Saber et al.[86] attempt to fulfill this prediction by introducing new analytical corrections and establishing a relation between the upwind and downwind actuators.

Fundamental equations

The analysis is split into the upstream and downstream half-cycles of the rotor. For both the upstream and downstream half-cycles, Paraschivoiu[77] defines the local relative velocity as in Equation (4.9).

$$V_{rel}^2 = V^2\left[(\lambda - \sin\theta)^2 + \cos^2\theta\cos^2\delta\right] \tag{4.9}$$

where the local tip speed ratio is expressed as $\lambda = \omega r/W$, θ is the azimuthal position and δ is a parameter specific to Φ-shaped VAWTs representing the inclination angle at a particular position on the blade. In this analysis, only H-shaped VAWTs will be considered, therefore $\cos(\delta) = 1$.

Subsequently, the angle of attach α can be calculated using Equation (4.10).

$$\alpha = \arcsin\left[\frac{\cos\theta\cos\delta\cos\alpha_0 - (\lambda - \sin\theta\sin\alpha_0}{\sqrt{(\lambda - \sin\theta)^2 + \cos^2\theta\cos^2\delta}}\right] \tag{4.10}$$

Using the angle of attack α and the relative velocity V_{rel}, the normal and tangential coefficients C_n, C_t can be calculated.

$$\begin{aligned} C_n &= C_l \cos\alpha + C_d \sin\alpha \\ C_t &= C_l \sin\alpha - C_d \cos\alpha \end{aligned} \tag{4.11}$$

Then, to be able to find the local 'interference factor' (induction factor) a, it needs to be iterated until the momentum balance in Equation (4.12) is satisfied.

$$F_{up/down} a = \pi(1-a) \tag{4.12}$$

$F_{up/down}$ is a function that describes the conditions at the upwind or downwind part of the rotor, defined in Equation (4.13).

$$F_{up,down} = \frac{Bc}{8\pi R} \int_a^b \left(C_n \frac{\cos\theta}{|\cos\theta|} - C_T \frac{\sin\theta}{|\cos\theta|} \right) \frac{V_{rel}^2}{V^2} d\theta \tag{4.13}$$

where B is the number of blades, c is the chord length, V_{rel} is the relative velocity and V is the incoming velocity (for the upwind half, $V = V_\infty$, for the downwind half, $V = V_\infty(1-a)$). The integration boundaries a, b are also dependent on whether the upwind ($a = -\pi/2, b = \pi/2$) or downwind ($a = \pi/2, b = 3\pi/2$ halves are considered.

The process of calculating angle of attack, relative velocity, normal and tangential forces and, iteratively, the interference factor a using $F_{up,down}$ is first done for the upwind half, until convergence is reached, after which the resulting induced velocities are used to compute the downwind half.

Limitations

- The model is invalid for high loadings, e.g. due to combinations of high tip speed ratios and high solidities.
- Only streamwise induction is calculated, therefore the lateral velocity component V_y is neglected. Paraschivoiu[77] stated that the effect of the lateral velocity is relatively small (<10% of V_∞), therefore it can be neglected in this analysis, although including it will improve the accuracy of the predicted loads.
- Streamtube divergence neglected, although this can be corrected for.
- The streamtubes are assumed to be independent, with no cross-flow or any other form of interaction between them.
- The time-averaged induction is estimated, rather than the instantaneous induction.
- The flow field is not predicted in any way, either around or inside the rotor. Disturbances to the flow field, such as those caused by blade vortex interaction, are not modelled.
- The effect of the downstream actuator disk on the upwind actuator disk is not taken into account.
- Reliant on 2D airfoil data for blade element component.
- 2D model neglecting tip effects and spanwise flow.

59

Results

Figure 4.6 provides a brief look at the performance of the double multiple streamtube model versus the multiple streamtube model of Strickland[101] that was in use at the time, in addition to some experimental results. Good agreement between experimental results and the new model is achieved until

the tip speed ratio exceeds 5. The multiple streamtube model seems to diverge much earlier, overestimating the performance of the turbine. This is likely due to the fact that the multiple streamtube model does not take into account the effect of the upstream induction on the downstream induction, which becomes quite significant at larger tip speed ratios.

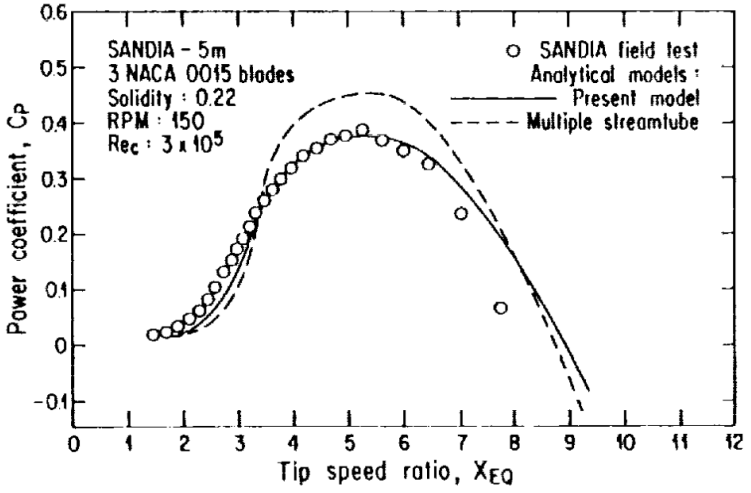

Figure 4.6: The DMST model (referred to as 'present model') compared to a multiple streamtube model and experimental data. Power coefficient C_P as a function of the tip speed ratio. Reproduced from Paraschivoiu[77].

A comparison of this model against other models is given in Section 4.7.

4.3 The actuator cylinder model

Some of the limitations of the double multiple streamtube model were noted by Madsen[59]. It led him to propose the so-called actuator cylinder model in his 1985 PhD thesis, aiming to improve upon the limited accuracy of the double multiple streamtube model.

Conceptually, the model can be likened to its horizontal axis wind turbine equivalent: the actuator disk model. The actuator disk model describes a pressure differential across a planar surface (See Section 3.1), whereas this surface is cylindrical with the actuator cylinder model.

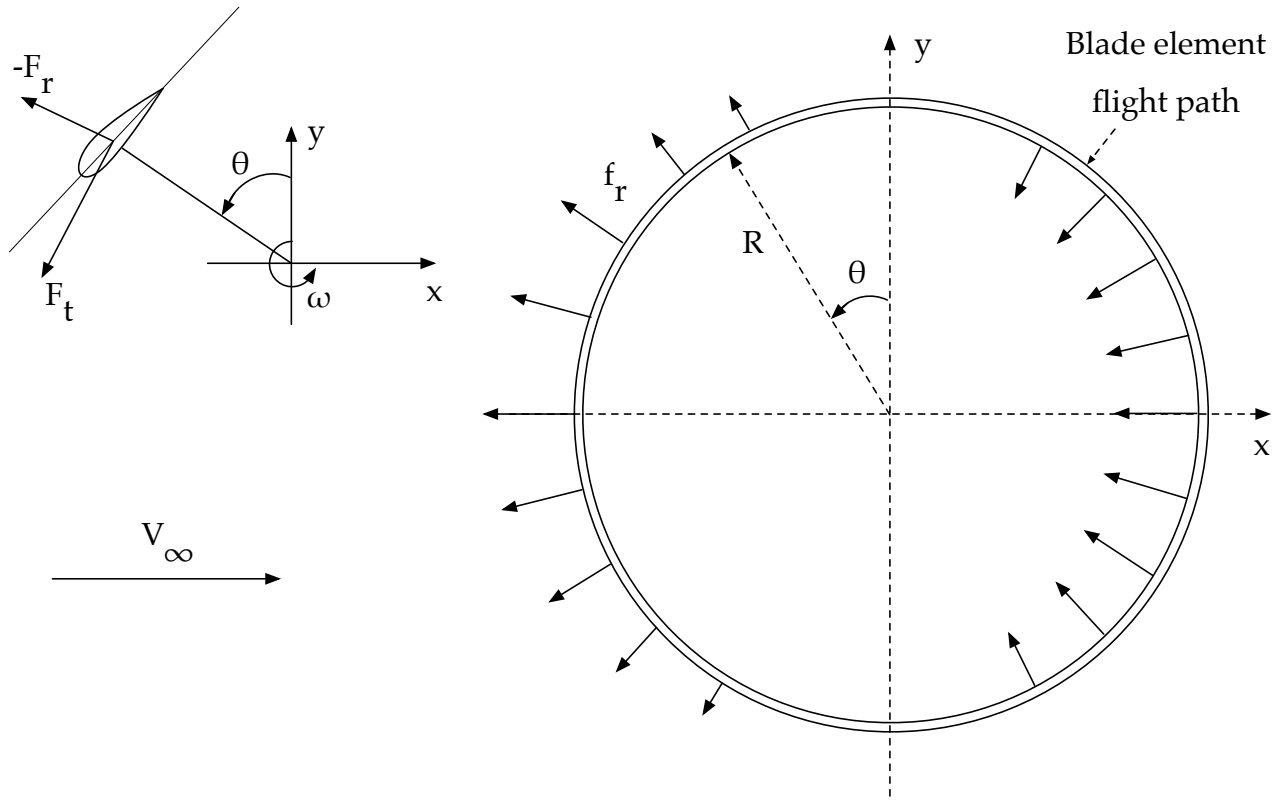

Figure 4.7: Plan view of the actuator cylinder representation of a vertical axis wind turbine (adapted from Madsen[59]).

4.3.1 Background

Horizontal axis wind turbines are often modelled using the actuator disk method, allowing for the application of momentum theory which forms the basis for the blade element momentum method as mentioned earlier.[97] Due to the VAWT's fundamentally different geometry and orientation however, actuator disk theory does not apply. The actuator cylinder model by Madsen[59] defines the ideal VAWT and its maximum power coefficient, much like the optimum HAWT rotor was defined by Glauert in BEM theory.[34]

While actuator disk theory models the swept area of the rotor as an actuator disk, the actuator cylinder considers the 'cylindrical' swept area of the VAWT rotor to be the non-planar actuator surface extracting power from the wind. Figure 4.8a shows the direction of the normal and tangential forces on the surface; the normal forces represent the forces due to the pressure jump from one side of the surface to the other and conversely result in the desired energy conversion when combined with the local relative velocity defined in Figure 4.8b.

Finding the relation between the pressure jump and relative velocity is one of the objectives of the actuator cylinder method. In short, Madsen achieves this by:

- Introducing perturbation velocities w_x and w_y into the Euler equations,
- Applying the continuity equation, resulting in a Poisson-type equation,
- Integrating the solutions of the Poisson-type equation over the regions where the prescribed (f) and induced (g) forces are acting,
- Integrating the resulting equations for the pressure field to yield the equations for perturbation velocities w_x and w_y.

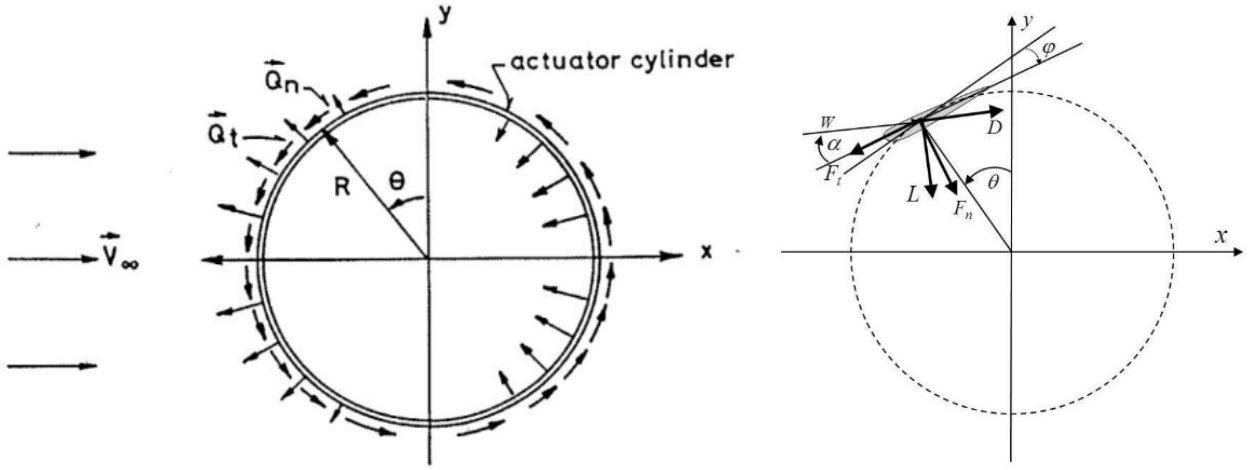

(a) Normal and tangential loading on the actuator cylinder (b) Blade element coordinate system

Figure 4.8: Representation of the cylindrical actuation surface used in the actuator cylinder model (Reproduced from Madsen et al.[64].)

The final solution resulting from this procedure consists of a linear and a non-linear part. The linear part is due to the prescribed forces (f) whereas the non-linear part is due to the induced forces (g). A commonly used extension to the actuator cylinder model that uses an approximation for the non-linear solution is described in Section 4.3.1. For the complete derivation of the solutions of the actuator cylinder model, the reader is referred to the full work of Madsen[59].

In the aerodynamic model comparison of Simão Ferreira et al.[92], the actuator cylinder model demonstrated good performance, vastly outperforming the existing multiple streamtube methods and agreeing with selected panel and vortex models.

Extensions to the actuator cylinder model

Modified Linear ACM The actuator cylinder model consists of a linear solution and a non-linear solution as described earlier in this section. Madsen[59] showed that the linear solution by itself is actually remarkably accurate and an analytical solution even exists for one particular type of loading. Therefore, rather than computing the computationally expensive non-linear solution as well, it is, in most cases, sufficient to compute only the linear solution and apply a correction to it to compensate for the underestimation of induced velocity by neglecting the non-linear computation. This approach is known as the modified linear actuator cylinder model, which is widely used today.

The correction that is applied to the induced velocity consists of a factor that amplifies the induced velocity to reduce the effects of the underestimation by the linear solution.Madsen et al.[61] shows that for uniform loading, the thrust coefficient of the VAWT based purely on the linear solution is equal to:

$$C_T = 4a_{lin} \tag{4.14}$$

where a_{lin} is the induction factor given by the linear actuator cylinder solution.

A well-known result from BEM theory[34] defines the thrust coefficient as:

$$C_T = 4a(1-a) \tag{4.15}$$

The factor difference between the thrust coefficients in Equations (4.14) and (4.15) is equal to k_a, given in Equation (4.16).

$$k_a = \frac{1}{1-a} \tag{4.16}$$

The induced velocity field should be multiplied with k_a to account for the effects of the non-linear AC solution without actually computing it, thereby saving significant computational time and allowing for the modified actuator cylinder model to be used as an effective engineering model.

The 2D actuator cylinder model is implemented in aeroelastic simulation code HAWC2[61] and offers significant benefits with regards to computational effort required when used in conjunction with the modified linear correction discussed in this section. The modified linear actuator cylinder model is shown to be in good agreement with the full model for a range of tip speed ratios.

Actuator-Cylinder squared De Tavernier and Ferreira[21] devised an extension to the actuator cylinder model that allows for the modelling of more than just the blades of the VAWT. Traditionally, using a single actuation surface, whether that is a disk or a cylinder, means that the effect of additional aerodynamic components such as the struts holding the blade in place cannot be modelled.

The actuator-cylinder-squared approach utilizes double concentric actuator cylinders with force fields that *both* modify the induced velocity field. At any point, the induced velocity can be computed as the component of the induced velocities from the two actuators, which is only possible because the modified linear version of the ACM is used. The approach can be likened to what is described by Ning[74], who investigated the use of actuator cylinder theory for multiple VAWTs in close proximity, except in the case of the AC^2 model there is zero distance between the two actuator cylinders.

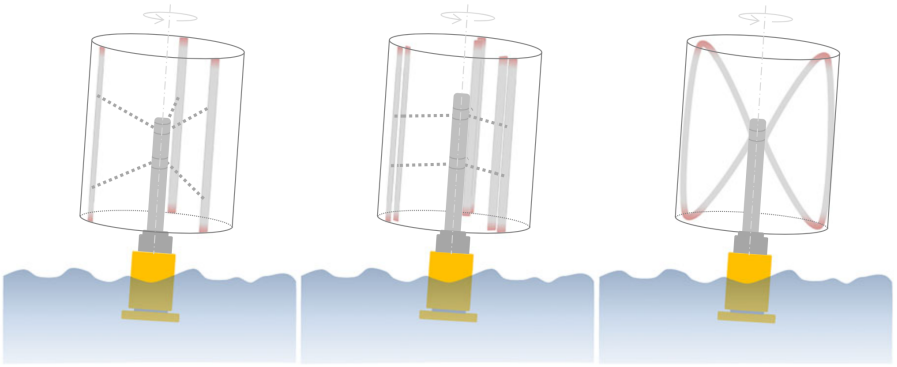

Figure 4.9: Potential use-cases of the actuator-cylinder-squared model (reproduced from De Tavernier and Ferreira[21]).

Figure 4.9 shows several unconventional VAWT blade configurations that the AC^2 model could potentially be used for, such as double-blade configurations[17] or double-rotor configurations[23]. Hara et al.[39] proposed a "quadruple-multiple-streamtube model" to investigate double-bladed VAWTs, which still relies on a correction for the MST model's inability to predict the influence of the downwind actuator on the upwind actuator. The AC^2 approach may be better suited for modelling this particular blade configuration.

3D Actuator cylinder model

In his 1988 paper entitled *"Application of Actuator Surface Theory on Wind Turbines"* Madsen[60] expanded upon planar actuator-disc theory that is usually used as one of the cornerstones of blade element momentum-based aerodynamic models. He describes actuator surface theory, in which the actuator is a surface of arbitrary shape. This can then be used to describe a range of different wind turbine types with varying actuator surfaces, including but not limited to disk-shaped (HAWT) and cylindrical (VAWT). In his paper, Madsen outlines the 3D formulation of the equations necessary to solve for the relation between the pressure jump and relative velocity for an arbitrary actuator surface exposed to a freestream velocity. These formulations originate from the work of Durand[28]. Madsen then applies these to the conventional actuator disk and to the actuator cylinder.

From the 3D equations for an arbitrary actuator surface, the equations for the 3D actuator cylinder model can be derived, which is potentially more accurate than the 2D formulation because it will take into account tip vortex effects without requiring corrections. Current implementations of the 2D actuator cylinder model, such as HAWC2's VAWT aerodynamic model, rely on modifications of the airfoil polars. They do this either by modifying (decreasing the performance of) the polar in a global manner, or by modifying local airfoil polars towards the tips of the rotor blade (the latter results in an actual non-constant load distribution, whereas the former is just a global decrease) .[80] An implementation of the 3D actuator cylinder model would likely result in greatly increased accuracy in aerodynamic modelling, although the computational cost and how it compares to higher-fidelity vortex and/or CFD models is not known.

4.3.2 Fundamental equations

Figure 4.7 shows how the vertical axis wind turbine can be represented in 2D by the actuator cylinder model. f_r denotes the radial volume force directed outwards from the cylinder on the upwind half and inwards on the downwind half.

f_r is responsible for creating the pressure differential across the surface of the cylinder, as defined in Equation (4.17).

$$\Delta p(\theta) = \lim_{\epsilon \to \infty} \int_{R-\epsilon}^{R+\epsilon} f_r(\theta) dr \tag{4.17}$$

The pressure differential $\Delta p(\theta)$, combined with the component of the incoming flow speed that is perpendicular to the surface of the cylinder ($v_r(\theta)$), enables the extraction of power, as in Equation (4.18) for the ideal VAWT rotor.

$$P_{ideal} = \int_0^{2\pi} v_r(\theta) \cdot \Delta p(\theta) \cdot R d\theta \tag{4.18}$$

The ideal power coefficient can subsequently be defined as follows:

$$C_{p,ideal} = \frac{P}{\frac{1}{2}\rho V_\infty^3 \cdot 2R} = \frac{\int_0^{2\pi} v_r(\theta) \cdot \Delta p(\theta) \cdot R \cdot d\theta}{\frac{1}{2}\rho V_\infty^3 \cdot 2R} \tag{4.19}$$

For a non-ideal turbine, the pressure differential $\Delta p(\theta)$ arises from the combined radial blade forces

$$\Delta p(\theta) = \frac{N \cdot F_r(\theta)}{2\pi R} \tag{4.20}$$

with the power coefficient being as in Equation (4.21):

$$C_p = \frac{P}{\frac{1}{2}\rho V_\infty^3 \cdot 2R} = \frac{\frac{1}{2\pi}\int_0^{2\pi} N \cdot F_t(\theta) \cdot \Omega \cdot R \cdot d\theta}{\frac{1}{2}\rho V_\infty^3 \cdot 2R} \tag{4.21}$$

Both Equation (4.19) and Equation (4.21) contain integrals which need to be solved in order to obtain the relationship between the pressure jump $\Delta p(\theta)$ and the velocity field. The actuator cylinder is assumed to be of infinite length, eliminating the z-direction from the calculation. Additionally, viscosity is deemed not important, resulting in an inviscid flow assumption. Due to these assumptions, the flow can be said to be governed by the incompressible 2D Euler equations, closed by the continuity equation.

The induced velocities w_x and w_y relate to the nondimensional (with respect to the freestream velocity) velocity components in streamwise (v_x) and crossflow (v_y) directions as in Equation (4.22).

$$\begin{aligned} v_x &= 1 + w_x \\ v_y &= w_y \end{aligned} \tag{4.22}$$

The relation between these induced velocities and the pressure differential is then provided in the Euler-type equations[3] shown in Equation (4.23), with f_x and f_y being the components of the volume force exerted by the fluid.

$$\begin{aligned} \frac{\partial w_x}{\partial x} + w_x \frac{\partial w_x}{\partial x} + w_y \frac{\partial w_x}{\partial y} &= -\frac{\partial p}{\partial x} + f_x \\ \frac{\partial w_y}{\partial x} + w_x \frac{\partial w_y}{\partial x} + w_y \frac{\partial w_y}{\partial y} &= -\frac{\partial p}{\partial y} + f_y \end{aligned} \tag{4.23}$$

The continuity equation (Equation (4.24)) ensures conservation of mass in the system.

$$\frac{\partial w_x}{\partial x} + \frac{\partial w_y}{\partial y} = 0 \tag{4.24}$$

Kármán and Burgers[47] showed that the system of Euler equations can subsequently be solved by making use of the general solution to a Poisson-type equation and respecting the boundary condition of the pressure $p \to 0$ when $(x, y) \to \infty$. For the full derivation of this solution, the reader is referred to the work of Madsen[59].

The solved induced velocities w_x and w_y are found to consist of a linear and a non-linear part. An analytical solution for the induced velocities exists for the linear part, which is shown in Equation (4.25).

$$\begin{aligned} w_x(x,y) &= -\frac{1}{2\pi}\int_0^{2\pi} \Delta p(\theta) \frac{-(x+\sin\theta)\sin\theta + (y-\cos\theta)\cos\theta}{(x+\sin\theta)^2 + (y-\cos\theta)^2} d\theta + K \\ \text{(before cylinder) } K &= 0 \\ \text{(inside cylinder) } K &= -\Delta p(\arccos y) \\ \text{(in the wake) } K &= -\Delta p(\arccos y) + \Delta p(-\arccos y) \\ w_y(x,y) &= -\frac{1}{2\pi}\int_0^{2\pi} \Delta p(\theta) \frac{-(x+\sin\theta)\cos\theta + (y-\cos\theta)\sin\theta}{(x+\sin\theta)^2 + (y-\cos\theta)^2} d\theta \end{aligned} \tag{4.25}$$

The solved axial induction velocity w_x consists of multiple parts, requiring a term K that is different before the cylinder, inside the cylinder and in the wake.

4.3.3 Mod-Lin ACM

The standalone linear solution is sufficient for modelling lightly loaded actuator cylinders (low thrust coefficient C_T) but starts to break down as the thrust coefficient increases. Figure 4.10 shows the power coefficient calculated by the linear (analytical) solution of the actuator cylinder model as a function of the total drag coefficient of the turbine C_D (comparable to C_T). Compared to the final (numerical) solution that is also shown, the linear solution behaves similarly until medium to high loadings, at which point it starts to grossly overestimate the power coefficient. A simplified solution is also shown, which includes neglecting a second order pressure term and assuming irrotational

flow. This simplified solution, though it is slightly closer to the final numerical solution, exhibits similar inaccuracy towards higher loadings.

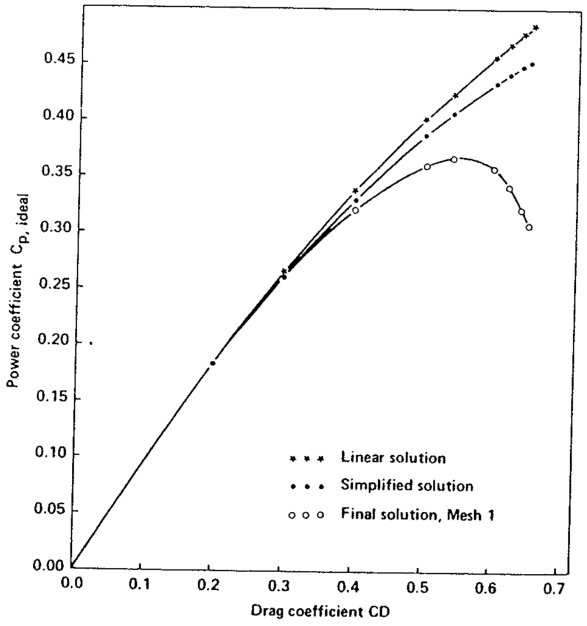

Figure 4.10: Linear and simplified analytical solutions of the actuator cylinder model, versus numerical results of the full model. The drag coefficient CD on the x-axis actually represents the thrust coefficient C_T (a nomenclature difference). Reproduced from Madsen[59].

To remedy these inaccuracies towards higher loadings, the induced velocity field is amplified using a correction based on the overall thrust coefficient of the turbine C_T, in a manner not dissimilar to the Glauert correction for horizontal axis wind turbines. This correction results in the modified linear actuator cylinder model (Mod-Lin ACM).

A polynomial with empirically defined coefficients (Equation (4.26)) is used to calculate the mean induction from the thrust coefficient C_T for the entire rotor. This is used to compute a correction factor k_a, with which the induced velocities w_x and w_y are multiplied, resulting in a corrected induced velocity field. The increasing influence of k_a with increasing overall rotor C_T is shown in Figure 4.11.

$$\begin{aligned} a &= 0.0892074 \cdot C_T^3 + 0.0544955 \cdot C_T^2 + 0.251163 \cdot C_T - 0.0017077 \\ k_a &= \left| \frac{1}{1-a} \right| \end{aligned} \tag{4.26}$$

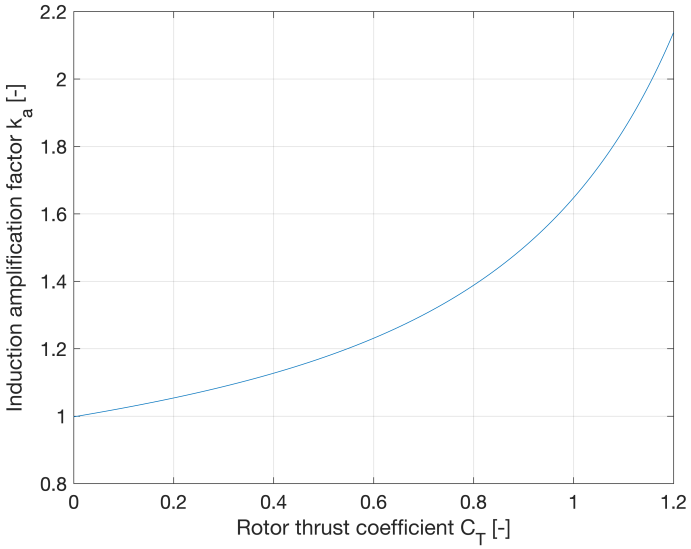

Figure 4.11: Mod-Lin correction factor k_a applied to the induction field to correct for inaccuracies at high loading (high C_T).

4.3.4 Limitations

- Steady model (time-averaged induction) for a highly unsteady problem.
- Inviscid flow assumption.
- Infinite number of blades assumption.
- Infinite blade length assumption.
- Reliant on 2D airfoil data for blade element component.
- 2D model neglecting tip effects and spanwise flow.
- Dynamic stall model necessary to correct for non-instantaneous lift.
- Time-averaged induction calculated, not instantaneous.

A comparison of this model against other models is given in Section 4.7.

4.4 HAWC2

HAWC2 is an aeroelastic design tool developed at the Technical University of Denmark.[54] It is capable of modelling the aerodynamics of both horizontal and vertical axis wind turbines, with the latter making use of a modified 2D actuator cylinder approach. Madsen et al.[61] described the process of implementing the actuator cylinder flow model for vertical axis wind turbines in HAWC2. At every time-step in the HAWC2 coupled turbine simulation, the actuator cylinder model is used to compute the induction field over the rotor, enabling accurate response of the aerodynamic model to changes in inflow, structural deflections and even dynamic inputs due to floating turbine foundations.

4.4.1 HAWC2 Near-Wake model

Although HAWC2 computes most other turbine parameters in 3D, the actuator cylinder aerodynamic model remains a 2D model, which results in an inherent inaccuracy. Corrections can be implemented in two ways:

- Modifying the airfoil polar to provide lower overall lift coefficients, similar to how in aeronautics a finite aspect ratio correction is applied for finite wings.[49] This will result in a more accurate prediction of the overall power but also cause an inaccurate spanwise load distribution.

- Modifying the airfoil polar differently at different spanwise locations, to simulate the expected load distribution.

Both of these methods are static and unaffected by changes in the dynamics of the system, which is potentially undesirable for a coupled aeroelastic load simulation tool such as HAWC2. The implementation of a near-wake model for vertical axis wind turbine modelling was intended to provide a more physical way of correcting for 3D effects as opposed to using a static polar correction. It is based on the work of Pirrung et al.[78] on trailed vorticity modelling for horizontal axis wind turbines in standstill conditions. A detailed description and analysis of the model is given by De Tavernier et al.[24].

Background as HAWT aerodynamic model

The trailing vorticity model was originally intended as an extension to HAWC2 to simulate HAWT blades under normal operation,[54,82] in addition to the existing BEM model.

Rather than directly using the Biot-Savart law to predict the induced velocity at a certain point due to a vortex element (as explained in more detail in Section 4.5.2), the near-wake model uses a single exponential function to approximate the decay of this induced velocity as a vortex line segment trails downstream. The overall induced velocity by the blade W_s^i is the sum of the velocities $W_{s,\nu}^i$ induced by every vortex line segment trailed from a particular section of a blade, as described in Equation (4.27). This approximation is done to save tremendous computational effort by avoiding the need for numerical integration of the Biot-Savart expression.

$$\begin{aligned} W_s^i &= \sum_{\nu=1}^{N_\nu} W_{s,\nu}^i \\ W_{s,\nu}^i &= W_{s,\nu}^{i-1} e^{-\Delta\beta/\Phi_{s,\nu}} + D_{w,s,\nu}\Delta\Gamma(1-e^{-\Delta\beta/\Phi_{s,\nu}}) \end{aligned} \tag{4.27}$$

Where subscripts i, s, ν indicate the timestep, blade section and vortex line segment, respectively. $\Delta\Gamma$ represents the magnitude of the trailing vortex and D_w is the initial induced velocity at the blade due to the blade section itself. As the wake develops, the induction due to the previously trailed vortex segments decays, but the newly trailed vortex segments provide additional induction.

The parameter $\Delta\beta$ in Equation (4.27) represents the angle that the blade rotates during a single timestep. In standstill conditions, the blade does not rotate and the parameter β is altered to reflect this. Additionally, due to the lack of rotation, the path of the trailing vorticity is neither helical nor circular in nature, but extends straight from the blade in the freestream direction, without any wake deformation occurring. This is considered adequate to simulate the flow field close to the blade, but accuracy decreases rapidly as the straight vortex filaments are convected downstream.

The Near-Wake model for VAWT

For the VAWT, the near-wake model also does not replace the 2D actuator cylinder model as the main aerodynamic model in HAWC2; it acts as an extension to it. At every time-step, the near-wake model utilizes a lifting-line approach (as described in the previous section) to calculate the induction of every blade using both the geometric inflow (due to rotation and windspeed) *and* the induced velocity calculated by the 2D actuator cylinder model. By feeding the resulting near-wake induction back into the actuator cylinder model for the next iteration, the actuator cylinder model is influenced by 3D effects predicted by the lifting line approach, whilst in essence remaining a 2D model.

This feedback loop between the near-wake model and the actuator cylinder model occurs at multiple spanwise locations. These split the 3D turbine into several virtual 'disks', the interaction between

which is taken into account using the near-wake model. This concept of splitting the 3D actuator cylinder into disks is visualized in Figure 4.12.

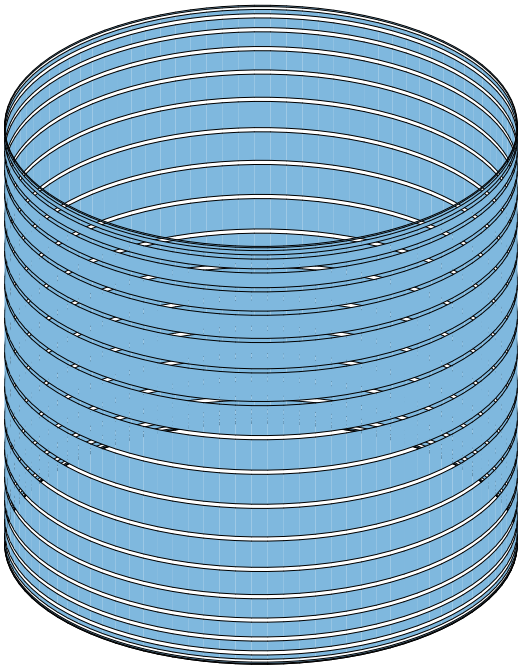

Figure 4.12: Visual representation of the 'disk stacking' concept used in HAWC2, where the 3D actuator cylinder is represented by stacked disks at cosine-spaced spanwise locations, in each of which the 2D actuator cylinder model is used. HAWC2NW actually models the interaction between these disks, whereas HAWC2 does not.

HAWC2 Near-Wake therefore forms a sensible compromise between a fast 2D aerodynamic model and a slower 3D model, enabling HAWC2 to simulate VAWT performance more accurately without significantly increasing runtime. It is however important to be aware of the limitations that this coupling method introduces.

4.4.2 Limitations

- The wake decay is approximated by exponential functions, leading to a compounding error over time, as the trailing vorticity is convected downstream. This is however not as much of a problem, since it is only modelling the near wake and is not required to be accurate in the far wake.
- Due to the nature of the near-wake model, it is not able to take into account the panel inclination angle inherent to the geometry of Φ-shaped VAWTs, hence these cannot be modelled.
- This lifting-line-based trailed vorticity model is not used as the 'full' aerodynamic model, but merely as an extension to the 2D actuator cylinder model, with some remaining inherent limitations as described in Section 4.3.
- The wake of each blade is modelled independently, meaning one blade's wake has no influence on another blade. There is only some indirect coupling, since the near wake model feeds back into the 2D actuator cylinder model.
- The shed wake is assumed to continue in a straight line, e.g. wake curvature and far-wake effects are not taken into account.

4.4.3 Results

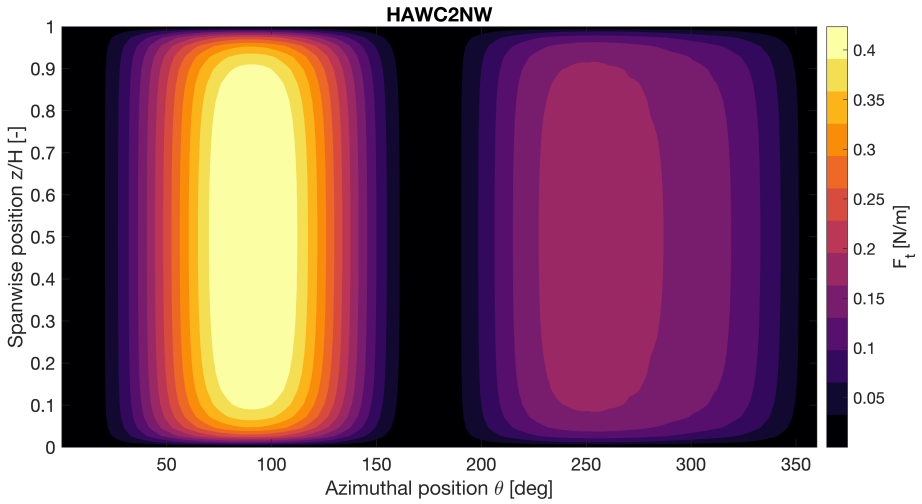

Figure 4.13: HAWC2 Near-Wake. Spanwise tangential force $F_t[N/m]$ as a function of azimuthal position θ using reference VAWT as described in Table 4.1.

Figure 4.13 shows the azimuthal and spanwise variation of the tangential force coefficient of the VAWT rotor, computed using HAWC2 with near-wake model. It is important to note that the HAWC2 turbine input has been set up in such a way that all structural and control influences are neglected, by setting all turbine members to high stiffness values and eliminating the controller entirely. Therefore, what is shown in these figures is purely the result of HAWC2's built-in actuator cylinder model for VAWTs, as well as the near-wake model described in this section.

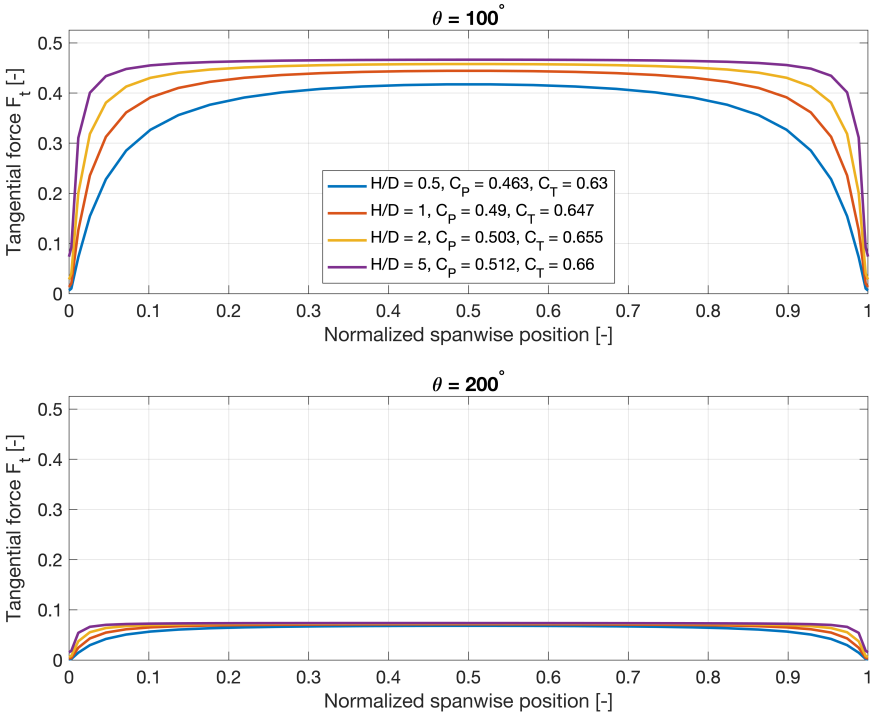

Figure 4.14: HAWC2 Near-Wake. Spanwise tangential force $F_t[N/m]$ at $\theta = [100°, 200°]$ for varying turbine aspect ratio $H/D = [0.5, 1, 2, 5]$, using reference VAWT as described in Table 4.1.

Figure 4.14 shows a snapshot of the tangential force on the blade at two different azimuthal positions, for varying turbine aspect ratios. Here it can be seen that the higher the turbine aspect ratio, the sharper the loads drop to zero towards the tips of the blades. The load distribution for H/D = 0.5 starts decreasing already close to the midspan position. The midspan tangential force is also lower for lower turbine aspect ratios.

4.4.4 Variation with number of blades

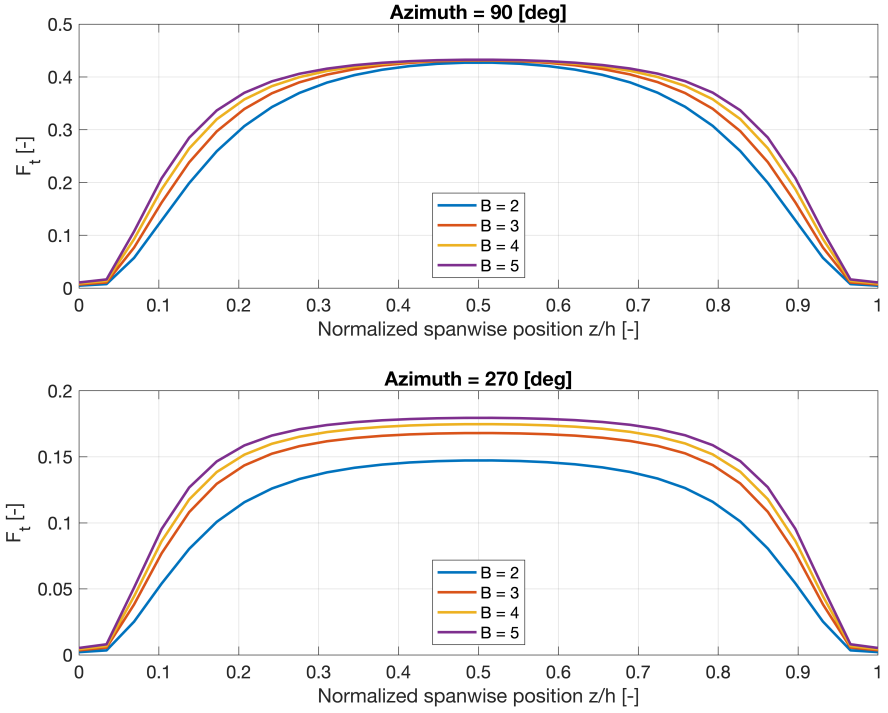

Figure 4.15: HAWC2 Near-Wake. Spanwise tangential force $F_t[N/m]$ using reference VAWT as described in Table 4.1, with varying number of blades, at two azimuthal positions.

Figure 4.15 shows the variation of the tangential loading at two different azimuthal positions for varying number of blades. While the maximum normal loading remains the same, the maximum tangential loading increases with increasing blade number. Additionally, the tip effect that results in a more gradual drop-off of the loads towards zero seems to increase with decreasing blade number.

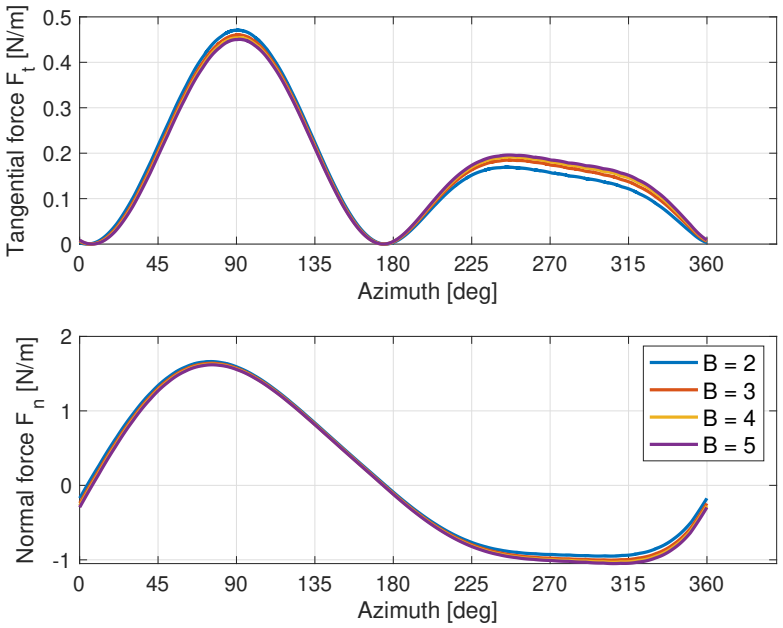

Figure 4.16: HAWC2 Near-Wake. Azimuthal variation of tangential and normal force F_t, F_n at the midspan location using reference VAWT as described in Table 4.1, with varying number of blades.

Figure 4.16 shows the azimuthal variation of the tangential and normal force for different blade numbers. It can be seen that the induction model in HAWC2 does indeed exhibit some type of coupling that varies by blade number, likely due to the fact that the blade-independent output from the near-wake model is fed back into the 2D actuator cylinder induction model, which partially takes the influence of multiple blades into account. However, as can be seen, the forces on one blade for different blade numbers are approximately similar in order of magnitude, so the influence of many blades on the induction field will be significant due to the overall sum of the forces involved. If the interaction between the blades is not explicitly taken into account, which it is not in the near-wake model, a higher blade number will result in significant inaccuracy of the induction model.

4.5 Vortex models

4.5.1 Background

Vorticity-based models rely on the concepts of vorticity and circulation as defined in potential flow theory. The explanation given here is adapted from Katz and Plotkin [48].

Vorticity ω is defined as the curl of the velocity field, in this case using the momentum equation of which the curl is taken such that $\nabla \times u = \omega$, as shown in Equation (4.28).

$$\begin{aligned} \frac{Du}{Dt} &= \frac{\partial u}{\partial t} + u \cdot \nabla u = -\nabla p + f + \mu \nabla^2 u \\ \frac{D\omega}{Dt} = \nabla \times \frac{Du}{Dt} &= \nabla \times \frac{\partial u}{\partial t} + \nabla \times (u \cdot \nabla u) \\ &= -\nabla \times \nabla p + \nabla \times f + \nabla \times (\mu \nabla^2 u) \end{aligned} \tag{4.28}$$

The result of Equation (4.28) can then be further simplified resulting in the vorticity equation Equation (4.29), containing a source flow term and a sink flow term.

$$\frac{D\omega}{Dt} = \nabla \times f + \mu \nabla^2 \omega \tag{4.29}$$

Circulation is expressed mathematically as in Equation (4.30), as illustrated by Figure 4.17. Consider an open surface S, bounded by curve C, with a tangential velocity component $d\vec{s}$. Circulation can then be defined as the vorticity integral over S (2^{nd} integral in Equation (4.30)), or the contour integral along C of the aforementioned tangential velocity component (1^{st} integral in Equation (4.30)).

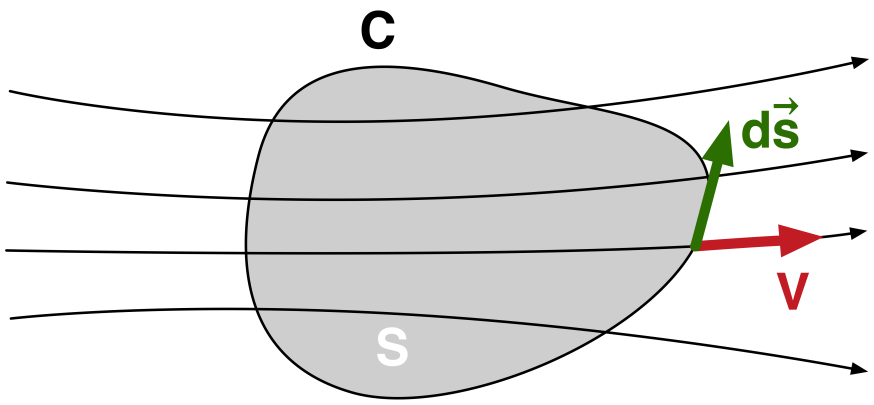

Figure 4.17: Circulation represented graphically using the open surface S that is bounded by the curve C.

$$\vec{\Gamma} = -\oint_C \vec{V} \cdot d\vec{s} = -\iint_S \vec{\nabla} \times \vec{V} dS = -\omega \iint_S \vec{\omega} dS \tag{4.30}$$

The second theorem of Helmholtz states that a line of vorticity entering the aforementioned surface C cannot end there, but instead has to continue through back to where it started, resulting in a rate of change of vorticity of zero.

Through the Kelvin-Stokes theorem, Helmholtz' second theorem imposes a similar restriction on the rate of change of circulation of a finite wing or blade. In 2D, as shown in Figure 4.18, this means that an airfoil in a flow generates a certain amount of circulation $\Gamma_{airfoil}$. But, due to the implications of Helmholtz's vortex theorems, the rate of change of this circulation must be zero in time, so an equal and opposite circulation Γ_{wake} must exist to make this so.

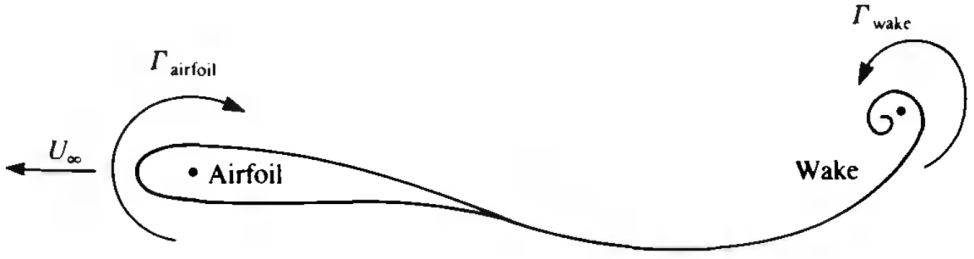

Figure 4.18: Circulation on an airfoil (reproduced from Katz and Plotkin [49])

Figure 4.19 shows the lifting line model for a 3D wing, including the bound vortex due to the circulation around the airfoil moving through the flow, the starting vortex that counters it and the free wake vortices that are generated from the tips of the wing. Due to Helmholtz's second theorem, which states that a vortex line cannot abruptly end in a fluid, the bound vortices on the wing must be countered by equal and opposite vortices. This is best represented physically by the 'shedding' of trailing vortices, forming a free wake.

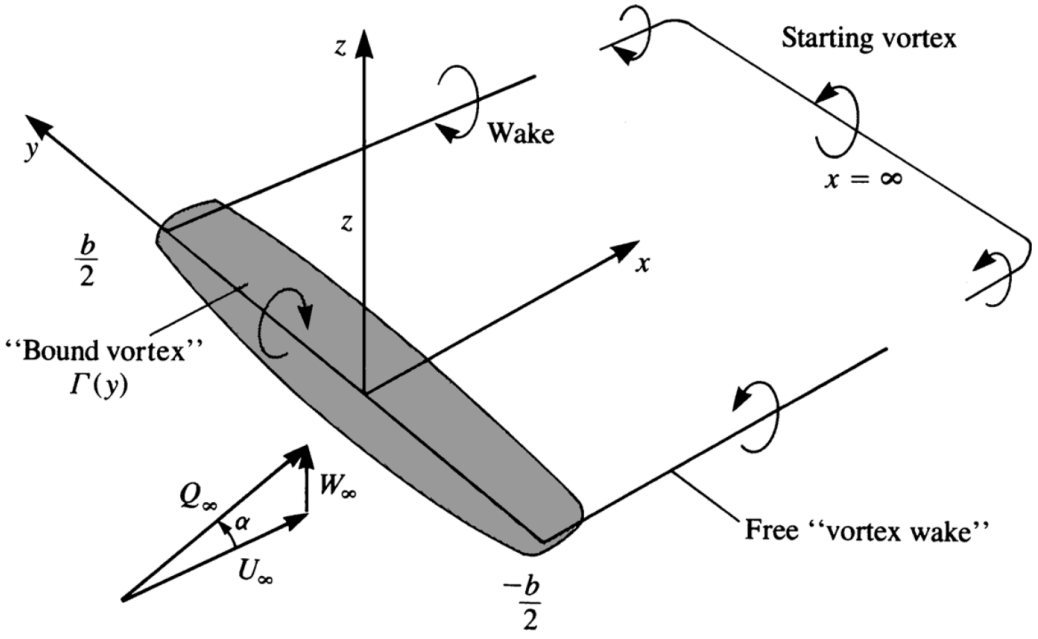

Figure 4.19: Circulation on a 3D wing (reproduced from Katz and Plotkin [49])

Vortex models are often based on this lifting line method originally developed by Prandtl, which concentrates the chordwise circulation on a 3D to a circulation distribution $\Gamma(y)$ on the $\frac{1}{4}$ chord point, along a line in the spanwise direction. The resulting closed vortex system is then composed of the lifting line bound vorticity $\Gamma(y)$, the trailing vorticity arising from the wing tips and the shed vortices in the far wake, satisfying Helmholtz's vortex theorems.

It should be noted that the lifting line method makes use of thin airfoil theory to calculate aerodynamic forces on the wing or blade and therefore do not take into account airfoil geometry. Panel methods also exist, which describe a lifting surface rather than a lifting line and are able to take into account airfoil geometry, curvature and the resulting chordwise variation of circulation.

Lifting line and panel methods can be used to model a wake in time. There are two ways of conducting this wake time development:

- Frozen wake vortex model, which assumes a wake shape that is frozen in time, even though it is propagated behind the wing due to the freestream velocity and geometry of the wing.
- Free wake vortex model, which develops the wake by calculating the induced velocities caused by the wake as well as the circulation on the wing itself. This results in a deformed wake, unlike the frozen wake which remains of the same shape and size.

Existing vortex codes

U2DiVA
Simão Ferreira [89] developed an unsteady 2D free wake vortex panel code based on the formulation of Katz and Plotkin [49]. It models the near wake using a vortex particle method and the far wake using vortex points.

Ferreira proposed a method to improve existing momentum-balance based DMST models using the 2D vortex code. The U2DiVA code shed some light on the wake development due to the downwind and upwind halves of the VAWT rotation, where the existing DMST models seemed to overestimate wake development due to the downwind actuator disk.

Another interesting conclusion from this research was that flow curvature effects and blade pitching, while important for local blade loading, have little to no effect on the induction field of the rotor as a whole. This enables the use of vortex models such as U2DiVA to 'design' the optimal induction field, followed by a blade design to match. For BEM-based models such as the DMST model, the blade design is the major design parameter which leads to an induction field based on the work done by the local aerodynamic forces on the blade. Having the blade design be a product of the induction field, rather than the other way around, results in increased model performance and accuracy in favor of the vortex methods, effectively rendering the DMST approach obsolete (even with the modified DMST model, when supplemented by forces calculated using vortex models).

ARDEMA2D
The two-dimensional unsteady vortex particle code ARDEMA2D is based on the work of Deglaire [26] and works using virtual airfoil profiles to account for flow curvature effects, generated with a conformal mapping method.

VDART3
VDART3 was developed for Sandia National Laboratories by Strickland et al. [102], who previously came up with the DMST approach. The authors validated the code using experiments in a water tank rather than a wind tunnel, to aid in flow visualisation and enable high Reynolds number operating conditions. The code was meant to be able to accurately predict blade loading as well as development of the near wake of the turbine.

CACTUS
VDART3 was used as the basis for a new model by Murray and Barone [72] called CACTUS (Code for Axial and Crossflow Turbine Simulation) that was primarily intended for use in marine applications such as tidal turbines and wave energy extractors. Simulations of a demonstration VAWT were also performed and showed promising results with regards to the accuracy of the CACTUS model compared to experimental data.

Zanon et al. [115] developed a double-wake vortex panel method to model the wake of the VAWT in dynamic stall. The reason for using a double-wake vortex model is because the single-wake vortex model, whilst accurate for higher tip speed ratios ($\lambda \geqslant 3$), results in inaccuracies in loads, induced velocity field and vorticity at lower tip speed ratios. Where traditional panel methods work with a panel at the trailing edge, where the shed circulation is calculated, the double-wake method introduces an additional panel at the flow separation point. Therefore, vortex elements are being shed

from two points instead of one, which is a more accurate representation of the physical wake of the blades undergoing flow separation.

Dixon[27] developed a 3D unsteady multibody free wake panel code specifically for VAWTs, with the ability to accurately predict the wake development of the VAWT in 3D, including aerodynamic phenomena such as dynamic stall and the blade-wake interaction that is experienced by the VAWT blades. This method was validated using a multitude of flow measurement techniques such as particle image velocimetry (PIV), smoke-trails and water tank dye injection. Variables affecting the wake development that are investigated are tip speed ratio and height-rotor diameter ratio, amongst others.

4.5.2 CACTUS 3D

CACTUS (Code for Axial and Crossflow Turbine Simulation) was developed at Sandia National Laboratories and refined by Murray and Barone[72] to include modelling of vertical axis wind turbine aerodynamics. The code eschews traditional momentum-based methods in favor of a free wake vortex method, which enables it to more accurately model the effect of various rotor loadings on the wake and thus the aerodynamic performance of the turbine. It has been chosen as the vortex model used in the model analysis of this thesis for its relative ease of use and the availability of computed data using the parameters of the reference VAWT as shown in Table 4.1. The rapid increase in computing power in the 2000's enabled the use of vortex methods in the design phase, rather than final validation, for which CFD methods are now preferred. CACTUS is based on a free wake vortex method, meaning it takes into account self-induction of the wake as well as induced velocities due to the blades themselves. The wake therefore deforms over time, contrary to a frozen (fixed) wake method where the wake retains its shape whilst being convected downstream. The two distinctions of this model will henceforth be referred to as 'CACTUSfree' and 'CACTUSfixed'.

Fundamental equations

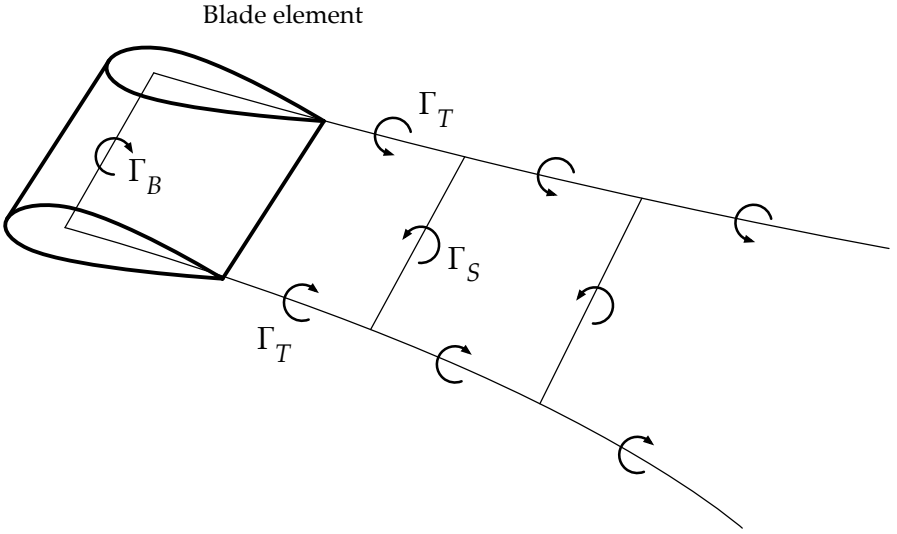

Figure 4.20: Wake of a blade element represented by a vortex lattice system.

Figure 4.20 shows the representation of a blade element wake using a vortex lattice system. The vortex lattice system consists of a bound vortex on the blade Γ_B, trailing vortices Γ_T and shed vortices Γ_S. The magnitude of the bound vortex Γ_B is equal to $\Gamma_B = \frac{1}{2} \cdot U \cdot c \cdot C_L$, with C_L determined for each

section and angle of attack from the local 2D airfoil polar. The magnitudes of the trailing and shed vortices are time-dependent and related to the bound circulation as in Equation (4.31). They are also dependent on the spanwise position y and the distance between blade elements dy.

$$\begin{aligned} \Gamma_T(y,t) &= \Gamma_B(y,t) - \Gamma_B(y+dy,t) \\ \Gamma_S(y,t) &= \Gamma_B(y,t-dt) - \Gamma_B(y,t) \end{aligned} \tag{4.31}$$

Helmholtz's theorem,[49] which states that circulation must be conserved along a vortex line, dictates how the trailing and shed vorticity vary due to the spanwise and temporal variation of the bound circulation. Unlike with horizontal axis wind turbines, the bound circulation Γ_B on a rotating VAWT blade is constantly changing as it experiences a rapid variation in angle of attack during a single revolution.[38]

Having established the vortex lattice system, the velocity field can subsequently be calculated using the Biot-Savart law.[49] The velocity vector $\vec{q_P}$ at a certain point P in space, induced by a segment of the vortex lattice system, is shown in Equation (4.32). $\vec{r_1}$ and $\vec{r_2}$ are the distance vectors from point P to both ends of the vortex line segment, respectively.

$$\vec{q_P} = \frac{\Gamma}{4\pi} \frac{\vec{r_1} \times \vec{r_2}}{|\vec{r_1} \times \vec{r_2}|^2} (\vec{r_1} - \vec{r_2}) \cdot \left(\frac{\vec{r_1}}{|\vec{r_1}|} - \frac{\vec{r_2}}{|\vec{r_2}|} \right) \tag{4.32}$$

When the induced velocity field has been determined, a blade element model is used to evaluate the static and dynamic loads on the blades, resulting from the angle of attack, the rate of change of the angle of attack and the induced velocity. These are then again used as inputs for the next timestep in order to compute the magnitudes of the bound, shed and trailing circulation and the cycle repeats itself.

CACTUS is also able to take into account several complex aerodynamic effects (provided the flow remains attached) such as flow curvature, added mass effects and induction due to bound circulation. The latter is particularly interesting, since it is a 3D effect that is generally ignored in all lower-fidelity models.

Limitations

- Blades are divided up into blade element sections, the loads on which are computed using 2D airfoil data. This means that the flow local to the blade element section is assumed to be two-dimensional.
- Results close to the tip of the blades (and close to any other discontinuities) are prone to errors introduced by the vortex core size.
- Obtaining a converged simulation using this model takes a significant amount of runtime even on a high powered computing server, in contrast with other previously mentioned models, which run quickly on a local machine.

Results

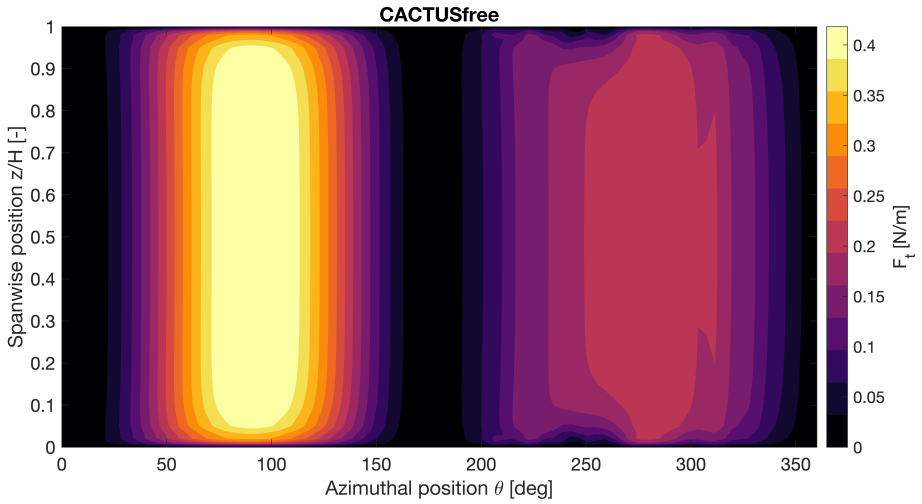

(a) CACTUS free-wake model.

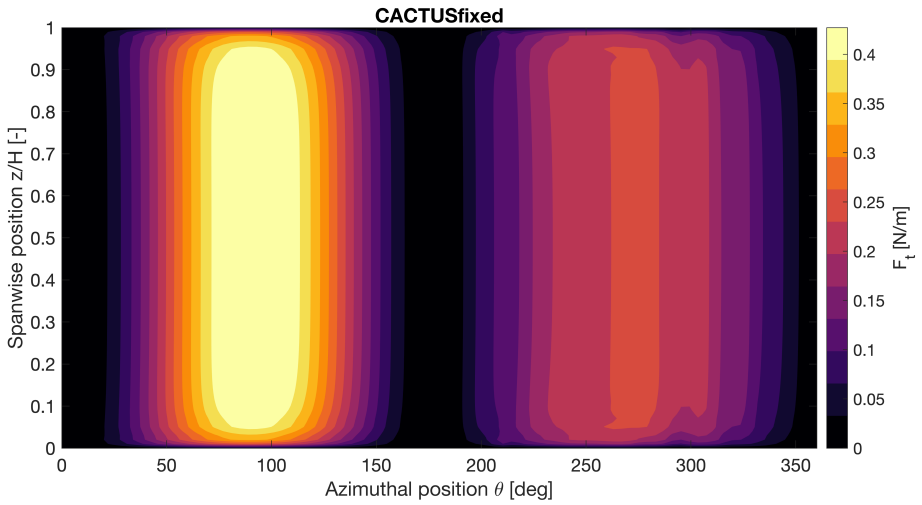

(b) CACTUS fixed-wake model.

Figure 4.21: Spanwise tangential force $F_t[N/m]$ as a function of azimuthal position θ using reference VAWT as described in Table 4.1.

Figure 4.21 shows the tangential force for both the fixed-wake and free-wake versions of CACTUS, which exhibit mostly the same characteristics in the upwind region, with slight differences in the downwind region. Overall, the azimuthal and spanwise variation of these model results are in line with what is expected from a simulation of a turbine with a low turbine aspect ratio ($H/D = 1$, in this case).

Figures 4.22 and 4.23 shows spanwise results for the tangential force at two different instanteneous azimuthal positions. While the spanwise trend is similar across the two models, the difference between turbine aspect ratios is more pronounced for the free-wake model. This suggests that the interaction of the blade's wake with itself and that of other blades is significant when examining different turbine aspect ratios. A fixed-wake model which 'fixes' the wake shape after it has been shed from the blade is potentially unable to capture the full extent of the 3D finite turbine aspect ratio phenomenon.

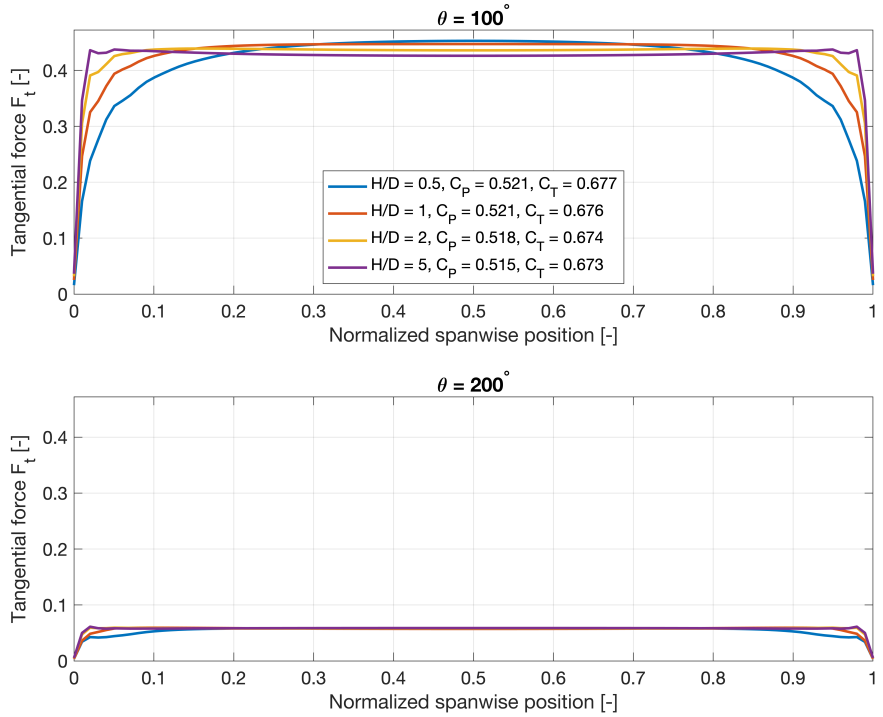

Figure 4.22: CACTUS free-wake model. Spanwise tangential force $F_t[N/m]$ at $\theta = [100°, 200°]$ for varying turbine aspect ratio $H/D = [0.5, 1, 2, 5]$, using reference VAWT as described in Table 4.1.

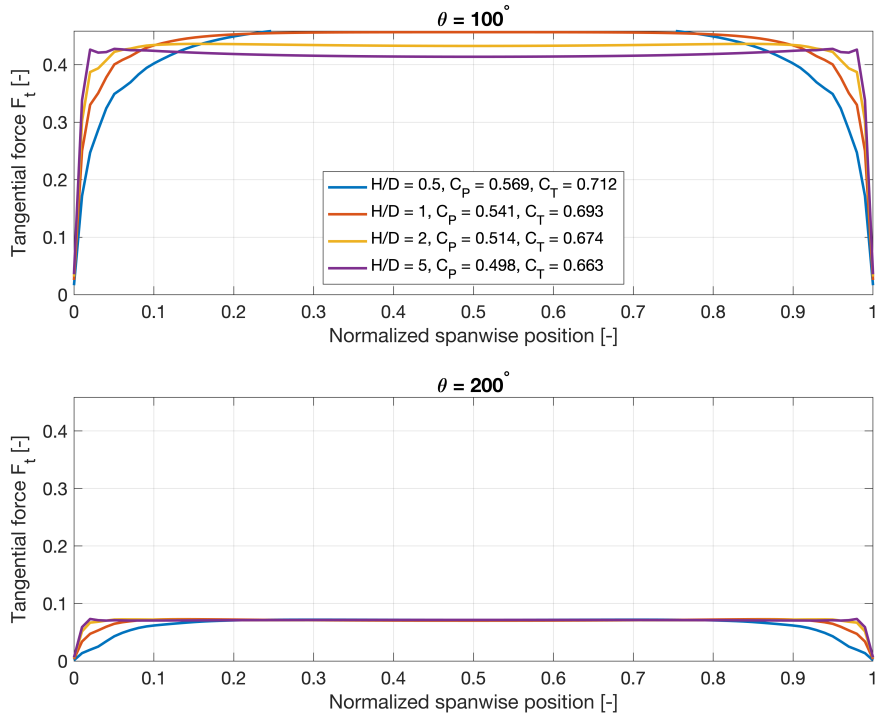

Figure 4.23: CACTUS fixed-wake model. Spanwise tangential force $F_t[N/m]$ at $\theta = [100°, 200°]$ for varying turbine aspect ratio $H/D = [0.5, 1, 2, 5]$, using reference VAWT as described in Table 4.1.

4.6 Computational fluid dynamics models

4.6.1 Background

Aerodynamic modelling using computational fluid dynamics is considered to be of very high fidelity but comes at a significant cost in terms of computational requirements. This is due to the nature of CFD methods, where the fluid domain is discretized into a mesh and the Navier-Stokes equations are solved numerically for every element in the mesh. This mesh has to be fine enough to resolve small-scale flow phenomena, resulting in a large number of mesh elements to be solved and therefore a large amount of computations required to yield a solution, even for one timestep.

There are three main subcategories of CFD modelling, each with its own level of fidelity and computational effort required.

- **Reynolds-averaged Navier-Stokes (RANS) models** make use of a time-averaging of the Navier-Stokes equations. This time-averaging results in a closure problem caused by there being four equations and 10 unknowns in the system. This closure problem is subsequently solved using a turbulence model, including but not limited to the $k-\epsilon$ model, the $k-\omega$ model or mixing length model as defined by Prandtl. While the time-averaging procedure and inclusion of turbulence models results in a solution to the Navier-Stokes equations that is relatively quick to solve compared to direct numerical methods, it does introduce inaccuracies into the solution.
- **Large eddy simulations (LES)** make use of a filtering approach that filters out smaller flow structures that would take a lot of time to compute and instead approximates these using, for example, the Boussinesq eddy viscosity approximation. No time-averaging occurs so the method is more accurate than RANS models, but there is still a certain degree of approximation that negatively impact the accuracy of the solution.
- **Direct numerical simulations (DNS)** do not employ any turbulence models to resolve small-scale flow structures and instead opt to numerically solve the Navier-Stokes equations directly. This method is highly computationally intensive and is therefore often passed over in favor of RANS or LES models.

Rezaeiha et al.[84] outlined a set of guidelines for modelling VAWT aerodynamics using computational fluid dynamics in order to investigate the impact that various computational parameters may have on the results of such simulations. They carried out 110 CFD simulations of two VAWTs for a range of tip speed ratios and rotor solidities. Their conclusions impose limits on the azimuthal increment $d\theta$ used in simulations, the time step needed to resolve flow phenomena such as blade-wake interaction and dynamic stall, as well as the minimum distances of the domain outlet and inlet as a function of turbine diameter.

4.6.2 The actuator line model

Traditionally, computational fluid dynamics (CFD) models have been computationally expensive, to a prohibitive extent, for use in engineering calculations. The unsteady nature of VAWT aerodynamics however demands much more accurate modelling, with lower-fidelity models often resulting in larger errors compared to their HAWT equivalents. Actuator line modelling simplifies the lifting geometry to a one-dimensional vortex filament, resulting in a faster model as compared to, for example, fully resolved RANS-based models. The actuator line model used here is that of Bachant et al.[4], referred to as turbinesFoam due to it being implemented in open-source CFD modelling suite OpenFOAM.

Fundamental equations

Blade element theory is integrated into this model to predict the forces on each blade section, as in Equation (4.33).

$$
\begin{aligned}
L &= \frac{1}{2}\rho A C_l |\vec{V_{rel}}|^2 \\
D &= \frac{1}{2}\rho A C_d |\vec{V_{rel}}|^2 \\
M &= \frac{1}{2}\rho A c C_l |\vec{V_{rel}}|^2
\end{aligned}
\tag{4.33}
$$

Having calculated the force on a single actuator line element, its resulting effect on the flow field is calculated by using the force as input to the instantaneous Navier-Stokes equations in the form of a body force term, as shown in Equation (4.34).

$$
\frac{D\vec{u}}{Dt} = -\frac{1}{\rho}\nabla p + \nu\nabla^2\vec{u} + F_{turb} \tag{4.34}
$$

The actuator line approximation means that this force is now acting on a single point in space, for every actuator line element, rather than being spread out chordwise across a blade section. To avoid the numerical instability that may result from projecting a force on a single point in the mesh (and the resulting steep gradients) the force is distributed amongst nearby cells using a Gaussian function. This step is called force smearing and may potentially result in inaccuracies if the width of the Gaussian spreading function is not set properly. Bachant et al.[4] discussed proper procedures for setting this width, relating it to the cell size of the neighboring mesh.

Limitations

- Blades are divided up into blade element sections, the loads on which are computed using 2D airfoil data. This means that the flow local to the blade element section is still assumed to be two-dimensional.
- Similar to how the vortex core size affects the results of the CACTUS/vortex model, the actuator line CFD model is heavily influenced by the effects of force smearing, which may introduce inaccuracies near discontinuities such as blade tips. Meyer Forsting et al.[69] investigated this phenomenon and explained that the vortex core problem and adverse effects resulting from force smearing are in fact manifestations of the same issue. They also suggest a dynamic correction for the actuator line model that is able to alleviate some of the inaccuracies introduced by this limitation.
- For tip effects to be properly taken into account, this model still employs an end effects correction, which, while effective, is still an empirical correction and not an accurate physical representation of the tip effect phenomenon.
- Obtaining a converged simulation using this model takes a significant amount of runtime even on a high powered computing server, in contrast with other previously mentioned models, which run quickly on a local machine. Even CACTUS simulations are significantly faster than the actuator line CFD model, although the fact that a lifting line approximation is used means that this type of CFD model is still much faster than a fully resolved CFD simulation of a VAWT blade.

Results

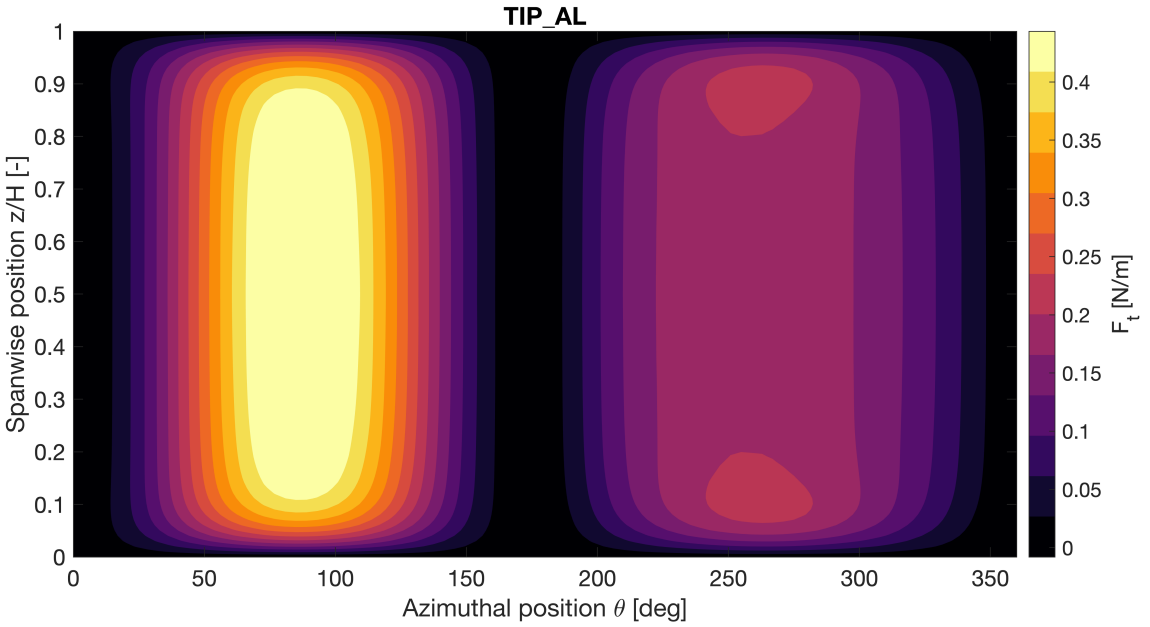

Figure 4.24: TurbinesFoam actuator-line model with end effects correction enabled. Spanwise tangential force $F_t[N/m]$ as a function of azimuthal position θ using reference VAWT as described in Table 4.1.

Figure 4.24 shows the spanwise tangential force distribution over the VAWT rotation. The influence of the end effects correction is clearly visible, as the tangential force tapers off towards the edges of the blade.

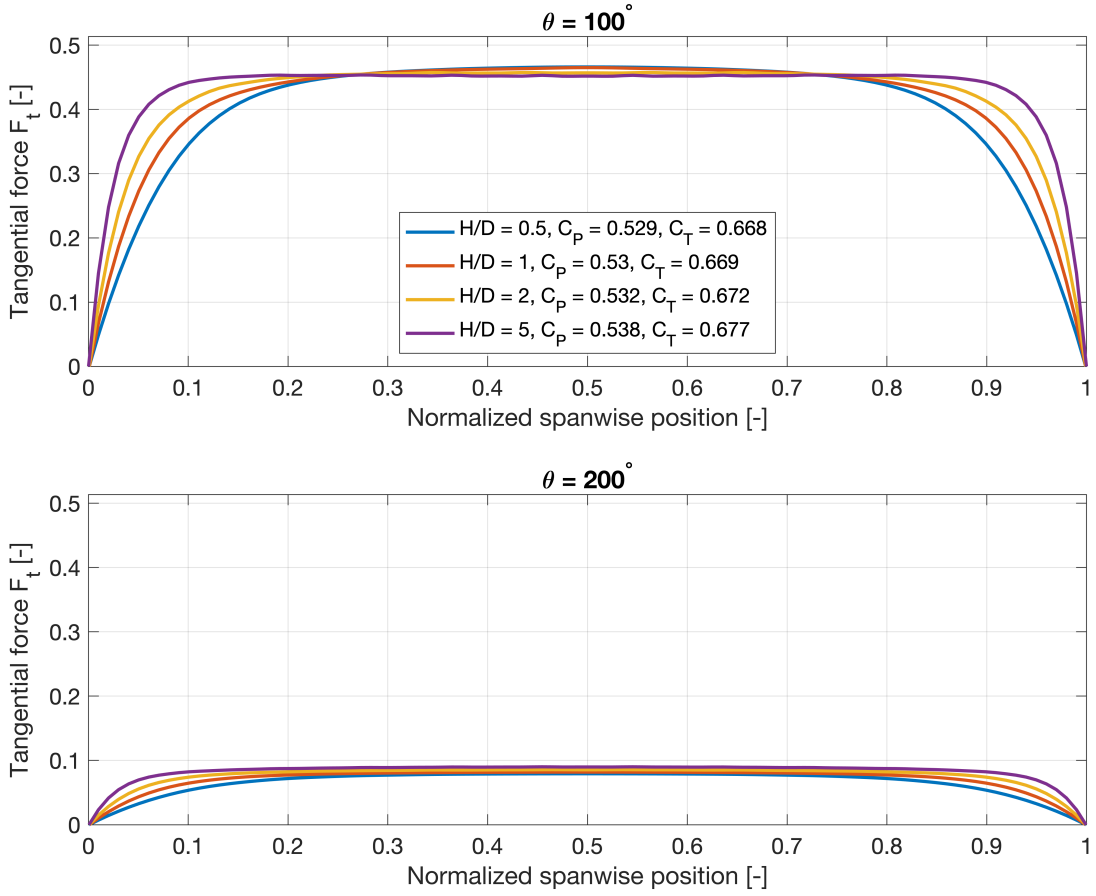

Figure 4.25: TurbinesFoam actuator-line model with end effects correction enabled. Spanwise tangential force $F_t[N/m]$ at $\theta = [100°, 200°]$ for varying turbine aspect ratio $H/D = [0.5, 1, 2, 5]$, using reference VAWT as described in Table 4.1.

Figure 4.25 shows the variation of the spanwise tangential force with turbine aspect ratio H/D. It can be seen that high H/D result in a flatter spanwise distribution, although this effect is more pronounced at azimuthal angles where high loading is encountered, such as halfway the upwind half of the rotation ($\pm\theta = 100°$). It should be noted that for the actuator line model, its built-in end effects correction is enabled. This provides a method of reducing the loads to zero towards the tips of the blades, but this method is empirical and thus not very physically accurate, despite delivering good results. Without this end effects correction, the actuator line model actually predicted an increased angle of attack and increased loads towards the blade tips. This is physically inconsistent and likely an unwanted side-effect of the force smearing approach mentioned earlier in this section.

4.7 Comparison of model results

This section presents a comparison of the aerodynamic models described in Table 4.2, also indicating the source of the results. Parts of this analysis have been published in the work of De Tavernier et al.[24].

Figure 4.26 shows the integral parameters C_P and C_T for all models. For the 3D models (HAWC2 NW, CACTUSfixed, CACTUSfree and Actuator Line) the integral parameters were computed at the midspan section, for a turbine with an aspect ratio of $H/D = 5$. This was done because at higher

Short model name	Description	Data source
UnsteadyBEM	Unsteady blade element momentum method[8]	Results obtained using MATLAB script provided by Martin O.L. Hansen
DMST	Double multiple streamtube model[77]	Results obtained by the author using a MATLAB script based on Paraschivoiu's DMST implementation.
2D AC	Two-dimensional actuator cylinder model[59]	Results obtained by the author using MATLAB script based on the implementation by Delphine De Tavernier.
HAWC2	Horizontal Axis Wind turbine simulation Code 2nd generation	Results obtained by the author.
HAWC2 NW	HAWC2 with near-wake correction for VAWT[78]	Results obtained by the author using HAWC2 NW binaries provided by Georg Pirrung.
CACTUSfixed/free	Free- and fixed-wake versions of the CACTUS vortex model[72]	Results provided by Delphine De Tavernier.
AL-CFD	Actuator line CFD model[4]	Results provided by Delphine De Tavernier.

Table 4.2: Aerodynamic models and data source attribution.

turbine aspect ratio, the midspan section approaches 2D conditions, enabling a comparison to be made.

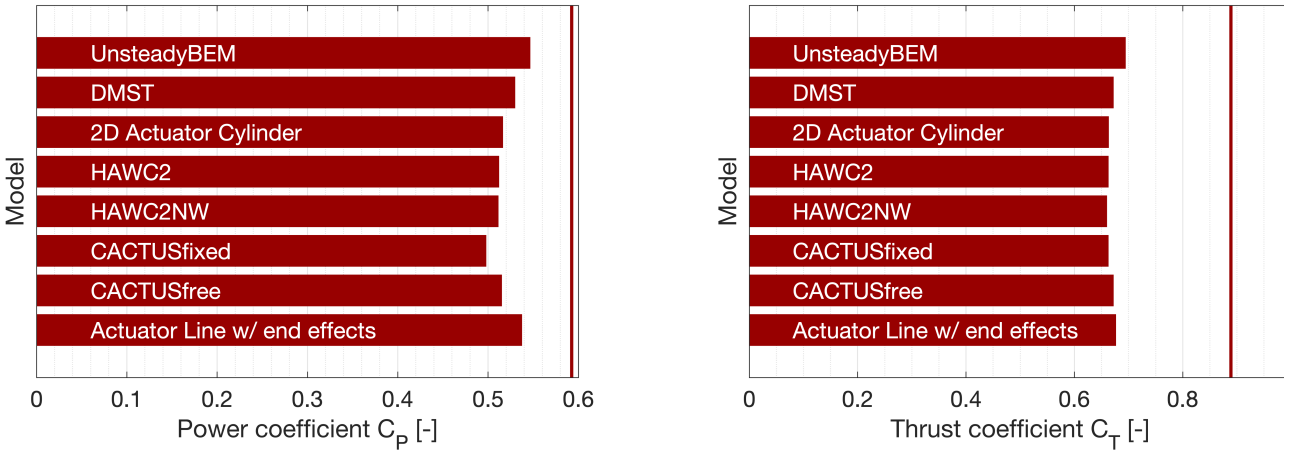

Figure 4.26: Power coefficient C_P and thrust coefficient C_T for all tested aerodynamic models, using reference VAWT as described in Table 4.1. Results from 3D models HAWC2 NW, CACTUS and Actuator Line are computed from midspan parameters for a turbine aspect ratio of H/D = 5.

What is not shown in Figure 4.26 is the runtime of each model, which varies by several orders of magnitude. The UnsteadyBEM, DMST and 2D actuator cylinder models (including HAWC2/HAWC2NW) take mere seconds to run, whereas the higher-fidelity models like CACTUS and the Acutator Line CFD model require several days (!) of runtime on high-powered computing servers in order to fully converge.

To be able to compare the induction models behind the tested aerodynamic models, it is useful to look at how each of the models modifies the angle of attack at different points in a single revolution of the VAWT. A blade on a VAWT rotor experiences a geometric angle of attack purely due to the combination of the turbine's rotation and the freestream velocity, without any induction present. Eliminating this geometric angle of attack enables a clearer view of how and where the aerodynamic models act. The parameter visible in Figure 4.27 is $\Delta\alpha$, as defined in Equation (4.35).

$$\begin{aligned} \alpha_{\text{geom}} &= \arctan\left(\frac{V_\infty \sin\theta}{\omega R + V_\infty \cos\theta}\right) = \arctan\left(\frac{\sin\theta}{\lambda + \cos\theta}\right) \\ \Delta\alpha &= \alpha_{\text{total}} - \alpha_{\text{geom}} \end{aligned} \tag{4.35}$$

The result is shown in Figure 4.27.

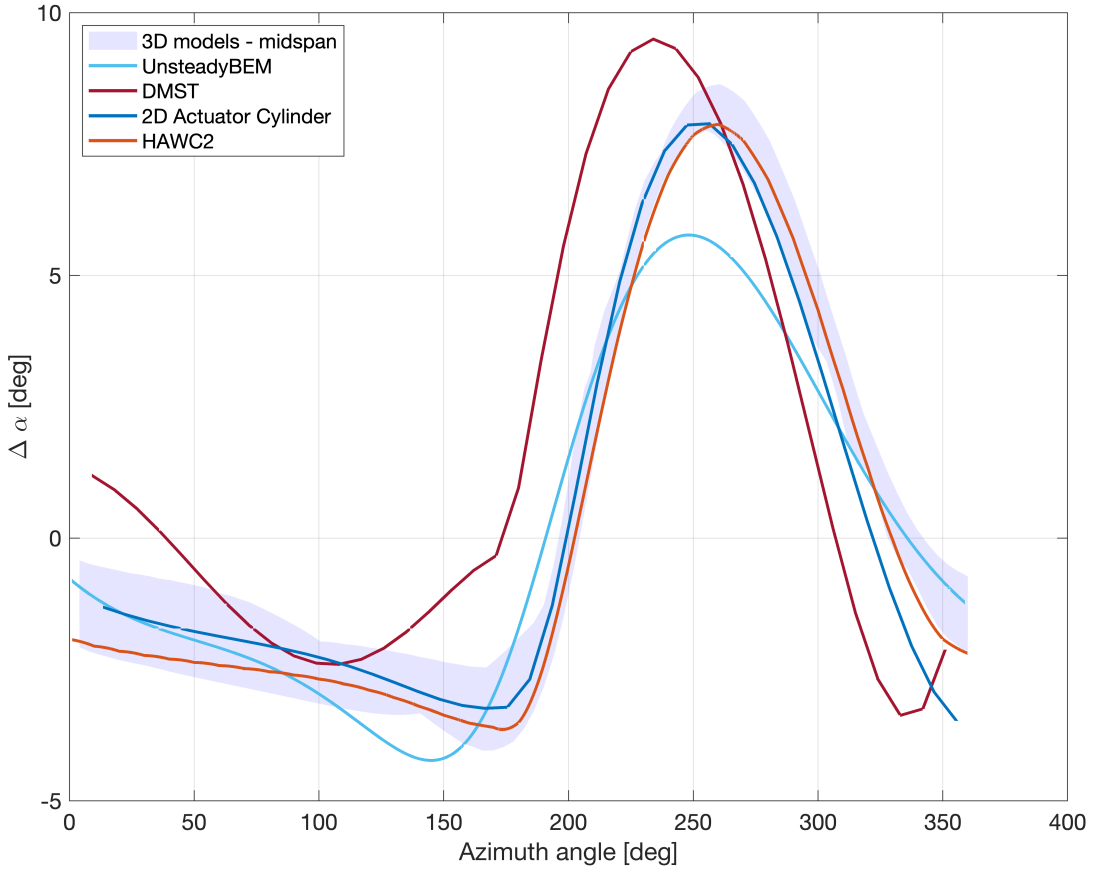

Figure 4.27: Change in angle of attack $\Delta\alpha$ with respect to the geometric angle of attack due to the rotation and wind speed, for the four 2D models. For reference, rotor midplane results for the 3D models are included using the blue shaded area.

Figure 4.27 also shows a range of the change in angle of attack $\Delta\alpha$ as calculated by the higher-fidelity, 3D models, in the form of the blue shaded area. Assuming these 3D models to be more accurate than the 2D models, the 2D actuator cylinder model, as well as HAWC2 which is effectively the same model, show promising results, keeping up with the 3D model range throughout the azimuthal range. The double multiple streamtube method shows an overestimation of the angle of attack across

the board. The unsteady BEM method seems to underestimate the angle of attack in the downwind region, perhaps due to the fact that the influence of the upstream region on the downwind region may not be taken into account.

Figure 4.28 shows the tangential force distribution over the blade at different azimuthal angles, for a turbine aspect ratio of H/D $= 1$. Overall, the models seem to agree well with each other in terms of the azimuthal and spanwise trends, although the downwind half of the rotation presents some challenges in terms of consistency of the distributions. The actuator line model (`TIP_AL`) shows two areas in the downwind region where the tangential force is higher than at the midspan, which could be a result of force smearing as mentioned in Section 4.6.2.

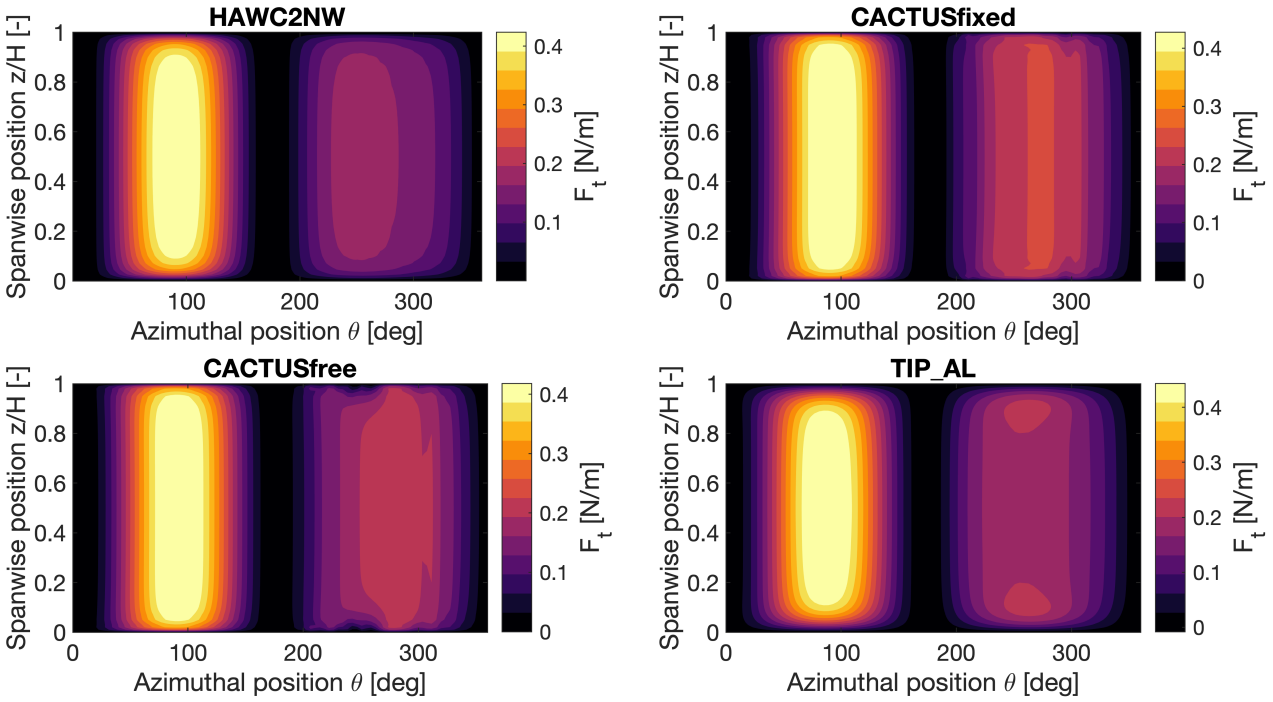

Figure 4.28: Spanwise distribution of tangential force versus azimuthal position for the 3D models, for H/D $= 1$

Figure 4.28 shows the normal force distribution for each model, exhibiting similar trends as the tangential force in Figure 4.28.

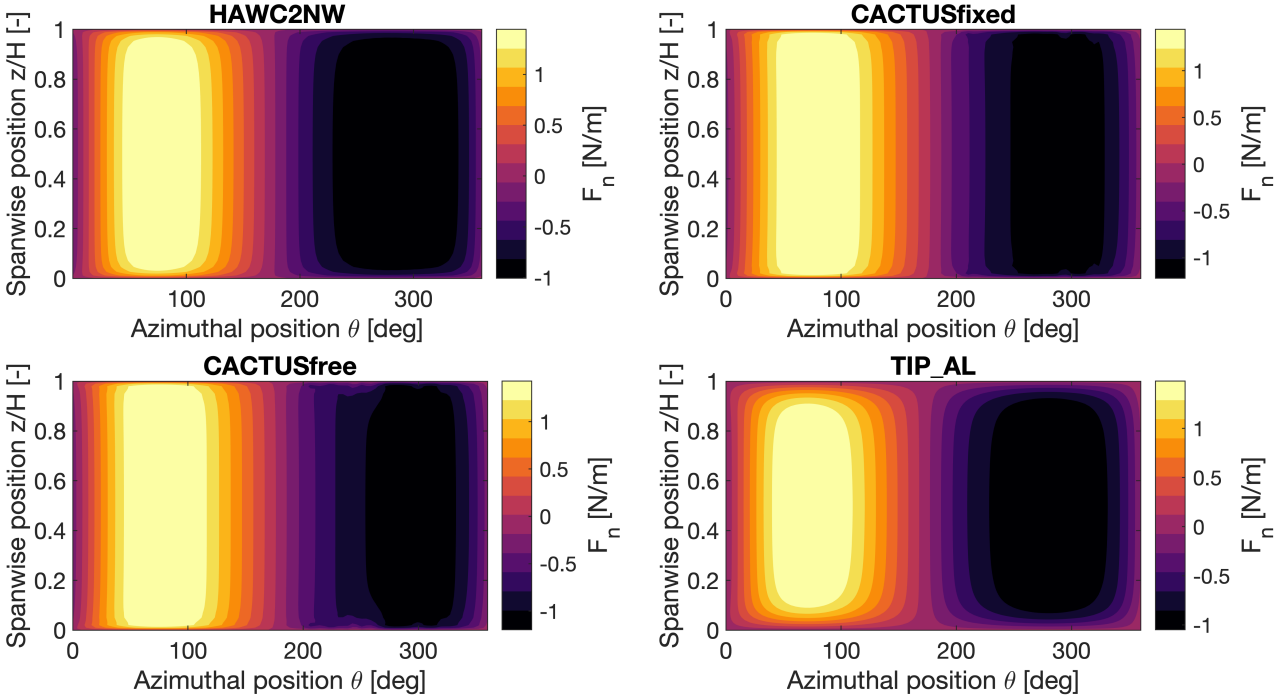

Figure 4.29: Spanwise distribution of normal force versus azimuthal position for the 3D models, for H/D = 1

Figure 4.30 shows the variation of the tangential and normal force at the midspan location, for the various 3D models. Here it can be seen

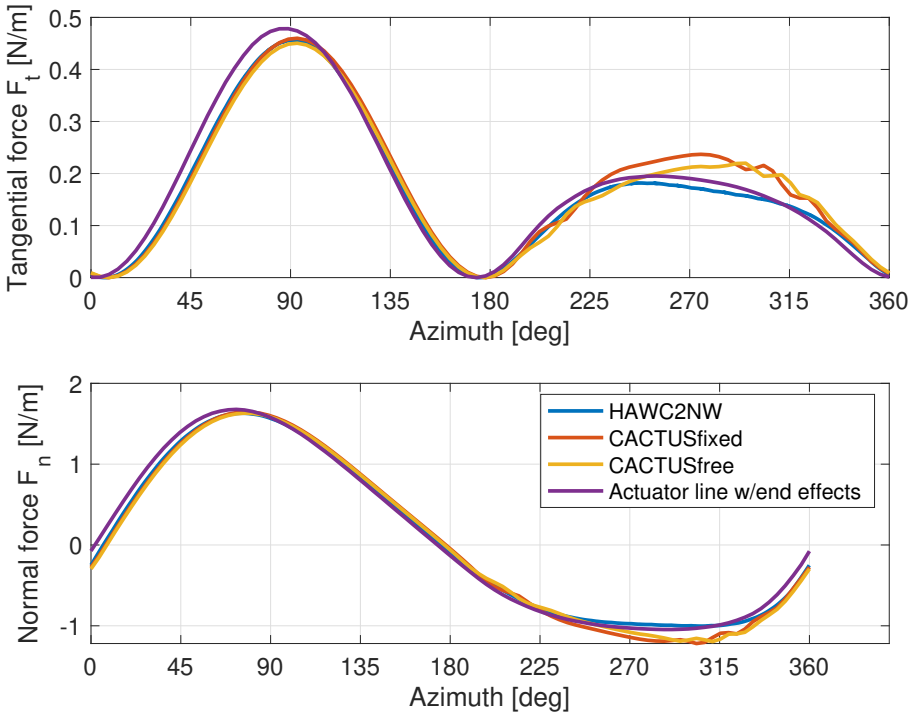

Figure 4.30: Azimuthal variation of tangential and normal force for the 3D models at the midspan location, for H/D = 1

4.7.1 Comparison at different aspect ratios

The 3D models are, to some extent, able to predict spanwise differences in loads, resulting from 3D effects. These 3D effects vary depending on the turbine aspect ratio H/D.

Figures 4.31 and 4.32 show the normal and tangential force at $\theta = 90°$ in the upwind region, for different turbine aspect ratios H/D. While the results at midspan do not deviate much, except for $H/D = 0.5$, there is quite some disparity between how each model chooses to let the loads on the blade approach zero towards the tips. The actuator line model with end effects correction seems to overcorrect, whereas both variants of CACTUS exhibit much steeper gradients towards the tips, without there being much difference between the lowest and highest H/D.

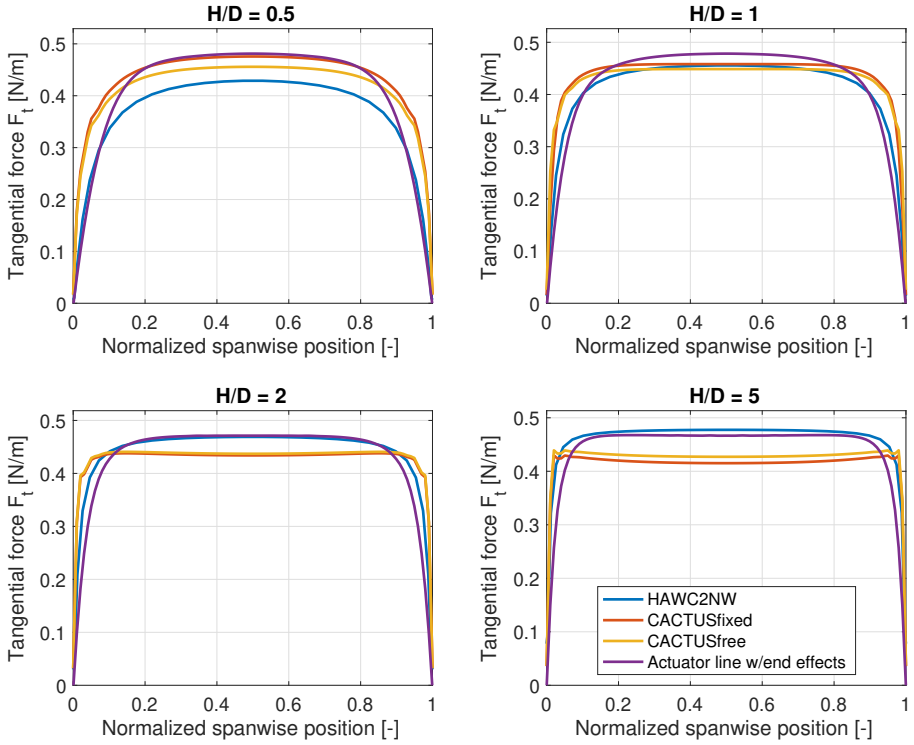

Figure 4.31: Spanwise distribution of tangential force at ($\theta = 90°$) for the 3D models, for four different turbine aspect ratios H/D.

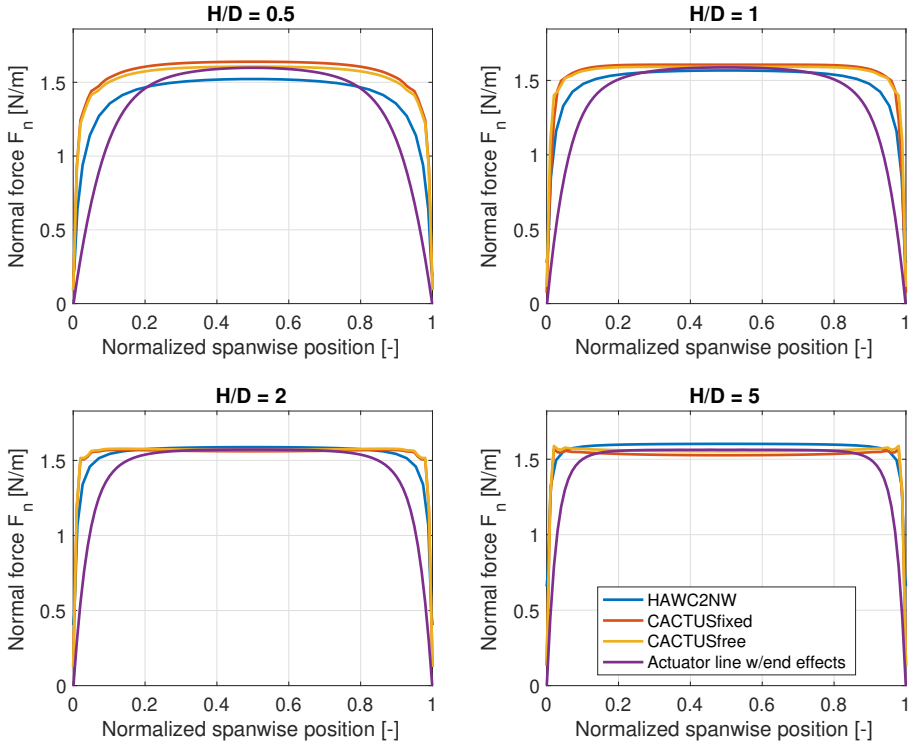

Figure 4.32: Spanwise distribution of normal force at ($\theta = 90°$) for the 3D models, for four different turbine aspect ratios H/D.

When examining a moment in the downwind region ($\theta = 270°$) Figures 4.33 and 4.34, the differences between the models become quite clear, in terms of their ability to predict forces on the turbine at different aspect ratios. These differences can mostly be explained by the fact that the CACTUS and actuator line models include dynamic stall to some extent, whereas HAWC2 NW has its dynamic stall model turned off. This results in significant differences in maximum normal or tangential force when taking a snapshot of the load distribution at a certain azimuth, as is done in Figures 4.33 and 4.34. When examining the temporal variation of the maximums of these forces, it is seen that the other models are lagging behind HAWC2 NW, due to its omission of a dynamic stall model resulting in instant availability of lift. This can be observed in Figure 4.30.

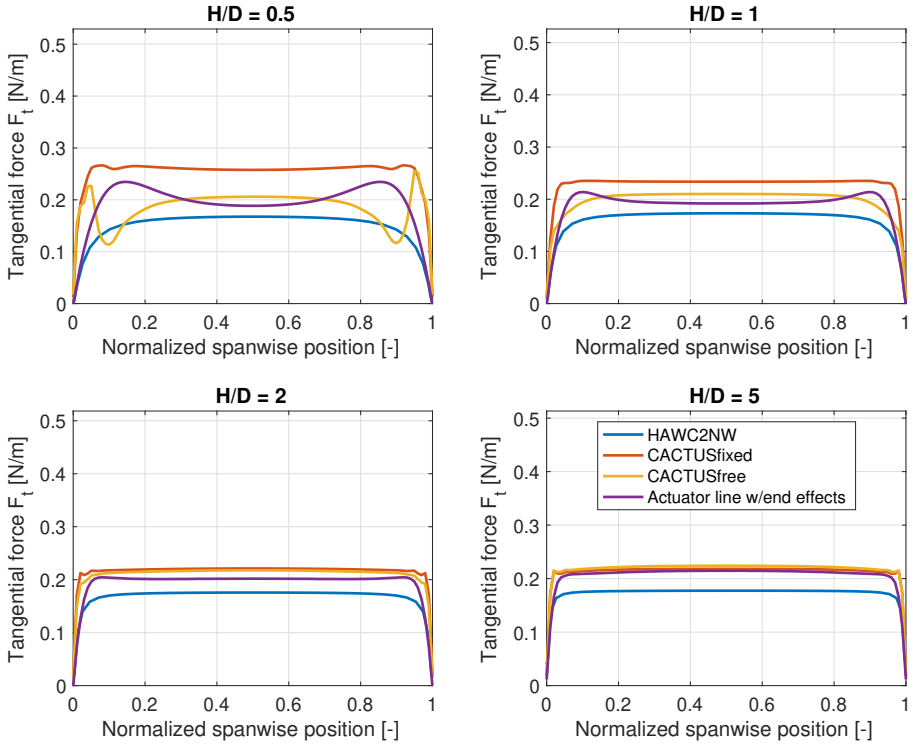

Figure 4.33: Spanwise distribution of tangential force at ($\theta = 270°$) for the 3D models, for four different turbine aspect ratios H/D.

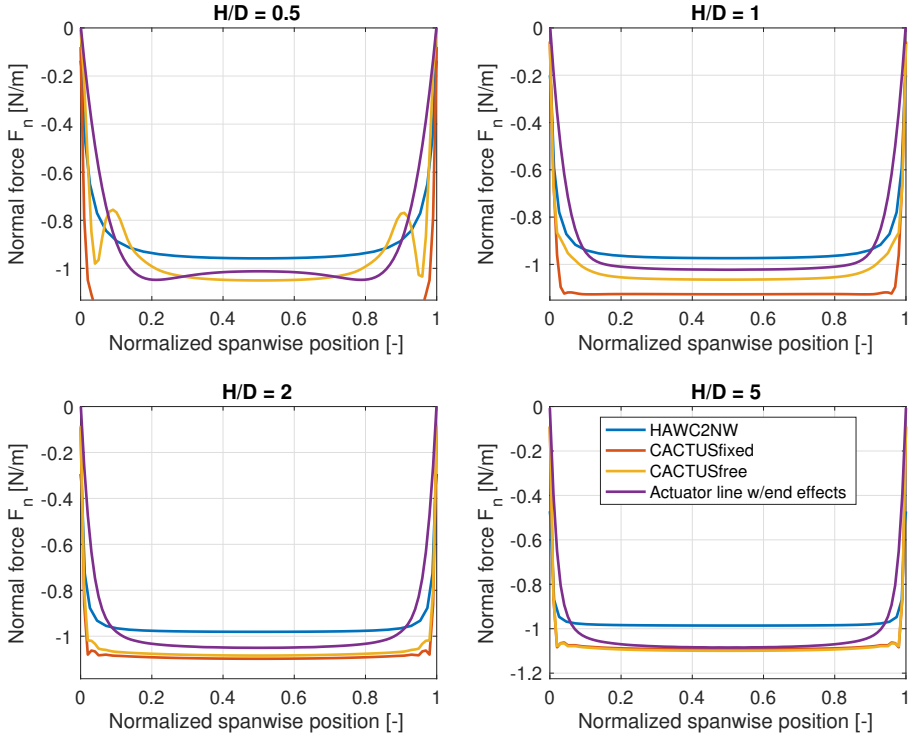

Figure 4.34: Spanwise distribution of normal force at ($\theta = 270°$) for the 3D models, for four different turbine aspect ratios H/D.

4.8 Synthesis

HAWC2 NW retains much of the accuracy of the higher-fidelity models such as CACTUS and the actuator line model, while offering a significantly lower runtime. This runtime decrease is on the order of minutes on a personal computer, versus hours/days for a full CACTUS or actuator line CFD simulation. Both the azimuthal and spanwise variation of normal and tangential forces are in reasonable agreement with the other models. This means 3D effects leading to a reduction to zero of the loads near the tips of the blades are being modelled sufficiently and the model could be used to predict power or other performance losses due to these effects. The tip correction employed by the actuator line CFD model appears agressive compared to the other models, predicting a significantly larger spanwise portion of the blade to be affected by a rapid decrease in loads towards the tip. Although an experimental data comparison (or a fully resolved CFD simulation) would be preferred to establish with certainty whether the model overcorrects, the nature of this tip correction versus the more physical interpretation offered by the CACTUS model suggests that this model may not accurately model the phenomena that occur at the tips. This may be due to the negative effects of force smearing as described in Section 4.6.2. For the second part of this thesis, the HAWC2 NW model will be used to conduct circulation control simulations in 3D, due to its fast runtime and ability to implement a pitching mechanism, which are both things that CACTUS and the actuator line CFD model are lacking. However, one should be mindful of the following important limitations of HAWC2 NW going forward:

- The straight-wake assumption does not allow for any wake curvature or other wake modification after vorticity has been shed from the blades to form this straight wake.
- The individual blades are not coupled using the lifting line model. This implies that every blade is moving through flow that is undisturbed by the other blades and therefore eliminates the effects of blade-vortex interaction. This effect only starts to become apparent when increasing the blade number and/or operating at low tip speed ratios.
- The lifting line approach is not valid for non-straight blades, such as those of a Φ-rotor VAWT or rotors with helical/otherwise angled blades.

Chapter 5

Circulation control

This chapter explores the path to flow control for vertical axis wind turbines. The aim is to follow the path from the highly simplified 2D actuator cylinder without blades to a fully 3D VAWT rotor and examine how flow control strategies have to be adjusted along the way. The chapter starts with an investigation into normal loading control on the 2D actuator cylinder, after which rotor blades and resulting pitch sequences are introduced. Subsequently, an attempt is made to study these simplified results using a 3D model, to examine whether they still hold up.

5.1 Loadform optimization for the ideal VAWT rotor

Madsen et al.[63] demonstrated that the performance of the ideal VAWT rotor, with an infinite number of blades of infinite length, can be assessed in terms of power and thrust coefficient C_P and C_T by modifying the normal loading Q_n, with this being the only variable. Q_n allows for the computation of all relevant velocities and resulting performance coefficients using the modified-linear actuator cylinder approach (Mod-Lin ACM) without iterating.

The reason only Q_n needs to be known in order to calculate the performance of the ideal VAWT rotor traces back to the actuator cylinder theory as described in Section 4.3. Madsen[59] theorized that the performance of the actuator cylinder can be determined using the pressure differential across the surface of the cylinder $\Delta p(\theta)$ and the velocity field $v_r(\theta)$ around the cylinder. The pressure jump is generated by the radial volume force f_r which is normal to the cylinder surface and proportional to the normalized loading Q_n.

Ertem et al.[30] proposed two strategies for creating an artificial loadform Q_n that is optimized to satisfy certain requirements, such as minimum/maximum C_P or minimum C_T. The first strategy involves generating Q_n using analytical expressions originally posed by Madsen et al.[63], as shown in Equation (5.1).

$$\begin{aligned} \tilde{\theta} &= \theta - \Delta\theta \cos\theta \frac{\pi}{180} \\ Q_n(\theta) &= \Delta Q_n + Q_{n,max} \cdot \frac{\sin\tilde{\theta}}{|\sin\tilde{\theta}|} \cdot \left(1 - |\cos\tilde{\theta}|^b + \frac{1}{2\pi}\sin\left(2\pi|\cos\tilde{\theta}|^b\right)\right) \end{aligned} \tag{5.1}$$

where:

- $\Delta\theta$ is a parameter in degrees that allows for stretching of the normal loading distribution.
- $Q_{n,max}$ is the magnitude of the maximum allowable normal loading in the distribution.
- b controls the curvature of the loadform.

- ΔQ_n shifts the loadform vertically.

There exist additional expressions that allow for asymmetry between the upwind ($0 < \theta \leqslant \pi$) and downwind ($pi < \theta \leqslant 2\pi$) regions, however the simplified expressions are favored for the purpose of this investigation.

The performance of the VAWT was calculated using the Mod-Lin ACM for all possible combinations of the loadform parameters in ranges shown in Equation (5.2). Results yielding thrust coefficients greater than 1 were discarded as those would likely exceed the validity limits of the Mod-Lin ACM, as per Figure 4.10.

$$\begin{gathered} -10^\circ < \Delta\theta < 80^\circ \text{ step size: } 5^\circ \\ -0.35 < Q_{n,max} < 0.35 \text{ step size: } 0.01 \\ 1 < m < 300 \text{step size: } 1 \\ -0.3 < \Delta Q_n < 0.3 \text{ step size: } 0.1 \end{gathered} \tag{5.2}$$

The resulting performance coefficients C_P and C_T are plotted in Figure 5.1. The calculation points are limited by the expressions for the ideal power and thrust coefficients as a function of the axial induction factor a, as in Equation (5.3). It can be observed that for higher power coefficients, there exists a range of thrust coefficients at which said power is achievable, rather than a single value as the ideal $C_P - C_T$ relationship would suggest. This means that power production is not necessarily linked to the instantaneous forces on the ideal turbine and therefore the thrust, which has previously been demonstrated by Simão Ferreira and Scheurich [90].

$$\begin{aligned} C_P &= 4a(1-a)^2 \\ C_T &= 4a(1-a) \end{aligned} \tag{5.3}$$

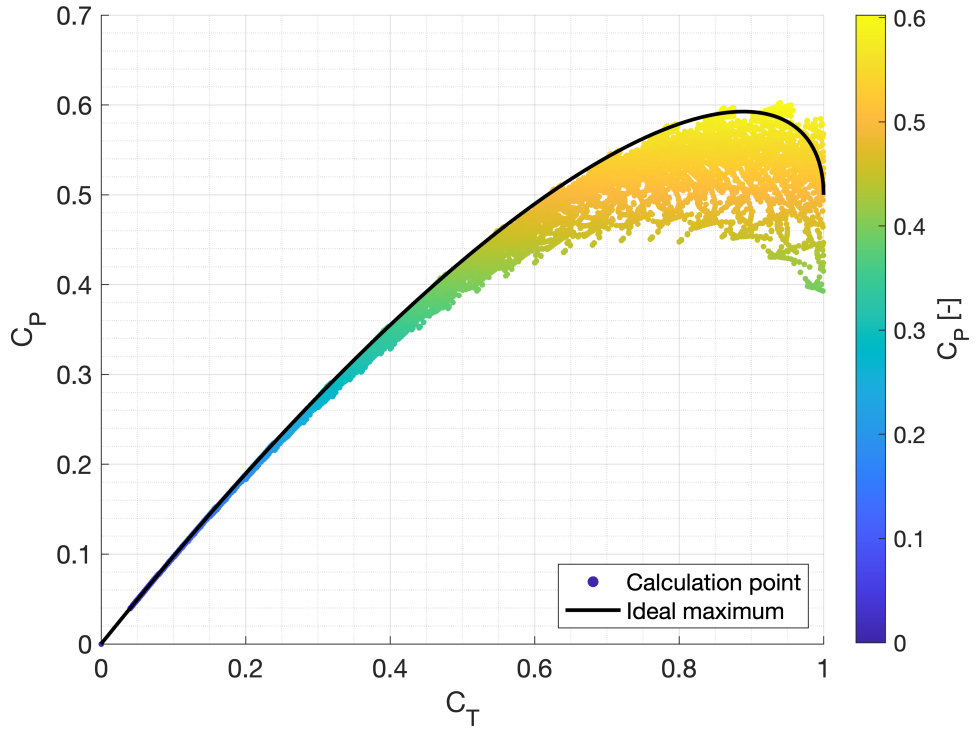

Figure 5.1: Performance of the VAWT calculated with the Mod-Lin ACM using combinations of the analytical loadform parameters: $0 < Q_{n,max} < 0.4$, $1 < m < 300$, $-10 < \Delta\theta < 80$.

Additionally, Figure 5.1 shows that for higher thrust coefficients $C_T > 0.8 - 0.9$, the power coefficients start to exceed the Betz limit, indicating that the validity of the Mod-Lin ACM starts to degrade after this point.

The second strategy involves generating the loadform Q_n using Bezier curves, constrained only by the absolute maximum loading $Q_{n,max}$. Ertem et al.[30] found that 15 linearly spaced Bezier points provides sufficient balance between loadform variety and computational effort. Both are shown in Figure 5.2. Although parameters for both can be tweaked, the Bezier-generated loadform appears more continuous at the transition between the upwind and downwind halves of the rotation ($\theta = 180°$). A performance graph such as Figure 5.1 was not computed for the Bezier approach, because the 15 different coefficients each represent a degree of freedom, resulting in far more possible combinations than the 3 parameters of the analytical approach.

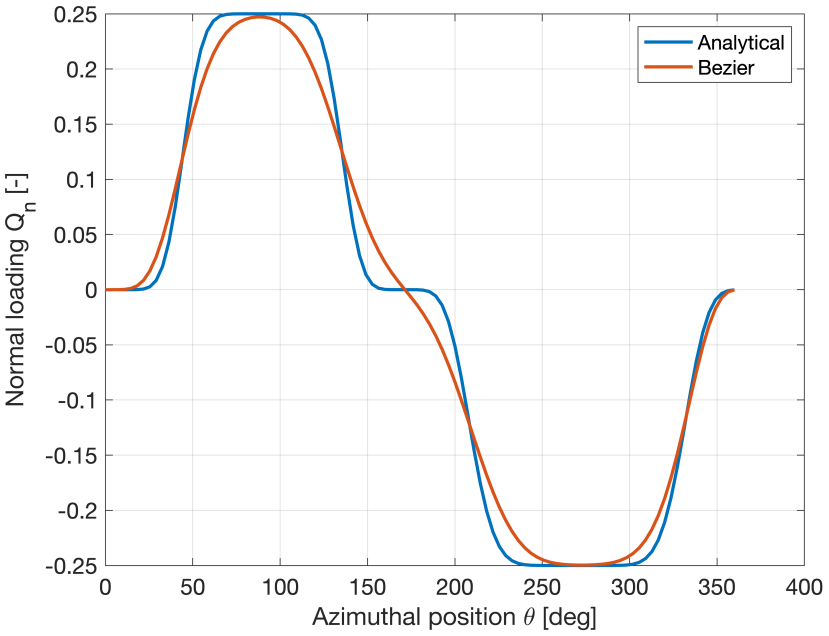

Figure 5.2: Examples of similar loadforms, generated using the analytic expressions in Equation (5.1) and using Bezier curves.

A constrained optimization technique, making use of MATLAB's `fmincon` function, is employed to find the optimal analytical and Bezier-based loadforms that result in maximum C_P. A number of constraints are utilized:

- The optimization is always constrained such that $C_T < 0.89$, to ensure the validity of the Mod-Lin ACM in the operating region as shown in Figure 4.10 and Figure 5.1.
- For the same reason, another constraint is to limit the maximum Q_n to 0.35.[30]
- The analytical loadform optimization is conducted both with a shift in normal loading ΔQ_n enabled and disabled.
- The Bezier-based optimization is limited by the fact that the values of the Bezier function at $\theta = 0°$ and $\theta = 360°$ have to match to ensure periodicity of the loadform.

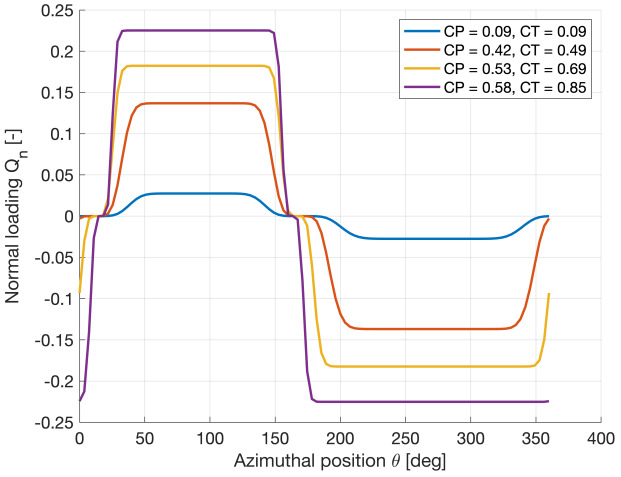

(a) Analytical

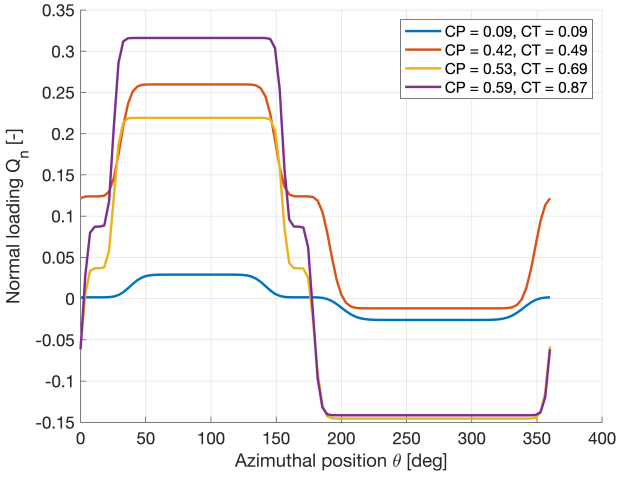

(b) Analytical, with Q_n shift

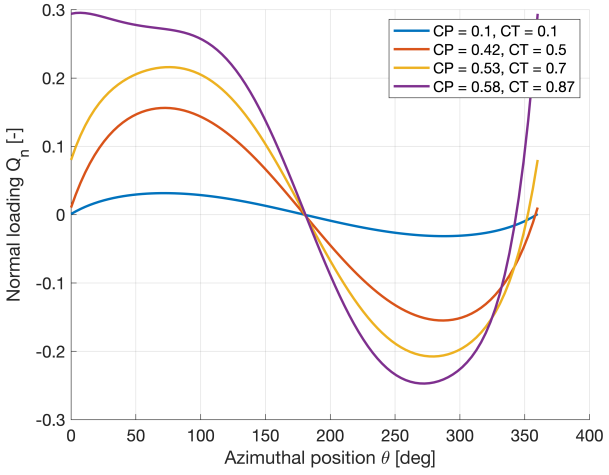

(c) Bezier

Figure 5.3: Loadforms optimized for maximum C_P at a prescribed C_T.

Figure 5.3 shows the results of optimizations with the objective of maximizing the power coefficient C_P whilst constraining the thrust to a certain value. Figure 5.3a shows the resulting analytical loadforms, which demonstrate that the thrust and power are varied by increasing the maximum normal loading $Q_{n,max}$ for a loadform with a high m (flat peaks) and only a slight stretching of the loadform favoring the downwind rotor half. When allowing for a vertical shift ΔQ_n, Figure 5.3b shows that positive shifts tend to be favored, biasing the maximum loading more towards the upwind rotor half.

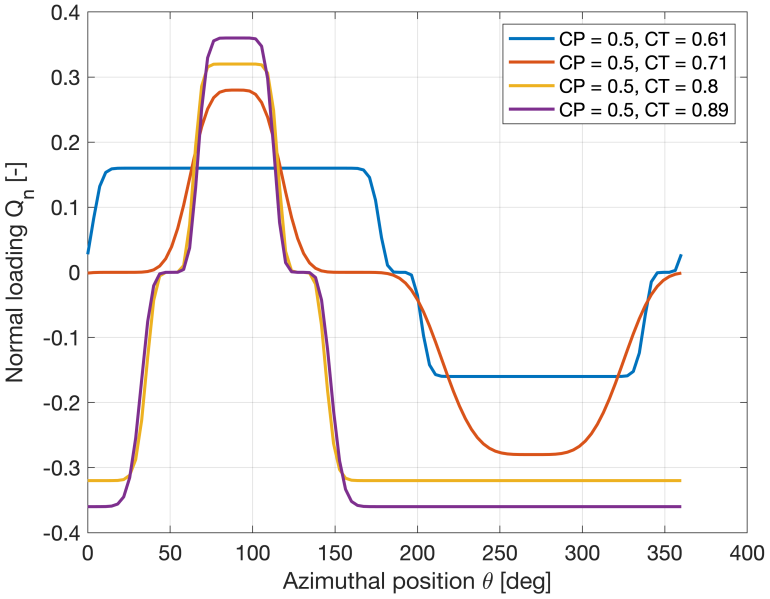

Figure 5.4: Analytical loadforms demonstrating that C_P can remain fixed (in this case to 0.5), whilst varying C_T.

Figure 5.4 is a result of plotting the normal loading for the calculations in Figure 5.1 that resulted in $C_P = 0.5$. For the same C_P, the loadforms resulting in minimum and maximum thrust (albeit capped at $C_T < 0.89$ to ensure validity of the Mod-Lin ACM). It is interesting to observe the loadform shapes necessary to ensure minimum and maximum thrust. For example, the minimum thrust loadform employs a low $Q_{n,max}$ and a large spread of the loading downwind and upwind, whereas the high thrust loadforms have sharp peaks in the upwind region and long stretches in the downwind region.

5.2 From loadform to pitch sequence

The previous section has attempted to develop an optimized normal loading distribution Q_n for certain objectives, using the ideal actuator cylinder. In this section, the rotor blades will be reintroduced into the equation, enabling a more realistic analysis. Circulation control of the rotor in order to achieve a given loadform Q_n is done using active pitch control of all blades. The blade pitch sequence required for this can be calculated using the actuator cylinder model, using the following procedure:[44]

- Insert target loadform Q_n into the Mod-Lin ACM.
- Compute induced velocities using Mod-Lin ACM formulation, without iterating.
- Calculate relative velocity and angle of attack.
- Calculate required lift coefficient C_l based on relative velocity and angle of attack, using Equation (5.5).
- Using the expression for the lift coefficient C_l as a function of the angle of attack α, calculate the difference between the current angle of attack and the angle of attack necessary to get the required lift coefficient. This gives the required pitch angle, $\theta_{p,req}$.

The desired lift coefficient C_l is related to the normal loading Q_n using the normal force F_n and normal force coefficient C_n as shown in Equation (5.4).

$$
\begin{aligned}
F_n &= \frac{1}{2}\rho V_{rel}^2 c C_n \\
C_n &= C_l \cos\alpha + C_d \sin\alpha \\
Q_n &= B\frac{F_n \cos\theta_p - F_t \sin\theta_p}{2\pi R\rho V_\infty^2}
\end{aligned}
\tag{5.4}
$$

Assuming $F_t = 0$ (only normal loading considered[1]) and $\theta_p = 0$ (no pitch angle yet), the equations in Equation (5.4) can now be combined, resulting in the desired lift coefficient $C_{l,des}$ (derived in Equation (5.5), where $\sigma = \frac{Bc}{2R}$).

$$
\begin{aligned}
Q_n &= B\frac{\frac{1}{2}\rho V_{rel}^2 c\left[C_l \cos\alpha + C_d \sin\alpha\right]}{2\pi R\rho V_\infty^2} \\
C_{l,des} &= \frac{1}{\cos\alpha}\left(\frac{2\pi}{\sigma}\frac{V_\infty^2}{V_{rel}^2}Q_n - C_d \sin\alpha\right)
\end{aligned}
\tag{5.5}
$$

The turbine that is used as a reference throughout this thesis, described in Table 4.1, uses an inviscid, 18% thickness airfoil polar, where $C_l = 1.11 \cdot 2\pi \sin\alpha$ & $C_d = 0$, which enables a straightforward relation between angle of attack, desired pitch angle and the desired lift coefficient as shown in Equation (5.6).

$$
\theta_{p,des} = \alpha - \arcsin\frac{C_{l,des}}{1.11 \cdot 2\pi} \tag{5.6}
$$

5.3 Direct pitch optimization

A more direct approach to pitch optimization can also be taken, by optimizing the 2D actuator cylinder for a combination of tip speed ratio, solidity and variable pitch distribution. This approach will be used to compare the effectiveness of variable pitch against fixed pitch turbines. It also allows for the inclusion of objectives other than targeting the desired lift coefficient $C_{l,des}$ as in Equations (5.5) and (5.6).

To be able to investigate the effectiveness of circulation control by active pitching in both 2D and 3D, a baseline case is required, against which any potential gains can be compared. In order to isolate the effect of variable versus fixed pitch, some constraints are imposed on this baseline case:

- The rotor must be optimized in terms of solidity σ (and thus chord length) and tip speed ratio λ.
- The thrust coefficient C_T of the optimized rotor should not exceed the validity limits of the Mod-Lin ACM (see Section 4.3).

The procedure for comparing the fixed pitch case to the variable pitch case is as follows:

1. Find the combination of solidity σ and tip speed ratio λ yielding the highest power coefficient.
    - Constrained by the validity limits of the modified linear actuator cylinder model ($C_T < 0.89, |Q_n| < 0.35$).

[1] At this point in the analysis, an ideal actuator surface is considered that lacks any concept of finite (number of) blade, therefore no tangential force is present.

2. Find the optimum variable pitch sequence, as well as combination of solidity σ and tip speed ratio λ.
   - Constrained by the validity limits of the modified linear actuator cylinder model ($C_T < 0.89, |Q_n| < 0.35$).
   - Pitch schedule should be periodic and continuous.

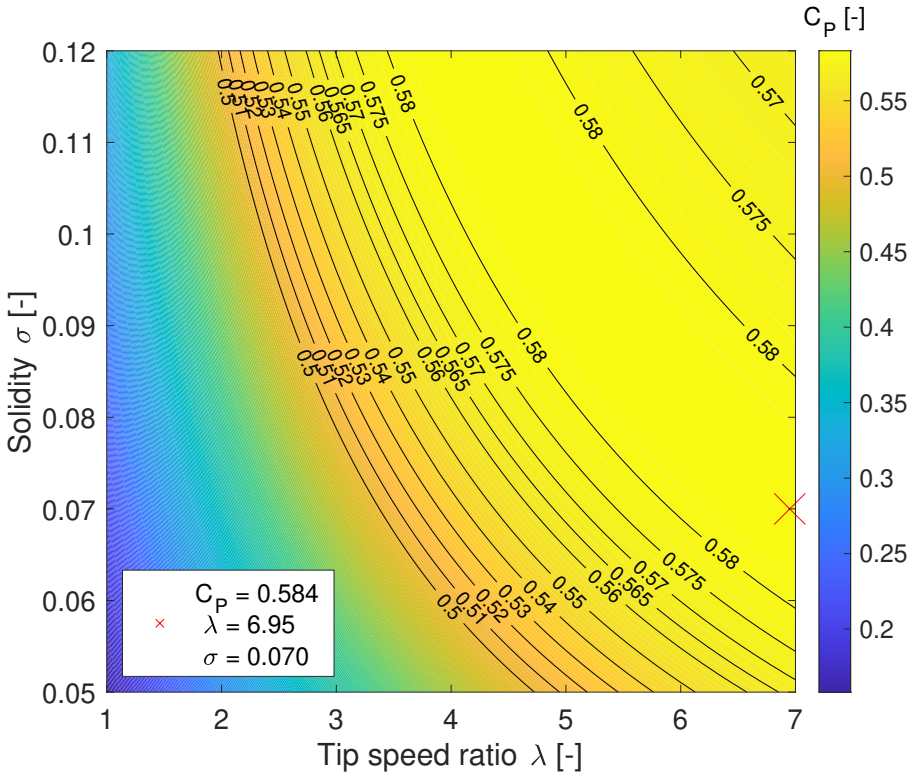

Figure 5.5: Power coefficient C_P as a function of tip speed ratio λ and solidity σ indicating the performance of an inviscid, 18% thickness airfoil polar with lift slope $1.11 \cdot 2\pi sin(\alpha)$.

Figure 5.5 shows the result of step 1 of this process, giving an indication of the performance that is to be expected from a specific airfoil polar. As this is an inviscid airfoil polar with zero drag, the performance is close to the theoretical Betz limit. Rather than a single maximum, there is an equipotential line of combinations of solidity and tip speed ratio where a maximum power coefficient can be achieved. This is different than for an airfoil with a non-linear lift slope, where a single point maximum can be found on the $C_P - \lambda - \sigma$ curve.

Adding a fixed pitch angle as a free variable to this performance analysis is theoretically not expected to alter the maximum power coefficient. Figure 5.6 shows power and thrust coefficients for fixed pitch and optimized variable pitch rotors. The maximum variable pitch C_P is in excess of the Betz limit of 0.593, which Madsen[59] suggests is possible for the ideal VAWT under certain conditions. In this case however, it is likely due to the fact that a linearized version of the actuator cylinder model is used which can cause slight errors for high thrust coefficients such as the one that the optimized turbine is operating at. Overall, the increase in power coefficient is minor, as is expected for a turbine with inviscid airfoil polar operating at optimum fixed pitch solidity σ and tip speed ratio λ .[23]

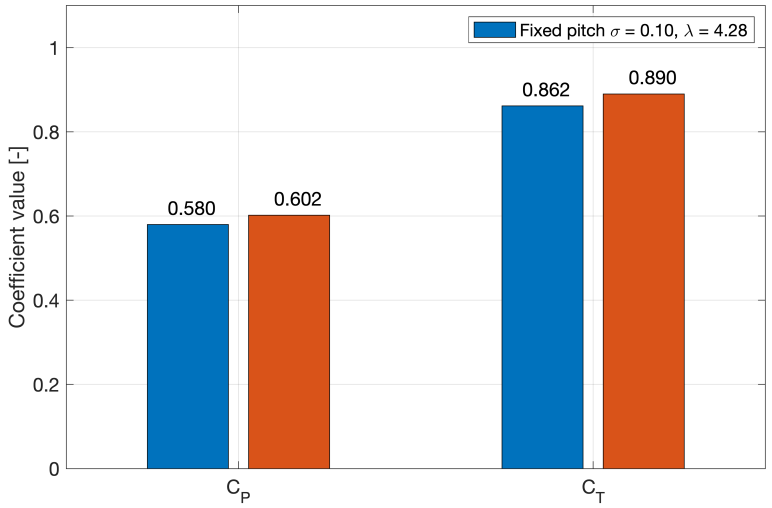

Figure 5.6: Power and thrust coefficients for optimal fixed and variable pitch rotors, using an inviscid, 18% thickness airfoil polar with lift slope $1.11 \cdot 2\pi$.

This polar has an approximately linear lift slope in the angle of attack region of importance of $-25 < \alpha < 25$. This has an important effect on the implementation of any fixed pitch angle and its result on the performance of the turbine. Figure 5.7 illustrates this effect by comparing fixed pitch angles of 0° and -5°. When imposing a fixed pitch angle of -5°, the angle of attack distribution is shifted upwards by 5°. This means that higher lift coefficients are reached in the upwind region ($0° < \theta < 180°$) while they are decreased in the downwind region($180° < \theta < 360°$). This trend translates directly to the shown tangential force F_t, which experiences a redistribution from the downwind region to the upwind region with the -5° fixed pitch angle. The tangential force is the primary driver of the power generated by the turbine and since it is merely redistributed and not increased in a meaningful way, the power coefficient stays the same. Future reference of the fixed pitch state of the turbine will therefore refer to a fixed pitch angle of $\theta_p = 0°$.

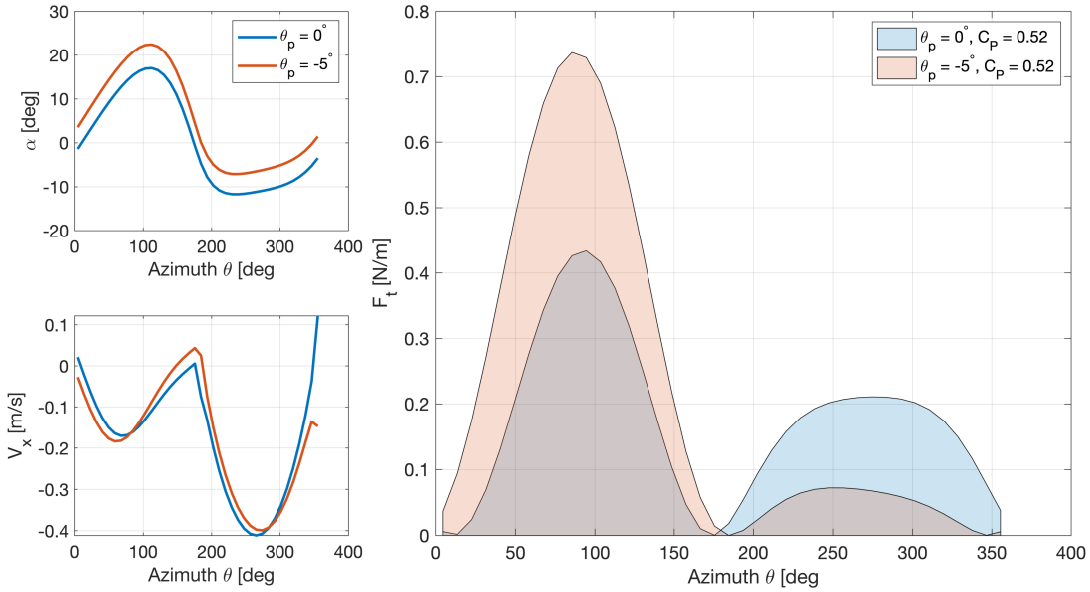

Figure 5.7: Comparison of tangential force, angle of attack and axial induction for fixed pitch angles of 0° and -5°.

5.3.1 Optimization

The optimization function used is MATLAB's `fmincon` nonlinear solver, which allows for both linear and nonlinear constraints in solving minimization problems. The selected algorithm used in the minimization problem is `active-set`, chosen for its efficacy in problems with non-smooth constraints (such as the constraint on maximum thrust coefficient discussed in Section 5.2). Its large initial step size also aids in speed with such a complex problem (N variables, all interdependent) without an effective initial guess (pitch sequence starts from all pitch variables being zero).

Chapter 6

3D circulation control using HAWC2 NW

In order to investigate the effects of circulation control and the optimized pitching mechanism introduced in the previous section, the HAWC2 aerodynamic model[61] with near-wake correction is used (HAWC2 NW). This allows modelling of the aerodynamic forces on the VAWT rotor in 3D, albeit with the limitations discussed in Section 4.4. The model is used in conjunction with a pitch servo .DLL module that allows for the specification of a time-series of pitch angles for each blade. This chapter will start by validating the blade pitching implementation with the 2D actuator cylinder model, as this is the model used in the optimization routine described in the previous chapter. Subsequently, different circulation control scenarios are introduced, each with unique constraints on the optimization. For each of the scenarios, the general set-up will be introduced, followed by a discussion of the results.

6.1 Pitching mechanism in HAWC2

Pitching the blades of the VAWT in HAWC2 is conducted using a pitch servo .DLL module.[61] This module makes use of several parameters to simulate a real-world pitch servo motor, such as the frequency of the servo module and the damping ratio used to dampen possible pitch oscillations. However, since the current analysis requires a purely aerodynamic model, without any structural or vibrational influences, the blade pitch angle will have to match the input pitch angle as closely as possible. To this end, parameters such as the servo frequency are set to high values (100Hz) and the damping ratio is set to 1.0 to eliminate any possible overshoot. Additionally, since the blade pitch angle is required instantly, the maximum pitch speed and acceleration are also set to unrealistically high values.

Preparing the pitch sequence for use in HAWC2 involves creating a file with a time-series of pitch angles for each blade, specifying which pitch angle each blade should assume at any given time. The pitch angle definition is shown in Figure 6.1. The inflow angle (Equation (6.1)) is the same for both models, although in HAWC2, all angles are defined in the opposite direction to the actuator cylinder model, and are therefore negative.

$$\Phi = \alpha + \theta_p \tag{6.1}$$

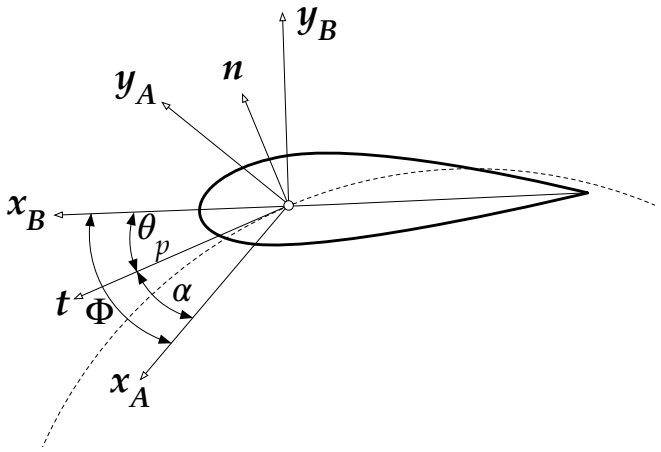

Figure 6.1: The blade pitch angle is defined as the angle between the coordinate system that is fixed to the rotational direction (normal/tangential directions n, t) and the blade coordinate system (x_B, y_B). The angle of attack is defined as the angle between the blade coordinate system and the aerodynamic coordinate system (x_A, y_A). Note that the angle of attack and pitch angle are defined differently in HAWC2 and the actuator cylinder model.

Figure 6.2 shows how an arbitrary pitch angle modifies the angle of attack distribution.

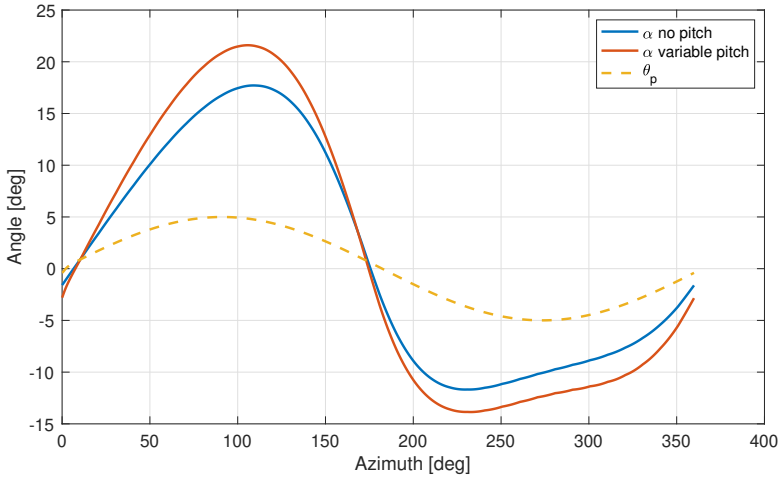

Figure 6.2: Angle of attack for zero-pitch and sinusoidal pitch distributions, using the actuator cylinder model definitions of relevant angles.

6.2 Calculating integral parameters in 3D

The simulation results from HAWC2 contain the normal and tangential forces F_n and F_t in the blade coordinate system, for every azimuthal position and for 40 different spanwise locations using a cosine distribution. These spanwise locations are illustrated in Figure 6.3. The cosine spacing ensures a higher resolution towards the blade tips, in order to properly capture the impact on blade loading caused by tip effects that occur.

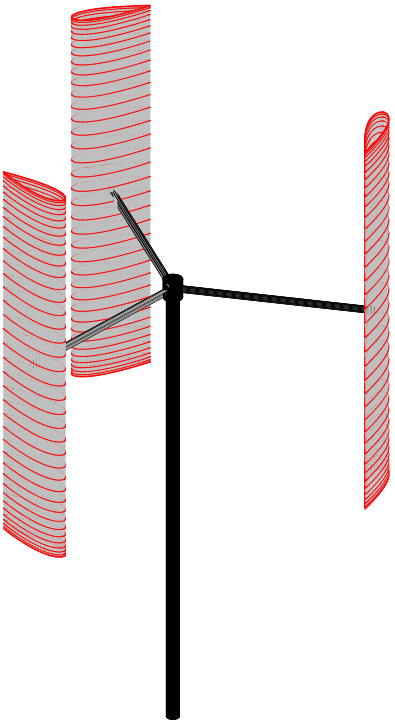

Figure 6.3: Illustration of 3-bladed VAWT indicating the cosine-spaced spanwise sections (red) for which output forces are provided. The tower and struts are displayed for illustrative purposes only and are not taken into account in the modelling.

From the normal and tangential forces F_n and F_t (in N/m) in the blade coordinate system, the nondimensional normal and tangential loadings Q_n and Q_t in the rotor coordinate system can be calculated according to Equation (6.2) for every combination of azimuthal and spanwise location.

$$\begin{aligned} Q_n &= B\frac{F_n\cos(\theta_p) - F_t\sin(\theta_p)}{2\pi R\rho V_\infty^2} \\ Q_t &= B\frac{F_t\cos(\theta_p) + F_n\sin(\theta_p)}{2\pi R\rho V_\infty^2} \end{aligned} \tag{6.2}$$

in which θ_p is the blade pitch angle at the current azimuth.

The integral 3D and 2D power coefficients are calculated by integrating the tangential loading Q_t over the azimuth and span (3D) or only over the azimuth (2D) according to Equation (6.3).

$$\begin{aligned} C_{P,3D} &= \int_{\frac{z}{H}=0}^{\frac{z}{H}=1}\int_{\theta=0}^{\theta=2\pi} Q_{t,3D}\cdot\lambda\cdot d\theta d\frac{z}{H} \\ C_{P,2D} &= \int_{\theta=0}^{\theta=2\pi} Q_{t,2D}\cdot\lambda d\theta \end{aligned} \tag{6.3}$$

The thrust coefficient is calculated in a similar manner (Equation (6.4)), but transformed to the global x, y coordinate system as the thrust acts parallel to the flow.

$$\begin{aligned} C_{T,3D} &= \int_{\frac{z}{H}=0}^{\frac{z}{H}=1}\int_{\theta=0}^{\theta=2\pi}\Big(Q_{n,3D}\sin(\theta) + Q_{t,3D}\cos(\theta)\Big)d\theta\cdot d\frac{z}{H} \\ C_{T,2D} &= \int_{\theta=0}^{\theta=2\pi}\Big(Q_{n,2D}\sin(\theta) + Q_{t,2D}\cos(\theta)\Big)d\theta \end{aligned} \tag{6.4}$$

For both Equations (6.3) and (6.4), θ is the azimuth angle, λ is the global tip speed ratio $\frac{z}{H}$ is the nondimensional spanwise position on the blade.

6.3 Cross-validation of variable-pitch aerodynamic simulation

Before utilizing the pitch optimization techniques described in the previous chapter, the method by which the pitch sequence is tested is to be validated against the 2D actuator cylinder model. To conduct this validation, a simple sinusoidal pitch with an amplitude of 5 degrees is used, as shown in Figure 6.2. The simulation is not run at optimal parameters, but at the reference solidity $\sigma = 0.085$ and tip speed ratio $\lambda = 3$.

As an initial check, the midspan power and thrust coefficients are compared between three different models: the 2D actuator cylinder model, HAWC2 with its regular 2D induction model and HAWC2 NW with the near-wake correction. Figure 6.4 shows that the power and thrust coefficients are comparable and the sinusoidal pitch actually results in an increase in power coefficient. It is important to note that for HAWC2 NW, which is a 3D model, the C_P and C_T at the midspan location are chosen and the turbine aspect ratio being simulated is $H/D = 100$, both of which are measures intended to have the power and thrust coefficients approximate the 2D situation as modelled by HAWC2 and the actuator cylinder model as closely as possible.

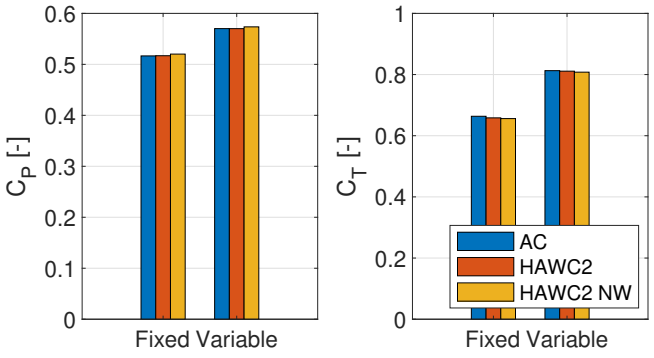

Figure 6.4: Comparison of power and thrust coefficients between the 2D AC, HAWC2 and HAWC2 NW models.

6.3.1 Integral parameters

Additionally, simulations are conducted for a variety of turbine aspect ratios (H/D). The power coefficients resulting from these simulations are presented in Figure 6.5.

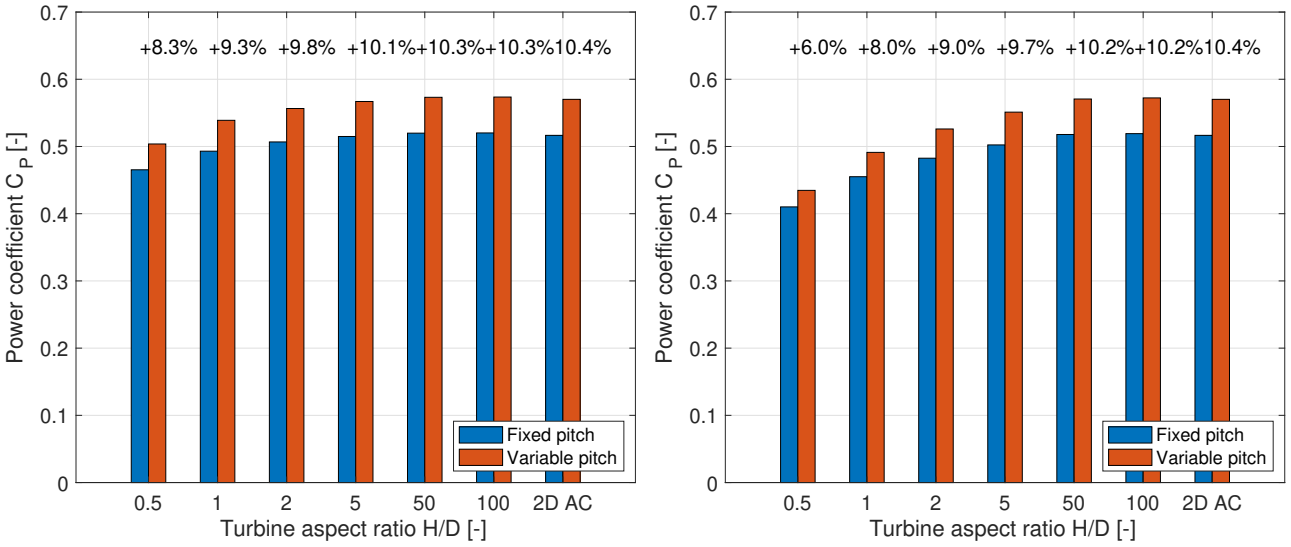

(a) Midspan power coefficient

(b) 3D (whole-turbine) power coefficient

Figure 6.5: Power coefficients for fixed and variable pitch, for varying turbine aspect ratio H/D.

Figure 6.5a shows that the midspan power coefficients increase with increasing turbine aspect ratio and approach the 2D power coefficients predicted by the 2D actuator cylinder model (shown as 2D AC). This is to be expected, since increasing the turbine aspect ratio is akin to imposing on the 3D model the assumption of having blades of infinite length. The 3D, whole-turbine power coefficients are shown in Figure 6.5b and exhibit a similar trend to the midspan equivalents. Here it can clearly be seen that the 3D power coefficient, midspan power coefficient and power coefficient predicted by the 2D actuator cylinder model converge to the same value as the turbine aspect ratio approaches very high values.

For both the 3D and midspan power coefficients, the increase in power coefficient due to the implementation of a variable pitch distribution increases with turbine aspect ratio. A preliminary conclusion can be drawn, namely that the 3D power losses are higher for short turbines (such as those with $H/D = 0.5$) compared to slender ones ($H/D \geqslant 5$).

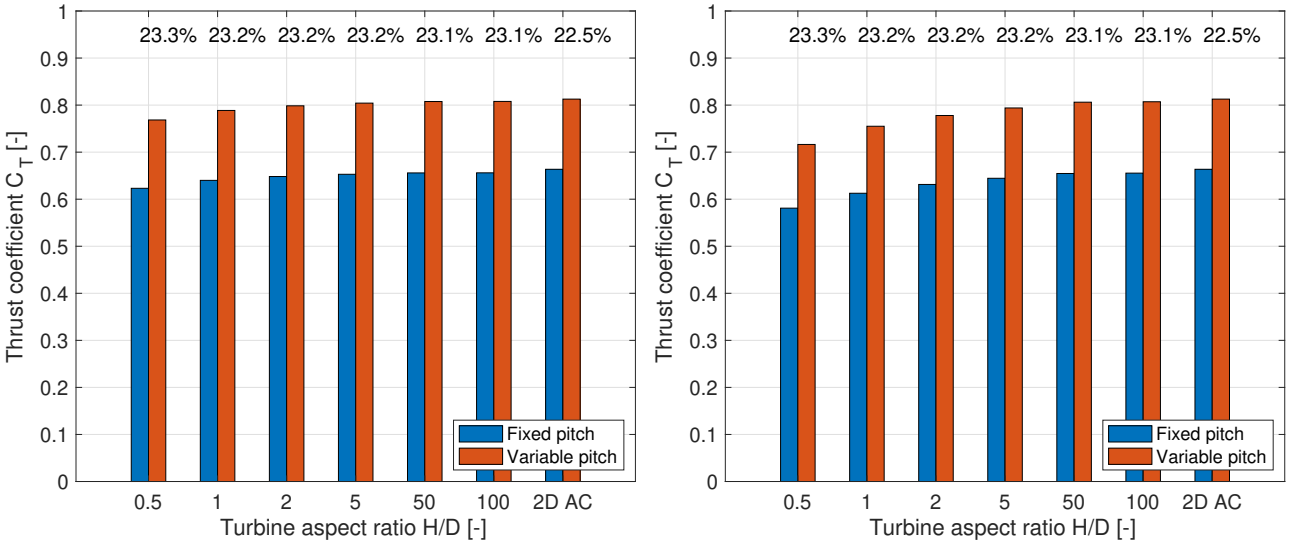

(a) Midspan thrust coefficient

(b) 3D (whole-turbine) thrust coefficient

Figure 6.6: Thrust coefficients for fixed and variable pitch, for varying turbine aspect ratio H/D.

The thrust coefficients shown in Figure 6.6 clearly show the increase in loading due to the variable pitch schedule as an increase in both midspan and overall thrust coefficient. The overall increasing trend in thrust coefficient with increasing turbine aspect ratio is shown too, which is particularly evident for the 3D thrust coefficient. Even though Figure 6.6b shows that the overall thrust coefficients are slightly lower for lower aspect ratios, the relative increase when moving to a variable pitch scheme is approximately 23 % and does not change significantly for different turbine aspect ratios as they are all tested using the same sinusoidal pitch sequence. This implies that the power gain from variable pitching is indeed proportional to the turbine aspect ratio, even though the slight increase in absolute thrust coefficient likely also plays a minor role.

Merely comparing the power and thrust coefficients is not enough to ensure proper validation of the pitch mechanism, however. Since they are integral parameters, the azimuthal distribution of normal and tangential loading behind them may be slightly different.

An important aspect to consider when comparing two different aerodynamic models is the streamwise and transverse induced velocities V_x and V_y, which are shown in Figure 6.7.

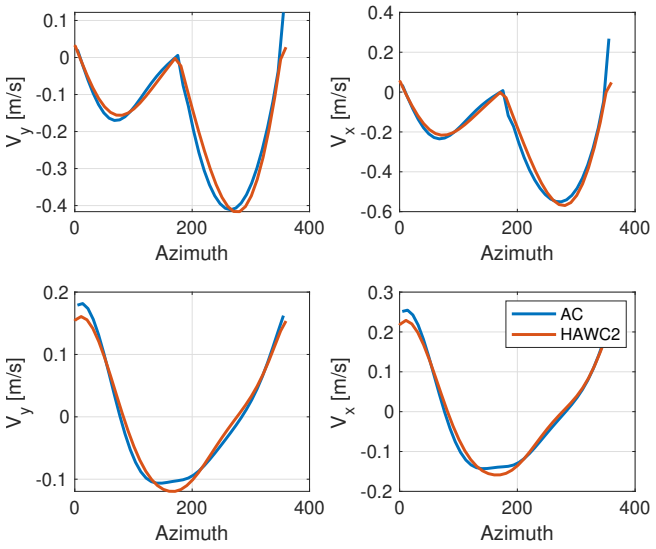

Figure 6.7: Axial and cross-flow induction velocities V_x and V_y at the midspan location, calculated by the actuator cylinder model and HAWC2 with near-wake correction for $H/D = 100$.

Figure 6.7 shows that for a high turbine aspect ratio of $H/D = 100$, the induction calculated by the 3D near wake model at the midspan location corresponds to results from the 2D actuator cylinder model, also for the variable pitch case.

6.4 Optimizing for maximum power coefficient

One potential application of circulation control is to maximize the power extracted from the flow using variable pitching, as compared to the fixed pitch VAWT. This was investigated in 2D in Section 5.2. Using the fixed pitch optimum tip speed ratio $\lambda = 4.28$ and solidity $\sigma = 0.096$ and an optimized variable pitch schedule, simulations are run for a series of turbine aspect ratios in HAWC2NW and the following results are obtained. The optimization is set up in such a way that the overall thrust coefficient C_T should remain the same between the fixed and variable pitch cases in 2D, such that the velocity field around the turbine can be expected to be similar.

Figure 6.8 shows the 3D power coefficients resulting from the simulations. The increase in power coefficient for the entire turbine ranges from 1.5% to 3.8%, although the latter results should be interpreted with the validity limits of the modified linear actuator cylinder model in mind (Section 4.3). HAWC2 also seems to overpredict the fixed-pitch and variable-pitch power when compared to the 2D actuator cylinder model. There are various differences between the 2D actuator cylinder model and HAWC2 to which this difference can be attributed:

- A different modified linear model is used, with its inherent inaccuracy at high thrust coefficients. Madsen et al.[61] details the way the actuator cylinder method is implemented in HAWC2 and mentions that the non-linear solution is obtained iteratively instead of applying a linear correction like in the 2D actuator cylinder model used in this thesis.
- HAWC2 evaluates the angle of attack at the $\frac{3}{4}$ chord point, whereas the 2D actuator cylinder model does this at the $\frac{1}{4}$ chord point. This could result in differences in effective angle of attack even though the same pitch input (which was originally optimized using the 2D actuator cylinder model) is applied, possibly resulting in higher loads on the blades and higher power/thrust coefficients.

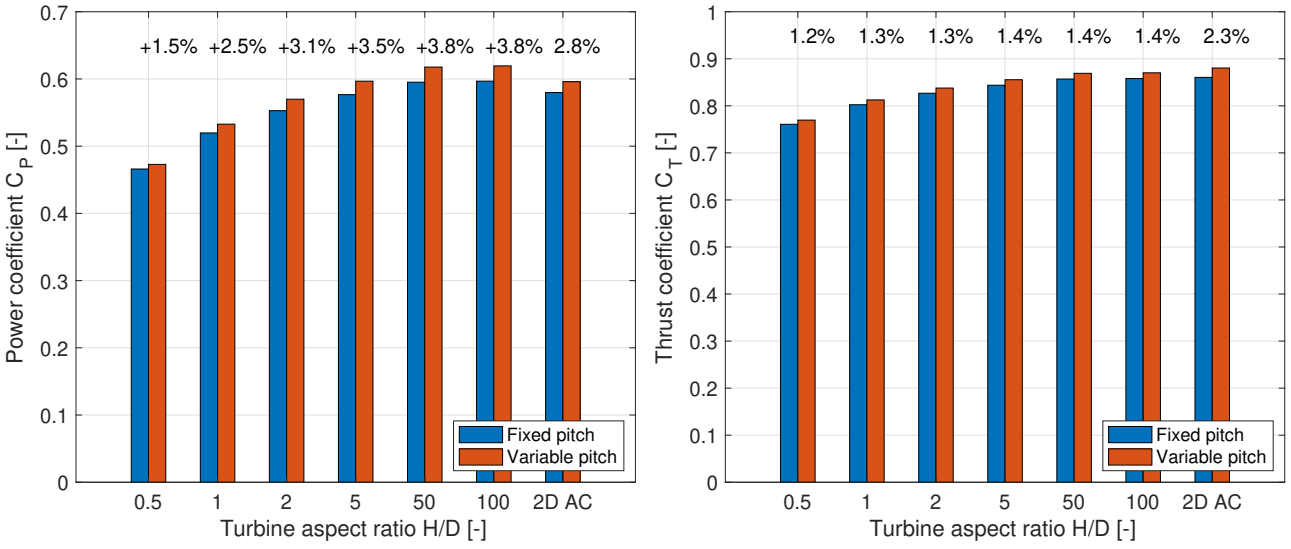

(a) 3D power coefficient

(b) 3D thrust coefficient

Figure 6.8: 3D power and thrust coefficients for fixed and variable pitch, for varying turbine aspect ratio H/D.

Figure 6.9 shows the reason why the variable pitch turbine is able to achieve higher power thrust coefficients, as considerably higher rotor normal and tangential forces are generated.

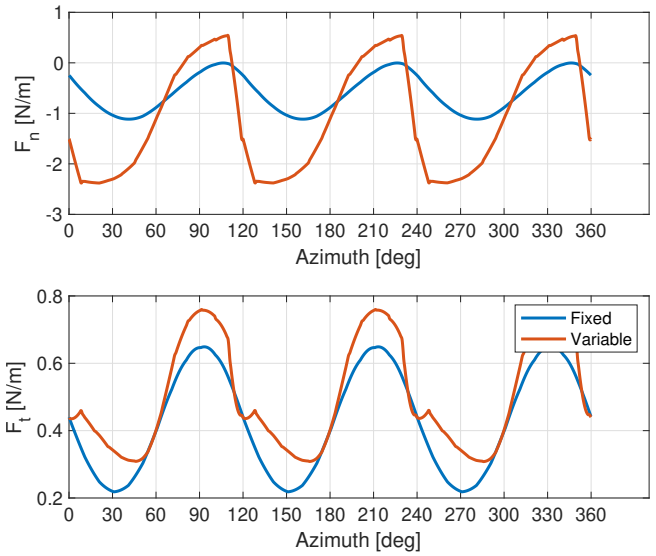

Figure 6.9: Combined normal and tangential loads at the midspan location for a 3-bladed VAWT, fixed pitch versus variable pitch optimized for maximum power.

Perhaps curiously, Figure 6.10 shows that the 2D pitch optimization resulted in almost all of the power being generated on the upwind side of the rotation, with the downwind side barely contributing.

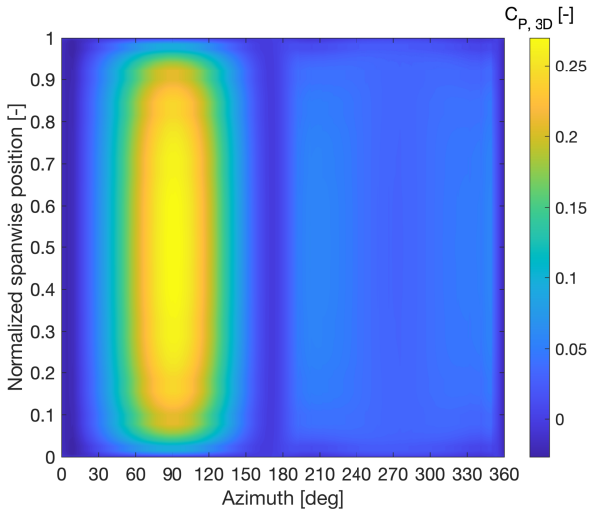

Figure 6.10: Local power coefficient of the variable-pitch turbine, using a pitch sequence optimized to provide maximum power. Fixed pitch version shown in Figure B.2.

6.5 Optimizing for a specified normal loading distribution

Madsen[59] explained the role of the normal loading Q_n (also referred to as the radial loading) in the power extraction by the actuator cylinder. Madsen et al.[63] discusses how the shape of the normal loading (also referred to as a loadform) influences the ideal power coefficient, in particular with regards to the symmetry of the loadform to the upwind or downwind half-cycles. In order to study this, it is useful to be able to generate a pitch sequence that will result in the desired loadform. While this was attempted for the ideal actuator cylinder, without blade element model, in Section 5.2, it does not represent a realistic situation when a finite number of blades is considered, even in the 2D case, or real airfoils with non-linear lift slopes are implemented. To accomplish this, an optimization strategy was devised consisting of the steps listed below:

- Generate a suitable normal loadform
  - For example using Equation (6.5), using maximum normal loading $Q_{n,max}$ and loadform shape parameter b.
  - Optionally, modify the loadform to create thrust asymmetry by varying F_{asym}
  - Calculate the thrust coefficient C_T and verify that the validity limits of the 2D actuator cylinder model are not exceeded ($C_T < 0.89$).
  - Insert loadform into actuator cylinder model without iteration (Section 4.3) to obtain the ideal power coefficient $C_{P,i}$as in Equation (4.19).
- Select a tip speed ratio λ and solidity σ at which to operate the actuator cylinder model
  - This can either be a predetermined, reference tip speed ratio λ and solidity σ or optimum values for the fixed-pitch situation.
- Minimize the difference between the target loadform $Q_{n,target}$ and the resulting loadform from the actuator cylinder model, by varying the variable pitch distribution at N locations, for an actuator cylinder with N cells.
  - The minimization objective ΔQ_n is expressed in Equation (6.6).[1]
  - The maximum pitch angle is constrained depending on the validity range of the airfoil polar[2].
  - (Optional) The pitch rate $\frac{\Delta\theta_p}{2\pi/N}$ is constrained to avoid steep pitch gradients at the upwind/downwind transition location at $\theta = \pi$.

$$\begin{aligned} Q_{n,target} &= Q_{n,max} \cdot \sqrt{\frac{1+b^2}{1+b^2\cdot\sin^2(\theta))}} \cdot \sin(\theta) \\ Q_{n,upwind} &= (1+F_{asym})\cdot Q_n (0<\theta<\pi) \\ Q_{n,downwind} &= (1-F_{asym})\cdot Q_n (\pi<\theta<2\pi) \end{aligned} \tag{6.5}$$

$$\Delta Q_n = \sum_{i=0}^{i=N} \left| Q^i_{n,target} - Q^i_{n,result} \right| \tag{6.6}$$

[1] Another method of optimizing pitch to achieve a specific Q_n was attempted, using multi-objective optimization with the ΔQ_n at every discretized azimuthal position being a minimization objective. This was a more targeted approach resulting in increased performance.

[2] In the current analysis, this is not a problem since an inviscid airfoil polar with a linear lift slope is used.

The result of an example optimization for a symmetric loadform Q_n generated using Equation (6.5) is shown in Figure 6.11.

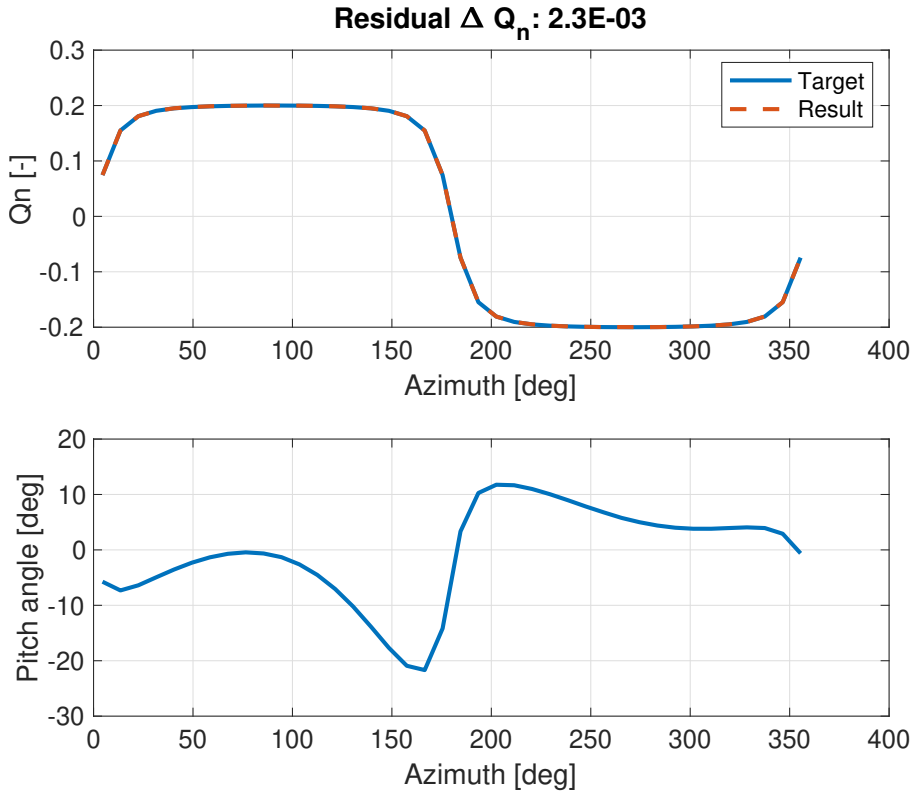

Figure 6.11: Pitch sequence optimization to obtain desired loadform, generated using Equation (6.5) with b = 5 & $Q_{n,max}$ = 0.2. Turbine is operating at a fixed-pitch optimum tip speed ratio λ = 3.42 and σ = 0.058.

The obtained pitch sequence can subsequently be simulated in 2D and 3D using HAWC2 and the procedure described in Section 6.1. Figure 6.12 shows the 2D results of this simulation, with the intended normal loading Q_n replicated accurately in HAWC2 using the pitch sequence.

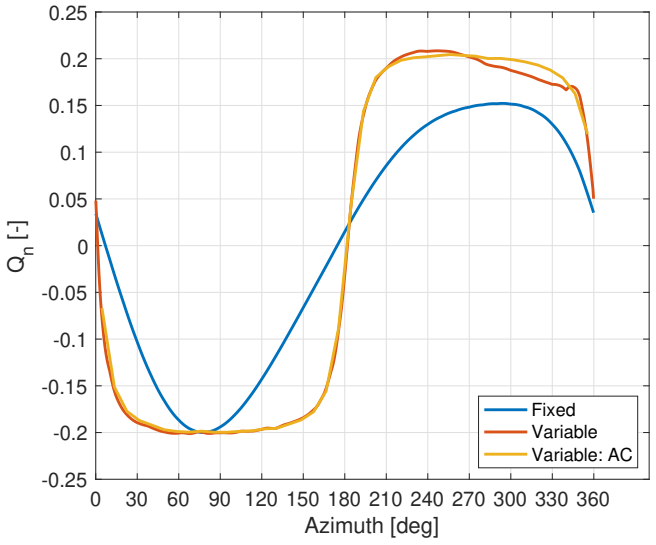

Figure 6.12: Normal loading Q_n using modified pitch sequence in HAWC2 compared to the fixed-pitch and the actuator cylinder model. Note: the sign of the normal loading is reversed as this figure depicts the output in HAWC2's coordinate system. Conventionally, the normal loading is positive upwind and negative downwind.

HAWC2NW subsequently allows for further analysis in 3D, as is presented in Figure 6.13a. It can be seen that the normal loading reduces to 0 near the extreme spanwise locations due to tip effects. The normal loading is still uniform in the azimuthal direction, as it was originally intended to be.

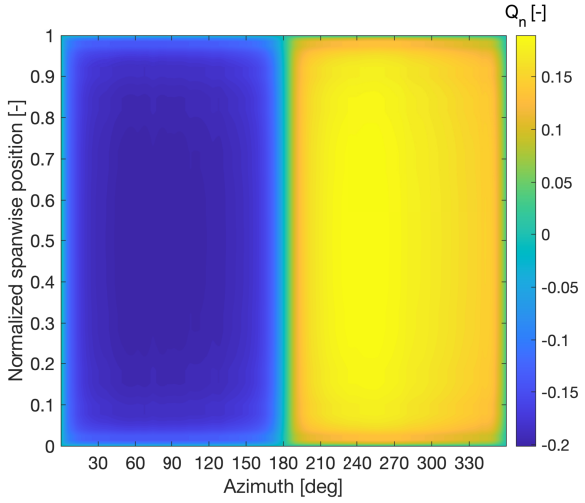

(a) Normal loading Q_n using modified pitch sequence in HAWC2 NW with H/D = 0.5. (Fixed pitch equivalent shown in Figure B.3)

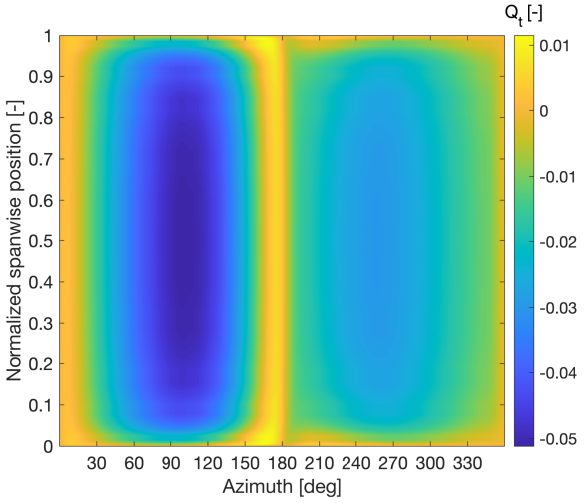

(b) Tangential loading Q_t using modified pitch sequence in HAWC2 NW with H/D = 0.5. (Fixed pitch equivalent shown in Figure B.4)

Figure 6.13b shows the tangential loading resulting from the normal loading. It is this tangential loading which is ultimately responsible for the power generated by the turbine shown in Figure 6.14.

Figure 6.14 shows the local power coefficient of the turbine subjected to the previously found pitch sequence. Compared to the fixed-pitch equivalent (Figure B.5), there is more power being generated in the downwind region due to the redistribution of normal loading into a uniform shape.

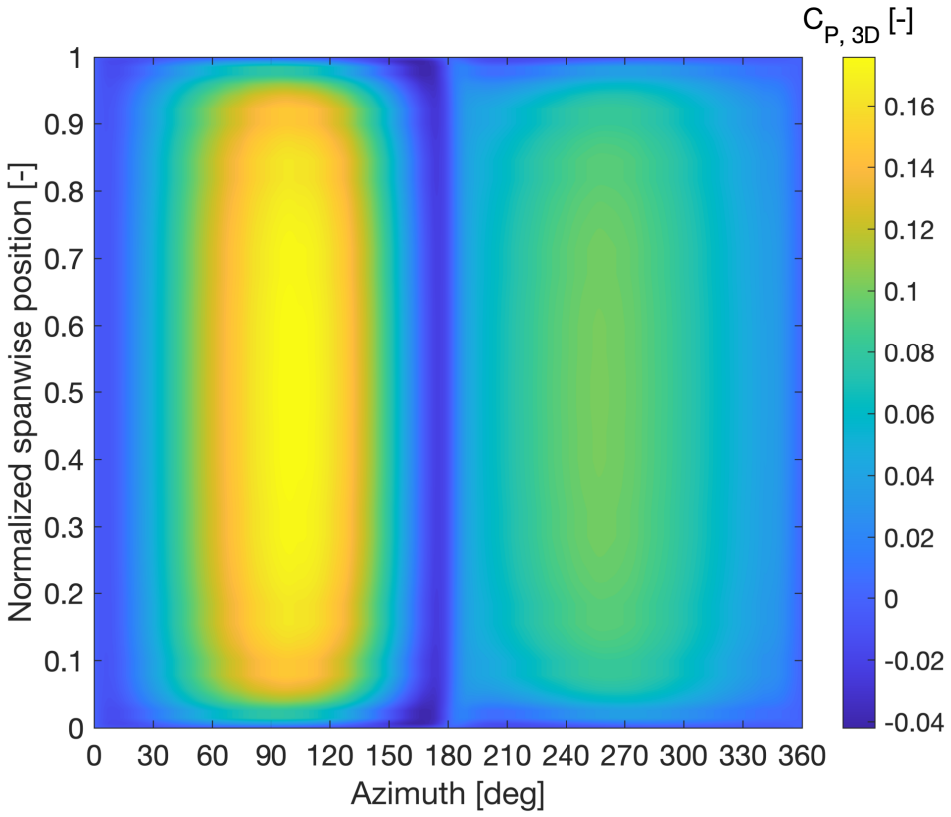

Figure 6.14: Local power coefficient C_P as a function of azimuth and spanwise position. (Fixed pitch equivalent shown in Figure B.5)

6.6 Relationship between loading distribution and turbine aspect ratio

In this section, the relationship between the uniformity of the normal loading distribution and turbine aspect ratio is investigated.

The parameter K_T that is used to express the concept of load uniformity is given as Equation (6.7).

$$K_T = \frac{C_{T,upwind}}{C_{T,upwind} + C_{T,downwind}} \tag{6.7}$$

where the upwind and downwind thrust coefficients $C_{T,upwind}$, $C_{T,downwind}$ are defined as in Equation (6.8).

$$\begin{aligned} C_{T,upwind} &= \int_0^{\pi} (Q_{n,upwind} \cdot \sin\theta + Q_{t,upwind} \cdot \cos\theta) d\theta \\ C_{T,downwind} &= \int_{\pi}^{2\pi} (Q_{n,downwind} \cdot \sin\theta + Q_{t,downwind} \cdot \cos\theta) d\theta \end{aligned} \tag{6.8}$$

6.6.1 2D

A uniformly distributed normal loading has K_T=0.5, while increasing and decreasing K_T shifts the loading upwind and downwind respectively, as shown in Figures 6.15 and 6.16. Note that the target normal loading is not completely square to avoid unrealistically high pitch gradients at the discontinuities ($\theta = 0°, \theta = 180°$), since HAWC2 NW is intended to simulate a real turbine even though the current analysis reduces it to an aerodynamic simplification as much as possible.

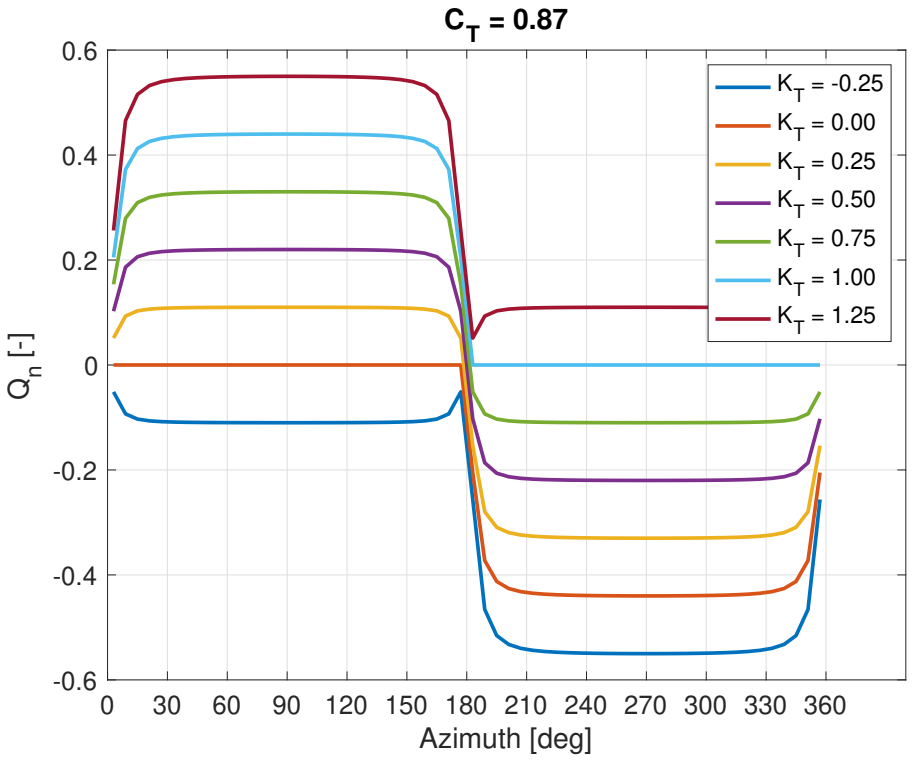

Figure 6.15: Target normal loading distributions for $-0.25 < \frac{C_{T,up}}{C_{T,up}+C_{T,down}} < 1.25$.

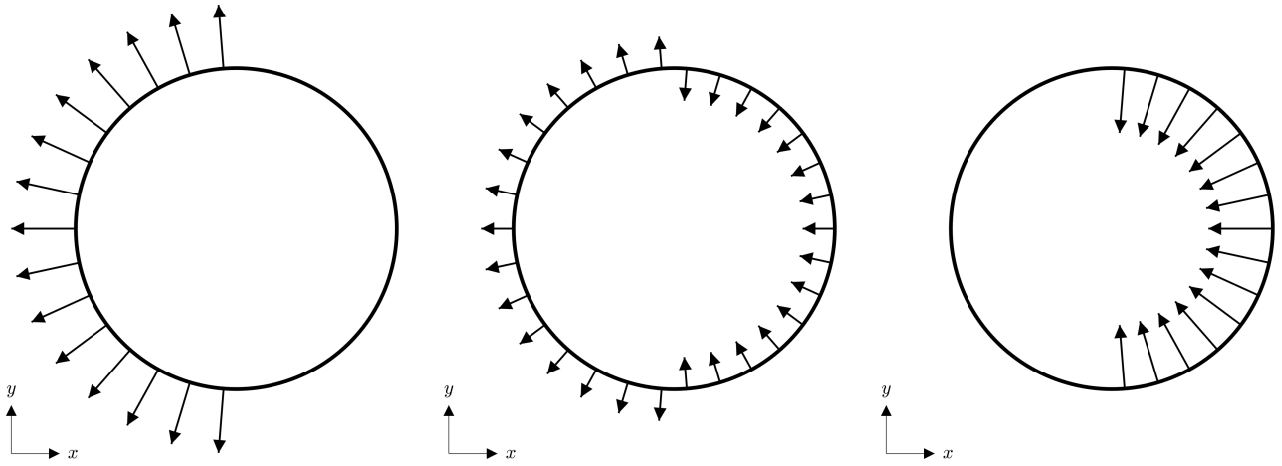

(a) $K_T = 1$ (fully upwind) (b) $K_T = 0.5$ (uniform) (c) $K_T = 0$ (fully downwind)

Figure 6.16: Diagram of normal loading on the actuator cylinder for three values of $K_T = \frac{C_{T,up}}{C_{T,up}+C_{T,down}}$.

Varying K_T to redistribute the loading should result in the same overall C_T (when this C_T is defined as being purely resulting from the normal loading). For a linear airfoil polar and in the 2D case, the ideal power coefficient $C_{P,i}$ and thrust coefficient C_T, as defined in Equation (6.9), should therefore also remain unaffected by a change in K_T.

$$\begin{aligned} C_{P,i} &= \int_0^{2\pi} Q_n(\theta)\frac{V_n}{V_\infty}d\theta \\ C_T &= \int_0^{2\pi} Q_n(\theta)\cdot\sin(\theta)d\theta \end{aligned} \tag{6.9}$$

where V_n is the velocity normal to the surface of the actuator cylinder, V_∞ is the freestream velocity, θ is the azimuth and $Q_n(\theta)$ is the normal loading distribution.

This phenomenon occurs because the 2D aerodynamics of the VAWT are characterized primarily by shed vorticity from locations where the force field surrounding the actuator cylinder changes. If the overall thrust coefficient - and therefore the loading - remains the same, then it does not matter how the loading is distributed between the upwind/downwind half-cycles, because the overall loading will cause the same change in the force field. Since vorticity is only shed where the force field changes, the wake is also not dependent on how the loading is distributed. Figure 6.17 presents integral parameters C_P and C_T for the 2D actuator cylinder model when inserting pitch sequences that result in normal loading distributions with $-1.5 < K_T > 1.5$. It is shown that the power and thrust coefficients do not change significantly when shifting the loading upwind or downwind, illustrating that the 2D VAWT performance is indeed independent from how the loading is distributed.

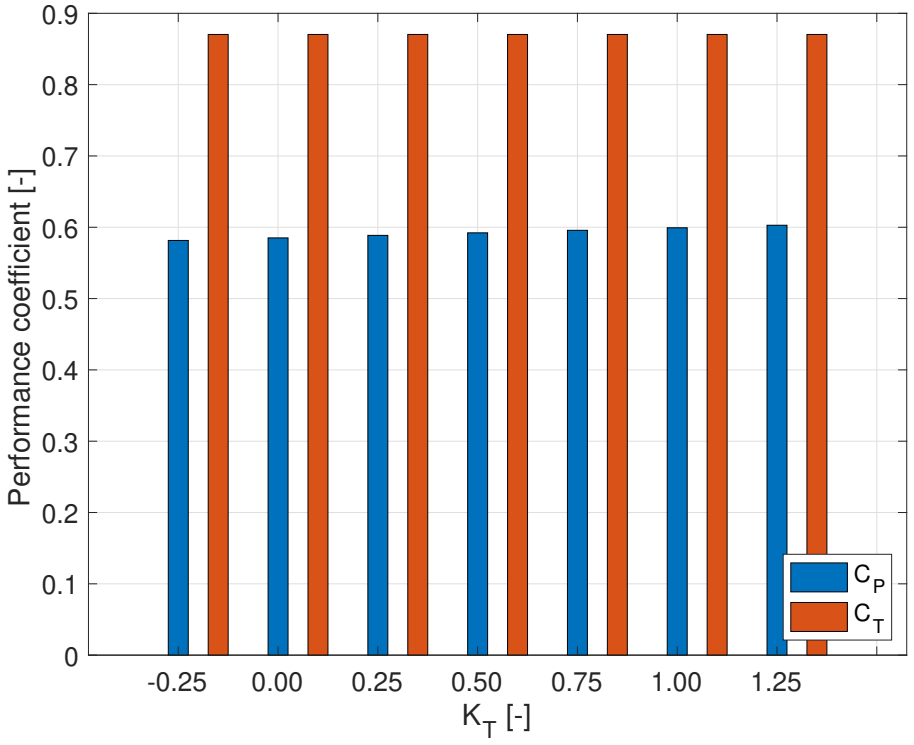

Figure 6.17: Verifying that ideal power coefficient C_P and thrust coefficient C_T are not influenced by a change in loading distribution K_T.

6.6.2 3D

When considering the three-dimensional vorticity field around the VAWT, there is an additional direction in which the force field is changing and vorticity is shed. Now, the blade tips also induce tip vortices which alter the velocity field surrounding the turbine and subsequently influence its wake. The effect of these tip vortices relative to the overall blade loading is more pronounced for lower turbine aspect ratios (see for example Figures 4.31 and 4.32) and tends to zero as the turbine aspect ratio increases.

De Tavernier et al.[25] conducted CFD simulations of an actuator cylinder with non-uniform loading distribution. Figure 3.6 in Section 3.3.2 shows the streamwise velocity in the wake of such an actuator cylinder for the three different loading configurations outlined in Figure 6.16. These figures show that the wake shape (and thus the velocity field) is drastically influenced by the loading distribution on the actuator cylinder. Therefore, one can expect the aerodynamic performance to be different as well.

In order to study the effects of redistributing the normal loading in 3D, the optimization strategy that was outlined in Section 6.5 is used to obtain a pitch sequence for each of the loadforms shown in Figure 6.15. These pitch sequences are then inserted into HAWC2 NW and simulations are conducted for turbine aspect ratios $H/D = 0.5, 1, 2, 5, 50, 100$. The two highest aspect ratios serve as a 2D reference, since at such significant blade length, the results are comparable to a model with blades of infinite length.

Figure 6.18a shows the pitch angle distributions optimized to yield a normal loading with a specified $K_T = \frac{C_{T,up}}{C_{T,up}+C_{T,down}}$. The resulting normal loading calculated by HAWC2 NW for a high aspect ratio is shown in Figure 6.18b, alongside the 2D optimization target Q_n. The HAWC2 NW results, while not an exact match, exhibit a normal loading with approximately the intended ratio of thrust coefficients C_T.

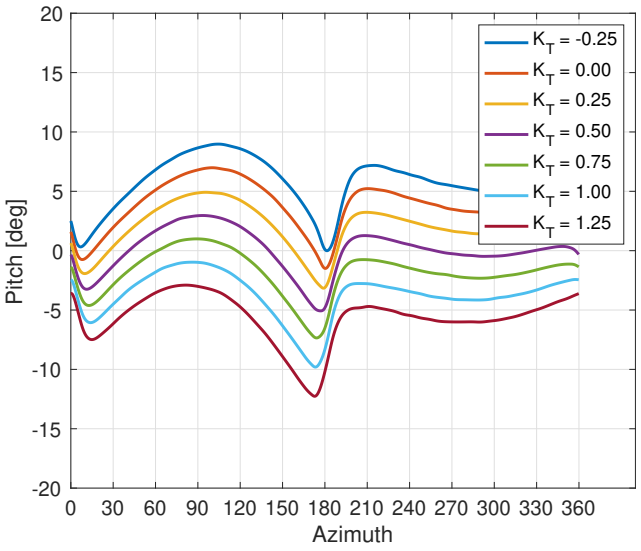

(a) Pitch distribution used to obtain target loadform ($\lambda = 7$, $\sigma = 0.06$).

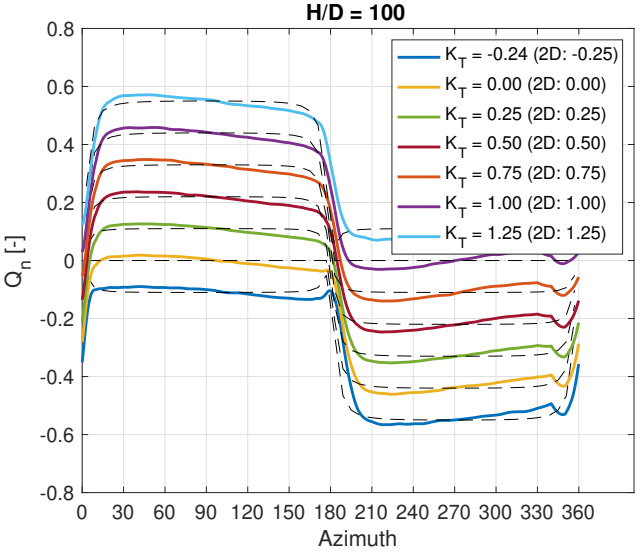

(b) Resulting loadform calculated using HAWC2 NW, at midspan for H/D = 100, compared to target loadform.

Figure 6.18: HAWC2 NW pitch input and target/resulting loadforms for various $-0.25 < K_T < 1.25$.

This analysis is modelled after Simão Ferreira et al.[93], who conducted simulations using the 3D ideal actuator cylinder model to analyse the effects of the normal loading distribution on the flow field surrounding the VAWT. This work and related discussions[88] are also the source of the load distribution parameter K_T and the inspiration behind figures such as Figure 6.19.

The results are shown in Figure 6.19, where the ratio of the 3D power coefficient to the 2D power coefficient (that of H/D = 100) is compared across turbine aspect ratios H/D, as a function of K_T. At $K_T = 0.5$, the 3D power coefficient is closest to the 2D value. A shift of the loading towards the upwind or downwind half of the rotation results in a discrepancy between $C_{P,3D}$ and $C_{P,2D}$, which is far more drastic for low turbine aspect ratios such as H/D = 0.5. As H/D increases, this relationship tends toward the 2D case, in which the C_P is the same regardless of K_T.

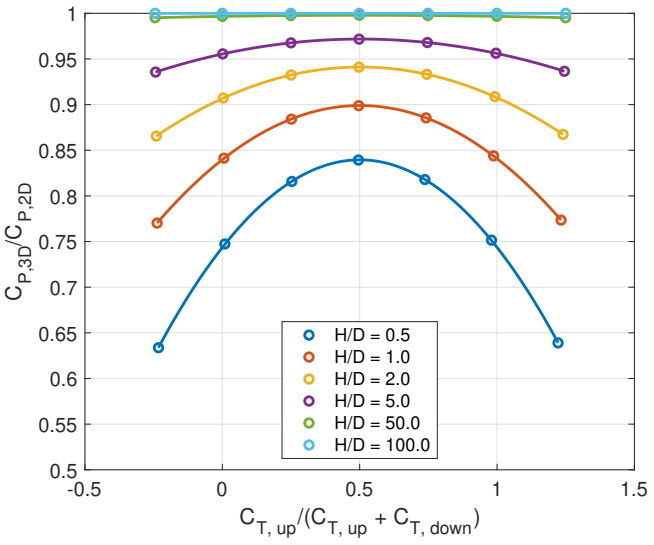

Figure 6.19: Ratio of 3D to 2D (H/D = 100) power coefficient, for varying distributions of normal loading upwind/downwind, for different turbine aspect ratios and $\lambda = 7$, $\sigma = 0.06$. (An animated version of this figure is shown in Figure B.9 in Appendix B)

Figure 6.20a shows the actual 3D power coefficient for the various loading distributions, which exhibits a comparable relationship to the $C_{P,3D}/C_{P,2D}$ ratio shown in Figure 6.19. The power coefficient does however still trend slightly upward when shifting the loading from downwind to upwind. Calculating the ideal power coefficient $C_{P,3D,i}$ using Equation (6.9) instead of the real power coefficient from Q_t results in this trend being all but eliminated, as shown in Figure B.8.

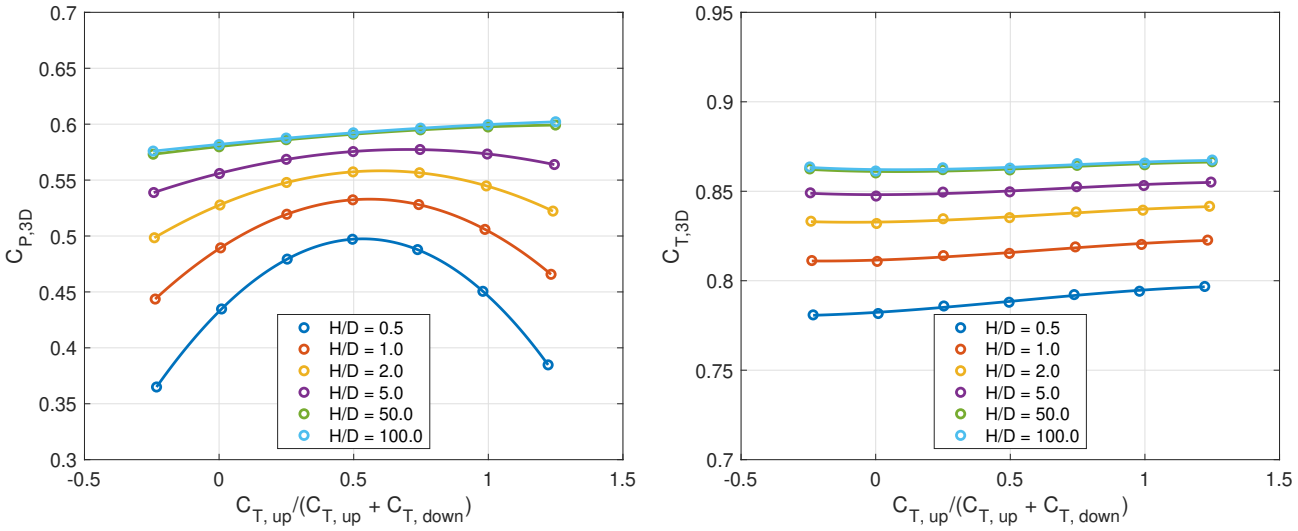

(a) $C_{P,3D}$ (b) $C_{T,3D}$

Figure 6.20: 3D power and thrust coefficients for varying distributions of normal loading upwind/-downwind, for different turbine aspect ratios. $\lambda = 7$, $\sigma = 0.06$

It should be noted that due to the way the simulations were set up, each of the turbine aspect ratios in Figure 6.20a has a different maximum power coefficient at $K_T = 0.5$ and a different overall thrust coefficient (as shown in Figure 6.20b). This is because one pitch sequence is used per normal loading distribution, for all aspect ratios, so the lower $H/D = 0.5$ case will experience larger losses due to 3D effects and therefore a lower thrust coefficient, even at uniform loading.

The symmetry of the relationship can be attributed to the fact that, when the load is distributed fully downwind, there is no streamwise induction on the upwind half of the cylinder, allowing the flow to pass through to the downwind half of the actuator unimpeded. Similarly, when the loading is concentrated on the upwind actuator half, the downwind actuator half has no induction and therefore does not influence the overall flow field. In practice, this is difficult to accomplish, since a finite blade will always result in some flow impediment, which is likely why there is still some asymmetry present in Figure 6.20a. This asymmetry is already reduced when only the normal loading is considered in the calculation of the power coefficient, as in Figure B.8.

6.6.3 Examining the induction normal to the actuator surface

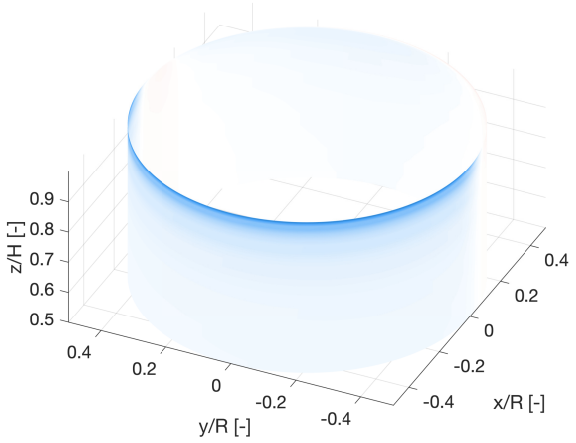

(a) K_T = 1 (fully upwind)

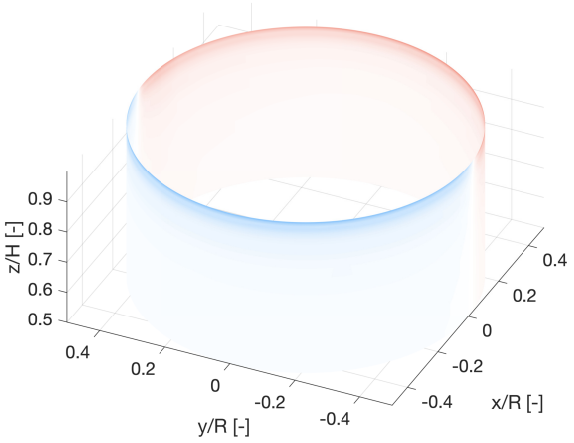

(b) K_T = 0.5 (uniform)

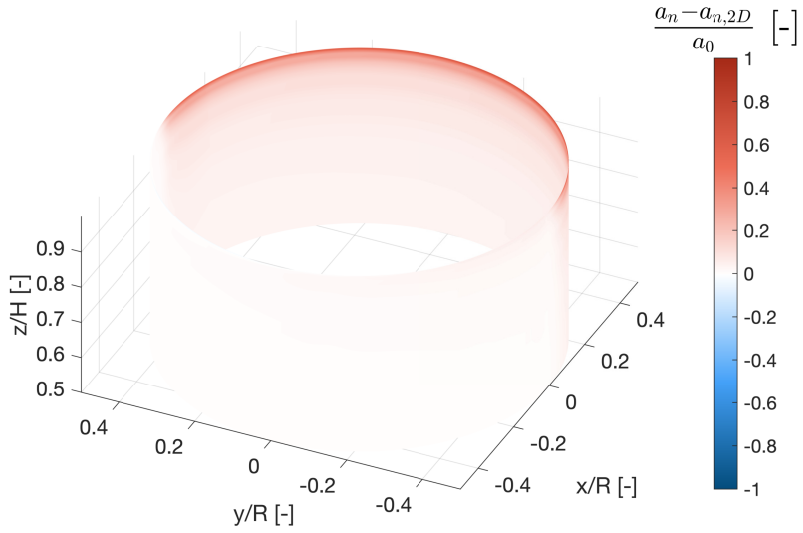

(c) K_T = 0 (fully downwind)

Figure 6.21: Difference between 3D (H/D = 0.5) and 2D (H/D = 100) normal induction a_n, normalized by the streamwise induction factor $a_0 = 1 - \frac{C_{P,3D}}{C_{T,3D}}$

Sinc the ideal power coefficient for the actuator cylinder is defined as $C_P = \int Q_n \cdot a_n \, d\theta$ and the normal loading Q_n is assumed to be constant for each half-cycle, the induction normal to the actuator cylinder surface a_n is an important metric in the power production on the actuator surface. Figure 6.21 shows the difference between the normal induction a_n for a 3D turbine geometry with H/D = 0.5 and a turbine geometry that is approaching 2D conditions (H/D = 100). This difference is normalized by the streamwise induction due to momentum theory ($C_T = 4a(1-a)$). It can be reasoned that there is a significant power loss (arising from the induction difference) occurring near the edges of the cylinder, where tip effects occur, for all three load distributions. This power loss is stronger for the fully upwind and fully downwind load distributions. There is also a noticeable power loss over the rest of the blade span in the azimuthal range where load is applied to the cylinder.

6.6.4 A closer look at power generation for low turbine aspect ratios

Figure 6.19 shows a clear decline in performance for turbines with low H/D and non-uniform loading compared to the 2D equivalent situation.

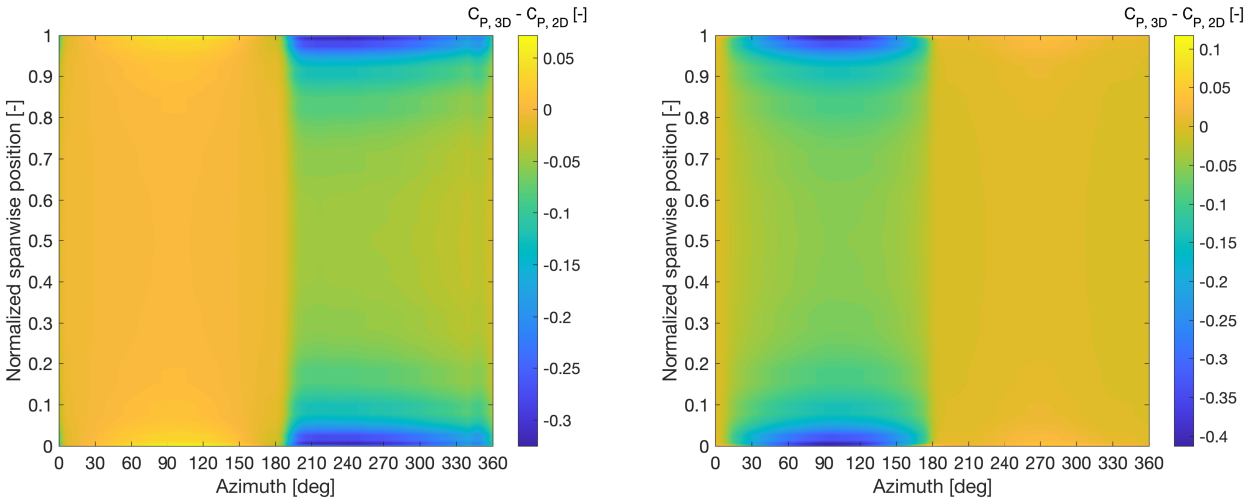

(a) $\frac{C_{T,up}}{C_{T,up}+C_{T,down}}$ = -0.25 (b) $\frac{C_{T,up}}{C_{T,up}+C_{T,down}}$ = 1.25

Figure 6.22: Difference between local power coefficient of a 3D low turbine aspect ratio (H/D = 0.5) and a 2D equivalent (H/D = 100).

Firstly, Figure 6.22 shows the power for a turbine where the normal loading has been shifted downwind and upwind. The corresponding Q_n and Q_t are shown in Figures B.6 and B.7 in Appendix B. Figure 6.22a shows that, when a non-uniform loadform is employed such that the loading is shifted downwind, large losses of power occur over the entire blade, but particularly near the tips. This is likely due to the very high normal loading experienced there, as can be seen in Figure B.6. The upwind side is largely unaffected, though so little power is being generated there that a difference between 3D and 2D would not be obvious. Figure 6.22b shows the same phenomenon occurring but for a shift in loading to the upwind side instead.

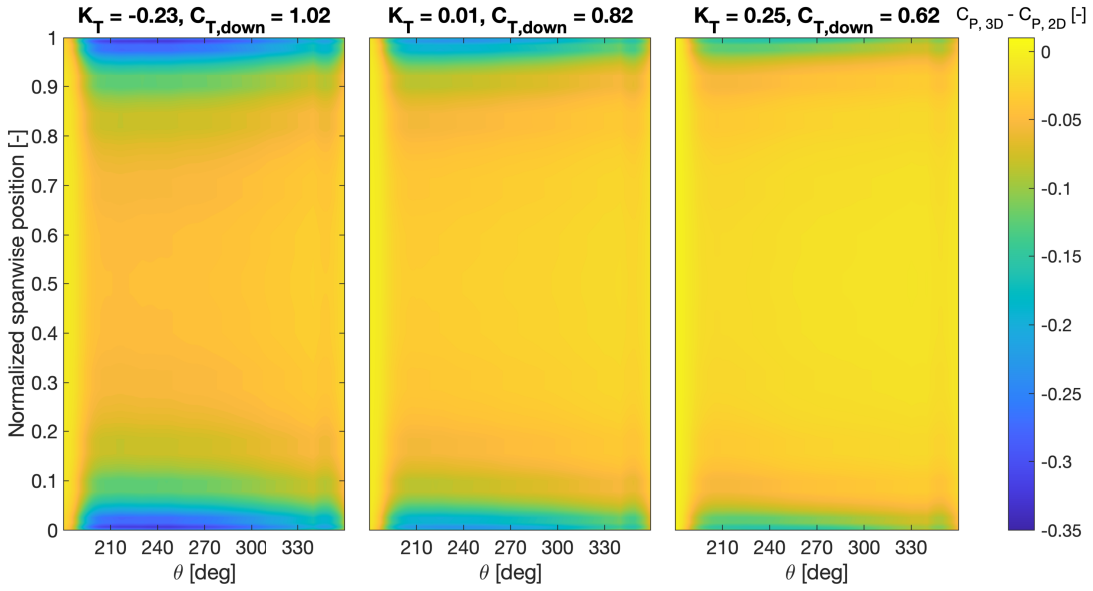

(a) Downwind shift

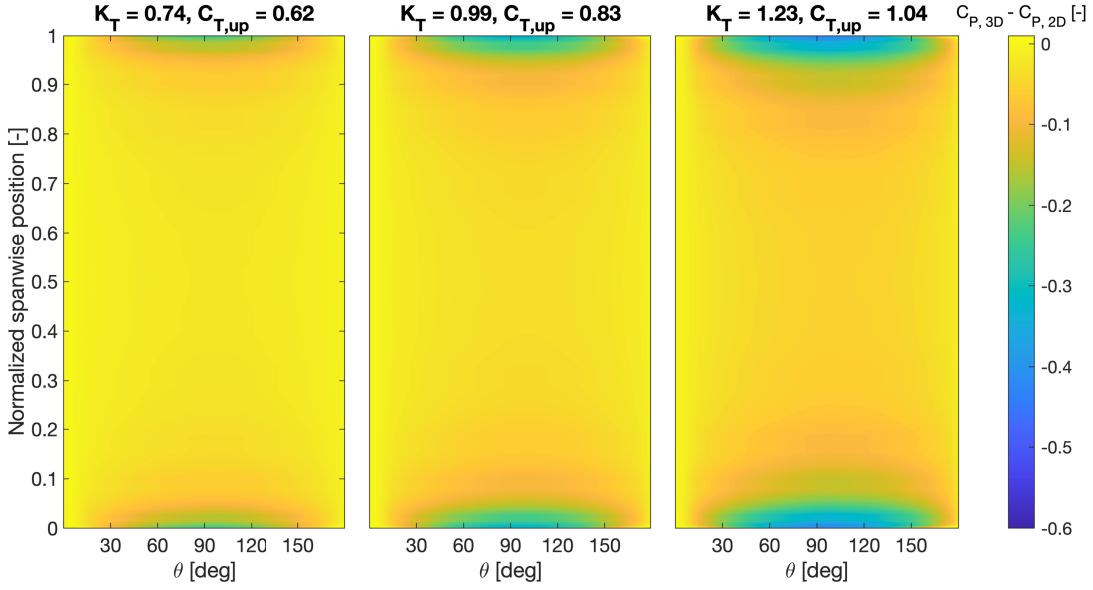

(b) Upwind shift

Figure 6.23: Difference between local power coefficient of a 3D low turbine aspect ratio (H/D = 0.5) and a 2D equivalent (H/D = 100) in the upwind and downwind regions, for different values of $K_T = \frac{C_{T,up}}{C_{T,up}+C_{T,down}}$.

Figure 6.23 shows the difference between 3D and 2D power coefficient for several different values of the load shifting parameter K_T. In Figure 6.23a, the load is shifted downwind to a varying extent. It can be seen that the thrust coefficient over that half-cycle becomes quite high at the extreme values of K_T, and the difference between $C_{P,3D}$ and $C_{P,2D}$ is significant, but this diminishes with less extreme load shifts (and therefore less extreme local thrust coefficients). Interestingly, a larger power deficit near the blade tips is observed for the most extreme downwind load shift in Figure 6.23a than for the most extreme upwind load shift in Figure 6.23b.

6.6.5 Optimizing power generation of a 3D VAWT

With the previous results in mind, it is interesting to note that the 2D pitch optimization (Section 5.2) results in an azimuthal power distribution shown in Figure 6.10 that is skewed towards the upwind side of the rotation.

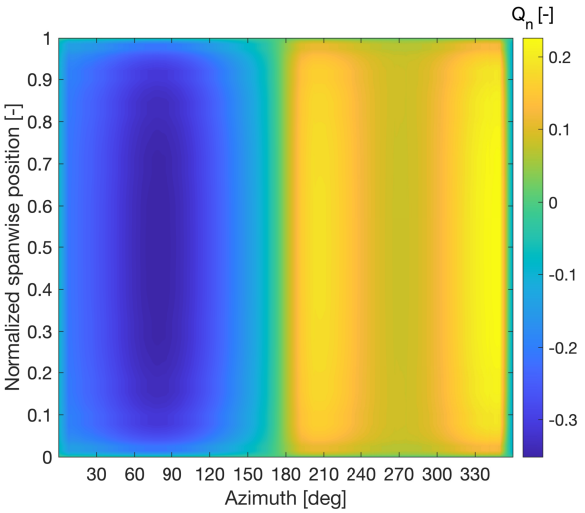

Figure 6.24: Normal loading distribution for the variable-pitch turbine optimized for maximum power, from Section 6.4, resulting in $K_T = 0.69$.

Figure 6.19 demonstrates that power losses in 3D can be minimized for low turbine aspect ratios by perfectly balancing the normal loading upwind and downwind. The normal loading of the VAWT that was optimized for maximum power in Section 6.4 is not uniform, but instead has $K_T = 0.69$, favoring the upwind side. This suggests a dissonance between the 2D optimization and the 3D results, meaning that the power of the low aspect ratio turbine could potentially be further increased by redistributing the normal loading to be uniform, contrary to what the 2D optimization may suggest.

6.7 Sensitivity analysis

6.7.1 Turbine aspect ratio H/D

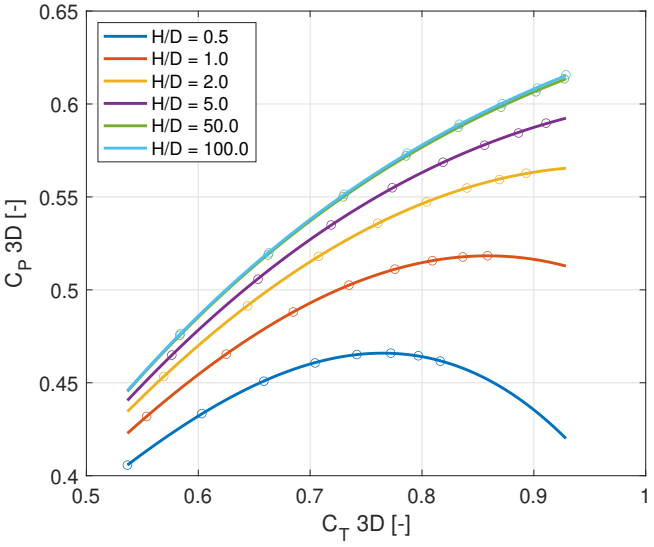

Figure 6.25: C_P-C_T relationship in 3D, generated by varying the solidity $0.05 < \sigma < 0.12$ at a fixed pitch optimum tip speed ratio of $\lambda = 4.28$.

Figure 6.25 shows the relationship between the three-dimensional power and thrust coefficient. It can be seen that the maximum achievable power coefficient for a certain solidity and tip speed ratio decreases with decreasing turbine aspect ratio H/D. Additionally, the C_P-C_T relationship becomes non-linear at lower thrust coefficients for lower turbine aspect ratios. This is an important conclusion which implies that the validity of a linear correction such as the one used in the 2D actuator cylinder model (Section 4.3) is reduced.

When exceeding a thrust coefficient of C_T 0.85, the C_P values for large turbine aspect ratios start to exceed the Betz limit, which could be an indicator of the linear model being insufficient at high thrust loadings. Interestingly, for the 2D actuator cylinder model, this phenomenon doesn't occur until C_T 0.9 (see Figure 5.1).

6.7.2 Number of blades B

HAWC2 NW includes the important assumption that the trailed wake of each blade is independent from the other in the near-wake correction model. Some amount of coupling between the blades exists, due to the fact that the loads calculated in the near-wake model are used as input to the actuator cylinder model, but overall, the blades are considered to be independent. The results of simulating multiple blade numbers in HAWC2 NW for a fixed-pitch turbine have been discussed in Section 4.4.4.

6.7.3 Solidity σ

Figure 6.26 shows how the 3D thrust coefficient is affected by the turbine aspect ratio H/D and solidity σ. For lower turbine aspect ratios, the thrust coefficient is significantly lower due to losses caused by 3D effects such as the tip vortex.

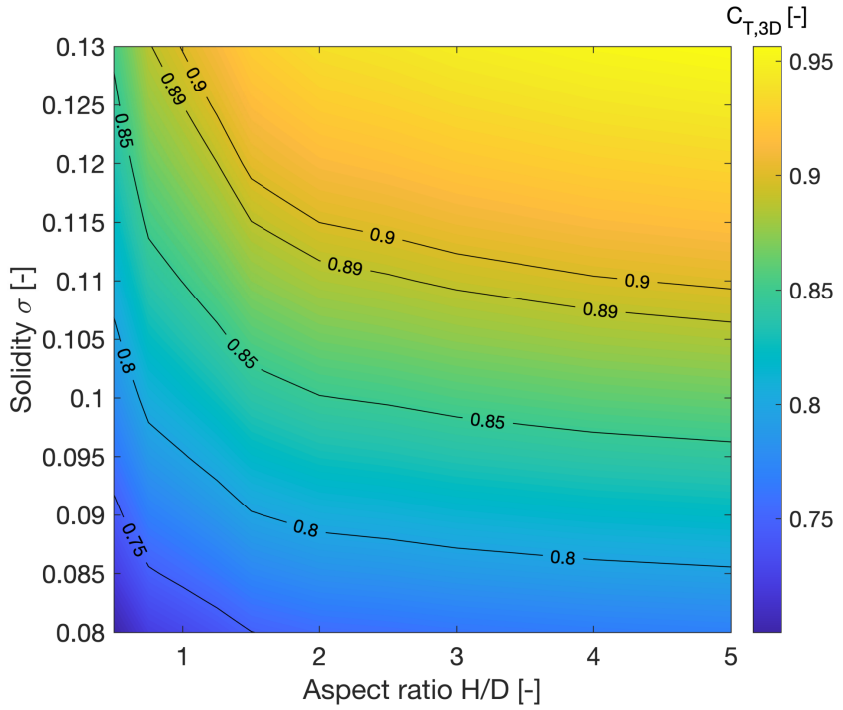

Figure 6.26: Relationship between solidity σ, thrust coefficient C_T and turbine aspect ratio H/D for a pitch distribution resulting in uniformly distributed loading, at a tip speed ratio λ = 4.28.

The simulations in this section, such as the results shown in Figure 6.20, were conducted using prescribed pitch sequences in such a way that combinations of upwind/downwind normal loading result in the same thrust coefficient across a single turbine aspect ratio. Because the same pitch sequence was used however, the thrust coefficient was *not* constant across turbine aspect ratio, instead varying as shown in Figure 6.26.

6.7.4 Tip speed ratio λ and loadform shape parameter b

In order to distinguish between unsteady effects and actual 3D effects on circulation control, a number of measures are taken:

- All simulations in this chapter are carried out at a relatively high tip speed ratio λ = 7, which will require less drastic pitch changes to achieve similar results.
- The chord length is reduced by 10x while the lift as given by the airfoil polar is increased by 10x. This changes the time constants for the bound circulation build-up in the near-wake model, resulting in a faster build-up of trailed vorticity based off of the already near-instantaneous bound vortex strength.[79]
- Any form of dynamic stall modelling is turned off.

These decisions make the approach more consistent with the overall strategy of simulating *without* a dynamic stall model enabled, to focus purely on 3D effects and eliminate unsteady influences. Any meaningful full turbine aerodynamic design would have to be considered with dynamic stall and unsteady flow modelling enabled in order to match real-world conditions.

Additionally, to achieve a loading that is as constant as possible on the downwind/upwind halfcycles, the loadform shape parameter b from Equation (6.5) used to generate the loadform is set to 10. The difference between low λ - low b and high λ - high b is illustrated in Figure 6.27, where simulations for $[\lambda = 4.28, \sigma = 0.096, b = 2]$ and $[\lambda = 7, \sigma = 0.06, b = 10]$ are compared. While the overall thrust coefficient is around $C_T = 0.89$ for both simulations, this is achieved using a drastically

lower pitch input for the higher tip speed ratio (Figures 6.27a and 6.27b) and a more constant normal loading ((Figures 6.27c and 6.27d) with a closer match of the target upwind/downwind loading ratio. This results in a more symmetric relationship between the power coefficient $C_{P,3D}$ and load ratio $K_T = \frac{C_{T,up}}{C_{T,up}+C_{T,down}}$.

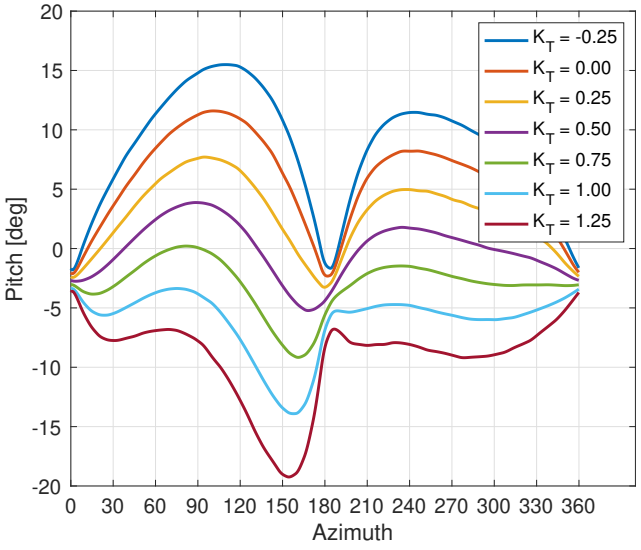

(a) Pitch input for $\lambda = 4.28$, $\sigma = 0.096$ and $b = 2$

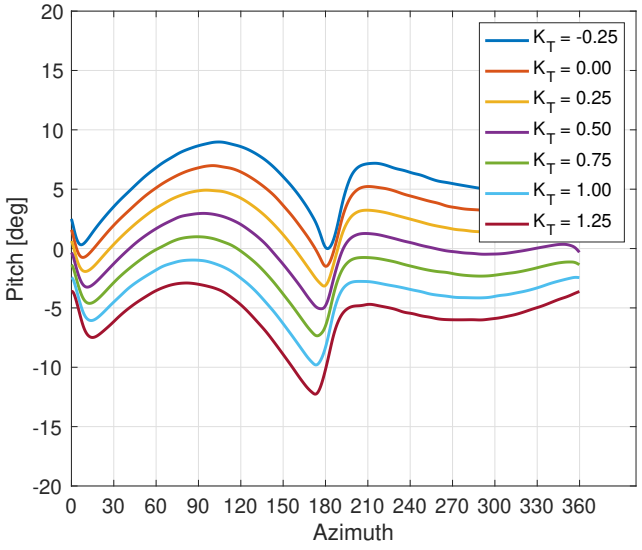

(b) Pitch input for $\lambda = 7$, $\sigma = 0.06$ and $b = 10$

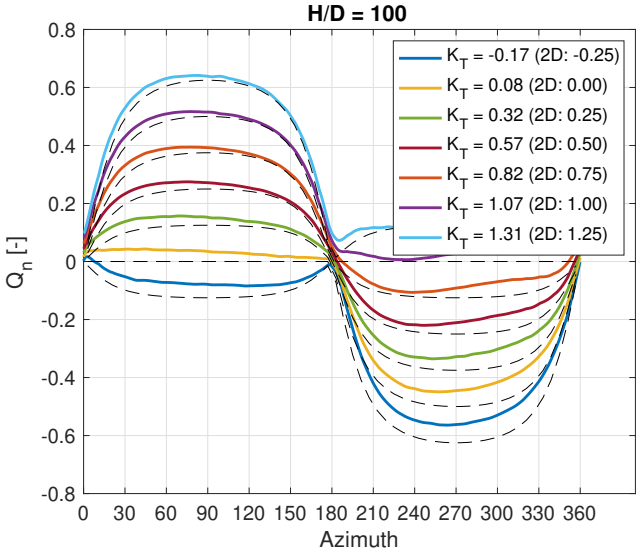

(c) Resulting and target Q_n for $\lambda = 4.28$, $\sigma = 0.096$ and $b = 2$

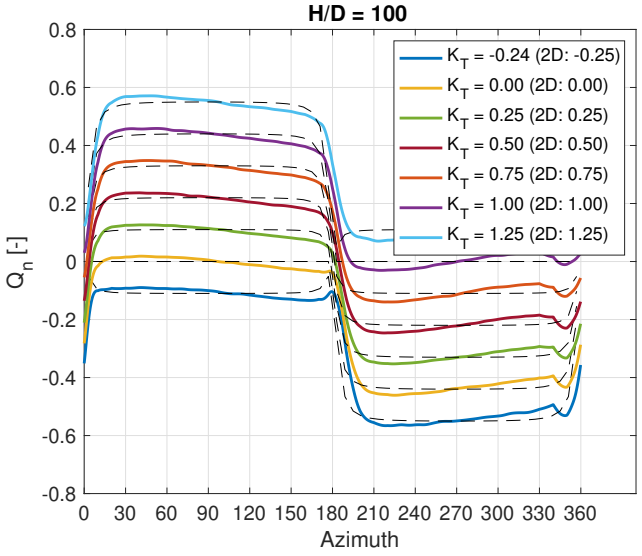

(d) Resulting and target Q_n for $\lambda = 7$, $\sigma = 0.06$ and $b = 10$

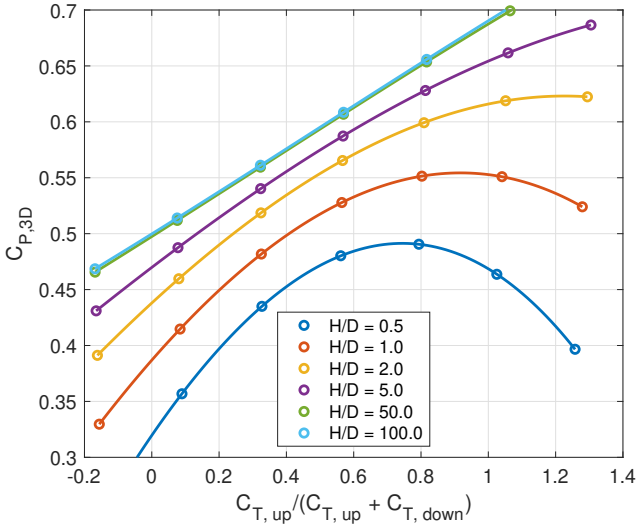

(e) $C_{P,3D}$ for $\lambda = 4.28$, $\sigma = 0.096$ and $b = 2$

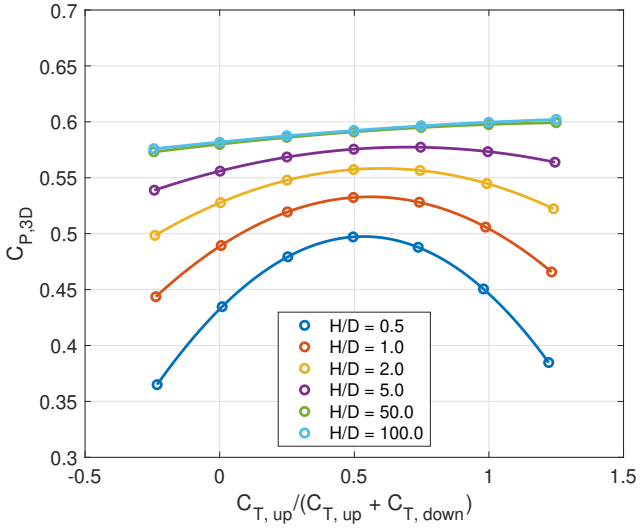

(f) $C_{P,3D}$ for $\lambda = 7$, $\sigma = 0.06$ and $b = 10$

Figure 6.27: Shifting normal loading upwind/downwind, for different turbine aspect ratios.

Chapter 7

Conclusions and recommendations

This chapter will provide an overview of the conclusions that can be drawn from the analysis conducted throughout this thesis. Additionally, several recommendations are made about aspects of the research that merit further investigation, either by further validating the results or by suggesting a topic that could potentially be interesting to pursue given the conclusions from the first part of the chapter. Lastly, a brief description of the contribution that this work provides to the field of vertical axis wind turbine aerodynamics will be given.

7.1 Conclusions

From the first part of this thesis, which discusses the available aerodynamic modelling techniques for vertical axis wind turbines in 2D and 3D, it can be concluded that insufficient medium-fidelity models exist that can reliably resolve the 3D and unsteady effects present in the flow field surrounding the H-rotor VAWT. Such models are not only required to predict the influence on turbine performance of phenomena such as dynamic inflow and turbulence, but also the difference between currently available 2D engineering models and the real performance of a finite-bladed, finite aspect ratio VAWT.

The need for three-dimensional engineering models arises from the existence of 3D effects in the VAWT flow field, consisting mostly of tip effects and finite number of blade effects. These result in a performance decrease that is dependent on the turbine aspect ratio H/D. Relying on two-dimensional models, particularly for turbines with low turbine aspect ratio ($H/D \leqslant 1$) results in significant performance overestimation compared to models which take into account 3D effects.

The quantitative model analysis shows that HAWC2 NW, consisting of an actuator cylinder induction model supplemented by a near-wake model to predict the VAWT flow field in 3D, shows good agreement with higher-fidelity models such as CACTUS and actuator line CFD while taking up a fraction of the computational effort. It should be noted that HAWC2 NW does offer decreased versatility compared to these higher-fidelity models in terms of modelling the turbine wake, due to its assumption that the wake trailed behind each rotor blade is straight and not influenced by the other blades. This implies that the accuracy of the results decreases with increasing number of blades, as blade interaction will start to play a larger role.

The second part of the thesis focuses on the effects of circulation control in 3D, studied using the HAWC2 NW model. It is shown that conducting a pitch optimization using the 2D actuator cylinder model with the objective of maximizing power results in a pitch schedule that does not necessarily provide maximum power in the 3D case, primarily due to the influence of tip effects. Achieving maximum aerodynamic power in 3D is shown to depend largely on whether the loading on the turbine is uniform across the upwind and downwind turbine half-cycles. A symmetric relationship between

load uniformity and turbine power coefficient is discovered that is dependent on the turbine aspect ratio. This relationship suggests that the power losses due to 3D effects can be minimized by implementing a variable pitching strategy that results in uniformly distributed normal loading. This implies that a 2D pitch optimization strategy, which might result in non-uniform loading, is not sufficient in order to optimize the blade pitch of a turbine of finite aspect ratio. A secondary conclusion is that HAWC2 NW is indeed able to capture the 3D effects that lead to a performance decrease due to non-uniform loading on a 3D vertical axis wind turbine, suggesting it could be a more suitable design tool for VAWTs compared to the current HAWC2 iteration, which relies solely on the 2D actuator cylinder model. However, validation of the results using higher-fidelity 3D models and non-uniform loading is necessary to confirm this.

7.2 Recommendations

The recommendations for further research that can be made are split into two categories. The first category encompasses validation studies for the model and its results as well as possible improvements, while the second category contains suggestions for improvements to VAWT performance that can be studied, based on the conclusions drawn in the previous section.

7.2.1 Validation and model improvement

The results of the second part of this thesis, regarding load control and its effects in 3D, should be validated using higher fidelity models to establish the accuracy of the present model, HAWC2 NW. While the first part of this thesis did compare results from HAWC2 NW to higher fidelity models, it did so for a fixed-pitch turbine. Therefore, the results for variable pitch schedules with the intention to obtain a certain (non-)uniform normal loading should be compared to similar set-ups in the higher fidelity models as well, to ensure that the validity of the HAWC2 NW model holds up under such circumstances. Suggestions for higher fidelity models that can be used are:

- CACTUS 3D
- Actuator line CFD models
- 3D actuator cylinder model

The latter model is particularly interesting, as comparing it to the 2D actuator cylinder model exposes the differences between the 2D and 3D VAWT flow field directly without any of the differences between the specific model formulations that could potentially hinder other comparisons. The reader is referred to the work of De Tavernier and Simão Ferreira[22] for an initial investigation using this model to study the 3D effects occurring for VAWTs.

The near-wake model implemented in HAWC2 NW has an important inherent limitation: it does not take into account the influence of one blade on the others directly. There is only an indirect link, consisting of the induced velocities from the trailed vorticity calculated by the near wake model which are used as input for the next iteration of the actuator cylinder model. As far as the actuator cylinder model is concerned, this modifies the velocity triangles resulting in a change in the loads.

A potential improvement to the model could be to modify the method in such a way that it includes the aerodynamic interaction between the blades directly, whilst still retaining the speed and simplicity of the current model. Since the current assumption that all blades are independently modelled can be considered a significant simplification of the real-world flow field, introducing this interaction would further increase the fidelity of the model. This may however be an impractical solution due to the way in which the trailed vorticity model and the actuator cylinder model are coupled, which

precludes such increased interaction. Additionally, since HAWC2 NW is based on a method for modelling trailed vorticity of HAWT blades in standstill conditions, the wake is assumed to be straight (e.g. it continues straight behind the blade) and frozen (e.g. the wake shape is not modified after being shed from the blade). The validity of this assumption is questionable for a real-world turbine and depends highly on the tip speed ratio and chord length of the blades. Introducing a measure of directionality to the wake emanating from each blade could potentially increase accuracy and therefore merits further investigation, although care should be taken to maintain the model's key speed advantage compared to higher fidelity models.

7.2.2 Mitigating the impact of aerodynamic assumptions and simplifications

In the present analysis, several key assumptions were made to simplify the flow field surrounding the VAWT. Future research could focus on one of these assumptions in order to make the aerodynamics resemble those of a real-world VAWT. The key assumptions that enable the present aerodynamic simplification are as follows:

- The flow field is considered to be symmetric around the turbine midplane, without boundary conditions such as the ground or ocean surface. As was briefly discussed in Chapter 2, Kinzel et al.[50] suggests that VAWTs in a farm configuration could potentially benefit from increased planform kinetic energy flux (inflow from above) as compared to HAWTs. As the current analysis assumes purely constant, one-dimensional inflow, this effect is not taken into account.
- A linear airfoil slope is used, creating an unrealistic airfoil polar that is useful when comparing induction models, but should be replaced with real airfoils when attempting to model the performance of a real VAWT. Using real airfoils is also of great importance when considering VAWT rotor design at different scales and speeds; the performance of VAWTs of different solidities and radii may be drastically affected by the local blade Reynolds number.
- Dynamic stall (Section 2.1.2) should be included in the analysis when one wishes to model the fully dynamic flow field and not just 3D effects. The omission of dynamic stall in the present analysis is not completely consistent, since the influence of shed vorticity on the trailed vorticity build-up is indeed modelled by HAWC2 NW even though dynamic stall models are turned off.
- The influence of turbine components such as struts and the tower, as well as possible components related to circulation control methods such as pitch servos and/or partial flaps, should be modelled as the turbine will likely incur an aerodynamic performance penalty due to these.
- The speed at which the pitching mechanism is able to change the blade pitch should be taken into account, as current optimized pitch schedules experience rapid pitch changes that may not be realistic with existing technology.
- Since the near-wake model in HAWC2 NW does not model the far wake, it is not possible to study the influence of a circulation-control modified wake on other nearby turbines.

It should be noted that this list only concerns factors affecting the aerodynamic accuracy of the analysis. To assess the performance of a real-world turbine, one would need to include structural, aeroelastic, control, electrical and possibly hydrodynamic analyses as well.

7.2.3 Improvements to VAWT performance and design

Since the analysis has shown that possible pitch optimization objectives in 2D do not necessarily result in comparable improvements in 3D due to the influence of 3D effects, a logical next step would be to conduct this pitch optimization using a 3D code, such as HAWC2 NW or the 3D actuator cylinder model. This has as a potential side-benefit that the optimization could result in a mitigation of 3D effects, something that is not included in the 2D optimization that has been conducted in this thesis.

Another means of mitigating 3D effects that result in loss of performance could be to introduce twist in the rotor blades towards the tips in an effort to delay the spanwise reduction-to-zero of loads and allow the overall blade loading to approach the two-dimensional case.

An important limitation of the current analysis is that no dynamic stall models were used in the 2D optimization and the 3D model, because the aim was to study 3D effects purely on the induction model, leaving airfoil aerodynamics out of the equation.

The inclusion of dynamic stall will almost certainly raise the issue of the rapidly pitching blades and associated dynamic effects. Optimizing whilst taking this into account may result in less agressive pitch schedules to minimize losses due to rapid pitching, whereas the current optimized pitch schedules often include steep & fast pitch changes at the transition between upwind and downwind turbine half-cycles (see Figure 6.18a, for example). Studying the dynamic effects of rapid pitching is also an essential precursor to any type of aeroelastic analysis on the VAWT in 3D, since dynamic loads much greater than their static equivalents may be generated, which would be detrimental to the overall fatigue load performance of the turbine.

The inclusion of dynamic stall and aeroelastic effects would greatly increase the applicability of the analysis to real-world turbine designs and is therefore recommended to be included in future studies.

The current analysis has only treated full-blade pitching as a means of circulation control, but if the aim is to potentially reduce performance losses due to 3D effects, it would be useful to study whether partial blade pitching could potentially be a viable alternative. Since the inboard region of the blade does not experience as much nuisance from tip effects, it may be better to focus the circulation control efforts on the outboard region. Such partial blade pitching could be carried out using outboard flaps or movable blade tips, for example. These concepts are illustrated in Figure B.10 in Appendix B.4.

Such partial blade pitching would likely reduce the significant cost associated with implementing a pitching system on a real-world turbine, as the pitch control components such as actuators and supporting structure would not need to carry and modify the loads on the entire turbine.

As has been concluded in the previous section, the 3D losses due to load uniformity are highly dependent on the turbine aspect ratio. Therefore, when considering the design of a particularly slender vertical axis wind turbine ($H/D > 2$), the cost associated with implementing a form of circulation control to achieve smoother loading and higher power could potentially be higher than the potential savings compared to a fixed pitch system, since the performance gains are less for higher turbine aspect ratios. Future investigations into the topic of 3D circulation control for VAWTs in real-world applications should therefore include a cost-benefit analysis to determine whether a variable pitch system is financially viable for a specific turbine geometry.

Lastly, due to the nature of the aerodynamic model used in the analysis, even though the shed vorticity is modelled in the far wake by the actuator cylinder model, the trailed vorticity is only modelled very close to the blade (by the near-wake model). Hence, without complete information on the shed and trailing vorticity in the far wake, the influence of one turbine on the next cannot be studied. Several sub-conclusions throughout this thesis and in recent literature[25] point to the drastically modified wake characteristics of a circulation-controlled vertical axis wind turbine. This raises the question of how such turbines operate in a farm configuration and how circulation control strategies can be altered to result in optimized farm performance, rather than optimized individual turbine performance.

7.3 Contribution to the field

Despite the myriad limitations and assumptions that were required to distill the necessary conclusions from this research, several important and valid concepts have been put forth that could aid the design of real vertical axis wind turbine concepts. In summary, the research that has been conducted in this thesis contributes to the field of vertical axis wind turbine aerodynamics in the following ways:

- The turbine aspect ratio H/D has been shown to be an important parameter in determining the losses due to 3D effects compared to a fully 2D VAWT rotor.
- HAWC2 NW has been shown to be a viable and fast means of computing the 3D aerodynamic performance of a VAWT, even though further validation with other, higher-fidelity 3D aerodynamic codes is a must. Additionally, the analysis in HAWC2 NW could quickly be expanded to include its built-in aeroelastic design capabilities, as well as potential flapping mechanisms as an alternative to full-blade pitching.
- Conducting a two-dimensional pitch optimization for circulation controlled VAWTs is insufficient and will result in non-optimal performance in the 3D case.
- A relationship between the turbine aspect ratio, upwind/downwind loading distribution ratio and the power coefficient has been established, providing important insights into the performance of a turbine design with certain geometry and loading distribution without having to conduct a fully three-dimensional simulation first.

Bibliography

[1] B. Akay, C. Simão Ferreira, G. J. Van Bussel, and G. Tescione. Experimental investigation of the wind turbine blade root flow. *48th AIAA Aerospace Sciences Meeting Including the New Horizons Forum and Aerospace Exposition*, pages 1–9, 2010. doi: 10.2514/6.2010-641.

[2] H. Akimoto, Y. Hara, T. Kawamura, T. Nakamura, and Y. S. Lee. A conformal mapping technique to correlate the rotating flow around a wing section of vertical axis wind turbine and an equivalent linear flow around a static wing. *Environmental Research Letters*, 8(4), 2013. ISSN 17489326. doi: 10.1088/1748-9326/8/4/044040.

[3] J. D. Anderson. Fundamentals of aerodynamics. 1984. ISSN 0001-1452. doi: 10.2514/152157.

[4] P. Bachant, A. Goude, and M. Wosnik. Actuator line modeling of vertical-axis turbines. pages 1–21, 2016. URL `http://arxiv.org/abs/1605.01449`.

[5] S. Baleriola, A. Leroy, S. Loyer, P. Devinant, and S. Aubrun. Experimental lift control using fluidic jets on a model wind turbine. *Journal of Physics: Conference Series*, 1037(2), 2018. ISSN 17426596. doi: 10.1088/1742-6596/1037/2/022014.

[6] G. Bangga, T. Lutz, and E. Krämer. Root flow characteristics and 3D effects of an isolated wind turbine rotor. *Journal of Mechanical Science and Technology*, 31(8):3839–3844, 2017. ISSN 1738494X. doi: 10.1007/s12206-017-0728-6.

[7] G. Bangga, A. Dessoky, T. Lutz, and E. Krämer. Improved double-multiple-streamtube approach for H-Darrieus vertical axis wind turbine computations. *Energy*, 182:673–688, 2019. ISSN 03605442. doi: 10.1016/j.energy.2019.06.083.

[8] G. Bangga, A. Dessoky, Z. Wu, K. Rogowski, and M. O. L. Hansen. Accuracy and consistency of CFD and engineering models for simulating vertical axis wind turbine loads. *Energy*, page 118087, 2020. ISSN 0360-5442. doi: 10.1016/j.energy.2020.118087. URL `https://doi.org/10.1016/j.energy.2020.118087`.

[9] L. Bergami, M. Gaunaa, and J. Heinz. Indicial lift response function: An empirical relation for finite-thickness airfoils, and effects on aeroelastic simulations. *Wind Energy*, 16(5):681–693, 2013. ISSN 10954244. doi: 10.1002/we.1516.

[10] A. Bianchini, F. Balduzzi, G. Ferrara, and L. Ferrari. Virtual incidence effect on rotating airfoils in Darrieus wind turbines. *Energy Conversion and Management*, 111:329–338, 2016. ISSN 01968904. doi: 10.1016/j.enconman.2015.12.056. URL `http://dx.doi.org/10.1016/j.enconman.2015.12.056`.

[11] M. Boudreau and G. Dumas. Vortex dynamics in the wake of three generic types of free-stream turbines. *Open Archives of the 16th International Symposium on Transport Phenomena and Dynamics of Rotating Machinery, ISROMAC 2016*, 2016.

[12] M. Boudreau and G. Dumas. Comparison of the wake recovery of the axial-flow and cross-flow

turbine concepts. *Journal of Wind Engineering and Industrial Aerodynamics*, 165(March):137–152, 2017. ISSN 01676105. doi: 10.1016/j.jweia.2017.03.010.

[13] J. Bremseth and K. Duraisamy. Computational analysis of vertical axis wind turbine arrays. *Theoretical and Computational Fluid Dynamics*, 30(5):387–401, 2016. ISSN 14322250. doi: 10.1007/s00162-016-0384-y.

[14] A. J. Buchner, J. Soria, D. Honnery, and A. J. Smits. Dynamic stall in vertical axis wind turbines: Scaling and topological considerations. *Journal of Fluid Mechanics*, 841(April):746–766, 2018. ISSN 14697645. doi: 10.1017/jfm.2018.112.

[15] T. Chatterjee and Y. Peet. Exploring the benefits of vertically staggered wind farms: Understanding the power generation mechanisms of turbines operating at different scales. *Wind Energy*, 22(2):283–301, 2019. ISSN 10991824. doi: 10.1002/we.2284.

[16] A. Choudhry, M. Arjomandi, and R. Kelso. Methods to control dynamic stall for wind turbine applications. *Renewable Energy*, 86:26–37, 2016. ISSN 18790682. doi: 10.1016/j.renene.2015.07.097. URL `http://dx.doi.org/10.1016/j.renene.2015.07.097`.

[17] P. V. D. Chougule and S. R. Nielsen. Simulation of flow over double-element airfoil and wind tunnel test for use in vertical axis wind turbine. *Journal of Physics: Conference Series*, 524(1), 2014. ISSN 17426596. doi: 10.1088/1742-6596/524/1/012009.

[18] P. V. D. Chougule, S. R. Nielsen, and B. Basu. Active blade pitch control for straight bladed darrieus vertical axis wind turbine of new design. *Key Engineering Materials*, 569-570(November 2015):668–675, 2013. ISSN 10139826. doi: 10.4028/www.scientific.net/KEM.569-570.668.

[19] J. O. Dabiri. Potential order-of-magnitude enhancement of wind farm power density via counter-rotating vertical-axis wind turbine arrays. *Journal of Renewable and Sustainable Energy*, 3(4), 2011. ISSN 19417012. doi: 10.1063/1.3608170.

[20] G. J. M. Darrieus. Turbine having its rotating shaft transverse to the flow of the current, 1931. URL `https://patents.google.com/patent/US1835018A/en`.

[21] D. De Tavernier and C. S. Ferreira. An extended actuator cylinder model: Actuator-in-actuator cylinder (AC-squared) model. *Wind Energy*, 22(8):1058–1070, 2019. ISSN 10991824. doi: 10.1002/we.2340.

[22] D. De Tavernier and C. Simão Ferreira. The need for dynamic inflow models for vertical axis wind turbines. *Journal of Physics: Conference Series*, 1356(1), 2019. ISSN 17426596. doi: 10.1088/1742-6596/1356/1/012036.

[23] D. De Tavernier, C. Simão Ferreira, A. Li, U. S. Paulsen, and H. A. Madsen. Towards the understanding of vertical-axis wind turbines in double-rotor configuration. *Journal of Physics: Conference Series*, 1037(2), 2018. ISSN 17426596. doi: 10.1088/1742-6596/1037/2/022015.

[24] D. De Tavernier, T. Griffith, and C. Simão Ferreira. Comparison of 3D aerodynamic models for vertical-axis wind turbines : H-rotor and Φ -rotor. In *TORQUE: the Science of Making Torque from Wind*, number In review, 2020.

[25] D. De Tavernier, C. Simão Ferreira, U. S. Paulsen, and H. A. Madsen. The 3D effects of a vertical-axis wind turbine : rotor and wake induction. In *TORQUE: the Science of Making Torque from Wind*, number In review, Delft, The Netherlands, 2020. European Academy of Wind Energy.

[26] P. Deglaire. *Analytical aerodynamic simulation tools for vertical axis wind turbines*. 2010. ISBN 9789155479138.

[27] K. R. Dixon. The Near Wake Structure of a Vertical Axis Wind Turbine: Including the Development of a 3D unsteady Free-Wake Panel Method of VAWTs. pages 1–217, 2008.

[28] W. F. Durand. Aerodynamic Theory. *Aerodynamic Theory*, 1934. doi: 10.1007/978-3-662-39765-7.

[29] D. M. Eggleston and F. S. Stoddard. *Wind Turbine Engineering Design*. van Nostrand Reinhold, 1987. ISBN 0442221959. URL https://www.osti.gov/biblio/5719832-wind-turbine-engineering-design.

[30] S. Ertem, C. Simão Ferreira, M. Gaunaa, and H. A. Madsen. Aerodynamic optimization of vertical axis wind turbine with trailing edge Flaps. *34th Wind Energy Symposium*, pages 1–23, 2016. doi: 10.2514/6.2016-1735.

[31] E. Ferrer and R. H. Willden. Blade-wake interactions in cross-flow turbines. *International Journal of Marine Energy*, 11:71–83, 2015. ISSN 22141669. doi: 10.1016/j.ijome.2015.06.001. URL http://dx.doi.org/10.1016/j.ijome.2015.06.001.

[32] W. Froude. On the Elementary Relation between Pitch, Slip and Propulsive Efficiency. *Transaction of the Institute of Naval Architects*, (19):22–33, 1920.

[33] M. Gaunaa. *Unsteady Aerodynamic Forces on NACA 0015 Airfoil in Harmonic Translatory Motion*. PhD thesis, Technical University of Denmark, 2002.

[34] Glauert, H. Glauert, W. F. Durand, and H. Glauert. Airplane Propellers. In *Aerodynamic Theory*, volume IV, pages 169–360. Springer, 1935. doi: 10.1007/978-3-642-91487-4{_}3. URL http://dx.doi.org/10.1007/978-3-642-91487-4_3.

[35] D. Greenblatt, M. Schulman, and A. Ben-Harav. Vertical axis wind turbine performance enhancement using plasma actuators. *Renewable Energy*, 37(1):345–354, 2012. ISSN 09601481. doi: 10.1016/j.renene.2011.06.040. URL http://dx.doi.org/10.1016/j.renene.2011.06.040.

[36] D. Greenblatt, A. Ben-Harav, and H. Mueller-Vahl. Dynamic stall control on a vertical-axis wind turbine using plasma actuators. *AIAA Journal*, 52(2):456–462, 2014. ISSN 00011452. doi: 10.2514/1.J052776.

[37] M. Hansen, M. Gaunaa, and H. A. Madsen. A Beddoes–Leishman Type Dynamic Stall Model in State-space and indicial formulations. Technical report, Technical University of Denmark, 2004.

[38] M. O. Hansen. *Aerodynamics of Wind Turbines*. Routledge, Chichester, UK, 5 2015. ISBN 9781315769981. doi: 10.4324/9781315769981. URL http://doi.wiley.com/10.1002/9781119994367.ch3https://www.taylorfrancis.com/books/9781315769981.

[39] Y. Hara, T. Kawamura, H. Akimoto, K. Tanaka, T. Nakamura, and K. Mizumukai. Predicting double-blade vertical axis wind turbine performance by a quadruple-multiple streamtube model. *International Journal of Fluid Machinery and Systems*, 7(1):16–27, 2014. ISSN 18829554. doi: 10.5293/IJFMS.2014.7.1.016.

[40] L. Henriksen, M. Hansen, and N. Poulsen. A simplified dynamic inflow model and its effect on the performance of free mean wind speed estimation. *Wind Energy*, (September 2012):n/a–n/a, 9 2012. ISSN 10954244. doi: 10.1002/we.1548. URL http://doi.wiley.com/10.1002/we.1548.

[41] I. Herráez, B. Akay, G. J. W. van Bussel, J. Peinke, and B. Stoevesandt. Detailed analysis of the blade root flow of a horizontal axis wind turbine. *Wind Energy Science*, 1(2):89–100, 2016. ISSN 2366-7451. doi: 10.5194/wes-1-89-2016.

[42] S. H. Hezaveh and E. Bou-Zeid. Mean kinetic energy replenishment mechanisms in vertical-axis wind turbine farms. *Physical Review Fluids*, 3(9), 2018. ISSN 2469990X. doi: 10.1103/PhysRevFluids.3.094606.

[43] J. Holierhoek, J. de Vaal, A. van Zuijlen, and H. Bijl. Comparing different dynamic stall models.

Wind Energy, 16(1):139–158, 1 2013. ISSN 10954244. doi: 10.1002/we.548. URL http://doi.wiley.com/10.1002/we.548.

[44] D. P. Houf. *Active Pitch Control of a Vertical Axis Wind Turbine*. PhD thesis, Delft University of Technology, 2016.

[45] N. O. Jensen. A note on wind generator interaction. *Risø-M-2411 Risø National Laboratory Roskilde*, pages 1–16, 1983. ISSN 01676105. doi: Riso-M-2411. URL http://www.risoe.dk/rispubl/VEA/veapdf/ris-m-2411.pdf.

[46] R. T. Jones. The unsteady lift of a wing of finite aspect ratio. Technical report, National Advisory Committee for Aeronautics. Langley Aeronautical Laboratory., Langley Field, VA, United States, 1940. URL https://ntrs.nasa.gov/search.jsp?R=19930091758.

[47] T. v. Kármán and J. Burgers. *General Aerodynamic Theory, Perfect Fluids*, volume II. Julius Springer, Berlin, 1935. doi: 10.1002/zamm.19360160114.

[48] J. Katz and A. Plotkin. *Low-speed aerodynamics, from wing theory to panel methods*. 1991. ISBN 0-07-100876-4. doi: 10.2514/3.45563.

[49] J. Katz and A. Plotkin. *Low-Speed Aerodynamics*. Cambridge University Press, 2 2001. ISBN 9780521665520. doi: 10.1017/CBO9780511810329. URL https://www.cambridge.org/core/product/identifier/9780511810329/type/book.

[50] M. Kinzel, Q. Mulligan, and J. O. Dabiri. Energy exchange in an array of vertical-axis wind turbines. *Journal of Turbulence*, 13(38):1–13, 2012. ISSN 14685248. doi: 10.1080/14685248.2013.825725.

[51] T. Knudsen and T. Bak. Simple model for describing and estimating wind turbine dynamic inflow. *Proceedings of the American Control Conference*, (1):640–646, 2013. ISSN 07431619. doi: 10.1109/acc.2013.6579909.

[52] J. Kweder. Applications of Circulation Control, Yesterday and Today. *International Journal of Engineering*, 4(5):411–429, 2010. ISSN 1985-2312.

[53] H. F. Lam and H. Y. Peng. Measurements of the wake characteristics of co- and counter-rotating twin H-rotor vertical axis wind turbines. *Energy*, 131:13–26, 2017. ISSN 03605442. doi: 10.1016/j.energy.2017.05.015. URL http://dx.doi.org/10.1016/j.energy.2017.05.015.

[54] T. J. Larsen and A. Hansen. *How 2 HAWC2, the user's manual*, volume 2. 2015. ISBN 9788755035836.

[55] J. G. Leishman. Challenges in modelling the unsteady aerodynamics of wind turbines. *Wind Energy*, 5(2-3):85–132, 4 2002. ISSN 1095-4244. doi: 10.1002/we.62. URL http://doi.wiley.com/10.1002/we.62.

[56] J. G. Leishman and T. S. Beddoes. A semi-empirical model for dynamic stall. *Journal of the American Helicopter Society*, 1989. ISSN 00028711. doi: 10.4050/jahs.34.3.3.

[57] J. Liu, H. Lin, and J. Zhang. Review on the technical perspectives and commercial viability of vertical axis wind turbines. *Ocean Engineering*, 182(March):608–626, 2019. ISSN 00298018. doi: 10.1016/j.oceaneng.2019.04.086. URL https://doi.org/10.1016/j.oceaneng.2019.04.086.

[58] C. Lubert. On some recent applications of the coanda effect. *International Journal of Acoustics and Vibrations*, 16(3):144–153, 2011. ISSN 10275851. doi: 10.20855/ijav.2011.16.3286.

[59] H. A. Madsen. The actuator cylinder: a flow model for vertical axis wind turbine. Technical Report September, Technical University of Denmark, 1985.

[60] H. A. Madsen. Application of actuator surface theory on wind turbines. *IEA R&D WECS, Joint action on Aerodynamics of wind turbines, Lyngby, Denmark*, (June 2018), 1988.

[61] H. A. Madsen, T. J. Larsen, L. Vita, and U. S. Paulsen. Implementation of the Actuator Cylinder flow model in the HAWC2 code for aeroelastic simulations on Vertical Axis Wind Turbines. In *51st AIAA Aerospace Sciences Meeting including the New Horizons Forum and Aerospace Exposition*, pages 1–12, Reston, Virigina, 1 2013. American Institute of Aeronautics and Astronautics. ISBN 978-1-62410-181-6. doi: 10.2514/6.2013-913. URL http://arc.aiaa.org/doi/10.2514/6.2013-913.

[62] H. A. Madsen, U. S. Paulsen, and L. Vitae. Analysis of VAWT aerodynamics and design using the actuator cylinder flow model. *Journal of Physics: Conference Series*, 555(1), 2014. ISSN 17426596. doi: 10.1088/1742-6596/555/1/012065.

[63] H. A. Madsen, U. S. Paulsen, and L. Vitae. Analysis of VAWT aerodynamics and design using the actuator cylinder flow model. *Journal of Physics: Conference Series*, 555(1), 2014. ISSN 17426596. doi: 10.1088/1742-6596/555/1/012065.

[64] H. A. Madsen, U. S. Paulsen, and L. Vitae. Analysis of VAWT aerodynamics and design using the actuator cylinder flow model. *Journal of Physics: Conference Series*, 555(1), 2014. ISSN 17426596. doi: 10.1088/1742-6596/555/1/012065.

[65] H. A. Madsen, T. Juul Larsen, G. Raimund Pirrung, A. Li, and F. Zahle. Implementation of the blade element momentum model on a polar grid and its aeroelastic load impact. *Wind Energy Science*, 5(1):1–27, 2020. ISSN 23667451. doi: 10.5194/wes-5-1-2020.

[66] K. W. McAlister, O. Lambert, and D. Petot. Application of the Onera Model of Dynamic Stall. *NASA Technical Paper*, 1984. ISSN 01488341.

[67] G. B. McCullough and D. E. Gault. Examples of three representative types of airfoil-section stall at low speed. *Journal of the Franklin Institute*, 215(1):111–113, 1 1933. ISSN 00160032. doi: 10.1016/S0016-0032(33)90161-1. URL https://linkinghub.elsevier.com/retrieve/pii/S0016003233901611.

[68] V. Mendoza and A. Goude. Improving farm efficiency of interacting vertical-axis wind turbines through wake deflection using pitched struts. *Wind Energy*, 22(4):538–546, 2019. ISSN 10991824. doi: 10.1002/we.2305.

[69] A. R. Meyer Forsting, G. R. Pirrung, and N. Ramos-García. A fast vortex-based smearing correction for the actuator line. *Wind Energy Science*, 5(1):349–353, 2020. ISSN 23667451. doi: 10.5194/wes-5-349-2020.

[70] P. G. Migliore, W. P. Wolfe, and J. B. Fanucci. Flow Curvature Effects on Darrieus Turbine Blade Aerodynamics. *Journal of Energy*, 4(2):49–55, 3 1980. ISSN 0146-0412. doi: 10.2514/3.62459. URL http://adsabs.harvard.edu/abs/1980STIN...8115542Mhttps://arc.aiaa.org/doi/10.2514/3.62459.

[71] F. N. Modi and D. N. R. Gilke. Computational Analysis of Various Airfoil Profile on the Performance of H-Darrieus Wind Turbine. *2018 IEEE International Conference on System, Computation, Automation and Networking, ICSCA 2018*, pages 1–5, 2018. doi: 10.1109/ICSCAN.2018.8541245.

[72] J. Murray and M. Barone. The Development of CACTUS, a Wind and Marine Turbine Performance Simulation Code. In *49th AIAA Aerospace Sciences Meeting including the New Horizons Forum and Aerospace Exposition*, number January, pages 1–21, Reston, Virigina, 1 2011. American Institute of Aeronautics and Astronautics. ISBN 978-1-60086-950-1. doi: 10.2514/6.2011-147. URL http://arc.aiaa.org/doi/10.2514/6.2011-147.

[73] B. G. Newman. Actuator-disc theory for vertical-axis wind turbines. *Journal of Wind Engineering and Industrial Aerodynamics*, 15(1-3):347–355, 1983. ISSN 01676105. doi: 10.1016/0167-6105(83)90204-0.

[74] A. Ning. Actuator cylinder theory for multiple vertical axis wind turbines. *Wind Energy Science*, 1(2):327–340, 2016. ISSN 2366-7451. doi: 10.5194/wes-1-327-2016.

[75] R. B. Noll, N. D. Ham, H. M. Drees, and L. B. Nichol. ASI/Pinson 1-kilowatt high-reliability wind system development. Phase 1. Design and analysis. 1982.

[76] V. L. Okulov and J. N. Sørensen. An ideal wind turbine with a finite number of blades. *Doklady Physics*, 53(6):337–342, 2008. ISSN 10283358. doi: 10.1134/S1028335808060128.

[77] I. Paraschivoiu. Double-multiple streamtube model for Darrieus in turbines. In *Second DOE/-NASA Wind Turbines Dynamics Workshop 04/1981; -1:19-25.*, 1981.

[78] G. Pirrung, H. A. Madsen, and S. Schreck. Trailed vorticity modeling for aeroelastic wind turbine simulations in stand still. *Journal of Physics: Conference Series*, 753(4):521–532, 2016. ISSN 17426596. doi: 10.1088/1742-6596/753/4/042007.

[79] G. Pirrung, V. Riziotis, H. A. Madsen, M. Hansen, and T. Kim. Comparison of a coupled near- and far-wake model with a free-wake vortex code. *Wind Energy Science*, 2(1):15–33, 2017. ISSN 2366-7451. doi: 10.5194/wes-2-15-2017.

[80] G. R. Pirrung. Dynamic tip loss modelling for H-VAWTs. 2019.

[81] G. R. Pirrung and M. Gaunaa. Dynamic stall model modifications to improve the modeling of vertical axis wind turbines. 2018. URL `http://orbit.dtu.dk/en/publications/dynamic-stall-model-modifications-to-improve-the-modeling-of-vertical-axis-wind-turbines(62796854-2dcb-4438-8d0c-fdeb59405347).html`.

[82] G. R. Pirrung, M. H. Hansen, and H. A. Madsen. Improvement of a near wake model for trailing vorticity. *Journal of Physics: Conference Series*, 555(1), 2014. ISSN 17426596. doi: 10.1088/1742-6596/555/1/012083.

[83] L. Prandtl and A. Betz. Schraubenpropeller mit geringstem Energieverlust - mit einem Zusatz von L. Prandtl. In A. Dillmann, editor, *Vier Abhandlungen zur Hydrodynamik und Aerodynamik*, chapter 4, pages 88–92. Universitätsverlag Göttingen, Göttingen, 1919.

[84] A. Rezaeiha, H. Montazeri, and B. Blocken. Towards accurate CFD simulations of vertical axis wind turbines at different tip speed ratios and solidities: Guidelines for azimuthal increment, domain size and convergence. *Energy Conversion and Management*, 156(September 2017):301–316, 2018. ISSN 01968904. doi: 10.1016/j.enconman.2017.11.026. URL `https://doi.org/10.1016/j.enconman.2017.11.026`.

[85] A. Rezaeiha, H. Montazeri, and B. Blocken. Active flow control for power enhancement of vertical axis wind turbines: Leading-edge slot suction. *Energy*, 189:116131, 2019. ISSN 03605442. doi: 10.1016/j.energy.2019.116131. URL `https://doi.org/10.1016/j.energy.2019.116131`.

[86] E. Saber, R. Afify, and H. Elgamal. Performance of SB-VAWT using a modified double multiple streamtube model. *Alexandria Engineering Journal*, 57(4):3099–3110, 2018. ISSN 11100168. doi: 10.1016/j.aej.2018.07.009. URL `https://doi.org/10.1016/j.aej.2018.07.009`.

[87] F. Scheurich, T. M. Fletcher, and R. E. Brown. Simulating the aerodynamic performance and wake dynamics of a vertical-axis wind turbine. *Wind Energy*, 14(2):159–177, 2011. ISSN 10954244. doi: 10.1002/we.409.

[88] C. Simão Ferreira. personal communication.

[89] C. Simão Ferreira. *The near wake of the VAWT 2D and 3D views of the VAWT aerodynamics*. PhD thesis, Delft University of Technology, 2009.

[90] C. Simão Ferreira and F. Scheurich. Demonstrating that power and instantaneous loads are decoupled in a vertical-axis wind turbine. *Wind Energy*, 17(3):385–396, 3 2014. ISSN 10954244. doi: 10.1002/we.1581. URL http://doi.wiley.com/10.1002/we.1581.

[91] C. Simão Ferreira, C. Hofemann, K. Dixon, G. Van Kuik, and G. Van Bussel. 3D wake dynamics of the VAWT: Experimental and numerical investigation. In *48th AIAA Aerospace Sciences Meeting Including the New Horizons Forum and Aerospace Exposition*, number January, pages 1–33, 2010. ISBN 9781600867392. doi: 10.2514/6.2010-643.

[92] C. Simão Ferreira, H. A. Madsen, M. Barone, B. Roscher, P. Deglaire, and I. Arduin. Comparison of aerodynamic models for vertical axis wind turbines. *Journal of Physics: Conference Series*, 524 (1), 2014. ISSN 17426596. doi: 10.1088/1742-6596/524/1/012125.

[93] C. Simão Ferreira, D. De Tavernier, and H. A. Madsen. On the 3D flow field of a Vertical Axis Wind Turbine modelled by the Actuator Cylinder. *Wind Energy*, (Unpublished), 2020.

[94] H. Snel. Heuristic modelling of dynamic stall characteristics. In *EWEC-Conference*. Bookshop for Scientific Publications, 1997.

[95] H. Snel and J. G. Schepers. Engineering models for dynamic inflow phenomena. *Journal of Wind Engineering and Industrial Aerodynamics*, 39(1-3):267–281, 1992. ISSN 01676105. doi: 10.1016/0167-6105(92)90552-L.

[96] C. E. Soraghan, W. E. Leithead, H. Yue, and J. Feuchtwang. Double multiple streamtube model for variable pitch vertical axis wind turbines. *31st AIAA Applied Aerodynamics Conference*, pages 1–12, 2013. doi: 10.2514/6.2013-2802.

[97] J. N. Sørensen. General Momentum Theory for Horizontal Axis Wind Turbines. In *Research Topics in Wind Energy*, volume 4, pages 43–58. Springer, 2016. ISBN 9783319221137. doi: 10.1007/978-3-319-22114-4{_}4. URL http://link.springer.com/10.1007/978-3-319-22114-4_4.

[98] J. N. Sørensen, W. Z. Shen, and X. Munduate. Analysis of wake states by a full field actuator disc model. *Wind Energy*, 1(2):73–88, 1998. ISSN 10954244. doi: 10.1002/(sici)1099-1824(199812)1:2⟨73::aid-we12⟩3.0.co;2-l.

[99] Stig Øye. Unsteady wake effects caused by pitch-angle changes. In *IEA R&D WECS Joint Action on Aerodynamics of Wind Turbines*, pages 58–79, 1986.

[100] Stig Øye. Dynamic stall, simulated as a time lag of separation. In *Proceedings of the 4th IEA Symposium on the Aerodynamics of Wind Turbines*, 1991.

[101] J. H. Strickland. The Darrieus turbine: a performance prediction model using multiple streamtubes. Technical report, Sandia Laboratories, 1975. URL https://www.osti.gov/biblio/5004816-darrieus-turbine-performance-prediction-model-using-multiple-streamtubes.

[102] J. H. Strickland, B. T. Webster, and T. Nguyen. A Vortex Model of the Darrieus Turbine: An Analytical and Experimental Study. *Journal of Fluids Engineering*, 101(4):500–505, 12 1979. ISSN 0098-2202. doi: 10.1115/1.3449018. URL https://asmedigitalcollection.asme.org/fluidsengineering/article/101/4/500/409476/A-Vortex-Model-of-the-Darrieus-Turbine-An.

[103] R. J. Templin. Aerodynamic performance theory for the NRC vertical axis wind turbine. Technical report, 1974.

[104] T. Theodorsen. General theory of aerodynamic instability and the mechanism of flutter. Technical Report 6, National Advisory Committee for Aeronautics, 6 1935. URL https://linkinghub.elsevier.com/retrieve/pii/S0016003235920221.

[105] E. B. Tingey and A. Ning. Development of a parameterized reduced-order vertical-axis wind turbine wake model. *Wind Engineering*, 2019. ISSN 2048402X. doi: 10.1177/0309524X19849864.

[106] C. Tongchitpakdee, S. Benjanirat, and L. N. Sankar. Numerical studies of the effects of active and passive circulation enhancement concepts on wind turbine performance. *Journal of Solar Energy Engineering, Transactions of the ASME*, 128(4):432–444, 2006. ISSN 01996231. doi: 10.1115/1.2346704.

[107] S. Van Der Horst, J. Van De Wiel, C. Simão Ferreira, and N. R. García. Flow curvature effects for VAWT: A review of virtual airfoil transformations and implementation in XFOIL. In *34th Wind Energy Symposium*, number January, pages 1–9, 2016. ISBN 9781624103957. doi: 10.2514/6.2016-1734.

[108] G. A. van Kuik. *On the limitations of Froude's actuator disc concept*. PhD thesis, Technische Universiteit Eindhoven, 1991.

[109] D. Vandenberghe and E. Dick. Second order harmonic pitch control for straight bladed vertical axis wind turbines. *IN: EWEC '86, EUROPEAN WIND ENERGY ASSOC. CONF. & EXHIB. PROC., (ROME, ITALY: OCT. 7-9, 1986), W. PALZ; E. SESTO (EDS.)*, 1986.

[110] A. Vergaerde, T. De Troyer, L. Standaert, J. Kluczewska-Bordier, D. Pitance, A. Immas, F. Silvert, and M. C. Runacres. Experimental validation of the power enhancement of a pair of vertical-axis wind turbines. *Renewable Energy*, 146:181–187, 2020. ISSN 18790682. doi: 10.1016/j.renene.2019.06.115.

[111] R. E. Walters and P. G. Migliore. The circulation controlled vertical axis wind turbine. *THIRD BIENNIAL CONF. & WORKSHOP ON WIND ENERGY CONVERSION SYSTEMS , MASSACHUSETTS, U.S.A. JBF SCI. CORP.*, 1977.

[112] J. P. Wilhelm, E. D. Pertl, F. A. Pertl, and J. E. Smith. Performance Predictions of a Circulation Controlled-Vertical Axis Wind Turbine With Solidity Control. In *ASME 2009 3rd International Conference on Energy Sustainability, Volume 2*, pages 1001–1007. ASME, 2009. ISBN 978-0-7918-4890-6. doi: 10.1115/ES2009-90350. URL http://proceedings.asmedigitalcollection.asme.org/proceeding.aspx?articleid=1648108.

[113] R. M. Williams and I. C. Cheeseman. *Potential Acoustic Benefits of Circulation Control Rotors*. 1978. ISBN 1111111111.

[114] S. Xie, C. L. Archer, N. Ghaisas, and C. Meneveau. Benefits of collocating vertical-axis and horizontal-axis wind turbines in large wind farms. *Wind Energy*, 20(1):45–62, 1 2017. ISSN 10991824. doi: 10.1002/we.1990. URL http://doi.wiley.com/10.1002/we.1990.

[115] A. Zanon, P. Giannattasio, and C. Simão Ferreira. A vortex panel model for the simulation of the wake flow past a vertical axis wind turbine in dynamic stall. *Wind Energy*, 16(5):661–680, 7 2013. ISSN 10954244. doi: 10.1002/we.1515. URL http://doi.wiley.com/10.1002/we.1515.

[116] M. Zhang and R. J. Stevens. Exploring a better turbine layout in vertically staggered wind farms. *Journal of Physics: Conference Series*, 1037(7):072041, 6 2018. ISSN 1742-6588. doi: 10.1088/1742-6596/1037/7/072041. URL http://stacks.iop.org/1742-6596/1037/i=7/a=072041?key=crossref.0a453f92c9a38a19b1fb1c2fb874ff7c.

[117] Z. Zhao, R. Wang, W. Shen, T. Wang, B. Xu, Y. Zheng, and S. Qian. Variable pitch approach for performance improving of straight-bladed VAWT at rated tip speed ratio. *Applied Sciences (Switzerland)*, 8(6), 2018. ISSN 20763417. doi: 10.3390/app8060957.

Appendix A

HAWC2 NW simulation set-up

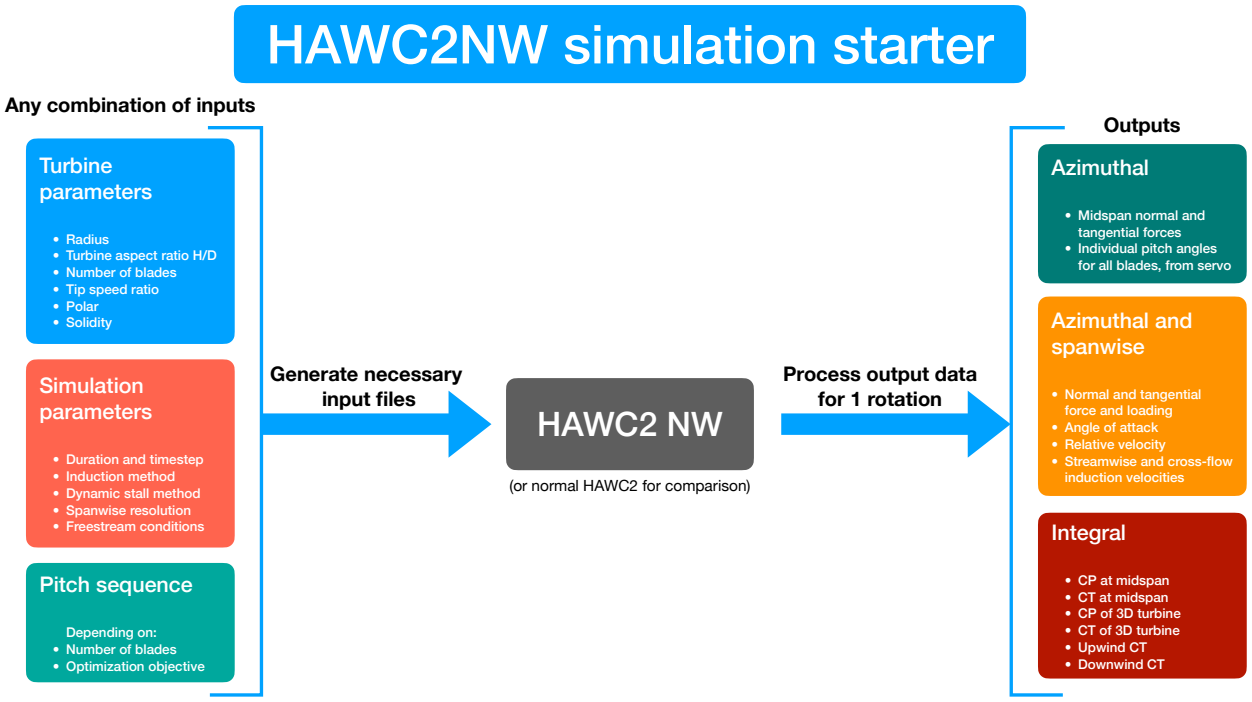

Figure A.1: Diagram of the simulation set-up by which results are obtained from HAWC2 NW.

Appendix B

HAWC2NW 3D results

B.1 Maximizing power

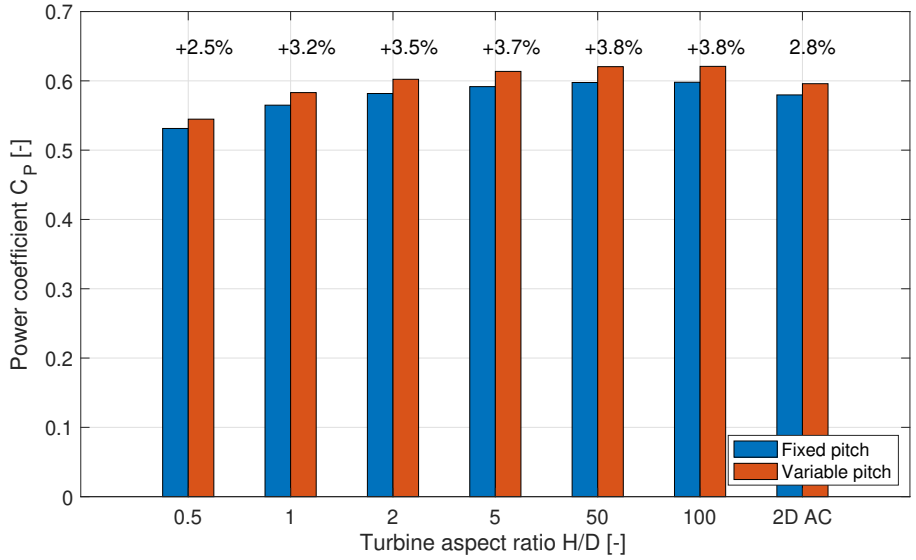

(a) Midspan power coefficient

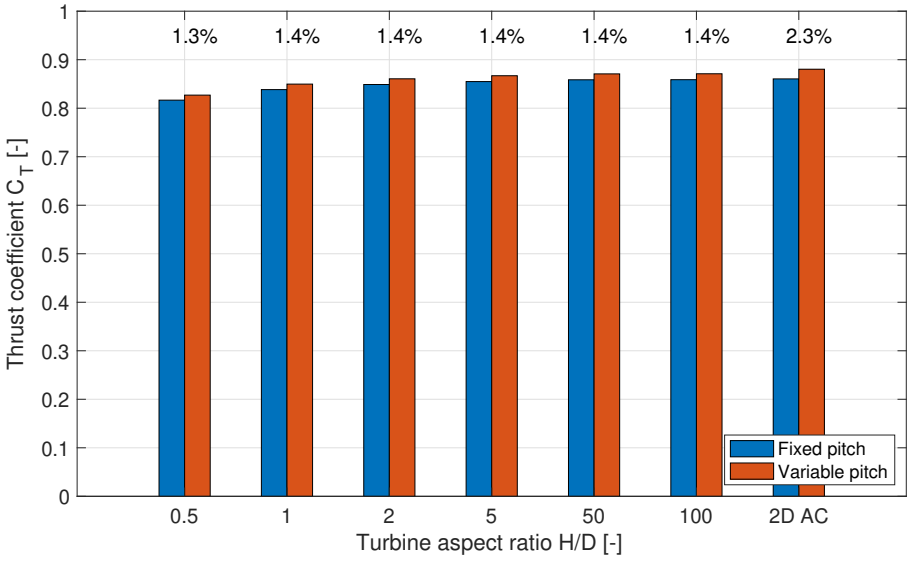

(b) Midspan thrust coefficient

Figure B.1: Midspan power and thrust coefficients for fixed and variable pitch, for varying turbine aspect ratio H/D. Optimized for maximum power.

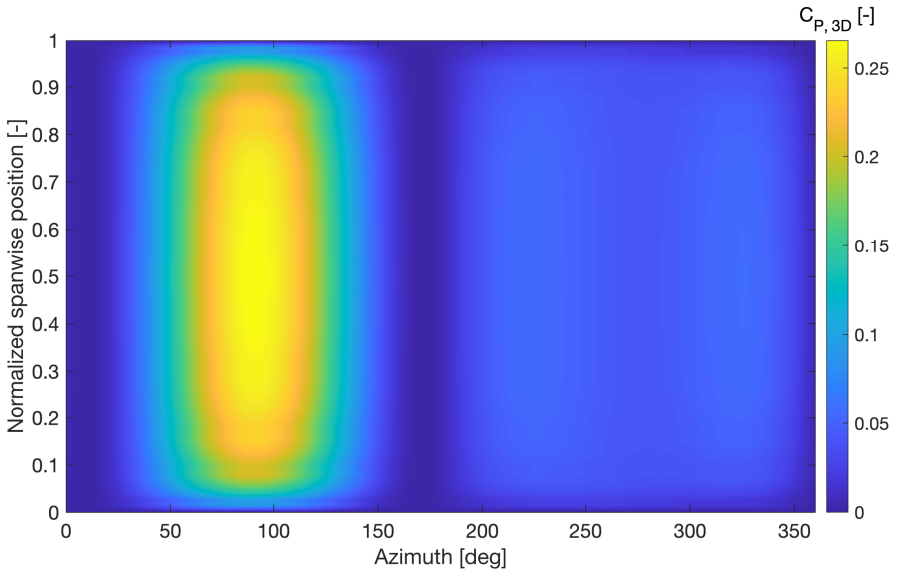

Figure B.2: Local power coefficient of the fixed-pitch turbine.

B.2 Normal loading limited to 0.2

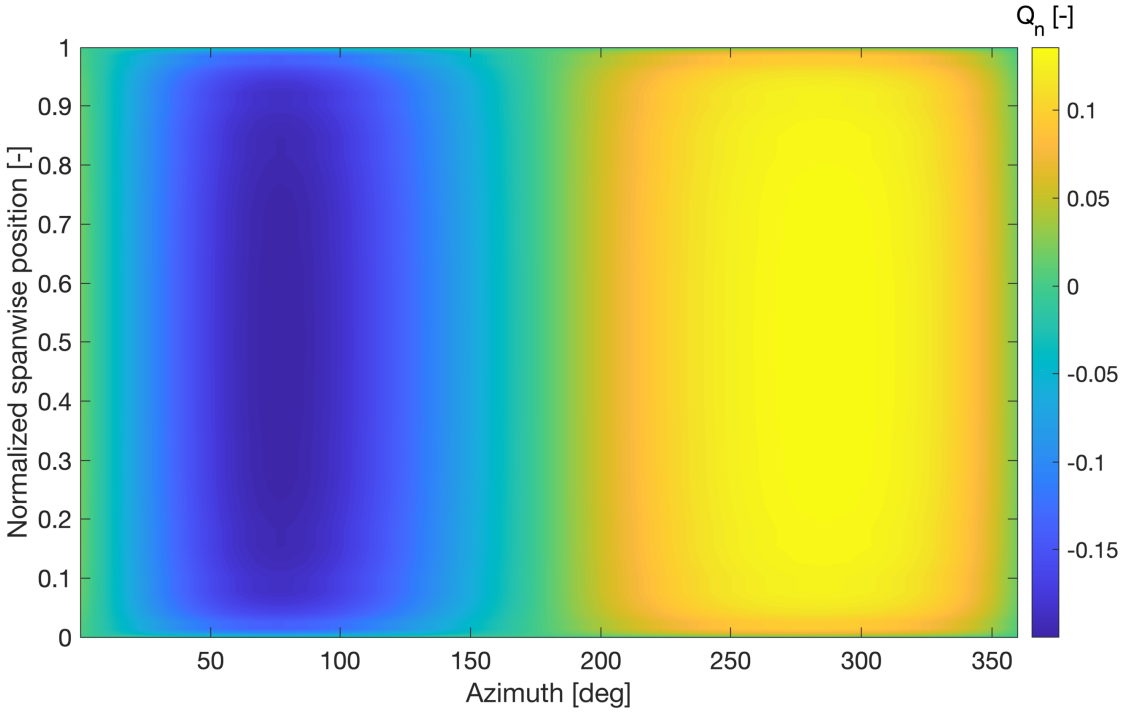

Figure B.3: Normal loading Q_n using modified pitch sequence in HAWC2 NW with H/D = 0.5.

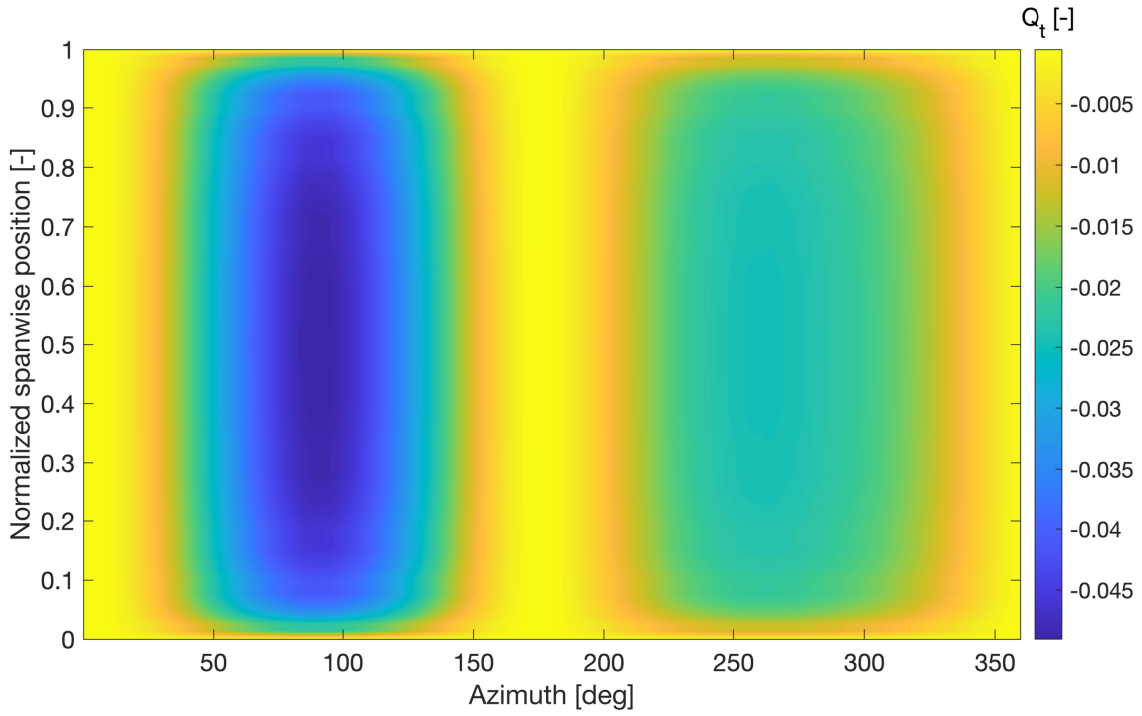

Figure B.4: Tangential loading Q_t using modified pitch sequence in HAWC2 NW with H/D = 0.5.

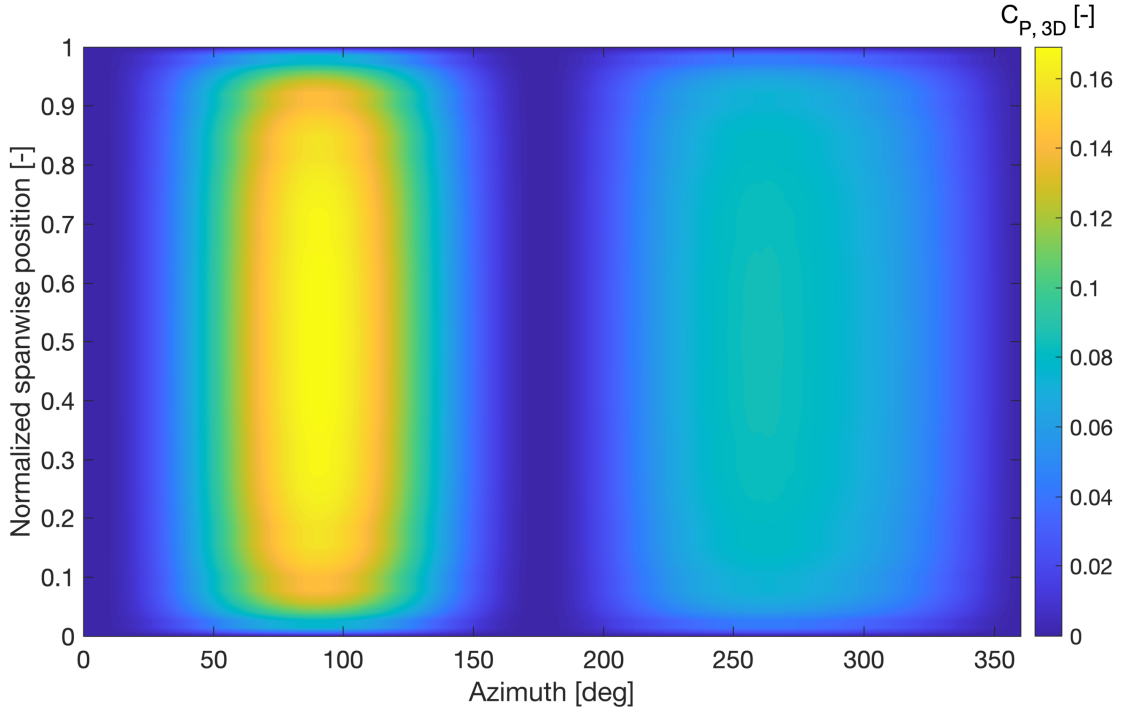

Figure B.5: Local power coefficient C_P as a function of azimuth and spanwise position for a fixed-pitch VAWT.

B.3 Loadshifting

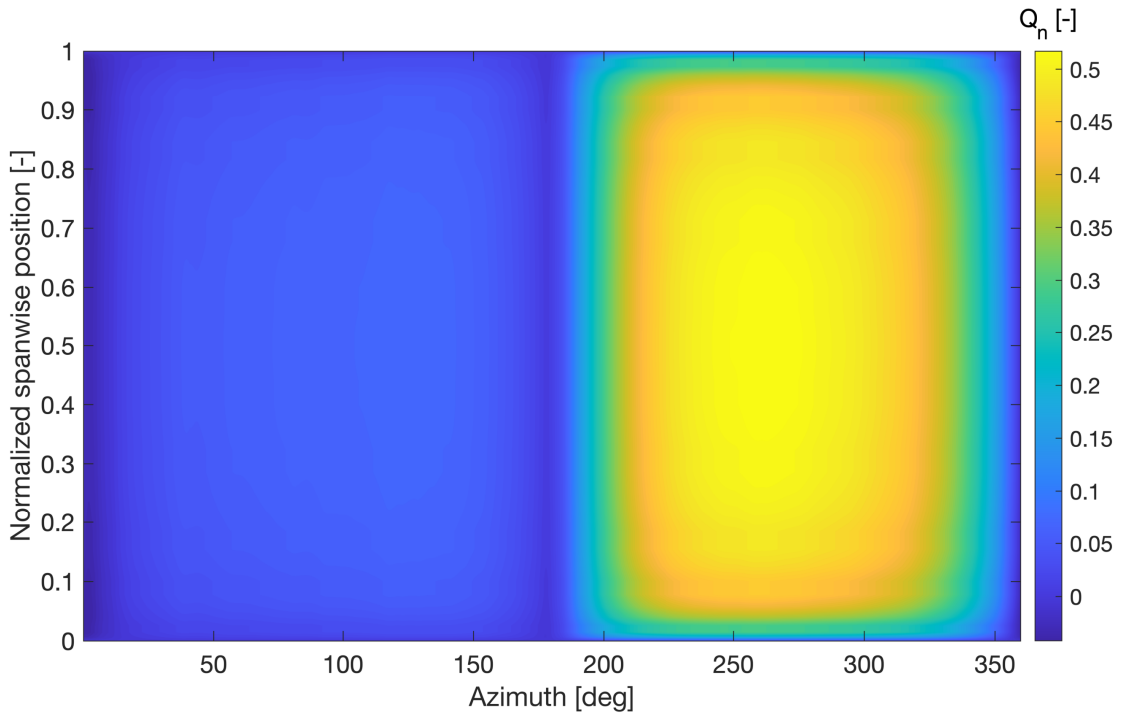

(a) $\frac{C_{T,up}}{C_{T,up}+C_{T,down}}$ = -0.15

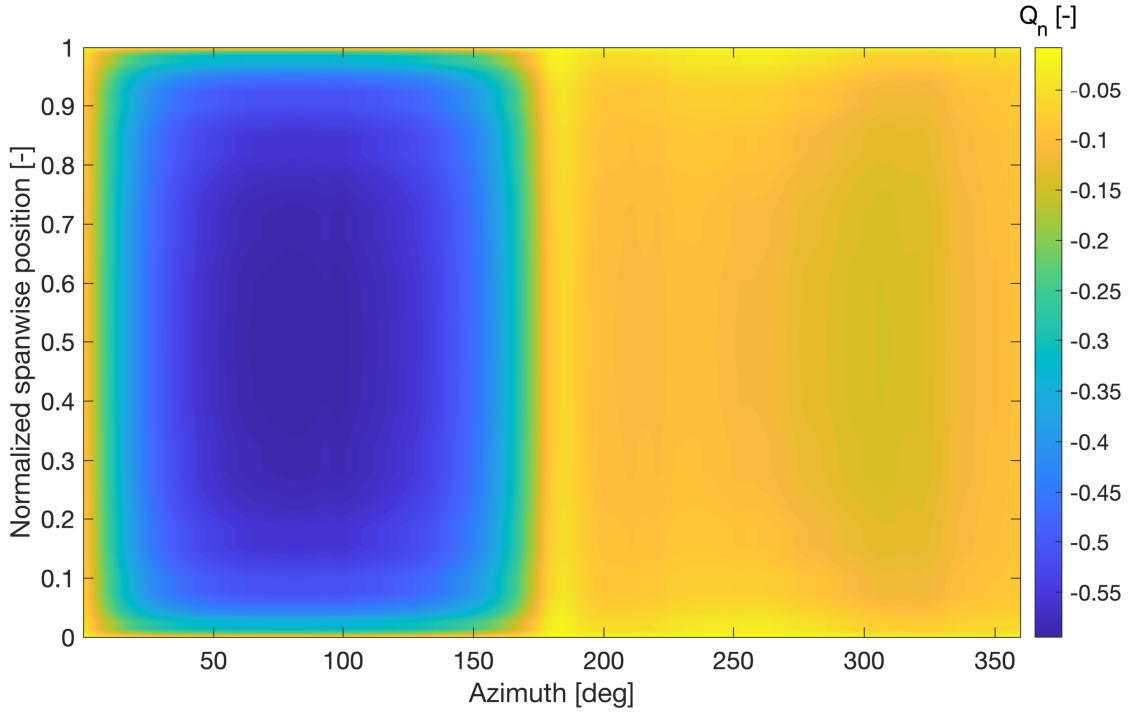

(b) $\frac{C_{T,up}}{C_{T,up}+C_{T,down}}$ = 1.26

Figure B.6: Normal loading distribution Q_n shifted downwind and upwind for $\lambda = 4.28$, $\sigma = 0.096$.

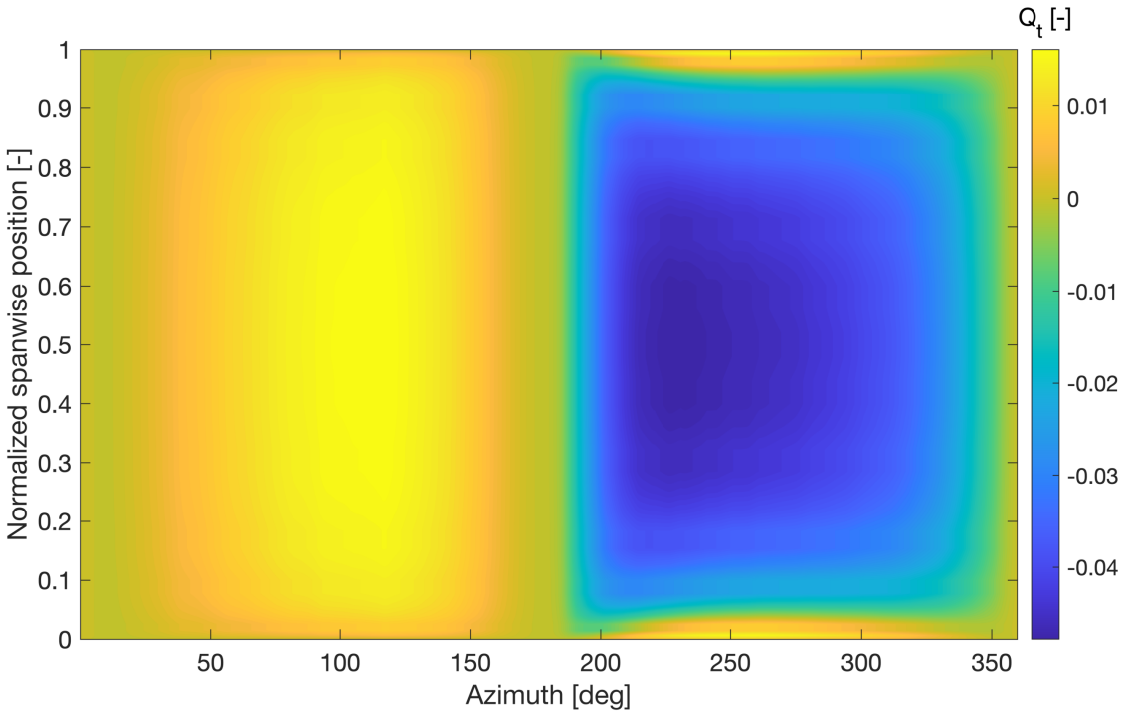

(a) $\frac{C_{T,up}}{C_{T,up}+C_{T,down}}$ = -0.15

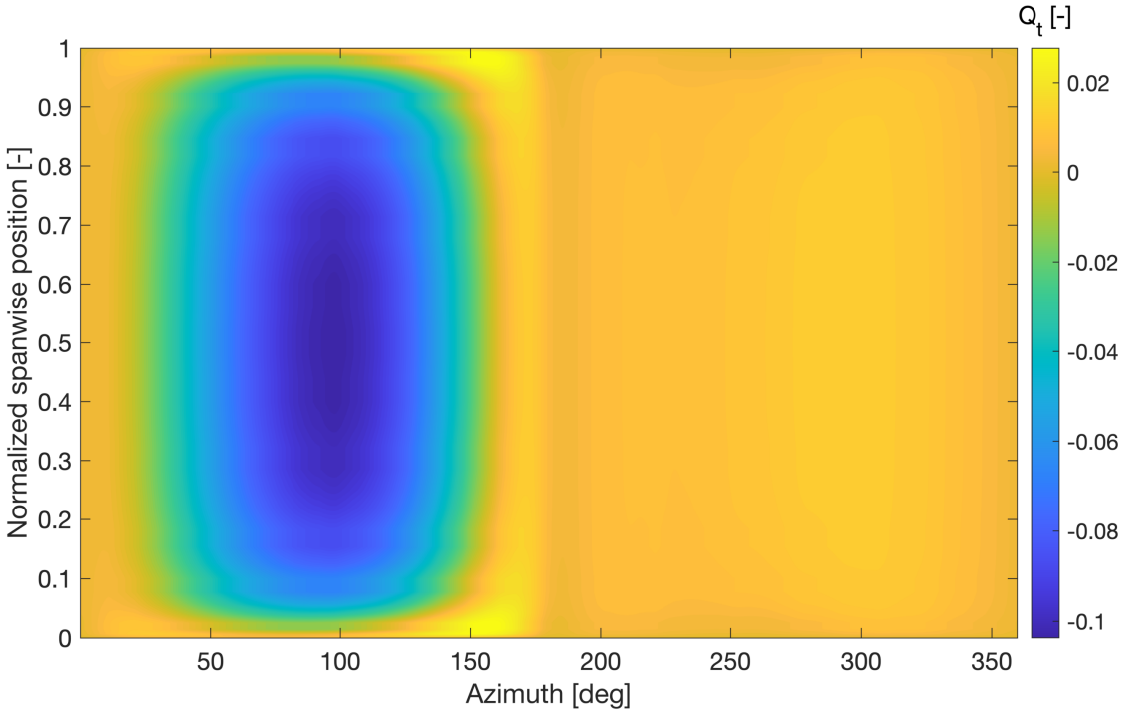

(b) $\frac{C_{T,up}}{C_{T,up}+C_{T,down}}$ = 1.26

Figure B.7: Normal loading distribution Q_n shifted downwind and upwind for $\lambda = 4.28$, $\sigma = 0.096$.

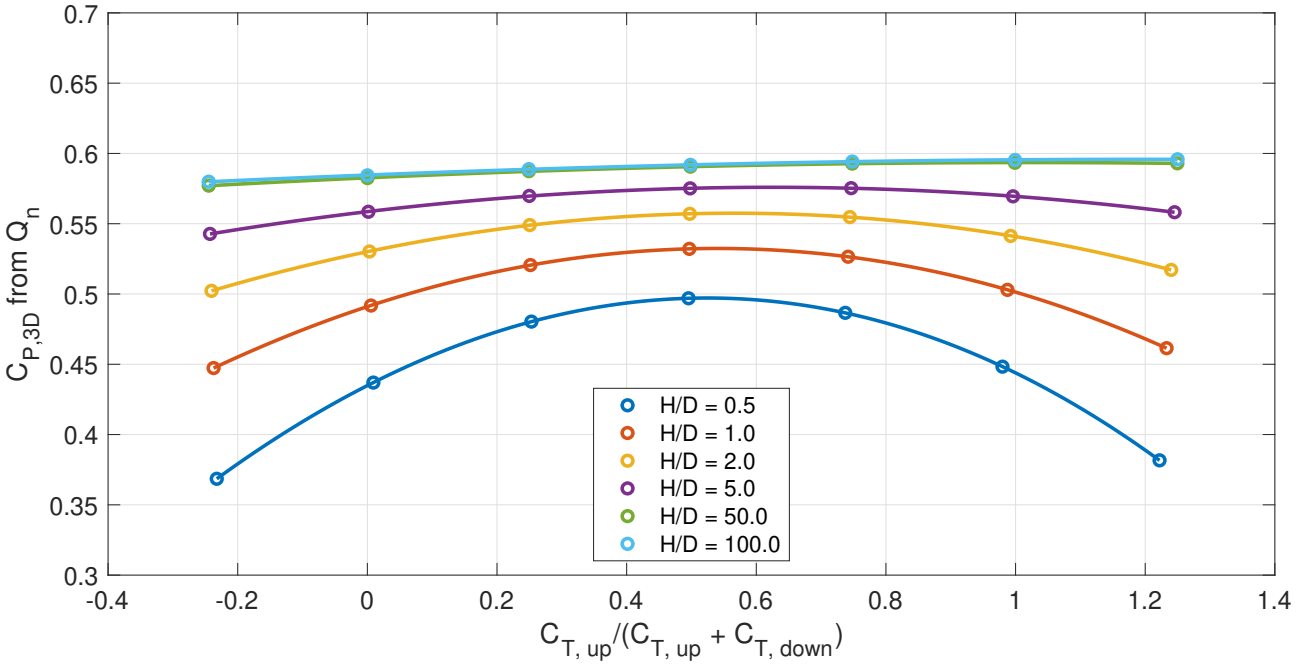

Figure B.8: 3D ideal power coefficient $C_{P,3D}$ calculated from the normal loading Q_n and normal velocity V_n using Equation (6.9) for varying distributions of normal loading upwind/downwind, for different turbine aspect ratios. Datapoints are fitted using a 3rd-degree polynomial to better illustrate the differences between turbine aspect ratios. $\lambda = 7$, $\sigma = 0.06$.

Figure B.9: Ratio of 3D to 2D (H/D = 100) power coefficient, for varying distributions of normal loading upwind/downwind, for different turbine aspect ratios. $\lambda = 7$, $\sigma = 0.06$ (Animated figure, please use Adobe Acrobat Reader for best results)

B.4 Alternatives to full-blade pitching

Figure B.10: Illustrations of different methods of circulation control by active pitching: full-blade, partial-blade and flapped. (Animated figure, please use Adobe Acrobat Reader for best results)